Ammonia and ion studies in the CERN CLOUD chamber

Dissertation

zur Erlangung des Doktorgrades

der Naturwissenschaften

vorgelegt beim Fachbereich 11 Geowissenschaften/ Geographie

der Johann Wolfgang Goethe-Universität

in Frankfurt Am Main

Von Joschka Pfeifer

Aus Heidelberg

Frankfurt 2022

Vom Fachbereich 11 Geowissenschaften/ Geographie der

Johann Wolfgang von Goethe Universität als Dissertation angenommen.

Dekan: Prof. Dr. Jürgen Runge

Gutachter: Prof. Dr. Jasper Kirkby

Prof. Dr. Joachim Curtius

Datum der Disputation:

Abstract

This work describes the development and characterization of two instruments and their data evaluation, which contributes to a better understanding of new particle formation and growth, as well as their interactions with clouds. Both instruments were characterized at the Cosmics Leaving Outdoor Droplets (CLOUD) experiment at the European Center for Nuclear Research (CERN).

The first instrument is a protonated water cluster chemical ionization-atmospheric pressure interface time-of-flight mass spectrometer (Water Cluster CI-APi-TOF). It was developed to selectively measure basic compounds, such as ammonia and amines, with low detection limits and fast response times. Measurements at the CLOUD chamber show ammonia detection limits of 0.5 pptv at 278K (80% relative humidity), with instrumental backgrounds of less than 4 pptv. Thanks to the low instrumental background and the fast response time, the possible role of ammonia in particle nucleation and growth could be investigated. It was shown that ammonia and nitric acid can efficiently condense on newly formed particles, which leads to rapid particle growth, even at high condensation sinks (under haze conditions). During these experiments, the measurements of the Water Cluster CI-APi-TOF showed that ammonia partitions from the gas into the particle phase. In the future, the Water Cluster CI-APi-TOF can contribute to further understand the role of ammonia in new particle formation.

The second instrument was developed to generate multiply charged particles and to enable experiments on their effects under atmospherically relevant conditions at CLOUD. The instrument is based on electrospray ionization and was named CHarged AeRosol GEnerator (CHARGE). The first experiments demonstrated the functionality of CHARGE and the injection of the particles into the CLOUD chamber was optimized. Several experiments to evaluate the effects of multiply charged particles under atmospherically relevant conditions have been designed and performed at CLOUD. All experiments involve the direct comparison between multiply charged particles and previously neutralized particles, both sets of particles produced via CHARGE. These direct comparisons show that multiply charged particles are successfully transported from CHARGE into the CLOUD chamber. Experiments on charge transfer between multiply charged particles with Cloud Condensation Nuclei (CCN) and expansion experiments comparing multiply charged particles with neutralized particles were performed. In the future, these experiments can contribute to better understand aerosol–cloud interactions.

A method to quantitatively measure ion-aerosol attachment coefficients as a function of number of charges was developed. The method utilizes data collected during the experiments at the CLOUD chamber. For the calculations, data from Differential Mobility Analyzer (DMA) and Electrical Aerosol Analyzer (EAA) instruments were used, namely the Neutral cluster and Air Spectrometer (NAIS). The measured coefficients were compared to leading theories in the field, showing good agreement with limiting sphere theories. The measurements and the associated experiments provide valuable insights for instruments that detect atmospheric ions or particles and operate under the assumption of charge equilibrium.

Kurzzusammenfassung

Diese Arbeit beschreibt die Entwicklung und Charakterisierung von zwei Instrumenten, die zum Verständnis der Bildung neu gebildeter atmosphärischer Partikel, ihres anschließenden Wachstumsprozesses sowie ihrer Wechselwirkungen mit Wolken beitragen. Beide Instrumente wurden beim Cosmics Leaving Outdoor Droplets (CLOUD) Experiment am Europäischen Zentrum für Kernforschung (CERN) charakterisiert. Das erste Instrument ist ein Flugzeit-Massenspektrometer, welches den Probeluftstrom unter Verwendung von protonierten Wasserclustern bei Atmosphärendruck ionisiert (Water Cluster CI-APi-TOF). Es wurde entwickelt, um Basen wie Ammoniak und verschiedene Amine mit niedrigen Nachweisgrenzen und kurzen Reaktionszeiten selektiv zu messen. Messungen an der CLOUD Kammer zeigen Detektionslimits von 0,5 pptv bei 278 K (80 % relative Luftfeuchtigkeit) für Ammoniak, bei instrumentellen Hintergründen von etwa 4 pptv. Dank des geringen instrumentellen Hintergrunds und der schnellen Reaktionszeit konnte die mögliche Rolle von Ammoniak beim frühen Partikelwachstum, beispielsweise in verschmutzten Großstädten, untersucht werden. Es wurde gezeigt, dass Ammoniak und Salpetersäure an neu gebildeten Partikeln kondensieren können, was zu einem schnellen Partikelwachstum führt, selbst unter Smog-Bedingungen. Bei diesen Experimenten zeigten die Messungen des Wasser-Clusters CI-API-TOF, dass Ammoniak aus der Gasphase entfernt wird und dementsprechend an den Partikeln kondensiert. Zukünftig kann das Water Cluster CI-APi-TOF dazu beitragen, die Rolle von Ammoniak bei der Partikelneubildung weiter zu evaluieren. Beispielsweise deuten aktuelle Studien darauf hin, dass Ammoniak und Salpetersäure in abgelegenen Gebieten zur Formierung neuer Partikel beitragen können.

Das zweite Instrument wurde entwickelt, um mehrfach geladene Partikel für weitere Experimente an der CLOUD Kammer zu erzeugen. Das Instrument basiert auf Elektrospray-Ionisierung und wurde als CHarged AeRosol GEnerator (CHARGE) bezeichnet. Erste Experimente demonstrierten die Funktionalität von CHARGE und die Transmission der mehrfach geladenen Partikel wurde optimiert. Bei CLOUD wurden mehrere Experimente zur Bewertung der Effekte mehrfach geladener Partikel unter atmosphärisch relevanten Bedingungen konzipiert und durchgeführt. Alle Experimente basieren auf dem direkten Vergleich zwischen mehrfach geladenen Partikeln mit zuvor neutralisierten Partikeln, die beide ursprünglich von CHARGE emittiert wurden. Diese direkten Vergleiche erlaubten es, zu zeigen, dass mehrfach geladene Teilchen erfolgreich von CHARGE in Richtung der CLOUD-Kammer transportiert werden. Experimente zum Ladungstransfer zwischen mehrfach geladenen Partikeln mit Cloud Condensation Nuclei (CCN) und Expansionsexperimente zum Vergleich mehrfach geladener Partikel mit neutralisierten Partikeln wurden durchgeführt. In Zukunft können diese Experimente zu einem quantitativen Verständnis von Aerosol-Wolken-Wechselwirkungen beitragen.

Es wurde ein Verfahren zur quantitativen Messung von Kollisionsratenkoeffizienten zwischen Ionen mit (mehrfach geladenen) Aerosolpartikeln als Funktion der Anzahl von Ladungen entwickelt. Das Verfahren nutzt Daten, die während der Experimente in der CLOUD-Kammer gesammelt wurden, um die Leistung von CHARGE zu quantifizieren. Für die Berechnungen wurden Daten von Differential Mobility Analyzer (DMA) und Electrical Aerosol Analyzer

(EAA) Instrumenten verwendet (es wurde ein Neutral cluster and Air Spectrometer (NAIS) verwendet). Die gemessenen Koeffizienten wurden mit führenden Theorien des Feldes verglichen und zeigten eine gute Übereinstimmung. Die Messungen und die damit verbundenen Experimente liefern wertvolle Erkenntnisse für Instrumente, die atmosphärische Ionen oder Partikel detektieren und unter der Annahme eines Ladungsgleichgewichts operieren.

Table of Contents

1- Introduction

1.1 Atmospheric Particles and clouds

Global Carbon Dioxide (CO_2) emissions continue to rise (IPCC, 2022). CO_2 is a greenhouse gas and is directly linked to global tropospheric temperature increase. It is considered to be the most important contributor to anthropogenic climate change (Hofmann et al., 2006). In 2022, the global mean temperature has risen by 1.1 K since the beginning of industrialization. Global temperature rise has been accurately predicted by climate models. However, predictions over several decades (e.g., until 2100) are subject to great uncertainty (Raäisaänen, 2007; IPCC, 2014; Harrison et al., 2015; IPCC, 2022). The climate sensitivity to doubling CO_2, for example, varies by several Kelvin degrees depending on the assumed radiative forcing of clouds (Cess et al., 1990; Andreae et al., 2005; Forster and Gregory, 2006; Martínez-Botí et al., 2015).

Because of their high albedo, it was suggested early on that clouds have a cooling effect on the Earth's surface temperatures (Sasamori et al., 1972; Schneider, 1972). Clouds also reflect (longwave) infrared radiation emitted from the Earth's surface, which is a warming effect. Satellite observations since the 1980s showed that reflection of shortwave solar radiation dominates and thus, clouds reduce net global radiative heating (Ramanathan et al., 1989; Seinfeld and Pandis, 2016; Kejna et al., 2021). Since several hundred percent of supersaturation is necessary to form cloud droplets from pure water, cloud formation always takes place in the presence of atmospheric particles, which act as cloud condensation nuclei (CCN) (Aitken, 1900; Köhler, 1921; Seinfeld and Pandis, 2016). Understanding atmospheric particles and their interaction with clouds is therefore important in predicting the future course of climate change.

In addition, atmospheric particles have an impact on human health and air quality (Mauderly and Chow, 2008; Guo et al., 2020). Air pollution causes cardiorespiratory and cardiovascular diseases (Lelieveld et al., 2019; Pye et al., 2021). Estimates of global premature deaths from air pollution caused by atmospheric particles vary greatly, e.g. depending on assumptions on toxicity, from 1.6 to 9 million (Lelieveld et al., 2015; Landrigan et al., 2018; Nault et al., 2021). Low-income countries are particularly affected, with air pollution causing a more significant excess mortality than, for example, tuberculosis or malaria (Landrigan et al., 2018; Nansai et al., 2021).

Atmospheric particles (aerosols) are ubiquitous in the atmosphere and range in size from a few nanometres to several micrometres (Pruppacher and Klett, 2010). They can directly affect the radiation budget of the earth's atmosphere through scattering and absorption of light (direct aerosol effect) (Went, 1960). Depending on their properties (e.g. their absorption spectrum), the direct aerosol effect can either increase or decrease radiative forcing in a range from around +0.4 (fossil fuel black carbon) to -0.8 (sulfate aerosol) W m^{-2} (Haywood and Boucher, 2000). The total range of effective radiative forcing by atmospheric aerosol–radiation interaction is estimated to be in the range between -0.14 to -0.71 Wm^{-2} (Bellouin et al., 2020).

When they act as CCN, aerosols contribute to the formation of clouds. Their number concentration and their size distribution affect both, the albedo ("Twomey effect") and the lifetime of a cloud ("cloud lifetime effect" or "Albrecht effect")(Twomey and Warner, 1967; Twomey, 1974; Albrecht, 1989). Both effects are together termed the indirect aerosol effects (Twomey and Warner, 1967; Twomey, 1974; Lohmann and Feichter, 2005; Quaas et al., 2020). The global estimate of the indirect aerosol effect is in the range of about -1 W m^{-2} (Hansen et al., 1997; Lohmann and Feichter, 2005). However, the uncertainty of the estimates is large: Observed changes in the radiation fluxes in recent years point to a total net cooling effect of aerosols of -2 to -0.4 Wm^{-2} (90% CI; direct and indirect aerosol effects) (Bellouin et al., 2020).

In general, a larger number concentration of smaller cloud particles (and drops) yields a higher albedo and at the same time increases the lifetime of a cloud, which implies more cooling (Takemura et al., 2005; Lohmann and Feichter, 2005; Pruppacher and Klett, 2010; Christensen et al., 2020). Since supersaturation at which aerosols act as CCN depends on their size, hygroscopicity and chemical composition, the indirect aerosol effect varies with aerosol source terms and their subsequent growth processes (Lohmann and Feichter, 2005; Takemura et al., 2005; Seinfeld and Pandis, 2016; Christensen et al., 2020). When discussing the sources of aerosol particles, a distinction is made between primary and secondary aerosols. Primary aerosols are transported directly into the atmosphere, for example wind-blown dust or sea salt. Secondary aerosols are formed directly in the atmosphere, either by condensation of vapours on primary aerosol particles, or by chemical reactions between vapours, which is called new particle formation (or nucleation) (Seinfeld and Pandis, 2016). The contribution of nucleation processes to the global CCN budget in the boundary layer is about 45 to 55% (assuming a supersaturation of 0.2%) (Merikanto et al., 2009).

Number concentrations of cloud droplets and CCN in clouds are dominated by rapid evaporation and condensation processes, which further complicates estimation of the indirect aerosol effects. In addition, on the top and bottom layer of clouds, many particles are charged and tend to evaporate and collide more efficiently than their neutral counterparts (Zhou and Tinsley, 2007; Guo and Xue, 2021). Little is known about how particles can nucleate in these environments and grow rapidly to act as CCNs before being lost to larger particles.

This thesis deals with the development and quantification of two instruments that could help to better understand the formation of new particles and particle–cloud interactions. Additionally, quantitative calculations are shown to infer collision rate coefficients between multiply charged particles with oppositely charged particles (ion–aerosol attachment coefficients), based on the data obtained during experiments using one of the two instruments described in this work.

1.1.1 CERN CLOUD experiment

The Cosmic Leaving Outdoor Droplets (CLOUD) experiment at CERN (European Organization for Nuclear Research) is an aerosol chamber, which allows to study atmospheric particles under controlled and clean conditions (Kirkby et al., 2011; Duplissy et al., 2016). The chamber consists of electropolished stainless steel, and its volume is 26.1 m^3. It is permanently flushed with a gas mixture from cryogenic nitrogen and oxygen. The background

contamination of the chamber is in the low pptv to sub-pptv range and has been characterized in several studies (e. g., Schnitzhofer et al., 2014; Pfeifer et al., 2020). The chamber temperature can be kept constant, with an internal vertical temperature gradient of ±0.1K. Temperatures between 183 and 373K are possible. Other parameters, such as relative humidity (from <0.5 to 101%) or the mixing of the chamber can also be precisely controlled (Dias et al., 2017). Trace gases are fed into the chamber either using gas bottles, or by evaporation of chemicals from the liquid phase. For this, heated water baths are used, where the chemicals are stored in glass jars, which are stored in stainless steel containers. Mass flow controllers help to control the concentrations of trace gases fed to the chamber. Several Mercury lamps allow controlled experiments under predefined wavelengths (between about 200 and 700nm).

A comprehensive suite of instruments is connected to the chamber during the experiments. Particle distributions are measured, for example, using differential mobility analysers (DMA) coupled to condensation particle counters (CPC). Depending on the instrument, particle concentrations for the size range from a few nanometers (e. g., Particle Size Magnifier (PSM) and "DMA train") to several micrometers (e.g. Optical Particle Counters (OPC), such as the "WELAS") are continuously measured (Tritscher et al., 2013; Lehtipalo et al., 2014; Stolzenburg et al., 2017; Palas, 2022). Trace gases are measured using both optical and mass spectrometers. The mass spectrometers use different ionization techniques to selectively detect important components, such as sulfuric acid, nitric acid or ammonia and amines (Bell et al., 2009; Kürten et al., 2011; Hoch et al., 2014; Breitenlechner et al., 2017; Pfeifer et al., 2020). On the one hand, components are systematically measured with calibrated instruments (e. g., sulfuric acid or ammonia). On the other hand, suspect screening and non-target approaches are used to analyse multicomponent systems. Mass spectra are analysed for possible reaction products, based on information from precursor gases (suspect screening). When multiple components are involved (which increases uncertainties in suspect screening), algorithms are used to suggest likely components in the mass spectrum according to their mass-to-charge ratios (non-target approach) (Schymanski et al., 2015; Stark et al., 2015; Timonen et al., 2016).

Throughout the continuously controlled experiments at low contaminant levels, CLOUD has been able to significantly increase scientific knowledge about atmospheric new particle formation, growth of atmospheric particles and the involvement of charge in recent years (e.g., Kirkby et al., 2011; Almeida et al., 2013; Kirkby et al., 2016; Wang et al., 2020, 2022). Figure 1 shows a picture of the CLOUD chamber at CERN during the CLOUD14 experiments.

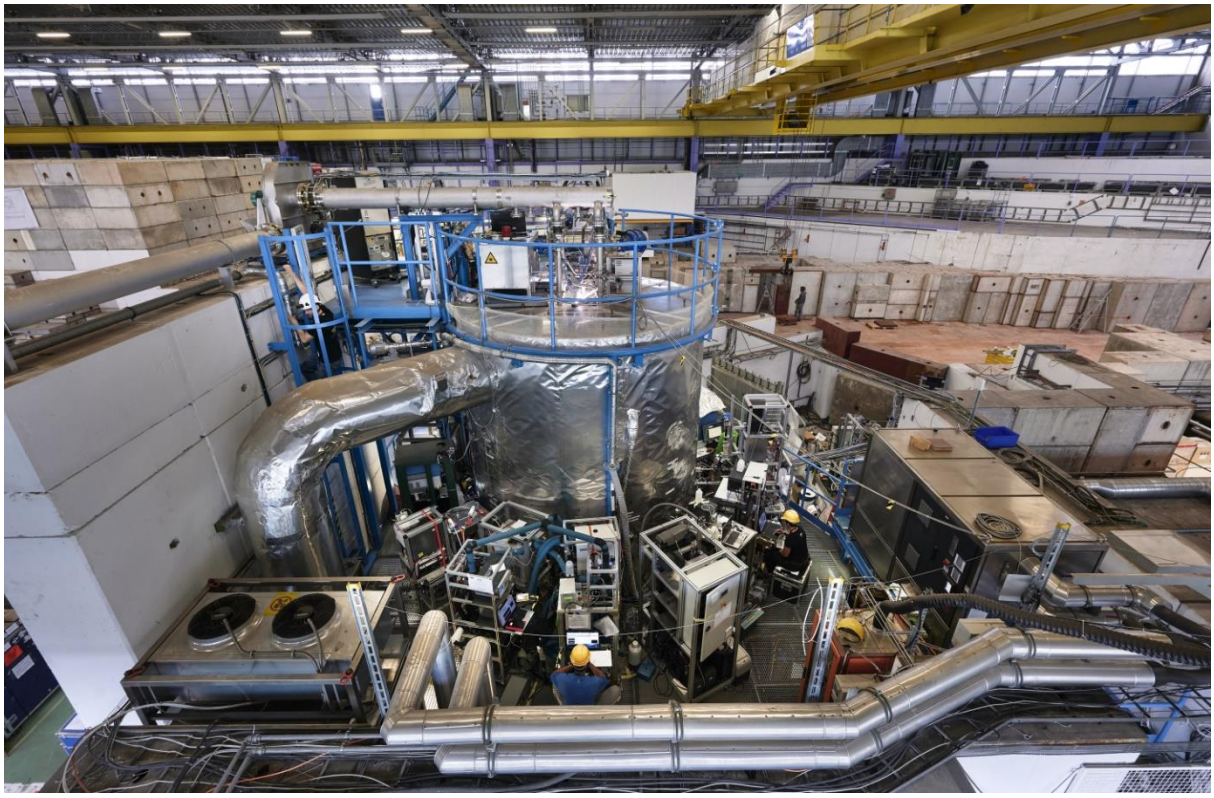

Figure 1: *Picture of the CLOUD chamber at CERN during the CLOUD14 experiments (CERN, Topic: CLOUD Experiment, Article: From cosmic rays to clouds, Image: 23.September 2019).*

1.1.2 New Particle Formation (NPF)

New particle formation refers to the formation of secondary aerosol particles through gas-to-particle conversion. As a prerequisite, gas-to-particle conversion requires chemical reactions in the gas phase that produce low or extremely low volatile products. These reaction products can grow into thermodynamically stable clusters through further reactions and collisions, which is called nucleation. The newly formed small particles have great mobility and are quickly lost through collisions with larger particles. Accordingly, NPF also includes the subsequent condensational growth of these particles until they reach a size where they have a sufficient survival probability (Friedlander, 1977; Kulmala et al., 2014, 2017). In the following, the current understanding of nucleation and subsequent growth of newly formed particles is summarized.

1.1.2.1 Nucleation

In nucleation theory, the formation of a thermodynamic stable phase from an initially metastable phase is described. For example, supercooled droplets in clouds can freeze on solid particles, which is called ice nucleation (or crystallization of the supercooled water) (Pruppacher and Klett, 2010; Seinfeld and Pandis, 2016). While the transition from the liquid to the (thermodynamic stable) solid phase is also relevant for atmospheric research, this work primarily considers transition from the gas phase to the liquid or solid phase. In case of atmospheric NPF, nucleation describes the formation of clusters of a critical size, from which growth through agglomeration of surrounding vapour exceeds the rate of evaporation and they thus continue to grow. Clusters, which reach this critical size, are considered newly formed

particles and the rate at which those particles form per time and volume is called the nucleation rate (Hegg and Baker, 2009; Seinfeld and Pandis, 2016).

In general, a distinction is made between the species and the surfaces involved in nucleation (Seinfeld and Pandis, 2016):

- Homogeneous nucleation describes nucleation without involvement of additional surfaces (e.g., ions are considered "additional surfaces" here). Conversely, in heterogeneous nucleation, additional surfaces are involved.
- Homomolecular nucleation involves a single species (e.g., water in a supersaturated environment), while in heteromolecular nucleation, multiple species are in involved (e.g., water and sulfuric acid).

There are two approaches to describe classical nucleation theory) (Volmer and Weber, 1926; Seinfeld and Pandis, 2016): A kinetic approach and a constrained equilibrium approach (thermodynamic approach). While the kinetic approach is based on balance equations between agglomeration and evaporation, the thermodynamic approach is based on the difference in chemical potentials between the phases involved. In both cases, an energy barrier must be overcome, above which a cluster is considered thermodynamically stable and will thus continue to grow (Seinfeld and Pandis, 2016). The height of this barrier defines the nucleation rate, and it depends on the saturation ratio, the temperature, and the particle size. In case of homogeneous or homomolecular nucleation, new particle formation will only occur if the environment is supersaturated with respect to the individual vapor. In case of heteromolecular or heterogeneous nucleation, the energy barrier is often lower, even if the concentration of one substance is significantly higher than that of the other (Hegg and Baker, 2009; Seinfeld and Pandis, 2016). An example for this is binary nucleation of sulfuric acid and water, where sulfuric acid occurs in much lower concentrations than water. Nevertheless, the nucleation rates are many times higher than in the case of pure water (Kulmala and Laaksonen, 1990; Vehkamäki et al., 2002; Benson et al., 2008). Both approaches share a so-called capillary approximation: For processes that take place at the molecular level, bulk properties such as density or surface tension are used, which can result in large errors (Volmer and Weber, 1926; Curtius, 2006; Hegg and Baker, 2009; Seinfeld and Pandis, 2016).

Laboratory experiments to determine nucleation rates are carried out, for example, using expansion chambers, upward thermal diffusion chambers or aerosol chambers such as the CLOUD chamber at CERN (see, e. g., Schmitt, 1981; Rudek et al., 1999; Kirkby et al., 2011). Initially, it was thought that binary sulfuric acid–water nucleation is the main source for atmospheric new particle formation (see e.g. Kulmala and Laaksonen, 1990; Weber et al., 1996; Kulmala et al., 1998). Observations of volcanic eruptions showed that global temperatures drop, due to an increase in sulfuric acid concentration and subsequent cloud formation (e. g., Sigurdsson, 1990; Sassen, 1992). Atmospheric sulfuric acid is formed from oxidation of SO_2 and OH and has been measured in the troposphere, with concentrations of around $1 \cdot 10^4$ to about $2 \cdot 10^7$ cm^{-3} (Curtius et al., 2001; Cai et al., 2021; Beck et al., 2022; Zauner-Wieczorek et al., 2022). In case of binary sulfuric acid–water nucleation, measured atmospheric nucleation rates are usually higher than those measured in laboratory experiments.

This indicates that further vapours besides sulfuric acid and water are responsible for nucleation (Weber et al., 1996).

Model simulations and quantum chemical calculations show that ammonia can stabilize sulfuric acid clusters through acid–base reactions and thus further increase nucleation rates (Kurtén et al., 2007a; Kürten, 2019). This has been confirmed by laboratory experiments at CLOUD (Kirkby et al., 2011; Kürten et al., 2016a). The ground-level concentrations of ammonia are in the range of a few pptv (e. g., around 200 pptv in rural forests) to more than 50 parts per billion (ppbv) in megacities (You et al., 2014; Wang et al., 2015). Stronger bases than ammonia are amines, such as dimethylamine. Dimethylamine is more rare in the atmosphere (especially in rural areas), with measured mixing ratios of a few pptv (Hanson et al., 2011; You et al., 2014). However, experiments at CLOUD and atmospheric measurements revealed that dimethylamine mixing ratios as low as 5 pptv are sufficient to increase nucleation rates by three orders of magnitude compared to 250 pptv ammonia (Almeida et al., 2013; Kürten et al., 2014).

Additionally, oxidized organic compounds can be well suited for nucleation by stabilizing small clusters in mixtures with acids (Zhang et al., 2004; Zhao et al., 2013) or by nucleating on their own (Kirkby et al., 2016). Volatile Organic Compounds (VOC; e.g. monoterpenes) react with OH, O_3 or NO_3 in the atmosphere and form peroxy-radicals. Subsequent auto-oxidation mechanisms can result in ultralow-volatile organic compounds (ULVOCs) (Crounse et al., 2013; Ehn et al., 2014; Schervish and Donahue, 2020), which can nucleate by themselves (Kirkby et al., 2016). Source terms for organic compounds are either emissions from plants or trees (e.g. alpha-pinene) or anthropogenic emissions (e.g. toluene) (Schmitt et al., 1983; Guenther et al., 2012; Schwantes et al., 2017). Additionally, in the marine environment, iodine species can also drive strong nucleation events and rapidly form new particles (O'Dowd et al., 2002b; Sipilä et al., 2016; He et al., 2021b).

In some cases, nucleation rates are enhanced in the presence of ions. Ions stabilize the clusters early on through Coulomb forces and can thus counteract evaporation. In addition, collision rates of charged clusters with neutral (polar) clusters are enhanced (Yu and Turco, 2000; Seinfeld and Pandis, 2016; Kirkby et al., 2016; He et al., 2021a). The effects of charge and multiply charged particles are discussed in a separate chapter (chapter 1.3).

While these observations explain near-surface nucleation events very well, new particle formation events in the upper troposphere are subject of active research. For example, only very small amounts of ammonia are expected in the upper troposphere, since ammonia is very soluble in water. Recently, however, Höpfner et al. measured ammonia mixing ratios of about 10-25 pptv in the upper troposphere during Asian summer monsoon (using satellite data). In addition, solid ammonium nitrate particles were measured in the upper troposphere (Höpfner et al., 2016, 2019). A recent experiment conducted at CLOUD showed that nucleation from sulfuric acid, nitric acid and ammonia in the upper troposphere can explain new particle formation in this region (Wang et al., 2022). Ammonia measurements with good time resolution and low detection limits, as shown in this thesis, can help to answer remaining questions related to role of ammonia in nucleation and aerosol formation in the future.

1.1.2.2 Growth of atmospheric particles

While large atmospheric particles continue to grow through condensation and coagulation until they can finally act as CCN, for smaller particles, coagulation is a dominant sink: They can collide with larger particles and in that case, they cannot contribute to CCN formation. Thus, a high Coagulation Sink (CS) drastically reduces the probability of newly formed particles to survive. In literature, the most crucial size range for this loss process is often referred to as the "valley of death" and it applies to particles below a size of about 10 nm. Newly formed particles can therefore only survive (and later act as CCN) if their growth rate is able to compensate for the coagulation sink (Friedlander, 1977; Seinfeld and Pandis, 2016; Kulmala et al., 2017; Mahfouz and Donahue, 2021a, b; Marten et al., 2022).

In general, freshly nucleated particles grow by vapor condensation (see e.g. Kulmala et al., 2014; Seinfeld and Pandis, 2016). Their rate of condensational growth depends on the size of the colliding entities, as well as the molecular weight, diffusivity, vapor pressure and equilibrium vapor pressure of the involved species. In addition, not all molecules will stick to a particle after collision. In literature, this is usually represented by a sticking coefficient, which describes the probability that a molecule will stick to the particle after collision (Fuchs and Sutugin, 1971; Seinfeld and Pandis, 2016). While many substances can contribute to condensational growth, usually species with low volatility, high molecular mass and sufficiently large atmospheric concentrations are particularly important (Kulmala et al., 1998; Nieminen et al., 2010; Seinfeld and Pandis, 2016).

Particle growth often involves multiple species, where the importance of individual species varies with their ambient concentration, particle size and particle composition (Kulmala et al., 2014; Tröstl et al., 2016; Lehtipalo et al., 2018). Sulfuric acid is considered an important compound for growth of new particles, due to the high acidity and the low volatility (Kulmala et al., 1998; Birmili et al., 2003; Paasonen et al., 2009). Quantum chemical calculations show that at relative humidity of 80%, every sulfuric acid molecule has two water molecules attached and even 10% of the sulfuric acid molecules have three water molecules attached (Eisele and Hanson, 2000; Kurtén et al., 2007b). Besides, acid–base reactions, such as those between ammonia and sulfuric acid reduce evaporation rates of newly formed particles (Kirkby et al., 2011; Kürten et al., 2016a; Kürten, 2019). Those reactions can play a key role in particle growth, since they help to stabilize newly formed particles (see e.g. Kurtén et al., 2007a; Yue et al., 2010; Kirkby et al., 2011; Lehtipalo et al., 2016; Myllys et al., 2019; Yin et al., 2021).

Ambient measurements of particle compositions confirm that ammonium sulphate has a large mass fraction in newly formed particles (see e.g. Smith et al., 2005; Wu et al., 2015). At the same time, although sulfuric acid plays an important role in NPF, the concentrations are often insufficient to explain observed atmospheric growth rates (Riccobono et al., 2012). Environmental measurements and laboratory experiments show that organic compounds (e.g. oxygenated organic molecules) often play a central role for growth of newly formed particles (e.g., O'Dowd et al., 2002a; Riipinen et al., 2012; Schobesberger et al., 2013). Experiments at CLOUD confirm that extremely low volatile organic compounds (ELVOCs) play a major role in early growth when the Kelvin curvature effect of small particles is dominant. As soon as particles increase in size, more abundant compounds with higher volatility can contribute to

further particle growth (Tröstl et al., 2016). The abovementioned species can explain atmospheric NPF at low condensation sink, for example in rural regions. However, their growth rates are not sufficient to explain new particle formation at high coagulation sink, for example in megacities. Kulmala et al. (2017) therefore suggested that either the sticking coefficient — which is usually assumed to equal unity — is much smaller than expected in theory, or that growth rates could be higher, due to unknown mechanisms (Kulmala et al., 2017).

During experiments at CLOUD, the ammonia measurement technique presented in this thesis facilitated studying the condensation of ammonia and nitric acid at atmospherically relevant conditions. Due to the good time resolution of the ammonia measurements, it was possible to show that NH_3 and HNO_3 condense rapidly on newly formed particles, once they reach a specific size (of about 5 nm, which is referred to as the activation diameter). Thus, in the presence of ammonia and nitric acid, particles can grow promptly (with growth rates of about 100 nm/hr), which increases their survival probability at haze conditions (Wang et al., 2020; Pfeifer et al., 2020; Marten et al., 2022).

To highlight the impact of NPF and subsequent growth on earth's climate, Figure 2 shows the possible change in global potential temperature (at an elevation of 1000m) for the case that monoterpenes are neglected in NPF. The simulation is carried out using the UK Earth system model (UKESM) (e.g., Mulcahy et al., 2020, 2022). The model utilizes parameterizations for NPF, as described in Dunne et al. (2016). Two simulations are performed: with and without monoterpenes. As shown in Figure 2, the global potential temperature would rise by around 0.2 K on average and- in some regions- by up to 1.4K. While further discussion on this figure is out of the scope of this work, the clear effect highlights the importance of quantifying the numerous processes involved in NPF for predicting earth`s climate temperatures.

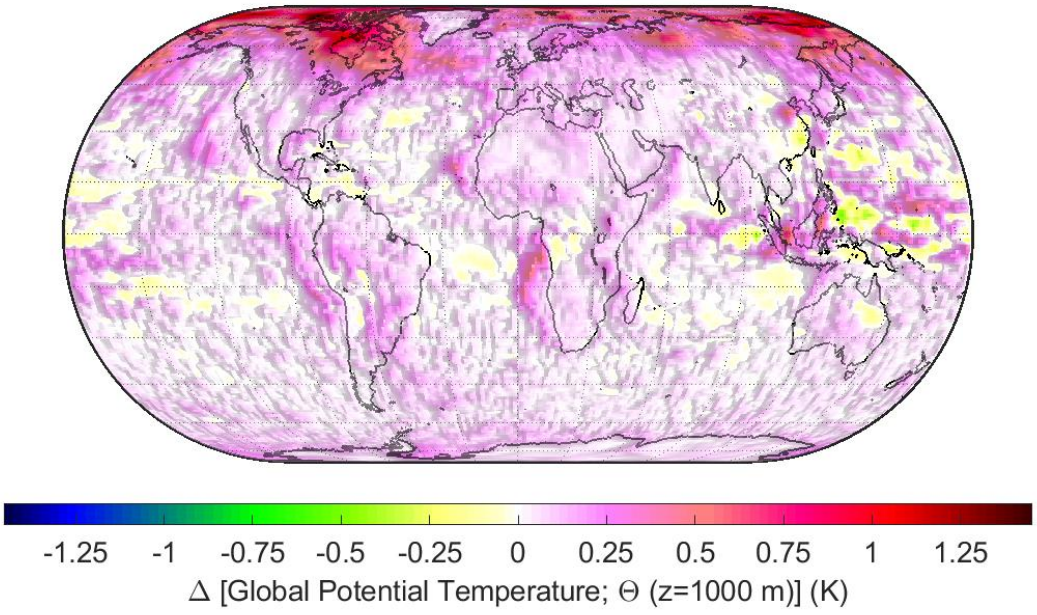

Figure 2: *Change in global potential temperature (1000m altitude) if monoterpenes were ignored in a global climate model (UKESM). The global potential temperature would rise by around 0.2 K on average and locally by up to 1.4K. The simulation was carried out by the*

author of this thesis, in collaboration with Ananth Ranjithkumar (University of Leeds; Fig.: J.P.).

1.1.3 Charged Particles

To understand NPF and subsequent growth of newly formed particles to CCN size, as well as the behaviour of CCN in clouds, it is essential to understand the effects of charged particles (i.e., small ions, singly charged particles and multiply charged particles). In the atmosphere, charged particles span a wide range of different sizes and charge states. Collisions of muons and pions (from galactic cosmic rays) or collisions of alpha particles (emitted during radioactive decay, e.g., from radon) with molecules permanently produce small ions, as well as photoionization (Smith and Spanel, 1995). So-called precursor ions such as O_2^+, N^+, O^- or O_2^- are formed in the troposphere. These can either recombine through collisions with each other (and thus become neutralized), or they react with water and surrounding molecules and grow into cluster ions (Sayers, 1938; Smith and Spanel, 1995). Ions can increase nucleation rates by reducing evaporation rates of small molecular clusters (Katz, 1970). They stabilize those clusters by enhancing polar interactions (Kusaka et al., 1995; Seinfeld and Pandis, 2016). Laboratory experiments, atmospheric measurements and model studies show that ions increase nucleation rates in both, acid-base and organic systems (see e.g. Kirkby et al., 2011; Almeida et al., 2013; Kirkby et al., 2016; Merikanto et al., 2016; Yan et al., 2018).

In addition, the growth rate of small particles in the presence of ions could be increased by ion-polar collision enhancement (Lehtipalo et al., 2016; He et al., 2021a). Ions and charged particles collide enhanced with larger (neutral) particles compared to neutral particles among themselves (Fuchs and Sutugin, 1971; Hoppel and Frick, 1986; Gopalakrishnan and Hogan, 2012; López-Yglesias and Flagan, 2013). This in turn increases their loss rate at large coagulation sinks compared to neutral particles (Mahfouz and Donahue, 2021a, b). At the same time, the charge is transferred to the larger particles in the event of a collision, which can lead to the formation of multiply charged particles above a certain size (Guo and Xue, 2021).

Due to their importance in numerous processes, ions were therefore of interest since the early days of atmospheric research. Long before the discovery of small aerosol particles, researchers focused on investigating the origin of atmospheric ions and charge (see e.g. Coulomb, 1789; Kelvin, 1859). The first breakthrough laboratory experiments to understand charge carriers in the atmosphere was carried out by Wilson (Wilson, 1900). Wilson developed an expansion chamber that was connected to an XRay generator. In these experiments, the condensational activation of water by ions could be observed for the first time (Wilson, 1900; Flagan, 1998). Subsequent studies dealt intensively with the diffusion of ions in ambient air (Thomson, 1898; Langevin, 1905; Nolan, 1924; Flagan, 1998).

Instruments were developed early on to measure the diffusion coefficients of ions in air and to link them to their electrical charge, their electrical mobility, and their size (McClelland, 1898; Zeleny, 1900). So-called condensers were initially used, in which ionized gas was passed between two electrodes, with a potential difference applied (Townsend, 1900). By varying the voltage on these electrodes, ions of different mobility could be detected, where a Faraday cup was used for detection (Nolan, 1924; Sagalyn and Faucher, 1954). It was found early on that

ions have different mobilities, with the mobilities later being linked to particle size (Millikan, 1910; Nolan, 1924; Israël, 1951, 1970). Differential mobility measurements (with several segments for detection of different mobilities) were an obvious solution, but difficult to achieve because the sensitivity of the measurement was affected, e.g., by current fluctuations caused by the high voltage supplies of the capacitors (DeBitetto, 1955). With the improvement in sensitivity of those measurements using so-called fluctuation compensators (e.g., DeBitetto, 1955), Differential Mobility Analyzers (DMA) and Electric Aerosol Analyzers (EAA) have become important in measuring atmospheric particles (Knutson and Whitby, 1975; Winklmayr et al., 1991; Flagan, 1998; Mirme and Mirme, 2013; Stolzenburg et al., 2017; Amanatidis et al., 2021). These instruments are widely used to study atmospheric NPF and particle growth. For example, in a typical DMA setup, particles initially brought into a charge steady state are transported through a column that includes inner and outer electrodes (Knutson and Whitby, 1975; Flagan, 1998). Charged particles are guided through this column with a sheath flow, where they are deflected towards the inner electrode by a potential difference. Only particles with a certain mobility can leave the instrument and be detected. Those particles are typically measured by using a condensation particle counter. Some instruments have multiple differential detection zones, e.g., Electrical Aerosol Analysers comparable to the Neutral cluster and Air Spectrometer (NAIS) which is used in this work (see Mirme and Mirme, 2013). Differential Mobility Analyzers and Electrical Aerosol Analyzers use so-called transfer functions to obtain a particle distribution in terms of mobility. These functions describe the probability that an observed particle with the mobility Z_p will be detected. They depend on the flow rates (e.g., sample air flow, sheath air flow, exhaust flow), the instrumental dimensions in the DMA (e.g., the length of the electrodes), the potential differences and the expected trajectories of the measured ions (Flagan, 1998). Transfer functions can deviate from theoretically predicted "ideal" transfer functions. Diffusional losses of particles and deviations from their expected trajectory can reduce the resolution of the measurement, broadening the transfer function (Flagan, 1998). Space charge effects and multiply charged particles, which can occur directly after ionization, can increase diffusional losses due to coulomb repulsion (Flagan, 1998; Fu et al., 2011; Seinfeld and Pandis, 2016). Further, multiply charged particles are more mobile than singly charged particles and thus they interfere with the mobility distribution and increase the error of the estimated particle size distributions obtained with Differential Mobility Analyzers (Liu and Pui, 1975). This is usually corrected for in the data inversion (e.g., Wiedensohler, 1988; Mirme and Mirme, 2013; Stolzenburg et al., 2022). However, the approaches differ (e.g., depending on the geometry of the instruments) and the differences can become significant (Kangasluoma et al., 2020; Stolzenburg et al., 2022). Further details on the topic of ion measurements and measurement of atmospheric particles are summarized in Flagan (1998).

Initially it was assumed that all atmospheric particles which enter the analyzer section of the DMA are singly charged (Nolan, 1924; Hogg, 1931). However, discontinuities in the measured distributions were noticed early on, which were an indication for the presence of multiply charged particles (Nolan and Kennan, 1948; Junge, 1955). Hewitt (1957) determined the charge per unit mass of aerosols passing a segmented condenser (Hewitt, 1957). In his measurements, aerosols were generated using a Sinclair LaMer generator and subsequently charged using

corona discharge. During this experiment, three main peaks were observed in the condenser, indicating three different charge states (Hewitt, 1957; Flagan, 1998). Further experiments also confirmed the presence of multiply charged particles and their interference with the singly charged distributions (Junge, 1955; Langer et al., 1962; Hurd and Mullins, 1962; Israël, 1970; Flagan, 1998). Initially, a Boltzmann distribution was used to estimate the charge distributions. However, it turned out that flux matching theories, which describe the collision rates of charged particles in the transition regime in terms of so-called trapping distances, better reflect particle charging when measuring ions (Natanson, 1960; Fuchs, 1963, 1964; Fuchs and Sutugin, 1965, 1971). Flux matching theories describe the transfer of charge (through ions) to a particle surface from a distant outer region. In the outer region, ions move according to classic diffusion and electrophoretic migration. As soon as the charged particles are at a certain distance from the particle surface, they reach the so-called capture distance (classically a mean free path from the particle). This defines the inner region where the trajectories of the ions are influenced by the particle, for example by Coulomb forces (Hoppel and Frick, 1986). The probability for an ion to collide with a particle can be calculated by considering, for example, the ions initial velocity components. The theory has been expanded over the years, by including image charge effects, or through more precise calculations of the trajectories of ions in the outer region (Hoppel and Frick, 1986; López-Yglesias and Flagan, 2013).

Multiply charged particles continue to affect particle measurements and their accuracy. Today, there are numerous calculations that compete with or are based on flux matching theory (Gatti and Kortshagen, 2008; Gopalakrishnan and Hogan, 2012; Tamadate et al., 2020a; Suresh et al., 2021). However, there is a lack of measurements to verify said theories, especially for small particles with high Knudsen numbers in the transition and in the free molecular regime (i.e., when the mean free path of the surrounding molecules is larger than the size of the particles). In this case, the mean free path of molecules in air exceeds the size of the (multiply charged) aerosol particles. Since multiply charged particles can also significantly influence the measurements and can also influence experiments due to their increased collision rate coefficients with particles of opposite charge, it is important to understand them quantitatively ((Tamadate et al., 2020b; Pfeifer et al., 2022),

Another atmospheric measurement technique that requires a basic understanding of the behaviour of multiply charged particles in air is mass spectrometry. Multiply charged particles and space charge can affect the trajectories of analyte and product ions by Coulomb forces. In addition, due to their increased electrical mobility (similar to DMA measurements), they can interfere with singly charged ions (Meyerson and Haar, 1962). At the same time, however, this increased mobility of multiply charged particles is also exploited: Electrospray ionization (ESI) combined with mass spectrometry is often used to detect ions that would otherwise be too heavy and are above the cut-off size of mass spectrometers (Andrianova et al., 2018). In this way, low and high molecular weight species can be detected simultaneously. In medicine and biology, this is used to obtain and measure multiply charged proteins, which actually have a mass-to-charge ratio above the cutoff size of mass spectrometers when singly charged (see e.g. Kebarle, 2000; Peters et al., 2019). In atmospheric research, ESI is used to obtain information about the chemical composition of aerosol particles (Pospíšilová, 2019; Surdu et al., 2021). Multiply charged particles from ESI also ionize some analyte species, which do not ionize in

solution (Kebarle, 2000). Understanding the collision rate coefficients of these multiply charged particles with small ions (e.g. produced from GCR) is important for the quantitative measurement of these multiply charged analytes (Tamadate et al., 2020b).

Besides their (sometimes intended and sometimes unintended) importance in various atmospheric measurement techniques, multiply charged particles also play an important role in the atmosphere itself, for example in thunderstorms. Because of its impressive appearance, the occurrence of lightning was an early area of atmospheric research (Winkler, 1746; Franklin, 1752; Watson, 1753). The origin of lightning from collision of ice particles (e.g. graupel) in air was suspected early on (Winkler, 1746). Particles in thunderclouds are expected to contain hundreds to thousands of charges, with large amounts of space charge scattered throughout (Takahashi, 1978; Saunders, 1993; Stolzenburg et al., 1998). Charge is transferred by collision of graupel (Takahashi, 1978; Saunders et al., 1991). The high charge numbers are originally caused by a combination of several processes, especially, convection and the global electrical circuit of the atmosphere are important (Rycroft and Harrison, 2012). There is a potential difference of about 250 kV between the ionosphere and the earth's surface. Since the atmosphere acts like a resistor and the atmospheric pressure increases exponentially towards the earth’s surface, the resistance is highest in the lower troposphere. The largest part of the potential difference is therefore in the troposphere (Rycroft et al., 2008; Rycroft and Harrison, 2012). The potential difference causes a fair-weather electric field of about 130 V/m, which is directed towards the earth’s surface. This causes a downward flow of positive ions and an upward flow of negative ions (Rycroft and Harrison, 2012). Thunderstorms act like generators here: Negative charges are transported to the earth’s surface and positive charges to the upper atmosphere (Mach et al., 2011). The distribution of the charge in those clouds is often explained by difference of conductivity within the clouds compared to the surrounding air, or by convection that transports the surrounding ions into the cloud (e.g., Chalmers, 1958; Vonnegut, 1963; Zhou and Tinsley, 2007; Rycroft and Harrison, 2012). However, measurements with radiosondes and field meters suggest that charge is distributed in a more complex way. For example, Stolzenburg et al. (1998) measured four main charge regions, which alternate in polarity (Stolzenburg et al., 1998).

Additionally, a huge amount of space charge is expected on the top and bottom layer of tropospheric clouds (e.g. low clouds at 2 kilometres altitude), which are not associated with thunderstorm events (Zhou and Tinsley, 2007). The conductivity in clouds is lower than that of the surrounding air, due to the presence of liquid water droplets (Harrison et al., 2015). Thus, according to Gauss Law, there must be electrical charge at the top and bottom of the cloud, with a current flowing through the cloud with the same density as the surrounding air above and below (Zhou and Tinsley, 2007; Nicoll and Harrison, 2010; Rycroft and Harrison, 2012). Due to this jump in conductivity, multiply charged particles containing 50 to 100 charges are expected on the top and bottom layer of those clouds according to model calculations (Zhou and Tinsley, 2007). Model simulations indicate that multiply charged particles — especially under the influence of the Earth's electric field — rapidly collide with each other (due to image charge effects) and with particles of opposite charge. Guo and Xue (2021) estimate that this effect is significant enough to significantly accelerate cloud droplet growth and thus enhance precipitation (Guo and Xue, 2021). In addition, their simulations indicate that charge is

transferred from small particles to large particles during collisions, which leads to multiply charged droplets under the influence of space charge. While there are experiments on the collision of multiply charged particles above 100 nm with negative ions (e.g., Beard et al. 2002), there is a lack of laboratory experiments to classify charge effects inside clouds.

Laboratory experiments to quantify the effects of charge and the development of a first instrument that can serve this purpose are discussed in this thesis. In addition, the fourth paper of this thesis shows first results of experiments carried out at the CERN CLOUD chamber. Collision rate coefficients of multiply charged particles in the size range below 10nm with negative ions are presented. These coefficients are important for both confirming theories in the field and helping quantifying different measurement techniques (as shown above), as well as for understanding the behaviour of multiply charged particles on the top layer of clouds, where a lot of (positively charged) space charge is expected.

1.1.4 Summary

This work combines two projects, where both are an important contribution to understand processes related to atmospheric particle growth and cloud formation. Some results of both projects are published in two first-author papers and two co-author papers, which are attached to this summary thesis and are referred to **as Paper 1, Paper 2, Paper 3,** and **Paper 4** in the next sections.

The development and quantification of an instrument for measuring ammonia at the CERN CLOUD chamber is described in **Paper 1** (Pfeifer et al., 2020). Using this instrument, **Paper 2** and **Paper 3** describe the rapid growth of newly formed particles due to nitric acid-ammonia condensation under atmospherically relevant conditions (Wang et al., 2020; Marten et al., 2022). The second project describes the development and characterization of a multiply charged particle generator at the CERN CLOUD chamber. The instrument and first experiments are described in the third section of this summary thesis. The first measurements of ion–aerosol rate coefficients against multiply charged particles in the size range below 10nm under atmospherically relevant conditions are shown in **Paper 4**. They are particularly important for instruments that measure atmospheric particles and ions (such as Differential Mobility Analysers) but could also play an important role in clouds, where a lot of space charge is expected (Pfeifer et al., 2022 (submitted); Flagan, 1998; Zhou and Tinsley, 2007; Mirme and Mirme, 2013; Guo and Xue, 2021).

1.2 Ammonia measurements

1.2.1 Overview

Ammonia has a variety of source terms whence it is emitted into the atmosphere, for example, due to agricultural activity (e.g., fertilizers), catalytic converters in vehicles or by animal husbandry (e.g., animal excretions) (You et al., 2014; Seinfeld and Pandis, 2016; Liu et al., 2021). As already discussed in chapter 1.2, ammonia is of great importance for NPF (Jimenez et al., 2009; Kirkby et al., 2011; Kürten et al., 2016a). Globally, a large fraction of CCN formation involves ammonia (Dunne et al., 2016; Höpfner et al., 2019). Measurements in rural areas and in the upper troposphere indicate that ammonia also occurs in environments without direct sources (You et al., 2014; Höpfner et al., 2016; Jokinen et al., 2018; Yan et al., 2018). In the upper troposphere, ammonia could be relevant for NPF, despite the low concentrations expected there (Bianchi et al., 2016; Wang et al., 2022). However, for most measurement methods, the concentrations in these remote areas are either below the detection limit or they require a long time averaging, and thus have a poor temporal resolution (Bell et al., 2009; von Bobrutzki et al., 2010; Wang et al., 2015; Höpfner et al., 2016). The development of methods to measure ammonia with low detection limits and at the same time good time resolution is therefore of great importance.

Experimental techniques typically face several problems when measuring ammonia:

- Ammonia has a strong polarity. Since this also applies to water, it has hydrophilic properties. For this reason, the sensitivity of ammonia measurements often depends on ambient humidity (Kürten et al., 2016b; Pfeifer et al., 2020).
- Ammonia has a high gas phase diffusivity, due to its low molecular mass. Combined with the high polarity, ammonia molecules easily stick to walls. Measurements have correspondingly high wall loss rates. Besides these high loss rates, ammonia molecules from the walls can act as unwanted source terms when they later desorb from the walls (e.g., when temperature or humidity rises) and thus falsify the measurement (Massman, 1998; von Bobrutzki et al., 2010; Townsend, 2010; Roscioli et al., 2016; Pfeifer, 2018).
- The instrumental background can be very high, because ammonia source terms are diverse. For example, the human skin also releases ammonia and this can affect laboratory measurements (Li et al., 2020).

Ammonia is measured in the atmosphere using a variety of methods. For example, optical absorption methods such as differential optical absorption spectroscopy are used to measure ammonia at higher concentrations in megacities (Wang et al., 2015). In the upper troposphere, environmental satellites (ENVISAT) were able to measure low ammonia concentrations with detection limits of a few parts per trillion using Michelson Interferometer for Passive Atmospheric Sounding (MIPAS) averaged limb spectra (Burgess et al., 2006; Fischer et al., 2008; Höpfner et al., 2016). Cavity ringdown spectrometers are also widely used to measure ammonia (e.g., Bell et al., 2009; von Bobrutzki et al., 2010; Martin et al., 2016). While these methods can measure ammonia over a wide range of concentrations, they either have poor spatial or temporal resolution (satellite measurements), or their detection limits are insufficient to measure in remote areas. However, recent studies show that good time resolution is

important in understanding the role of ammonia during NPF events and cloud formation (Höpfner et al., 2019; Wang et al., 2020; Marten et al., 2022). For this reason, the use of time-of-flight mass spectrometers has increasingly intensified in recent years, since they can measure ammonia with good time resolution at low concentrations (Norman et al., 2009; Benson et al., 2010; Hanson et al., 2011; You et al., 2014). Multiple substances (besides ammonia) can be detected in parallel. In this work, a method for measuring ammonia, amines and iodine compounds using a newly developed chemical ionization mass spectrometer (CIMS) is presented. The following section briefly describes the method of CIMS, with a focus on the instrument developed in this work. The results obtained with this method are then briefly summarized. Further information can be found in **Paper 1** of the cumulative part, "Measurement of ammonia, amines and iodine compounds using protonated water cluster chemical ionization mass spectrometry" (Pfeifer et al., 2020).

1.2.2 Methods

The principle of mass spectrometry is based on the separation of ions according to their mass-to-charge ratio. This can be accomplished using a variety of techniques. For example, in quadrupole mass spectrometry, ions are separated by passing through one or more quadrupoles. Depending on the stability of their trajectory, ions with different mass-to-charge ratios are detected (Gross, 2017). In time-of-flight mass spectrometry (TOF-MS), ions are accelerated in an electric field under very low pressure (the pressure in the time-of-flight section is usually around $1 \cdot 10^{-7}$ hPa). Depending on the mass-to-charge ratio, the time of flight of the ions varies. In the end, the ions hit a detector, which is typically a secondary electron multiplier, e.g., a Micro Channel Plate (MCP). The measured current is converted to a digital signal using analog-to-digital converters. Time-of-flight mass spectrometers allow the parallel measurement of hundreds to thousands of different compounds, while quadrupole mass spectrometers need to scan individual mass-to-charge ratios (Gross, 2017). Consequently, the time resolution is increased, which makes TOF-MS advantageous for many research areas (Wollnik, 1993; Satoh et al., 2005; Gross, 2017; Wei et al., 2021).

Analyte ions can be generated via electrical ionization (EI) or via chemical ionization (CI) (Gross, 2017). In EI (also called "Electron Impact"), electrons collide with analytes at high kinetic energies (around 70 eV). The interpretation of the mass spectrum can, however, be complicated by pronounced fragmentation of analyte ions, which is typical for EI. In CI, analytes are ionized by chemical reactions with reagent ions, where the reagent ions are produced using EI ionization techniques (Munson and Field, 1966; Gross, 2017). With the correct choice of reagent ions, fragmentation can be significantly reduced compared to EI (Gross, 2017; Medhe, 2018). Ionization of analytes through reagent ions can occur in various ion-molecule reactions, in example, proton transfer reactions, (negative) charge transfer or ligand switching (Gross, 2017). Negative ions are well suited for measuring analytes with high electronegativity (e.g., sulfuric acid) (Kürten et al., 2011). For the measurement of ammonia, proton transfer reactions are suitable, due to its high gas phase basicity (818 kJ/mol) (Harrison, 1997). In this case, charge transfer between reagent ions and (neutral) analytes occurs when the gas phase basicity of the analyte exceeds that of the reagent ion. Gas phase basicity describes the ability of a chemical compound to accept protons during a chemical reaction. It

correlates linearly with the proton affinity, which also depends on the entropy of protonation and the temperature (e.g., ammonia has a proton affinity of 854 kJ/mol at 298K) (Harrison, 1997; Gross, 2017). Accordingly, reagent ions with a proton affinity that is lower than that of the analyte are suitable for chemical ionization during proton transfer reactions. In the case of ammonia or amines, many different reagent ions can be used because of their high proton affinity. For instance, ammonia has been measured in the past using protonated acetone, ethanol, protonated water or O_2^+ (Fehsenfeld et al., 2002; Nowak et al., 2002; Norman et al., 2009; Benson et al., 2010; You et al., 2014; Yao et al., 2016). If the difference in the proton affinities is large, exothermicity of the reaction and subsequent fragmentation increase. In addition, numerous other components in the sample air are ionized if they have a higher proton affinity than the reagent ion (Blake et al., 2009; Gross, 2017; Hansel et al., 2018). This can lead to depletion of reagent ions and lowers the selectivity of the measurement. To maximize selectivity and minimize fragmentation, a reagent ion with a proton affinity only slightly below that of ammonia is recommended. It has been shown that protonated water clusters are very well suited for the selective ionization of bases such as ammonia due to their high proton affinity (e.g., $H_3O^+(H_2O)$ has a proton affinity of 808 kJ/mol) (Sunner et al., 1988; Hanson et al., 2011; Aljawhary et al., 2013). In this case, protonated water (H_3O^+) is initially formed by collision of O_2^+ with water molecules. Afterwards, protonated water clusters are formed when H_3O^+ collides further with water clusters of the form $(H_2O)_n$. These reactions usually take place within a few microseconds (Sunner et al., 1988). A detailed reaction scheme is shown in **Paper 1** (Pfeifer et al., 2020)**.**

Reagent ions react with analytes in the so-called ion-molecule reaction zone (IMR). Depending on the approach, ionization of analytes occurs under different ambient pressures. For example, Proton Transfer Reaction-Mass Spectrometers (PTR-MS) operate their IMR under low pressure (around 10 hPa) (Ellis and Mayhew, 2014; Hansel et al., 2018). This is usually combined with an electric field (~10 to 70 V/cm), increasing the ratio of electric field strength (E) to buffer gas number density (N) (Tani et al., 2004; Blake et al., 2009). An increased E-to-N ratio increases the collision energy between water clusters with surrounding buffer gas, which promotes fragmentation of larger clusters (Tani et al., 2004; Passananti et al., 2019). As a result, analytes are mainly ionized by H_3O^+, which enables the measurement of various VOCs with proton affinities below that of water clusters (e.g. alpha-pinene, benzene or toluene) (for more information, see, e.g., Tani et al., 2004; Ishizuka et al., 2010; Tripathi and Sahu, 2020).

Another approach is to operate the IMR at atmospheric pressure to increase the number of collisions of product ions with surrounding molecules (e.g., Chemical Ionization–Atmospheric Pressure interface–Time-Of-Flight–Mass Spectrometry, CI-APi-TOF-MS). This allows to measure components in thermodynamic equilibrium since an equilibrium is established in favour of the more stable ions (Eisele and Tanner, 1993; Kürten et al., 2011; Simon et al., 2016). Usually, the ion source is separated from the high-vacuum area by a so-called pinhole (with a diameter of around 0.5 mm) (Gross, 2017). So-called hybrid instruments are often used for CI-APi-TOF measurements. These use one or more quadrupoles as ion guides between the ion source and the time-of-flight section (Gross, 2017). Depending on the ratio of DC voltage to AC voltage applied to the quadrupoles and the frequency of the alternating voltages, the transmission for ions with different mass-to-charge ratios is maximized (Junninen et al., 2010;

Gross, 2017). The pressure in the quadrupole chambers is below the pressure of the ionization area and above the pressure of the time-of-flight section (Junninen et al., 2010). Therefore, ions collide with molecules when transported towards the time-of-flight section. The kinetic energy and the axial movement of the ions is thereby reduced. This process significantly increases the transmission of product ions during CI-APi-TOF measurements, since the ion beam is focused on a central axis before it reaches the time-of-flight region (Junninen et al., 2010). Once the ions reach the time-of-flight section, they are accelerated by a high voltage pulse before being detected (e.g. when they hit a MCP) (Gross, 2017).

The ion source developed in **Paper 1** operates at atmospheric pressure and it is coupled to a High Resolution Tof (HTOF) from TOFWERK AG (Switzerland), which is a time-of-flight mass spectrometer containing two quadrupoles before the time-of-flight section: The Small Segmented Quadrupole (SSQ) followed by a Big Segmented Quadrupole (BSQ). The SSQ mainly affects the sensitivity and the transmission of the ions, while the BSQ affects resolution and sensitivity (Junninen et al., 2010; TOFWERK AG, 2013). The pressure in the SSQ region is at around 2 hPa and it drops to around 10^{-2} hPa in the BSQ region. Depending on the voltages applied to the BSQ, the E-to-N ratio increases and fragmentation of analyte ions due to collision with surrounding molecules becomes more important (Zapadinsky et al., 2019; Passananti et al., 2019).

Many ion sources have the pinhole of the mass spectrometer arranged in parallel to the sample air flow. For example, this setup is common when measuring sulfuric acid (Eisele and Tanner, 1993; Kürten et al., 2011). Reagent ions are introduced a few centimetres in front of the pinhole and a sheath flow is often used to minimize wall loss rates and to separate the sample from radicals (such as OH) that form in the initial ion generation process. This enables the measurement of product ions in thermodynamic equilibrium (Sunner et al., 1988; Eisele and Tanner, 1993). With this setup, due to the long response time, depletion of primary ions is possible, especially when measuring highly concentrated substances (such as ammonia in megacities). This can limit the measurement of ammonia to mixing ratios with low upper limits.

The ion source presented in the **Paper 1** is a so-called crossflow chemical ionization source, which uses protonated water clusters for the selective ionization of ammonia and amines. Reagent ions are introduced orthogonal to the sample airflow, with the inlet to the mass spectrometer also orthogonal (sometimes slightly offset) to the sample airflow on the opposite side ("crossflow"). The principle of crossflow ion sources was first used by Eisele and Hanson (2000) to measure molecular sulfuric acid clusters (Eisele and Hanson, 2000). Hanson et al. (2011) used a crossflow ion source to measure ammonia and amines and demonstrated that this design can reduce reaction times for the product ion formation in the IMR significantly (Hanson et al., 2011). Figure 3 schematically summarizes the ion source and the HTOF used to characterize the measurement technique (Pfeifer et al., 2020). Further details on the ion source are summarized in **Paper 1**. The results obtained with the ion source are summarized in **Paper 1, 2 and 3** and in the next chapter.

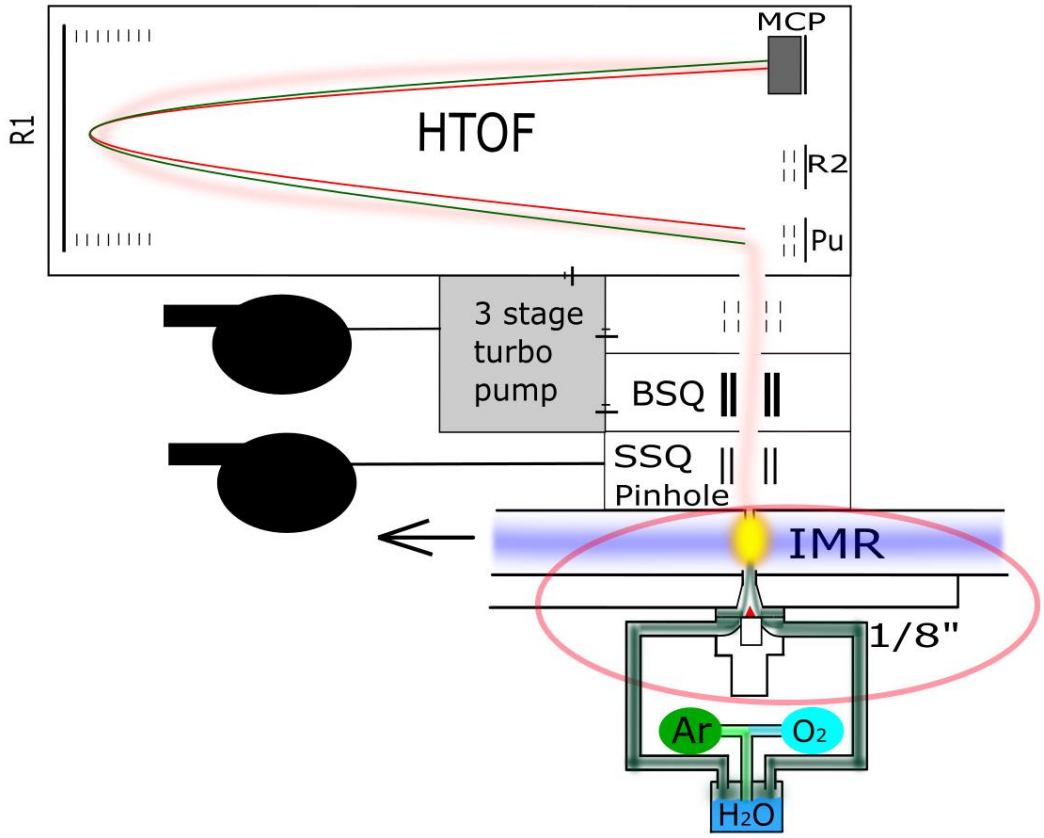

Figure 3: *Argon (labelled as Ar; 95%) and oxygen (labelled O_2; 5%) first pass through a water bath (labelled H_2O). The reagent ions (protonated water clusters) are then generated by flowing the saturated mixture around a corona needle in positive mode (Kürten et al., 2011). In the Ion-Molecule Reaction Zone (IMR), the protonated water clusters finally meet the sample air, with basic components being selectively ionized. The product ions enter the mass spectrometer (HTOF) through a pinhole. They pass the Small Segmented Quadrupole (SSQ; p ~ 2 hPa) and the Big Segmented Quadrupole (BSQ; p ~ $1 \cdot 10^{-2}$ hPa) before being accelerated by a high voltage pulse (Pu) in the time of flight section (p ~ $1 \cdot 10^{-7}$ hPa) (Junninen et al., 2010). The low pressure in the mass spectrometer is maintained by a three-stage turbo pump (TOFWERK AG, 2013). A reflectron (consisting of several ring-shaped electrodes that lie at an increasing potential and form a repulsing electric field (R1)) first decelerates the ions and finally accelerates them towards the detector, which is a microchannel plate (MCP) (Mamyrin, 1994). Details on the instrument setup and the generation of the reagent ions are summarized in Pfeifer et al., 2020.*

1.2.3 Results

The development of the ion source proved to be successful. The ion source has the following properties:

- Reagent ion depletion is minimized by the short ion-molecule reaction time (<1 ms).
- The compact arrangement allows operation without sheath flow, which makes the ion source economical.
- Contact surfaces are minimized throughout the instrument to provide a minimal surface area for molecules to stick, thus reducing instrumental background. This allows measuring ammonia and amines with maximum response time at low detection limits.

Ammonia background levels of about 4 pptv were measured at 80% relative humidity and 278 K. The detection limit was determined to be 0.5 pptv. This is well below the detection limit from previous publications (e.g. Norman et al., 2009; Benson et al., 2010; Yu and Lee, 2012; You et al., 2014; Dong et al., 2022). Mixing ratios of more than 10 ppbv can be measured without significant depletion of reagent ions. In addition, it was shown that the instrument has a very fast response time of a few seconds. Combined with the low background concentrations, the instrument allows to measure ammonia even under rapidly changing conditions, such as in case of fast ammonia-nitric acid condensation (Wang et al., 2020; Marten et al., 2022).

In addition, dimethylamine could be measured with a detection limit of about 0.05 pptv. The theoretical concentrations of dimethylamine were estimated from MFC readout data, considering wall loss rates and chamber dilution loss. It was possible to show that the calibration factor of ammonia can be scaled to the calibration factor of dimethylamine, where the upper limit of uncertainty is 350%. Furthermore, it could be shown that the instrument is able to measure numerous iodine components. A comparison with a nitrate CI-APi-TOF (which ionizes in negative mode) showed that iodic acid can be reliably detected, even at low concentrations. The measurement is reliable over a wide range of mixing ratios and it is comparable to using nitrate as reagent ions (which is often used to measure iodine components) (e.g. Sipilä et al., 2016). This makes the instrument suitable for the reliable measurement of components that can be relevant for nucleation in remote areas, such as coastal regions.

Moreover, due to the short response time of the instrument, it was possible to demonstrate the condensation of ammonia and nitric acid on newly formed particles quantitatively during experiments conducted at the CERN CLOUD chamber (Wang et al., 2020; Marten et al., 2022). It was possible to show that ammonia concentrations in the gas phase decrease when newly formed particles reach a critical diameter (about 4–5 nm). At the same time, growth rates due to condensation of ammonia with nitric acid of more than 100 nm/hr could be observed. Figure 4 shows the measurement of ammonia during a rapid growth experiment conducted during CLOUD 13 (2019). It is shown that the measured mixing ratios decrease as soon as the particles (measured by nSMPS in Figure 4 (Tritscher et al., 2013; Lehtipalo et al., 2014)) reach a critical diameter. At the same time, a decrease in nitric acid concentration (measured by a bromide CI-APi-TOF mass spectrometer) could be observed, which demonstrates the involvement of ammonia and nitric acid on rapid particle growth (Wang et al., 2020, 2021; Marten et al., 2022).

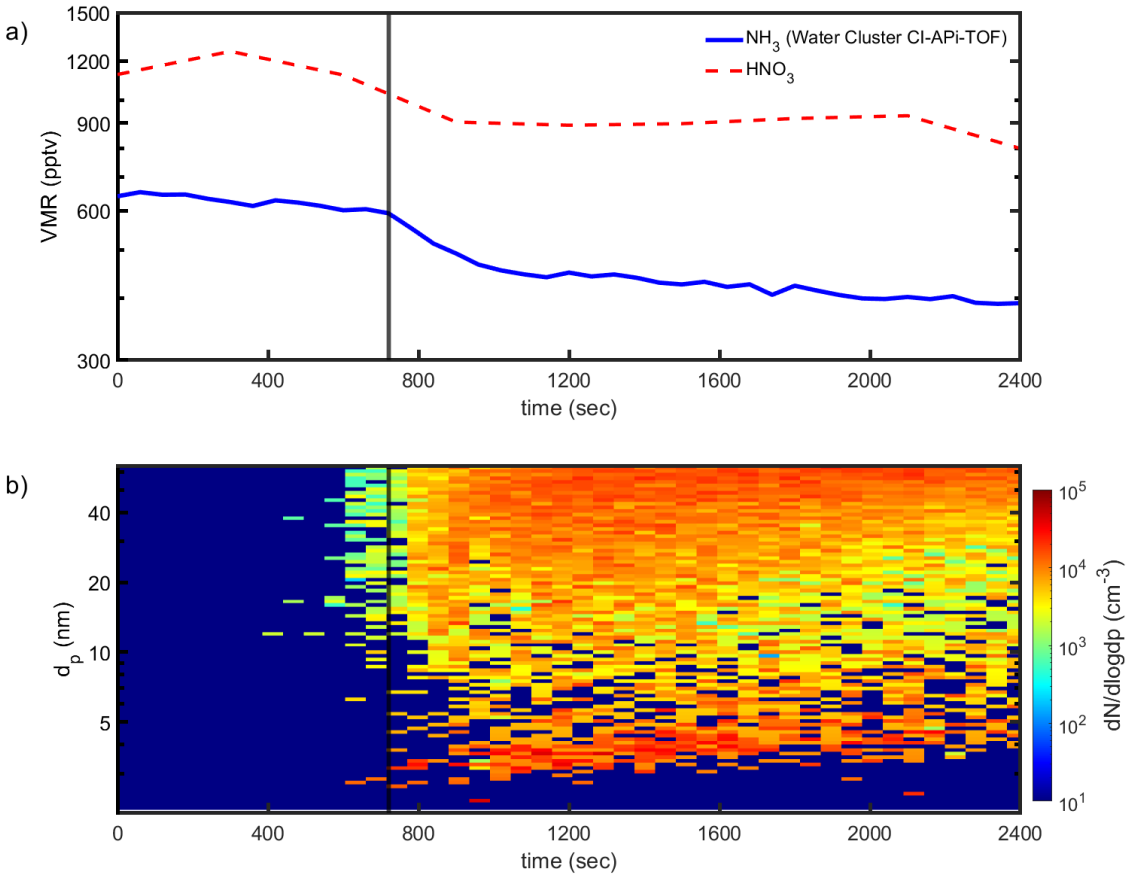

Figure 4: *Measurement of ammonia during experiments at CLOUD13. The measurement of ammonia and nitric acid (using a bromide chemical ionization mass spectrometer, see Wang et al., 2021) is shown in panel a)). At the same time, the particle distribution (measured by a nSMPS) is shown in panel b)). The black line in panel a) and b) shows the time where the Water Cluster CI-APi-TOF measures a clear drop in gas phase ammonia concentration. The response time of the Water Cluster CI-API-TOF presented in this work allows to show quantitatively that ammonia and nitric acid can rapidly condense on newly formed particles as soon as a certain activation diameter (about 4–5 nm) is reached. The gas-phase ammonia concentration decreases during the rapid growth events since ammonia condenses with nitric acid into the particle phase (panel a)). A comparison with a PICARRO instrument (shown in* ***Paper 1****) establishes that the response time of the Water Cluster CI-API-TOF is significantly lower than that of existing instruments. Quantitative experiments on this highly dynamic system were only possible with the development of the Water Cluster CI-API-TOF.*

1.2.4 Summary

Paper 1 describes a new crossflow ion source coupled to a time-of-flight mass spectrometer. Analytes are ionized using protonated water clusters, and the instrument is thus called the Water Cluster CI-APi-TOF (Pfeifer et al., 2020). The instrument was characterized for ammonia measurements at the CERN CLOUD chamber during the CLOUD13 experiments (2019). Characterizations show short ion-molecule reaction times, low ammonia detection limits (0.5 pptv) and low instrumental backgrounds (about 4pptv for ammonia). The Water Cluster CI-APi-TOF was also characterized for the measurement of C_2-amines, where a

detection limit of <0.1 pptv was obtained. A comparison with a Nitrate CI-APi-TOF shows that the Water Cluster CI-APi-TOF can also detect different iodine compounds. A comparison of both instruments for the measurement of iodic acid was carried out and is described in **Paper 1** (Pfeifer et al., 2020).

The rapid condensation of ammonia and nitric acid on newly formed particles was shown during the CLOUD13 experiments. The fast response time of the water cluster CI-APi-TOF allowed to show that ammonia is removed from the gas phase while those particles grow rapidly as soon as they reach a certain activation diameter (about 4–5 nm). This is described in the co-author papers of this thesis (**Paper 2 and 3** (Wang et al., 2020; Marten et al., 2022)).

1.3 CHarged AeRosol GEnerator (CHARGE) and CHARGE experiments

1.3.1 Overview

Multiply charged particles play a key role in numerous instrumental setups. They are particularly important when measuring atmospheric (charged) particles (Hoppel and Frick, 1990; Flagan, 1998; Mirme and Mirme, 2013; Kwan et al., 2019). To measure aerosol distributions according to their particle mobility, atmospheric particles often pass ionizers (e.g., in DMA or EAA instruments). If analyte ions or charged particles deviate from the expected trajectory, for example due to coulomb forces, this can affect the resolution and the sensitivity of the measurement (Mirme, 1994; Flagan, 1998). Multiply charged particles have a higher electrical mobility than singly charged particles of the same size. Therefore, sophisticated inversion algorithms have been developed to correct for multiply-charged particles during mobility or size distribution measurements (e.g., Wiedensohler, 1988; Flagan, 1998; Mirme and Mirme, 2013; Stolzenburg et al., 2022). In case of electrospray mass spectrometry, on the other hand, the higher mobility of multiply charged particles is used to detect proteins, which are normally too heavy for detection (e.g., Kaddis et al., 2007; Sterling et al., 2011; Peters et al., 2019). As discussed in chapter 1.1.3, in atmospheric research, ESI is used to measure the chemical composition of aerosol particles (e.g., Surdu et al., 2021). Multiply charged particles are also common in atmospheric experiments, where their effects are often neglected to simplify calculations (e.g., Chan and Mozurkewich, 2001). In the atmosphere, singly charged ions play an important role in new particle formation and particle growth (e.g., Kirkby et al., 2016; He et al., 2021a; Mahfouz and Donahue, 2021a, b), whereas multiply charged particles are associated with numerous processes in clouds, particularly at the top and bottom of clouds (e.g., Zhou and Tinsley, 2007; Guo and Xue, 2021). To date, there has been a lack of measurements on the behaviour of multiply charged particles in air, as pointed out by numerous authors (Gopalakrishnan and Hogan, 2012; Tamadate et al., 2020a, b). However, experimental data are necessary to provide a basis for existing models, such as models describing ion–aerosol rate coefficients (e.g., Fuchs, 1963; Hoppel and Frick, 1986; Gatti and Kortshagen, 2008; Gopalakrishnan and Hogan, 2012; López-Yglesias and Flagan, 2013; Suresh et al., 2021). Additionally, increased collision rates of multiply charged particles in clouds can have non-negligible effects on the cloud lifetime (see e.g. Guo and Xue, 2021). In a recent study, Dépée et al. (2021) experimentally determined collection efficiencies of multiply charged particles (< 1 µm) with multiply charged cloud droplets. A chamber was used, through which droplets fall,

which were generated by a piezoelectric droplet generator. Inside the chamber, the drops encounter a laminar flow containing (charged) aerosol particles. The experiments show that the collection efficiency can vary over several orders of magnitude and increase sharply with the number of (opposite) charges increasing (Dépée et al., 2021). For particles in the free molecular regime, however, there are almost no measurements of collision rate coefficients of multiply charged particles. Tamadate et al. (2020b) measured coefficients of multiply charged Polyethylene Glycol 4600 (PEG 4600) molecules against small ions (~1 nm) in this size range using an electrospray generator (Tamadate et al., 2020b). The measured distribution (including all multiply charged particles) was compared with a simulated distribution (obtained through Molecular Dynamics (MD) Simulations) and it was shown that rate coefficients within an uncertainty of a factor of 2 could be obtained (where the coefficients were obtained from the MD simulations). While MD simulations are very detailed and consider, for example, the interatomic potentials of the colliding molecules, they require a lot of computing power. In addition, the experiments from Tamadate et al. (2020b) have only limited atmospheric relevance since PEG4600 molecules are negligible in the atmosphere.

In **Paper 4**, a method for measuring ion-aerosol rate coefficients of multiply charged particles (positive charge) with small ions is presented as a function of number of charges for small particles (below 10 nm). For this purpose, an instrument for generating multiply charged particles at the CERN CLOUD chamber was developed (the "CHARGE" instrument). An experiment to determine the coefficients quantitatively was then developed and carried out at CLOUD (named as *Experiment 1* in the next sections). A method was developed to calculate ion–aerosol rate coefficients during those experiments. The coefficients utilize the data collected by various instruments during *Experiment 1*. Finally, the measured coefficients are compared with existing models and theories from the field (i.e. with D'yachkov et al., 2007; Gatti and Kortshagen, 2008; Gopalakrishnan and Hogan, 2012; López-Yglesias and Flagan, 2013; Tamadate et al., 2020b).

While **Paper 4** shows the successful use of CHARGE to determine ion–aerosol rate coefficients, the instrument was not only developed for this purpose. Rather, CHARGE should also help to tackle several open questions related to the behaviour of multiply charged particles in clouds. As previously described, numerous multiply charged particles are expected, for example, in thunderstorm clouds or at the bottom and at the top of fair-weather clouds (Stolzenburg et al., 1998; Zhou and Tinsley, 2007; Rycroft and Harrison, 2012). The excess charge in these regions can enhance "electro-scavenging", due to image charge effects between multiply charged droplets (Tinsley et al., 2000). Simulations from Guo and Xue (2021) suggest that enhanced droplet collision due to multiply charged particles can weaken the aerosol-induced precipitation suppression effect, especially for small droplets (<10 μm) (Guo and Xue, 2021). In their simulations, Guo and Xue also suggest that charge is transferred from smaller (multiply) charged particles to larger particles (or droplets) upon collision. While there are numerous models and simulations on the behaviour of multiply charged particles in clouds, experiments specifically designed to test these propositions are lacking. The idea behind the CHARGE experiments is to experimentally confirm (or disprove) simulations, such as those presented by Guo and Xue (2021) under atmospherically relevant conditions. For this purpose, two further experiments were carried out at CLOUD (named *Experiment 2* and *Experiment 3*

in the next sections). In *Experiment 2*, charge transfer from multiply charged (small) particles to other (bigger) particles upon collision is evaluated. The aim of *Experiment 3* is to experimentally show (or disprove) further effects of multiply charged particles. For instance, the role of multiply charged particles on the aerosol-induced precipitation suppression effect should be evaluated to provide experimental data for simulations as shown by Guo and Xue (2021).

The following section briefly summarizes the principle of CHARGE and first results obtained from initial characterization experiments conducted at a laboratory at CERN (see section "CHarged AeRosol GEnerator (CHARGE)" in methods (1.3.2)). Afterwards, the CHARGE experiments (*Experiment 1, 2 and 3*) are summarized (see sections "CHARGE experiments at CLOUD" in methods (1.3.2) and results (1.3.3)). Detailed results obtained from *Experiment 1* are shown in **Paper 4** (Pfeifer et al., 2022). However, *Experiment 2* and *Experiment 3* are only evaluated qualitatively, due to missing information on full particle size distribution and gaps in the time series of some important instruments. Therefore, their results are only shown in the introduction part of this thesis (as a "proof-of-concept"). In the summary section (1.3.4), a brief outlook is provided on how *Experiment 2* and *Experiment 3* can provide more clear results in the future.

1.3.2 Methods

1.3.2.1 CHarged AeRosol GEnerator (CHARGE)

Concept of CHARGE

The CHarged AeRosol GEnerator (CHARGE) is an instrument, which is based on Electrospray Ionization (ESI). The aim of the CHARGE is to generate a large concentration of multiply charged particles and to direct them into the CLOUD chamber. The generated number of multiply charged particles should be sufficient to conduct experiments on their effects under atmospherically relevant conditions inside the chamber. Additionally, space charge effects should promote a homogenous distribution after their injection.

In Electrospray Ionization (ESI), a liquid solution is passed through a capillary, with a very strong electric field applied to the tip of the capillary. The tip often consists of stainless steel, where a high voltage is applied to create the electric field (Kebarle, 2000). When a positive voltage is applied ("positive mode"), positive ions accumulate at the surface of the solution, while the electric field causes negative ions to move towards the inside of the capillary. The positive ions experience a repulsive force among themselves. In addition, they are pulled out of the capillary by the electric field at the tip of the capillary. This causes them to taper and form a so-called Taylor Cone (Kebarle, 2000; Smith et al., 2002). During Electrospray, highly charged droplets are continuously emitted from the tip of the Taylor cone. The onset of Electrospray depends on the surface tension and the conductivity of the solution, as well as its flow rate through the capillary. It also depends on the geometry of the capillary (e.g., the radius) and the electric field encountered at the tip of the Taylor cone (De La Mora and Loscertales, 1994). Electrospray delivers a continuous current; thus, electrochemical reactions occur at the capillary, which permanently create positive ions or remove negative ions (Blades et al., 1991; Kebarle, 2000). Operation with negative voltage ("negative mode") is equivalent, where

negatively charged droplets are emitted. The number of charges, which a droplet carries after emission, depends on the surface tension of the solution, and it strongly depends on the radius of the droplet (Kebarle, 2000). Large droplets with high surface tension will carry more charges. At the same time, larger droplets are emitted from solutions with lower conductivity (at higher flow rates) (Kebarle, 2000). After their emission, the droplets rapidly evaporate. They reach a point, where Coulombic repulsion between the charges overcomes the surface tension of the droplets (the so-called Rayleigh limit) (Taflin et al., 1989; Kebarle, 2000). As a result, the drops explode ("Coulomb Explosion"), where numerous satellite drops are formed. These have about 2% the mass and 15% the charge compared to the original drops (Gomez and Tang, 1994). The process is repeated until ions and multiply charged particles in the nanometre size are formed.

In case of CHARGE, the following design considerations are particularly important during development:

- The ESI solution must be atmospherically relevant. Thus, many well-known solutions from ESI Mass Spectrometry cannot be used. A mixture of pure water with sulfuric acid (2% wt) was used as a first approach. Water has a very high surface tension, which is why the onset point for electrospray is at particularly high voltages (applied to the tip of the capillary). Sulfuric acid does not break this surface tension (Myhre et al., 1998). This complicates ESI operation, since electric discharges can occur at higher voltages, especially when operated in negative mode.
- The multiply charged particles must be transmitted to the CLOUD chamber, with minimized loss rates directly after emission from the capillary. This is a particular challenge, since CHARGE should be connected to a standard CLOUD port, meaning the particles are transported to the chamber through a pipe (length more than 20 centimetres). Due to space charge effects, high losses in the line are expected (Fu et al., 2011).
- To avoid contamination, only stainless steel and ceramics are used in the CHARGE design. The solution is delivered to CHARGE by using a continuous syringe pump (Univentor U-802 syringe pump). Only glass syringes (Hamilton series 1800) are used, which are connected to CHARGE's stainless-steel pipes using a short section of Polyetherether Ketone (PEEK) pipes.

Figure 5 summarizes the key steps relevant in the development of CHARGE prior to its deployment to the CLOUD chamber. The geometry of CHARGE is based on an approach as described in Smith et al. (2002). Electrostatic simulations were performed using GARFIELD assuming singly charged positive ions (one example is shown in panel a) in Figure 5; more information on GARFIELD can be found in Veenhof (1998)). To optimize transmission into the CLOUD chamber, various geometries were simulated. The geometries were created using the computational fluid dynamics software ANSYS R16.1. During those simulations, no specific chemical solution was simulated and thus, the operating conditions and the geometry differ from the laboratory experiments. The geometry shown in this example uses a capillary with an inner diameter of 200 µm (marked with a blue C in Figure 5). A perforated plate with an inner diameter of about 0.6 cm (outer diameter is 2 cm) is located about 1 cm behind the

capillary tip (*electrode 1*; E_1). In this simulation, a voltage of 1200 V is applied to the capillary, where 100 V is applied to electrode 1. Electrospray is emitted due to the potential differences between the tip of the capillary and electrode 1. The ions are transmitted through the perforated plate and then transported towards the CLOUD chamber using a drift tube (*electrode 2*; E_2) with a voltage of 10 V applied (length 4 cm; inner diameter 1.6 cm).

Panel b) in Figure 5 shows a schematic cross section of CHARGE as it was used during characterization experiments at a CERN laboratory (schematic drawing; geometry is not to scale). The geometry differs slightly compared with the simulations. A capillary with an inner diameter of 400 µm was used. In case of electrode 1, two different perforated plates were used, with varying inner diameter (1 cm and 3 cm; the outer diameter was at 5 cm in both cases). This is indicated by the dashed black line at electrode 1 in panel b). In both cases, electrode 1 was placed in front of the capillary, at a distance of 0.3 cm. Varying the inner diameter of electrode 1 is intended to optimize the transmission of the multiply charged particles and it is based on experiments reported by Fu et al. (2011), who conducted measurements on the transmission of multiply charged droplets using ESI (Fu et al., 2011). Electrode 2 has a length of 3.5 cm, with an inner diameter of 5 cm. Since CHARGE will be attached to a CLOUD port, there is another drift region behind electrode 2 (*electrode 3*; E_3 in panel b). Electrode 3 is grounded (0 V) and directly connected to the CLOUD chamber.

During all experiments and simulations, electrode 1 has a significantly lower voltage applied than the tip of the capillary. The voltage gradient between the counter-electrode and the tip of the capillary defines the strength of the electric field in the Taylor cone region and lowers the onset voltage of electrospray. At the same time, the transmission towards electrode 2 should be increased (Smith et al., 2002). During the initial tests of CHARGE, the instrument itself was used to measure the transmission of the highly charged droplets and the performance of the electrospray. This is indicated by the light blue trajectories in the scheme in panel b). During these tests, CHARGE was placed on a Teflon block (shown as a pink area in panel b)), which in turn stands on a metal plate. The metal plate simulates the transmission to the CLOUD chamber, and it is indicated in panel b) using a dashed, orange line. Electrospray solutions were varied (between 0.00025 % wt. and 10 % wt. sulfuric acid in water). The charge from the ESI droplets were detected using several Keithley electrometers, which were connected to the electrodes (I_1 to I_4 in panel b)). Panel c) shows the most important parts of CHARGE. The capillary is shown on the first photo, the electrodes 1 and 2 are shown on the second photo and the third photo shows the entire CHARGE prototype (including electrode 3). Panel d) shows a picture of the Taylor cone when electrospray is emitted (taken with a microscope camera).

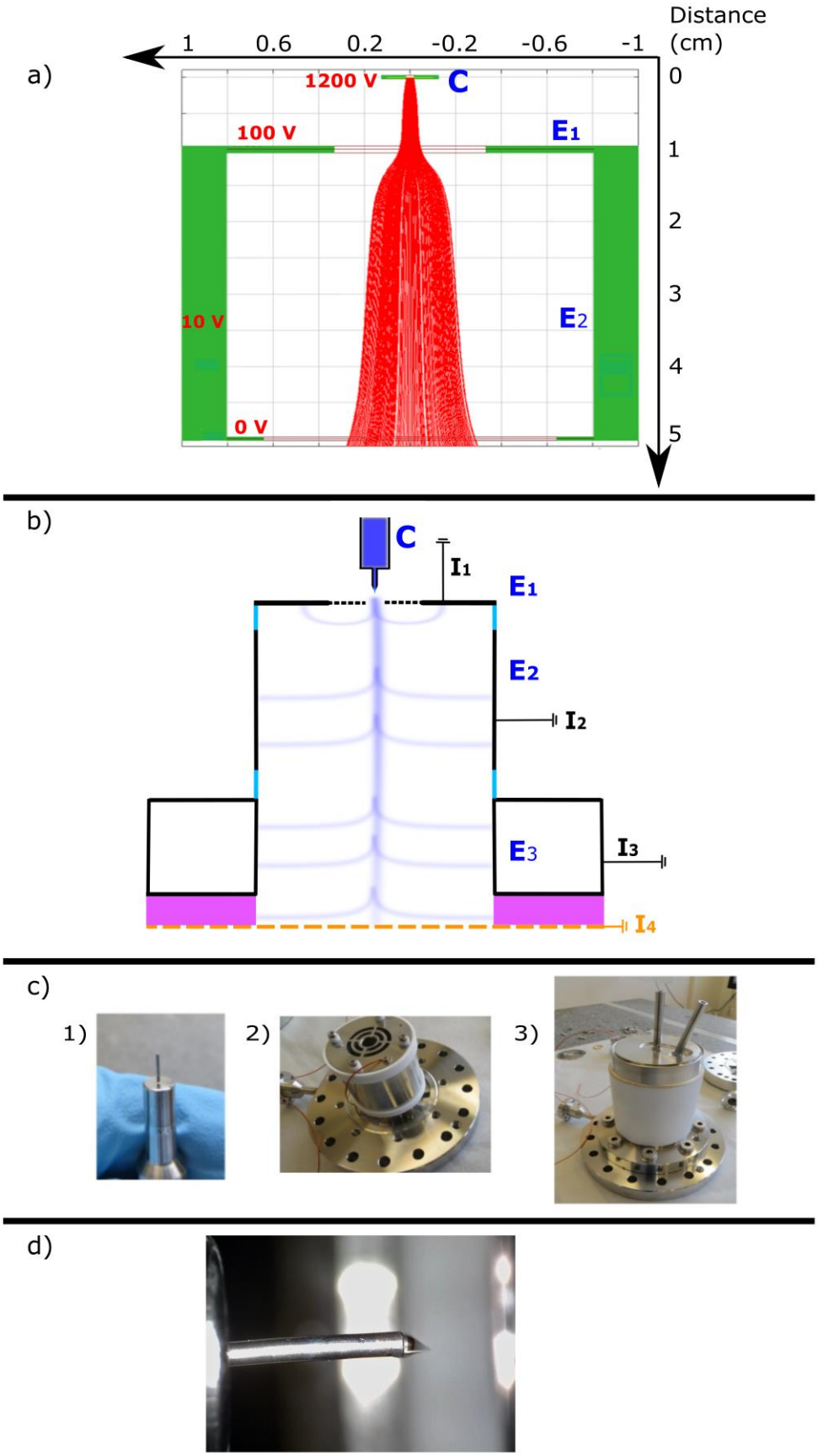

Figure 5: *First electrostatic simulations of the transmission efficiency of the CHARGE electrospray generator (panel a); assuming singly charged positive ions). Schematic cross*

section of CHARGE and scheme of initial tests (panel b)). The capillary is labeled with a blue C, the electrodes (electrode 1,2, and 3) are labelled as E_1, E_2 and E_3. The pink area in panel b) marks a perforated Teflon plate on top of which CHARGE was placed during some of the first laboratory experiments. Underneath is a grounded metal plate that should simulate transmission to the chamber. Current was measured synchronously using multiple Keithley electrometers (I_1 to I_4). The photos in panel c) show the capillary (picture 1), electrodes 1 and 2 (picture 2) and the final version of CHARGE (picture 3). Panel d) shows a picture of the Taylor cone (i.e., when electrospray is emitted) during one of the laboratory experiments (see CHARGE characterization at CERN laboratory). The picture was taken with a microscope camera. Further information is summarized in the text.

Two main goals were set for the initial CHARGE tests:

- **Verification of a stable electrospray**. For this purpose, the voltages at the electrodes (especially at the capillary) were gradually changed using a CAEN NDT 1470ET high voltage (HV) supply. During those measurements, the current was measured using the Keithley instruments (I_1 to I_4) and the HV supply. Each voltage setting was maintained for about 5 minutes to ensure measurement stability. In later experiments, a camera was also used to photograph the formation of electrospray. The tests show that when using the perforated plate with an inner diameter of 1 cm (electrode 1), more current is measured on electrode 1 compared with the current measured from the HV supply (see Fig. 6). There is no exact explanation for the deviations; however, the deviations are not large (see Fig. 6a). Since the Keithley has a better time resolution, the current on electrode 1 (I_1) was used to verify the electrospray in this case.
- **Optimization of Transmission Efficiency.** A setting was used, which ensures stable electrospray (based on the first experiments). The transmission efficiency for each section was determined. It is defined as the ratio of the total current emitted from the capillary (measured using the HV supply) to the current measured at each of the electrodes (multiplied by 100 for conversion to percentage). Due to the deviations between HV supply and Keithley (when operated on electrode 1), an error of ±90% was assumed for the calculations (see Fig. 6c).

During the tests, the voltages applied to the electrodes were changed in addition to the voltages applied to the tip of the capillary. In addition, the chemical solutions were varied (between 0.00025 % wt. and 10% wt. sulfuric acid in water), as well as the liquid flow rate through the syringe pump.

CHARGE characterization at CERN laboratory

The first experiments were carried out in a laboratory at CERN to find the best operating conditions for CHARGE to determine whether the CHARGE geometry is suitable for stable electrospray generation. The goal was to evaluate stable electrospray generation using sulfuric acid-water solutions. In addition, the transmission efficiency in the drift region (electrode 2) should be maximized by optimizing the voltage settings and the geometry of the CHARGE components. A sheath flow was not used during these initial experiments. However, this is of essential importance when operating at the CLOUD chamber, as will be discussed later.

Figure 6 summarizes some examples of the initial experiments. A time series of the current detected by a Keithley 6485 electrometer (which was installed at electrode 1) is shown in panel a). The voltage at the tip of the capillary is increased by serval tens of volts every few minutes. The naming convention in Fig. 6a is based on López-Herrera et al. (2004) who reported comparable experiments on electrospray with pure water. During "dripping mode", droplets are emitted irregularly, which is why only a low current is detected at the electrode. During "cone jet mode", a stable electrospray is generated, which is reflected by a stable emission current. If the voltage is further increased, the spray becomes unstable and highly charged particles are emitted irregularly, which is supplemented by corona discharge. This is characterized by a high standard deviation in the measured currents and referred to as "electric dripping mode". These observations are essentially consistent with those reported by López-Herrera et al. (2004), according to which pure water generates stable electrospray only over a narrow voltage range. While it is reasonable to assume that not all particles can be detected on electrode 1, panel a) shows that in the case of 1 cm inner diameter, almost all current is detected on electrode 1, which even shows higher values than the HV supply at specific settings (the current measured by the HV supply is shown with a grey line). For this reason, it is justified to show the measured current at electrode 1 in panel a) to evaluate electrospray generation.

Panel b) in Figure 6 shows experiments where the mass fraction of sulfuric acid in the solution was varied (between 0.00025 % wt. and 10 % wt.). In addition, the liquid flow rate delivered from the syringe pump was varied (represented by different symbols in the Figure 6). The transition from cone jet to electric dripping mode is recognized by a sharp increase in the measured current in panel b). The onset point of electrospray coincides with the plateau shown in panel a). In general, there is no strong dependency on the mass fraction of sulfuric acid. This is consistent with theory since the surface tension of the solution remains nearly constant when the sulfuric acid mass fraction is increased (Myhre et al., 1998). The flow rates do not significantly affect the onset point and the yield of the electrospray. Based on the test results, a solution of 2 % wt. was used during the CHARGE experiments. This solution offers a good compromise to protect the PEEK materials on the pipe section at the syringe pump (PEEK is only suitable for solutions with less than 10 % wt. sulfuric acid, see e.g.: CP Lab Safety (Official Webpage); Last visit: Nov 2022).

Figure 6 panel c) shows examples on test results on geometry dependency of the transmission efficiency (measured on electrode 2 and electrode 3, i.e. results obtained from I_2 and I_3). Two different geometries were used. The first geometry utilizes a perforated plate with 1 cm inner diameter as the first electrode (shown in magenta). For the second geometry, another perforated plate with 3 cm inner diameter was used as the first electrode (shown in blue). These tests are based on results from Fu et al. (2011), according to which the transmission efficiency increases significantly when the inner diameter of the first electrode is increased. The current was measured simultaneously on all electrodes and on the capillary (using several Keithley instruments on the electrodes and the HV supply on the capillary). Finally, the transmission efficiency shows the measured current at the respective electrode in relation to the current measured on the capillary using the HV supply (mean over a 10-minute period during stable electrospray generation). The distance to the capillary is given by the geometry of CHARGE: Since the length of the second electrode is 3.5 cm (as shown in Figure 5), charged particles

measured by I_2 are lost within this section. This is illustrated by the horizontal error bars in panel c). It turns out that an increase in the inner diameter of the first electrode significantly increases the transmission, while at the same time higher voltages must be applied to the tip of the capillary to obtain a stable electrospray. Comparable tests were also performed by varying the voltages on the electrodes. These are not shown in this work, because no significant dependence on transmission was found, whereas the geometry showed a crucial effect, as also suggested by Fu et al. (2011).

In conclusion, the first experiments at the CERN laboratory show that a stable electrospray is possible when using sulfuric acid-water solutions in positive mode (i.e., using positive voltages applied to the capillary and electrodes). Stable electrospray occurs over a narrow voltage range, as also reported by Lopez-Herrera et al. (2004). A clear dependency on the inner diameter of the perforated plate (electrode 1) was observed. The transmission of charged particles increases when the inner diameter is increased. Accordingly, CHARGE was operated with a perforated plate with an inner diameter of 3 cm during operation at CLOUD. Dependency on liquid flow rate and solution was negligible.

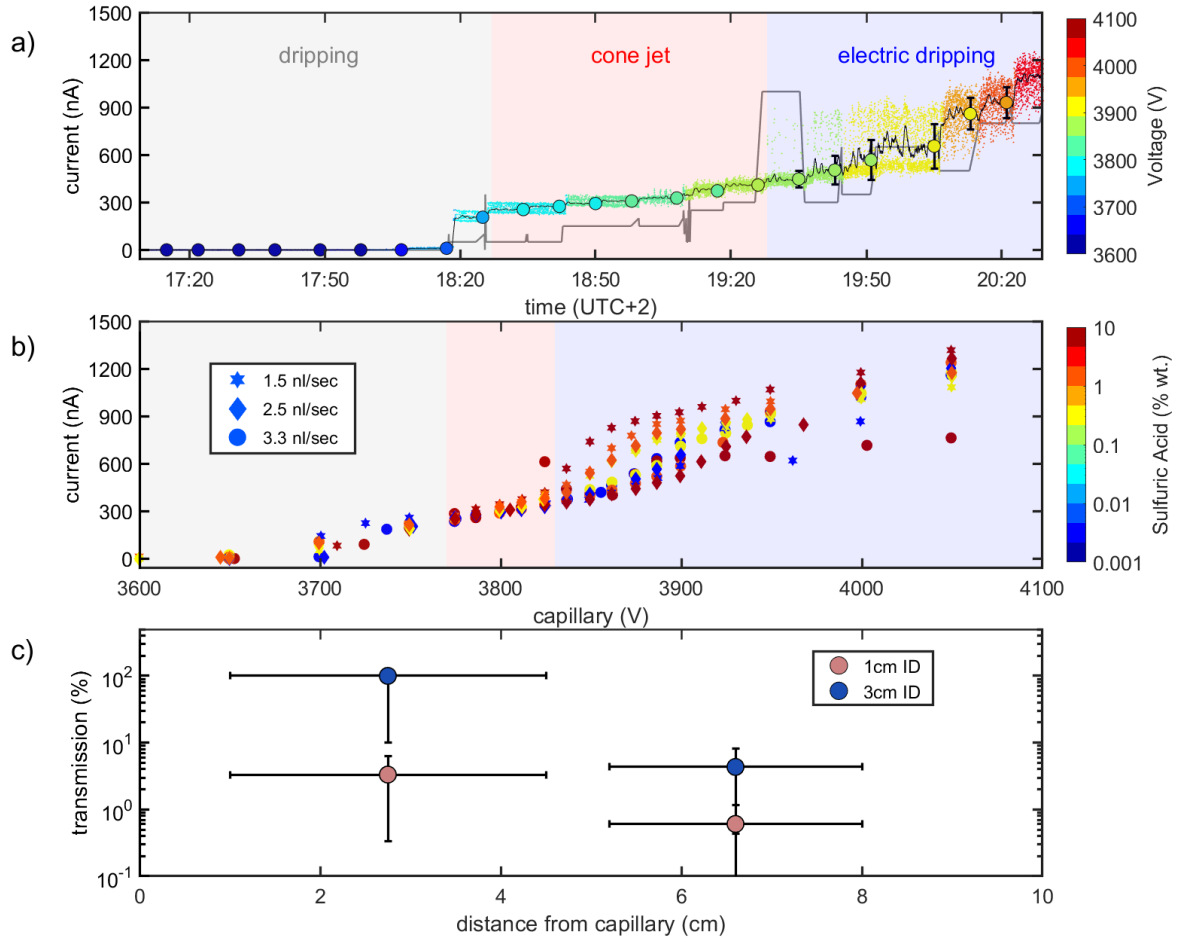

Figure 6: *Initial experiments to evaluate the performance of CHARGE. Panel a) summarizes basic tests on the operating conditions of electrospray. The colour scale indicates the applied voltage. An average (moving average of 30 seconds) is shown in black. Keithley readings are shown at electrode 1 when using an inner diameter of 1 cm. The grey line shows the readout from the HV supply (connected to the capillary) for comparison. Panel b) shows experiments,*

where the mass fraction of sulfuric acid was varied, as well as the flow rate delivered from the syringe pump. Variations in flow rate are shown using different symbols. The colour scale implies sulfuric acid concentration (in % wt.). In panel c), initial measurements on the transmission efficiency are summarized. Those are based on measurements on electrode 2 and 3. The horizontal error bars are defined by the length of the electrodes. The vertical error bar takes the deviations between the measured current from the HV supply and the Keithley at electrode 1 (when 1 cm ID is used) into account (as shown in panel a)). To account for this, an error of ±90% was assumed when calculating the transmission efficiency. Further information is summarized in the text.

CHARGE operating conditions at CLOUD Chamber

At the CLOUD chamber, the conditions are slightly different compared with the laboratory experiments. The particles are transported through a long pipe, which is connected to a CLOUD port behind CHARGE (and which was not present in the laboratory setup). The particles emitted from CHARGE must travel a far greater distance. Therefore, a sheath flow (~200 lpm) is necessary. This could not be tested in the laboratory before. CHARGE was connected to CLOUD's dry air line (which is at 0% relative humidity) to operate independently from the chamber flow. The dry air flow was introduced directly behind the tip of the capillary. Therefore, the liquid solution evaporates promptly from the tip of the capillary. In consequence, the liquid flow rate through the syringe pump must be increased by two orders of magnitude compared with the liquid flow rates shown in Fig. 6b. During the experiments, CHARGE was operated as follows:

- The liquid flow rate was set to 200 nl/sec.
- The HV on the tip of the CHARGE capillary was set to 5500 V, with the voltage on electrode 1 (3 cm inner diameter) set to 100 V. The voltage on electrode 2 was set to 10 V. This is comparable to operating conditions in the CERN laboratory (in case of using electrode 1 with 3 cm inner diameter).

To ensure stable operation, the electrospray was optically monitored by a camera during the CHARGE experiments. In addition, the current at the electrodes was permanently measured. All experiments were carried out in "positive ion mode", because we observed corona discharges during operation in "negative ion mode". Comparable results on operation of pure water in "negative ion mode" were reported in numerous other studies (due to the high surface tension of water) (Kebarle, 2000). This problem can be circumvented by decreasing the surface tension of the solution, for example by adding acetonitrile (about 49 % wt.) (see e.g. Rao et al., 2009). However, when using this solution, one can argue about the atmospheric relevance of the emitted particles (which is particularly important for the CHARGE experiments at CLOUD).

1.3.2.2 CHARGE Experiments at CLOUD (Methods)

The CHARGE experiments open multiple possibilities for research related to the effects of multiply charged particles under atmospherically relevant conditions (see section 1.3.1 (Overview)). As mentioned in section 1.3.1 (Overview), three experiments are shown in this work: *Experiment 1, Experiment 2,* and *Experiment 3*. An XRay source is installed in front of

the CHARGE during all experiments. The XRay source is switched on during some experiments to provide a comparison between charged (XRay switched off) and neutralized particles (XRay switched on) of comparable size (and chemical composition). During all experiments, several mass spectrometers and DMA instruments measure the gas phase and the particle distributions. Additionally, an Electrical Aerosol Analyzer (EAA) is used to me measure atmospheric ions and multiply charged particles (in case of the first CHARGE experiments, it is a Neutral cluster and Air Ion Spectrometer (NAIS); see e.g. Manninen et al., 2016). Some of the DMA instruments have their own neutralizers switched on, others have them switched off. The data allow comparison of the mobility spectrum between multiply charged particles (*XRay off*) with neutralized particles (*XRay on*). The objectives of the three experiments are summarized below.

1) *Experiment 1.* Evaluation of the performance of CHARGE. Two experiments are carried out for this. In the first experiment, the CHARGE is switched on, with XRay off. In the second experiment, both (CHARGE and XRay) are switched on. During those experiments, ion–aerosol rate coefficients are measured as a function of number of charges under atmospherically relevant conditions. The analysis is described in **Paper 4** of this thesis.
2) *Experiment 2.* Experiments on the charge transfer during collision of small multiply charged particles with larger particles. Larger particles (size range about 50–400 nm) are first fed into the CLOUD chamber, by evaporation of sulfuric acid in a heated container which is placed outside the CLOUD chamber. Afterwards, multiply charged particles (or neutralized particles) are added using CHARGE. These experiments are intended to investigate the coefficients with which the small (multiply charged) particles collide with the larger particles. In addition, the charge transfer to the larger particles is investigated. This is, for example, simulated in case of clouds by Guo and Xue (2021).
3) *Experiment 3.* Expansion experiments to evaluate electro-scavenging effects in clouds. The chamber pressure is increased. Afterwards, multiply charged particles (or neutralized particles) are fed into the CLOUD chamber (at overpressure), and subsequently a chamber pressure expansion is conducted. Optical Particle Counters (OPCs), such as the WELAS or the PINE, measure the composition of the droplets (in the micrometre size range) (see e.g. Palas Gmbh, Karlsruhe, Germany or Möhler et al. (2021)). The cloud lifetime is compared, whereby the entire measurement range from a few nanometres to several micrometres should be constantly measured to ensure mass closure. These experiments can be extended by injection of pre-existing aerosols (e.g., by adding 50–400 nm particles through the heated container used during *Experiment 2*).

Figure 7 shows a schematic drawing of *Experiment 1* (panel a)) and *Experiment 2* (panel b)). Figure 8 shows a schematic drawing of *Experiment 3*. The results from *Experiment 1* are presented in **Paper 4**. A major focus of the paper lies on the quantitative calculation of ion–aerosol rate coefficients as a function of the number of charges. The calculations are based on the data obtained during the experiments. The calculation methodology and the comparison of the results with existing models are described in detail in **Paper 4.** They are not discussed in

this introduction. In the next chapter, the main results of **Paper 4** are briefly discussed. Afterwards, the results from *Experiment 2* and *Experiment 3* are summarized. As already mentioned, both experiments are evaluated qualitatively, due to missing information on full particle size distribution and gaps in the time series of some important instruments. In the summary section (1.3.4), a brief outlook is discussed on how *Experiment 2* and *Experiment 3* can provide more clear results in the future.

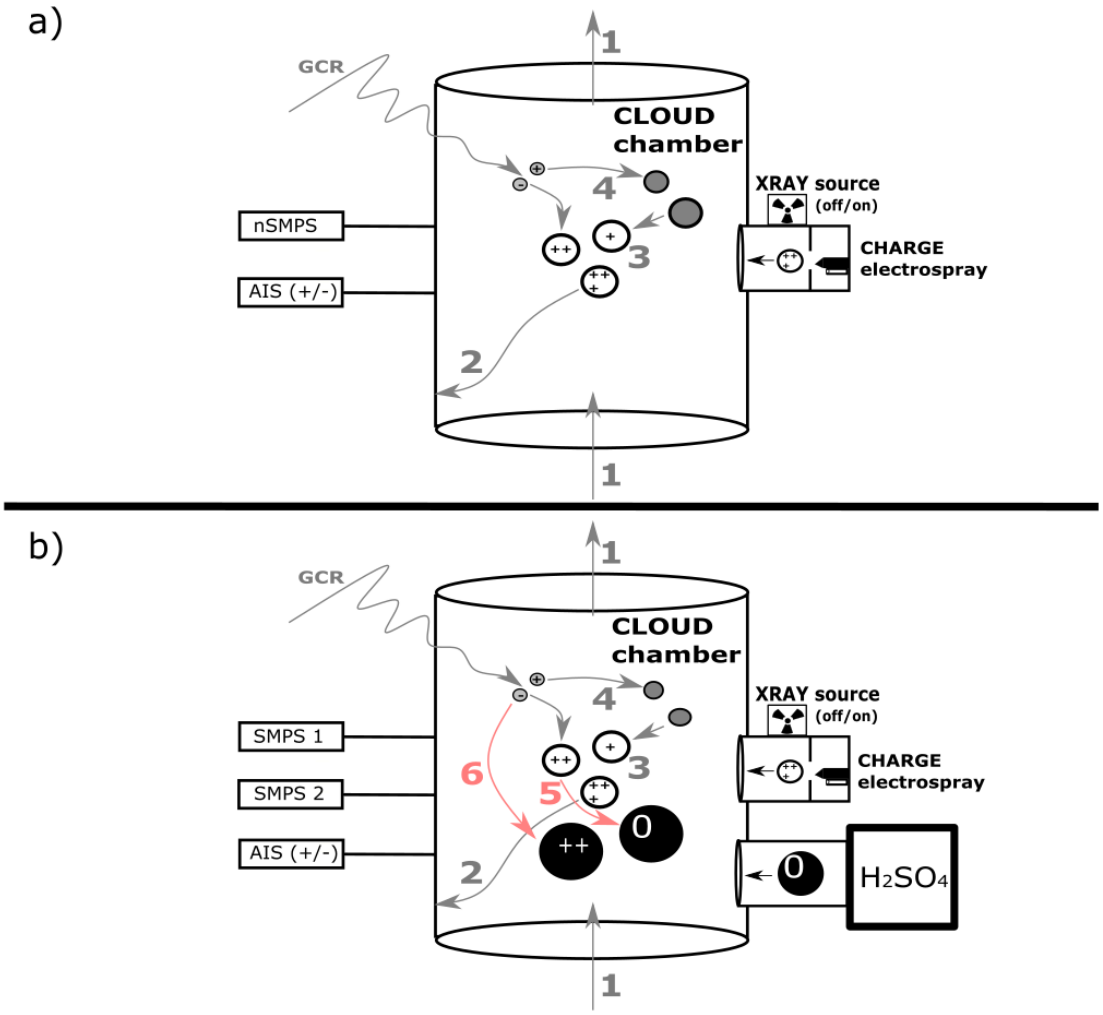

Figure 7: *Schematics of the first two experiments carried out during the CHARGE experiments. The first experiment's goal is to evaluate the performance of CHARGE (panel a)). The experiment enables measuring ion–aerosol rate coefficients for multiply charged particles. For this, the dominant chamber loss rates need to be defined: dilution loss (1), wall loss (2), aerosol–aerosol collisions (3), collisions of aerosols with ions produced by galactic cosmic rays (4). The analysis is described in* ***Paper 4****. Panel b) shows the second experiment. It is similar to Experiment 1, but attention is paid to the change in mobility distribution of the larger (50–400nm) aerosols (marked with a zero). Two comparable SMPS units are used for this: one with a neutralizer and one without neutralizer. Two further processes become relevant during these experiments: The multiply charged particles collide with the larger particles (5).*

If the large particles are charged (through charge transfer), they themselves become multiply charged (as indicated by the multiply charged black particle). Accordingly, the neutralization of the charge can then be determined by collision of small negative ions with the large particles (6).

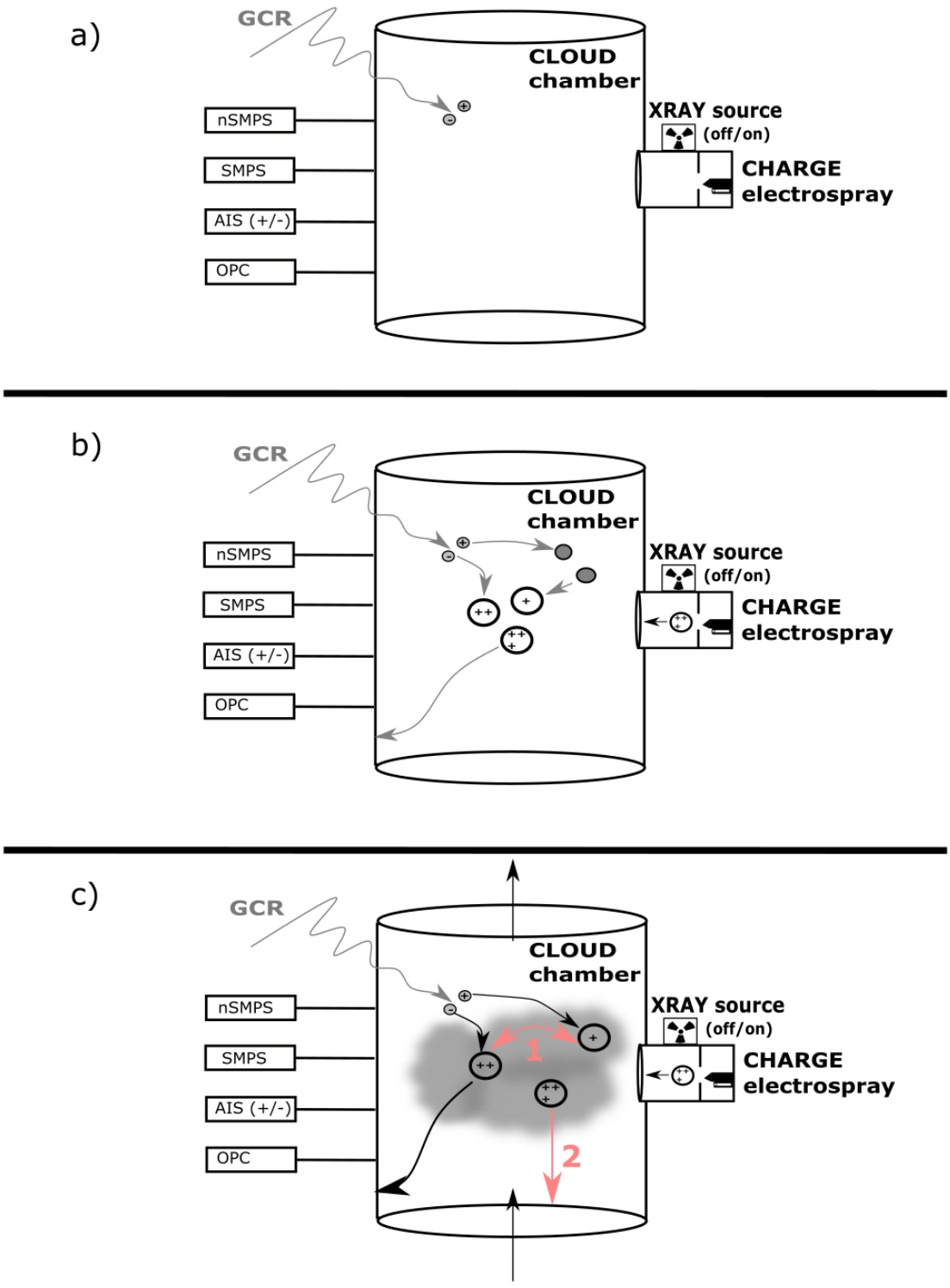

Figure 8: *Principle of the expansion experiments (Experiment 3). The three main steps are summarized in panel a), b) and c). First, the pressure in the chamber is increased from 5 hPa*

overpressure to around 200 hPa overpressure (panel a)). Meanwhile, there are no particles in the chamber and CHARGE is switched off. At overpressure, the multiply charged (or neutralized) particles are injected from CHARGE (panel b)). This is followed by expansion, after which the numerous instruments at the chamber measure the lifetime of the cloud, which is formed due to supersaturation during expansion (panel c)). Panel c) shows two loss terms that become important in Experiment 3 (in addition to the loss terms shown for Experiments 1 and 2): Possible "electro-scavenging" effects in the cloud caused by the multiply charged particles (1) and losses of larger droplets due to gravitational settling (2). It is important that the entire mass range is consistently covered by the instruments during the entire period of the experiments.

1.3.3 Results

1.3.3.1 CHARGE Experiments at CLOUD (Results)

Experiment 1

The first CHARGE experiments at CLOUD were performed to evaluate the performance of the instrument. The aim of the experiments is to show the production of multiply charged particles quantitatively by comparison with measurements carried out when charge inside the chamber is in steady state. In the first experiment, CHARGE was switched on and the multiply charged particles were fed directly to the CLOUD chamber with a sheath flow of 200 l/min. In the second experiment, the XRay was also switched on and neutralized particles (initially emitted from CHARGE) were fed into the chamber. Numerous mass spectrometers, OPCs, DMA and EAA instruments (i.e. the NAIS) constantly measure gas and particle phase during the experiments (Birmili et al., 1999; Manninen et al., 2009; Kürten et al., 2011; Breitenlechner et al., 2017; Wang et al., 2021; Surdu et al., 2021; Amanatidis et al., 2021; Möhler et al., 2021).

Figure 9 shows a time series of the experiments. A comparable (and extended) figure is also shown in **Paper 4**. As already described in section 1.3.2.2 ("CHARGE Experiments at CLOUD"), there are three stages: Injection, decay, and cleaning. During injection (I in Fig. 9), the particles from CHARGE are fed to the chamber. During the decay stage (D in Fig. 9), all voltages and flows from CHARGE are switched off. Thus, there is no source term for particles and effects of the multiply charged particles can be observed quantitatively. During cleaning stage (C in Fig. 9), wall and dilution loss are increased by ramping up the speed of the fans installed at the CLOUD chamber. An electric field is applied to the chamber and the flow rate through the chamber is increased simultaneously. This stage is important to get the chamber clean for the next experiments.

The first four panels from Figure 9 show the measurements of the NAIS during *Experiment 1*. Panel a) shows the total (uncorrected) number concentration of charged particles. The ratio between negative to positive particles is shown in Fig. 9b (size range 2–20nm). Panel c) shows the positive distribution, and panel d) shows the negative distribution (unit: $dN/dlogd_p$ (cm^{-3})). In the beginning of the time series, particles are fed to the chamber by CHARGE with the XRay turned off (XRay off). Afterwards, the XRay is switched on, together with CHARGE (XRay on). Since the NAIS assumes to measure ions from galactic cosmic rays during those experiments (i.e., mainly singly charged ions), it detects multiply charged particles with smaller

mobility diameters and overestimates their number concentration (since those particles carry more charge) (e.g., Mirme and Mirme, 2013; Manninen et al., 2016). In Fig. 9c, slight "bands" in the spectrum during XRay off experiments show these multiply charged particles. In addition, the ratio of positive to negative charge is not balanced, as shown in panels a) and b).

Paper 4 evaluates ion–aerosol rate coefficients as a function of number of charges. These measurements are based on the experiments shown in Figure 9. The coefficients are determined numerically based on first principles, which include the dominating production and loss rates. The methodology was developed by the author of this thesis and is summarized in **Paper 4**. Further information on the NAIS is summarized in Manninen et al. (2016).

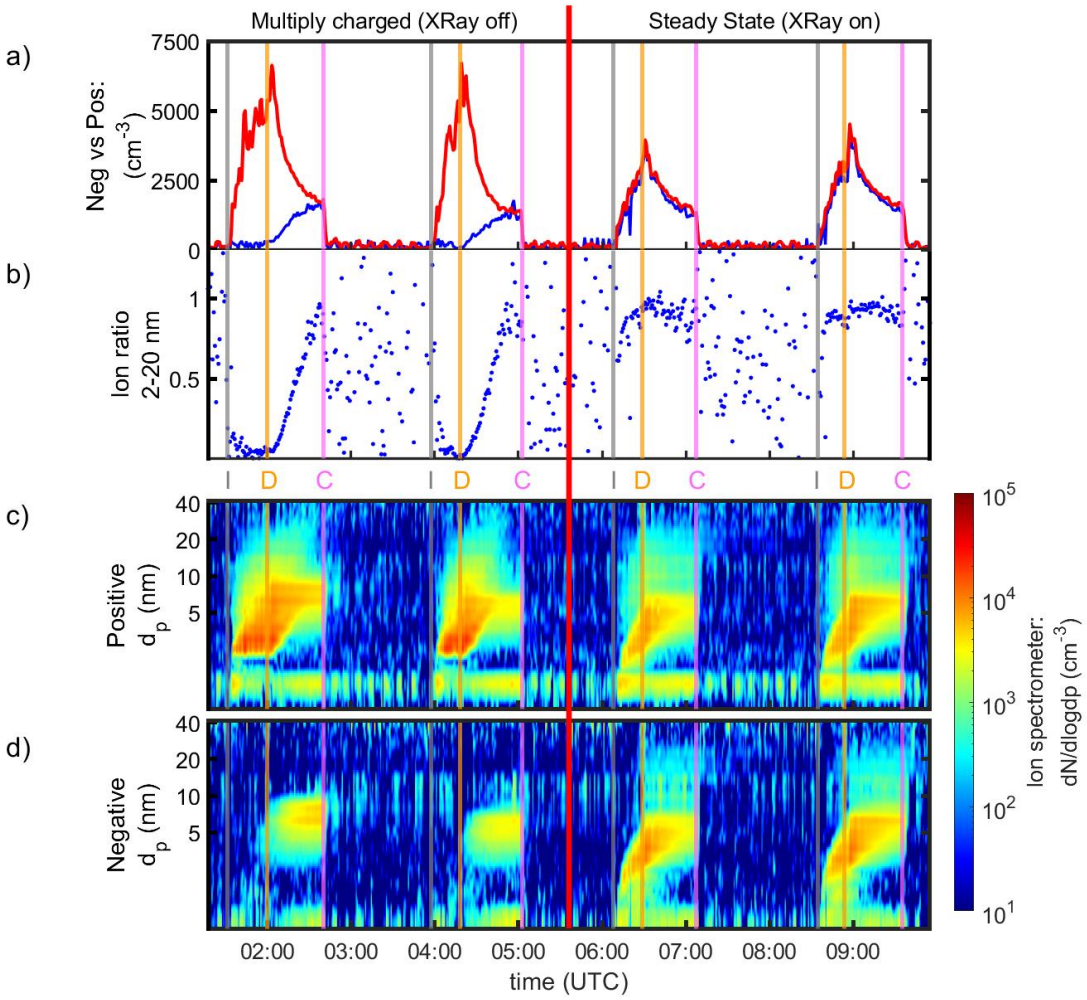

Figure 9: *Time series of the first experiments at the CLOUD chamber to evaluate the performance of CHARGE. Two "XRay Off" experiments are followed by two "Xray On" experiments. The measurement from the NAIS is shown. During XRay Off, no charge balance is observed. Opposed to XRay off experiments, in case of Xray On experiments, almost the same number of positive and negative ions are measured. The beginning of a new stage is shown using coloured lines: Injection stage (I), decay stage (D), cleaning stage (C). Further details can be found in the text and in* ***Paper 4****.*

Experiment 2

The collision of (multiply charged) particles produced by CHARGE with larger particles is investigated during *Experiment 2*. As in *Experiment 1*, a comparison is made between XRay on (neutralized particles from CHARGE) and XRay off (multiply charged particles from CHARGE). Before CHARGE injection, pure sulfuric acid is heated to 450 Kelvin in a bath (a so-called "Evaporator") and then fed into the chamber. Ideally, this results in a particle distribution with particles in a size range of around 100 nm. However, the measured size distribution is spread between about 50 and 400 nm. Figure 10 shows a time series of *Experiment 2*. The experiments are divided into four stages: Injection of large particles from the Evaporator (black line (I*) in Fig. 10), injection of particles from CHARGE (I in Fig. 10), decay (D) and cleaning (C). The first injection from the evaporator takes place within a few seconds (3 seconds was often sufficient). This is followed by a period of 20–30 minutes, where the particles equilibrate to see a clear effect of the charged particles during the second injection from CHARGE. The decay stage again allows to observe the charged particles and their collision with the larger particles without further source terms from CHARGE or the evaporator. This is followed by a cleaning stage, as already described for *Experiment 1*. During these experiments, two DMA-based instruments are installed to measure the particle mobility distribution. One of the instruments has its neutralizer switched on to measure the "real size" of the particles. The second instrument operates without neutralizer to measure the charge transfer between particles from CHARGE with particles from the evaporator. Charge transfer is reflected in a shift of the distribution towards with higher mobilities (i.e., towards smaller sizes). During the decay stage, the distribution slowly returns to its initial mobility (reflected in a shift towards larger sizes).

Figure 10 has a similar structure as Figure 9, with panels c) to f) showing the NAIS measurements. Again, an experiment without XRay is shown first and then another experiment with XRay. In addition, the measurements from the two DMAs are shown (panels a) and b)). Both measure the particle distribution from 10–400 nm. The first instrument (without neutralizer) is a custom-built scanning mobility particle sizer (SMPS) provided from Paul Scherrer Institute (PSI). It combines a long DMA section with a CPC (TSI 3010) (panel a)). It is used in numerous publications (e.g., Xiao et al., 2021; Marten et al., 2022). The second instrument is also a scanning mobility particle sizer, which is provided by the Leibniz-Institute for Tropospheric Research (TROPOS) and utilizes a radioactive source (Krypton 85) (Birmili et al., 1999). Both instruments assume that the charge distribution is in steady state. Accordingly, when the multiply charged particles are injected to the chamber, a shift of the distribution towards smaller sizes (higher mobilities) is observed in the DMA without neutralizer. At the same time, the size distribution obtained from the second DMA (with neutralizer) remains constant. This becomes particularly clear in Figure 10 during the decay stage (D). During injection (I) stage, this process is observed less clearly. Possibly, this is due to the high flow rate through CHARGE (200 l/min): During injection, the flow rates in the CLOUD chamber are not balanced. In Figure 10, the PSI SMPS has no neutralizer, however, the same experiments were repeated with the TROPOS SMPS neutralizer installed on the PSI SMPS (and the TROPOS SMPS operating without neutralizer). During those experiments, the TROPOS SMPS also shows a shift in mobility distribution, which confirms the qualitative

observation of charge transfer. However, a systematic difference between the distributions measured by both SMPS instruments is observed, also when charge is in steady state (i.e., without CHARGE injection). This difference has several reasons:

- Both instruments use different transfer functions to describe the particle distribution. This can lead to errors when there is no charge steady state or particles deviate from the ideal trajectory assumed in the respective transfer functions (e.g., due to surrounding space charge).
- During the experiments, the sampling line of the TROPOS SMPS was several meters long. In addition, the instrument was located below the CLOUD chamber. (The other SMPS was located on the middle platform of the chamber.) A long sampling line and differences in the positioning of the instruments can lead to different particle evaporation rates, depending on the temperature inside the sampling line and the residence time of the particles. This can cause systematic differences between the measurements.

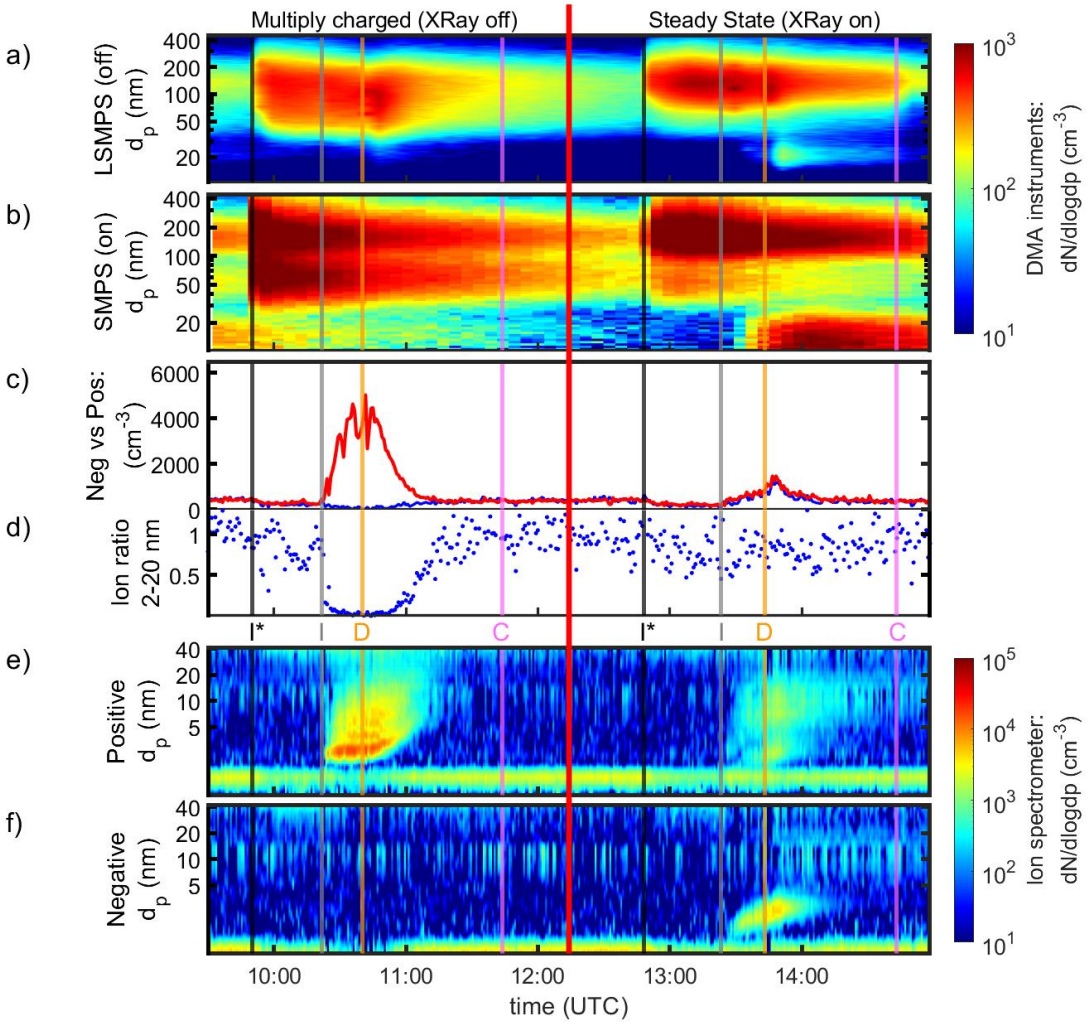

Figure 10: *Time series of Experiment 2 to show charge transfer from multiply charged particles to larger particles. One experiment with XRay is shown and another experiment without XRay. The measurement of two SMPS instruments are shown to cover the size range*

of the larger particles (Panels a) and b)). One instrument operates without neutralizer to show the shift in the mobility distribution when the multiply charged particles are added. This is indicated by an ("off") in the label of the y axis (panel a)). The SMPS shown in panel b) has its neutralizer switched on (indicated by an ("on") in the label of the y axis). The measurement of the NAIS is shown in panels c) to f), in the same order as in Fig.9. Like in Fig. 9, the beginning of a new stage is shown using coloured lines: Injection of aerosol from the heated bath (I), injection stage from CHARGE (I), decay stage (D), cleaning stage I. Further information is summarized in the text.*

The evolution of the distributions in the DMA without neutralizer (PSI SMPS) is shown in detail in Figure 11. Panel a) shows an experiment with XRay off, while panel b) shows an experiment with XRay on. In both cases, the black dashed line indicates the start of injection from CHARGE (i.e., the "baseline distribution"). The particle distribution shifts to smaller sizes (higher mobilities) when multiply charged particles are injected (panel a)). Over time, the distribution will slowly shift back towards its original size distribution during the decay stage (i.e., it shifts back to lower mobilities). This neutralization occurs due to collisions with negative small ions. After around 30 minutes, the distribution is comparable with the baseline distribution. Once the XRay is switched on, this shift is no longer observed, and the distribution remains almost stable (panel b)).

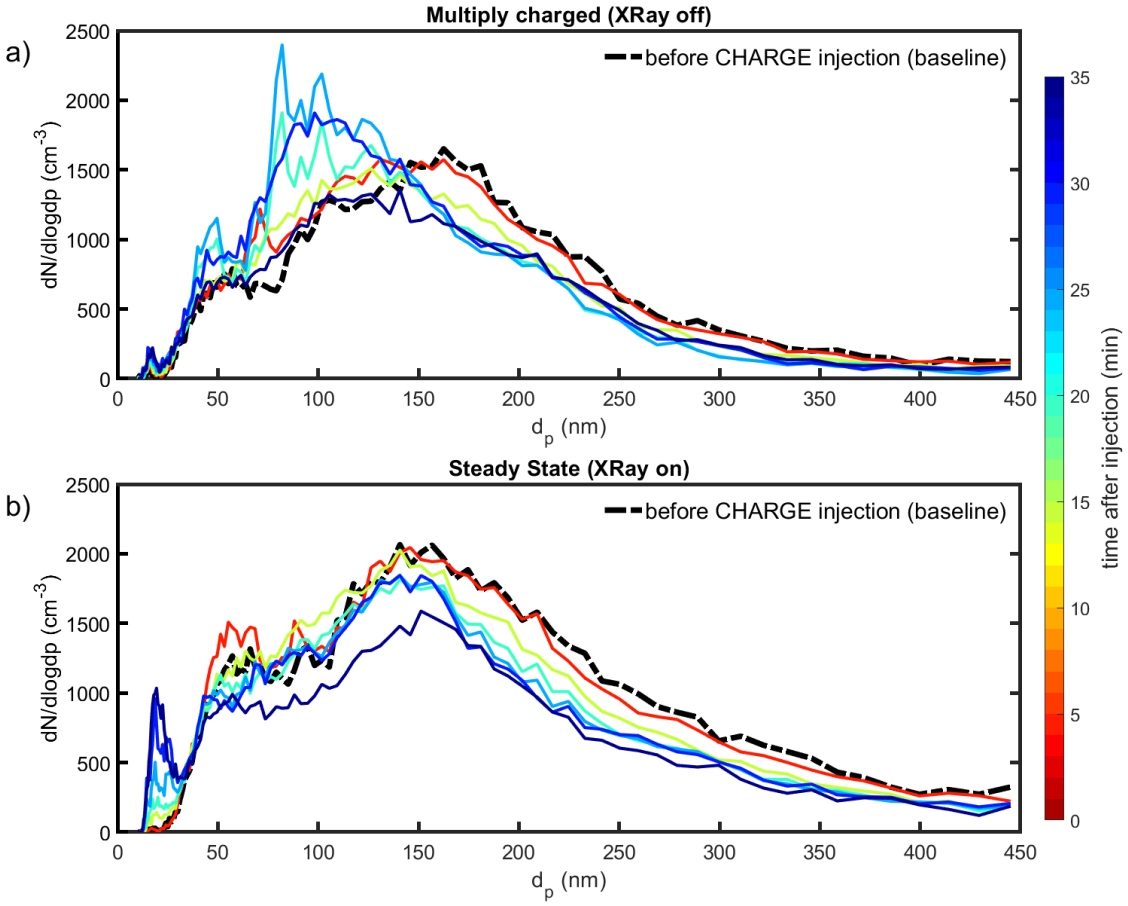

Figure 11: *Evolution of the mobility distribution (in mobility diameter (nm)) measured by the SMPS unit (without neutralizer) during both experiments. The experiments with XRay off (multiply charged particles) are shown in panel a). Panel b) shows experiments with XRay.*

The black dashed line shows the initial distribution from the evaporator measured directly before start of injection from CHARGE. The subsequent development of the distribution goes through two stages: Injection from CHARGE and subsequent decay (no injection). During the experiment with XRay, a distribution in the size range of about 20 nm is formed, which is not observed during experiments without XRay (possibly indicating NPF). In the experiment without XRay, a clear shift in the main distribution is observed, which indicates charge transfer to the larger particles. Further information is summarized in the text.

Experiment 2 shows qualitatively that charge is transferred from the multiply charged (small) particles to larger particles during collision. Afterwards, the (multiply charged) large particles are neutralized over time. Neutralization takes place through collision with negative small ions or with negatively charged particles (see e.g. Hoppel and Frick, 1986; Gopalakrishnan and Hogan, 2012; López-Yglesias and Flagan, 2013). The width of the particle distribution (50–400 nm) and the discrepancy between the SMPS instruments complicate calculation of rate coefficients during these experiments. However, the principle of *Experiment 2* and the results shown in this work are an excellent basis for future experiments. These experiments are unique and can provide an important experimental basis for various models (see e.g. Guo and Xue (2021)).

Experiment 3

While the first two experiments cover the size range from a few nanometres (*Experiment 1*) to particles in the size range of CCN (50 to 400 nm; *Experiment 2*), *Experiment 3* investigates the effect of charge in the size range of small cloud droplets (a few micrometres). A comparison was again made between CHARGE operation with XRay switched off (multiply charged particles) and operation with XRay on (steady state). The experiment has five stages: pressurizing, injection, expansion, decay, and cleaning. The cleaning stage is equivalent to the other experiments and described in the previous chapters. It is again used to prepare the chamber for subsequent experiments. As before, it should be ensured that there are no pre-existing aerosols in the chamber at the beginning of the next experiment. This is particularly important during the expansion experiments, since pre-existing aerosol increases the number concentration of CCN. A larger number of cloud droplets directly correlates with cloud lifetime, as described in numerous studies (see e.g. Albrecht, 1989; Small et al., 2009; Bender et al., 2019; Christensen et al., 2020; Misumi et al., 2022). After cleaning, the overpressure inside the chamber is increased to 200 hPa (pressurizing stage). For this purpose, a valve, which regulates the exhaust flow from the chamber, is closed. As soon as the 200 hPa overpressure is reached, CHARGE injects multiply charged (or neutralized) particles (injection stage). In the first experiments, the injection from CHARGE was carried out for 20 minutes each (both with the XRay switched off and on). As soon as CHARGE is switched off (and all flows from CHARGE into the chamber), the expansion stage starts immediately. The chamber pressure is reduced to the standard value of 5 hPa overpressure within 60 seconds. The decay stage is again equivalent to previous experiments and is used to measure the particle and gas phase at constant conditions. After about 60 minutes, the next cleaning stage begins.

Figure 12 shows a timeseries of two expansion experiments. As before, one experiment without XRay is shown first, and then one experiment with XRay switched on. Figure 12 has a similar

structure as Figure 10. Panel a) shows the measurement from the PSI SMPS. Like Figure 10, the measurement from the TROPOS SMPS is shown for comparison (panel b)). In contrast to *Experiment 2*, the neutralizers of both SMPS are switched on. The NAIS measurements are shown in panel c) to f), in the same order as in Figure 10 (*Experiment 2*): Total concentration of both polarities and ratio between positive and negative ions (2–20nm), distribution (positive channel), distribution (negative channel). Many instruments (SMPS, NAIS and several mass spectrometers) were not able to measure quantitatively at 200 hPa overpressure. They were thus disconnected from the chamber before the pressurizing stage. This is also shown in Figure 12: Before the start of a pressurizing stage (indicated with the letter P), all important instruments are separated from the chamber. This is indicated by the empty (white) areas (i.e., missing data) in Figure 12. The instruments are reconnected after the expansion stage (E). Because of these gaps, only qualitative statements about the observations in *Experiment 3* are possible. During these experiments, it is crucial to measure the number concentration of all particles without any gaps (see discussion on pre-existing aerosol in the beginning of this section).

Nevertheless, in this thesis, some observations are described qualitatively. Figure 12 shows that the number concentration of the particles in case of multiply charged particles (XRay off) is significantly lower than the number concentration in case of charge steady state (XRay on) after expansion. This is particularly evident from the SMPS measurements (panels a) and b)). The NAIS measurements in panel c) and d) indicate that no excess of positive charge compared to negative charge is observed during XRay off experiments. This contrasts with the results from *Experiment 1* and *Experiment 2*. At the same time, in the case of multiply charged particles (XRay off), almost no charged particles are measured by NAIS (see panels e) and f)). However, these particles are clearly detected during the experiments with XRay on even after expansion (right side in panel e) and f)). Although these observations indicate a clear charge effect, Figure 12 also reveals the need for continuous measurements during *Experiment 3*.

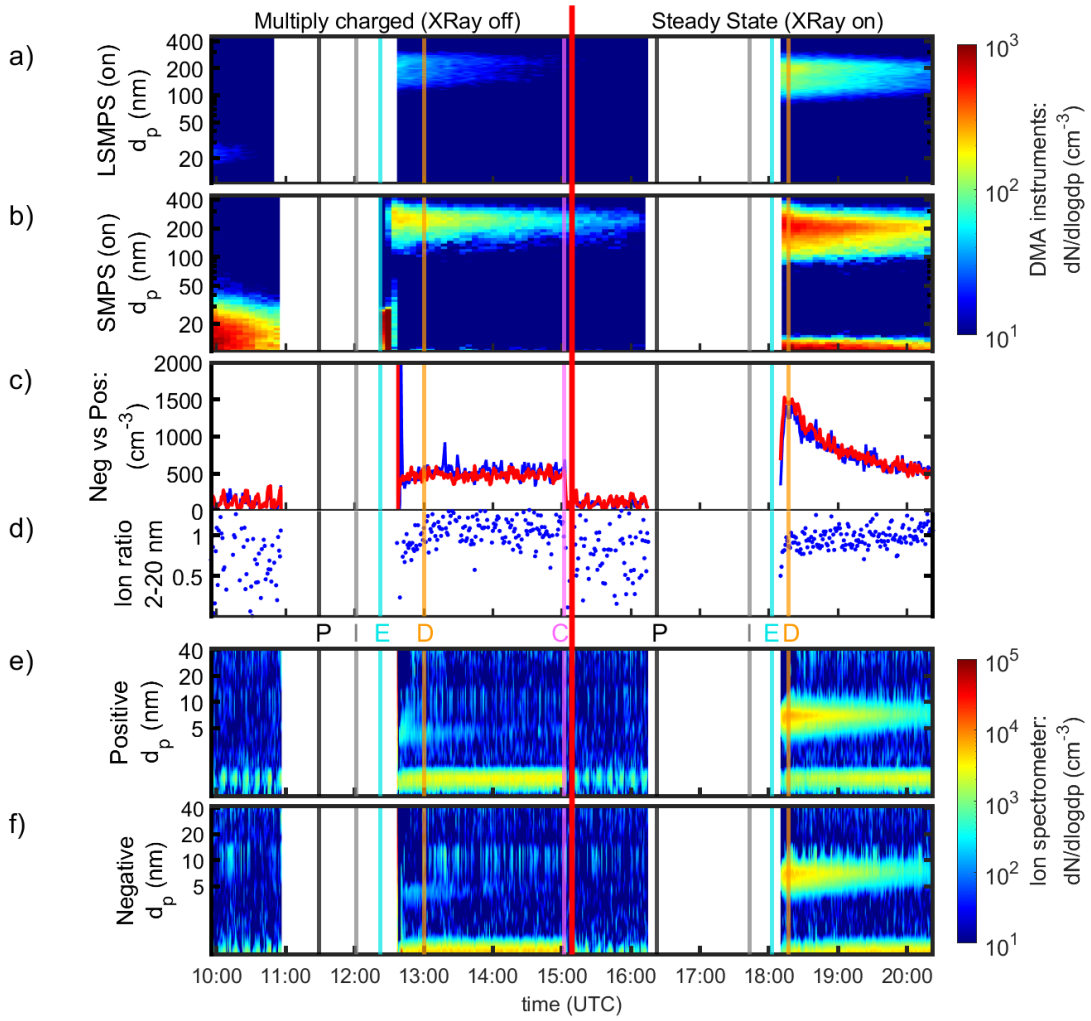

Figure 12: *Time series of Experiment 3 (expansion studies). Once again, an experiment with XRay off (multiply charged particles) and one with XRay on is shown. Panel a) and b) show the measurement of two SMPS instruments. During this experiment, both SMPS have their neutralizer switched on (indicated by an "on" in the label of the y axis). The measurement of the NAIS is shown in panels c) to f). The beginning of a new stage is again shown using coloured lines: Pressurizing (P), injection stage from CHARGE (I), expansion (E), decay stage (D), cleaning stage (C). Further information is summarized in the text.*

During the expansion stage (E) shown in Figure 12, the size of the droplets is measured in a range from 2 to 50 µm using an OPC (a so-called WELAS; see e.g. Palas GmbH, Karlsruhe, Germany or Möhler et al. (2021)). Figure 13 shows a short excerpt of the WELAS measurements during the expansion period, as well as the saturation ratio (S). The expansion starts when S>1. Panel a) shows the XRay off experiment from the previous Figure 12 (left side), while panel b) shows the experiment with XRay on (right side). It seems that larger droplets are detected in case of multiply charged particles, compared with charge steady state (XRay on experiments). In addition, the lifetime of the "cloud" seems reduced. While a clear charge effect is also indicated in Figure 13, this observation is only shown qualitatively, since a continuous time series of the pre-existing aerosol is missing during expansion (similar to Figure 12).

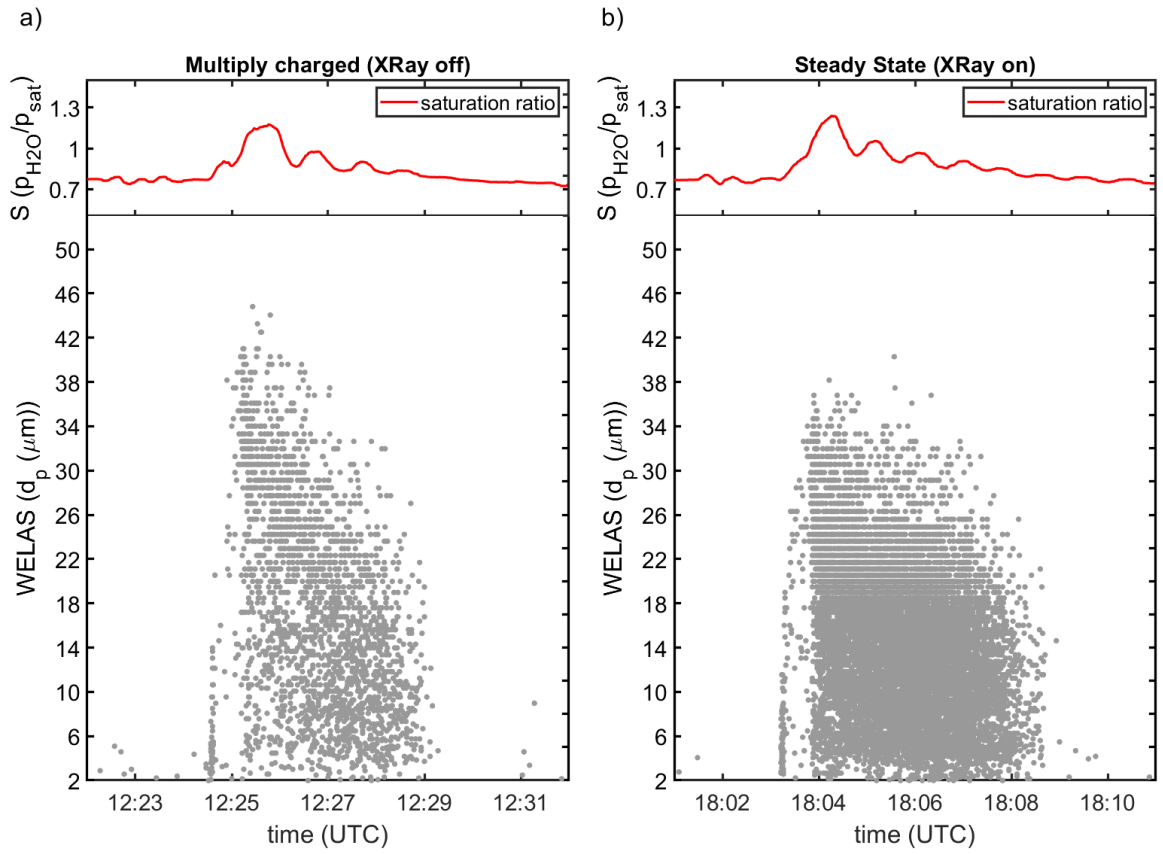

Figure 13: *Measurement of a WELAS instrument (total droplet counts; grey dots) during the expansion stages shown in Figure 12. Panel a) (left side) shows the measurements during experiments with XRay off, panel b) (right side) shows the same experiments with XRay on. Expansion starts when the saturation ratio (upper part in both panels; obtained from measurements of chamber pressure, temperature, and humidity) is bigger than one. Further information is summarized in the text.*

Experiment 3 shows qualitatively that charge effects in clouds could play an important role. Qualitatively, it is observed that the cloud lifetime is reduced when multiply charged particles are injected before expansion. The experiments have the potential to confirm simulations, such as those shown in Guo and Xue (2021). However, interpretations of *Experiment 3* are speculative: There are clear gaps in the time series of the DMA instruments and the NAIS. In addition, during the experiments, the SMPS instruments only cover a size range from 10 to 400 nm, while OPCs (i.e., the WELAS) cover a size range from >2 µm. All size ranges (also between 400 nm and 2 µm) must be measured continuously to obtain a quantitative statement from *Experiment 3*.

1.3.4 Summary

The second part of this thesis shows the successful development of an instrument (called CHarged AeRosol GEnerator (CHARGE)) to evaluate the effects of multiply charged particles at the CLOUD chamber at CERN. First characterizations conducted in a laboratory at CERN show that CHARGE generates a stable electrospray when operated in positive mode. Sulfuric acid–water solutions were used, with varying mass concentration of sulfuric acid (0.00025 % wt. to 10 % wt.). The experiments show that stable electrospray occurs over a narrow voltage range. Comparable results were reported for pure water by Lopez-Herrera et al. (2004). The transmission through CHARGE was optimized during the first tests. A dependency on the size of the inner diameter of the perforated plate (electrode 1) was observed (as also reported by Fu et al., 2011). The transmission of charged particles increases with the size of the inner diameter. The dependency of electrospray generation on liquid flow rate and solution was also evaluated.

The subsequent experiments at CLOUD show that CHARGE successfully directs multiply charged particles to the CLOUD chamber (using a sheath flow of around 200 lpm). Three experiments were designed and successfully performed to determine the effects of multiply charged particles under atmospherically relevant conditions. During all experiments, an XRay source is installed directly behind CHARGE to enable a comparison between multiply charged particles (XRay switched off; CHARGE switched on) with neutralized particles (XRay switched on; CHARGE switched on). The results obtained during *Experiment 1* allow the quantitative measurement of ion-aerosol rate coefficients and they are presented in **Paper 4**. However, *Experiment 2* and *Experiment 3* are only evaluated qualitatively, due to missing information on full particle size distribution and gaps in the time series of some important instruments.

Experiment 1 allows to demonstrate the basic operation of CHARGE. The (multiply charged) particles produced by CHARGE are characterized. After injection, the flow from CHARGE is switched off. Subsequently, the decay of the particles is observed. By defining the loss rates of the particles, a method for measuring ion-aerosol rate with small ions as a function of number of charges was developed. The data are based on measurements obtained from a nSMPS and a NAIS (e.g., Tritscher et al., 2013; Lehtipalo et al., 2014; Manninen et al., 2016). The coefficients are compared with established models from the field (D'yachkov et al., 2007; Gatti and Kortshagen, 2008; Gopalakrishnan and Hogan, 2012; López-Yglesias and Flagan, 2013; Tamadate et al., 2020b). The measurements agree well with several models, especially with the model from Gatti and Kortshagen (2008). For now, there are no comparable chamber experiments, and these novel results will help in the future to verify models for calculating ion–aerosol rate coefficients. The method and the results are presented in **Paper 4** (Pfeifer et al., 2022).

Experiment 2 allows to investigate the collision of (multiply charged) particles produced by CHARGE with larger particles produced by evaporation of pure sulfuric acid (inside a heated bath). Besides the NAIS, two SMPS instruments (provided by PSI ("PSI SMPS") and TROPOS ("TROPOS SMPS")) are used during the experiments, one with a neutralizer and one without a neutralizer (see e.g. Wiedensohler, 1988; Birmili et al., 1999). A shift in mobility is observed in the SMPS without neutralizer, while the mobility remains constant in the SMPS with neutralizer. *Experiment 2* allows to show the transfer of charge from small (multiply charged) particles to large particles during collision. Afterwards, the particles are neutralized by collision

with negative small ions (see e.g., Fuchs and Sutugin, 1965; Hoppel and Frick, 1986; López-Yglesias and Flagan, 2013; Seinfeld and Pandis, 2016). In this work, the results are only presented qualitatively. However, in the future, *Experiment 2* is an excellent basis to allow the calculation of rate coefficients between small ions with large, multiply charged particles (>100 nm). In addition, the charge transfer from multiply charged particles to larger particles can be shown quantitatively, and collision rates between these particles can be evaluated. However, to address these questions, *Experiment 2* needs to be repeated, addressing two issues demonstrated in this summary section:

- The particle distribution of the large particles covers a large size range (from 50–400 nm). Thus, the error introduced from the size dependency of the collision rate coefficients becomes huge (see e.g. Hoppel and Frick, 1986 or Seinfeld and Pandis, 2016). It is not possible with the current data to calculate collision rates without very rough assumptions on size dependency.
- A systematic difference between the distributions measured by the SMPS instruments is observed, also when charge is in steady state (i.e., without CHARGE injection). This could come from the positioning of the instruments at the CLOUD chamber. The PSI SMPS was located on the middle platform, while the TROPOS SMPS was located on the bottom of the chamber. Additionally, the sampling line of the TROPOS SMPS was several meters long. This can lead to evaporation of particles (before detection).

For this reason, it is recommended to repeat *Experiment 2*, where both SMPS instruments should be placed on the middle platform of CLOUD. In addition, the use of two structurally identical SMPS with the same transfer functions could be advantageous, since measurements from particle instruments can differ significantly, especially for smaller particles (Flagan, 1998; Kangasluoma et al., 2020; Stolzenburg et al., 2022). Nevertheless, the principle of *Experiment 2* and the results shown in this work are an excellent basis for future experiments.

Experiment 3 demonstrates qualitatively possible effects of multiply charged particles in clouds. Clear differences in particle number concentration after expansions are identified between experiments with multiply charged (XRay off) and neutralized (XRay on) particles. However, no quantitative conclusions can be drawn in this work since some instruments cannot measure at overpressure and had to be disconnected from the chamber for several minutes. In addition, the size ranges from >=2 nm to around 400 nm and from 2 µm to around 10 µm (or above) were covered by the installed instruments. However, it is necessary to cover the entire size distribution (ideally without any gaps). To draw clear conclusions from these experiments and to evaluate effects of aerosol number concentration on cloud lifetime (see e.g. Christensen et al., 2020; Guo and Xue, 2021), the experiments need to be repeated covering the whole size distribution (also from 400 nm to 2 µm). In addition, all important instruments need to measure quantitatively at 200 hPa overpressure. Nevertheless, the ideas shown in *Experiment 3* represent a solid basis to evaluate effects such as "electro-scavenging" in future experiments.

1.4 Personal contribution to the publications shown in this dissertation

Paper 1 (Pfeifer et al., 2020): The paper presents a new instrument for measuring ammonia, amines and iodine compounds at CLOUD. Detection limits below one part per trillion for ammonia are reported. As the first author of this work, I developed the first prototypes of the ion source presented in the paper in cooperation with Dr. Andreas Kürten. I performed the calibration experiments and I analysed the data presented in the manuscript. I wrote the manuscript.

Paper 2 (Wang et al., 2020): The paper describes the rapid condensation of ammonia and nitric acid on newly formed particles observed during experiments at CLOUD. I contributed to preparation of the CLOUD facility at CERN. I contributed to data collection, running the experiment and scientific discussion. The ammonia measurements of this paper are based on the instrument presented in Paper 1. The instrument was prepared and operated by me during the experiments. I analysed the ammonia data of the paper and I contributed to writing the manuscript (I wrote the technical section related to the ammonia measurement technique).

Paper 3 (Marten et al., 2021): The paper describes how newly formed particles can grow under haze conditions by ammonia-nitric acid condensation and thus survive before being scavenged by pre-existing particles. Before the experiments, I contributed to preparation of the CLOUD facility at CERN. I contributed to data taking and running the experiments. I contributed to the scientific discussion on comparison between modelled and measured ammonia concentrations and the formal data analysis of the paper. The measured ammonia data used in the paper for comparison with model results are based on the data collected from the instrument presented in Paper 1. During the experiments, the instrument was prepared and operated by me and I contributed to writing the manuscript (I wrote the technical section related to the ammonia measurement technique and contributed to discussion on discrepancies between measurement and model results).

Paper 4 (Pfeifer et al., 2022): The paper describes a novel experiment to measure ion–aerosol rate coefficients as a function of the number of charges. A numerical analysis method is presented that allows the measurement of the coefficients quantitatively and with high time resolution. The instrument used for the experiments (Multiply charged particle generator, CHARGE) was developed by me, in collaboration with Serge Mathot and Jasper Kirkby. I characterized the instrument and conducted electrostatic simulations to improve transmission efficiencies of multiply charged particles. I organized, designed, and led the subsequent experiments at CLOUD. I developed the method to analyse the data presented in the paper and to derive ion–aerosol rate coefficients. I wrote the manuscript.

1.5 Deutsche Zusammenfassung der Einleitung

Diese Dissertation kombiniert zwei Projekte, wobei beide dazu beitragen sollen, offene Fragen zu atmosphärischem Partikelwachstum und zu Wolkenbildung zu quantifizieren. Einige Ergebnisse wurden in jeweils zwei Erstautorpublikationen und zwei Coautor-Publikationen veröffentlicht, die dieser zusammenfassenden Arbeit beigefügt sind. Eine der Erstautorpublikationen ist zum Zeitpunkt der Veröffentlichung dieser Dissertation bei einem Journal („Atmospheric Chemistry and Physics“) eingereicht und befindet sich noch im Review Prozess.

Atmosphärische Partikel (Aerosolpartikel) sind allgegenwärtig in der Atmosphäre. Viele Aerosolpartikel haben dabei eine Größe von wenigen Nanometern (Seinfeld und Pandis, 2016). Durch Kondensation und Koagulation wachsen sie weiter an, wobei sie ab einer Größe von mehr als 50 Nanometern als Wolkenkondensationskeime (Cloud Condensation Nuclei, CCN) fungieren können (Pruppacher und Klett, 2010). Aerosol Partikel können den Strahlungshaushalt der Erdatmosphäre durch Streuung und Absorption von Licht direkt beeinflussen (direkter Aerosoleffekt) (Went, 1960). Abhängig von ihren Eigenschaften (z. B. ihrem Absorptionsspektrum) kann der direkte Aerosoleffekt den Strahlungsantrieb in einem Bereich von etwa +0,4 Watt pro Quadratmeter (Ruß aus fossilen Brennstoffen) bis -0,8 (Sulfat-Aerosol) Watt pro Quadratmeter entweder erhöhen oder verringern (Haywood und Boucher, 2000). Dabei sind die Unsicherheiten nach wie vor groß: Aktuelle Abschätzungen des effektiven Strahlungsantriebs durch atmosphärische Aerosol-Strahlungs-Wechselwirkung liegen in einem Bereich von -0,14 bis -0,71 Watt pro Quadratmeter (Bellouin et al., 2020).

Wenn sie als Wolkenkondensationskeime (CCN) wirken, tragen Aerosole zur Wolkenbildung bei. Ihre Anzahlkonzentration und ihre Größenverteilung beeinflussen sowohl die Albedo („Twomey-Effekt“) als auch die Lebensdauer einer Wolke („Albrecht-Effekt“) (Twomey und Warner, 1967; Twomey, 1974; Albrecht, 1989)). Beide Effekte zusammen werden als indirekte Aerosoleffekte bezeichnet (Twomey und Warner, 1967; Twomey, 1974; Lohmann und Feichter, 2005; Quaas et al., 2020). Die globale Schätzung des indirekten Aerosoleffekts liegt im Bereich von etwa -1 Watt pro Quadratmeter (Hansen et al., 1997; Lohmann und Feichter, 2005). Allerdings ist auch hier die Unsicherheit der Abschätzungen groß (Lohmann und Feichter, 2005). Werden indirekter und direkter Aerosoleffekt einbezogen, so deuten Veränderungen der Strahlungsflüsse in den letzten Jahren auf eine abkühlende Wirkung von Aerosolpartikeln in einem Bereich von -2 bis -0,4 Watt pro Quadratmeter hin (90 % Konfidenzintervall; direkte und indirekte Aerosoleffekte) (Bellouin et al., 2020). Da Aerosolpartikel abkühlend wirken und dabei sowohl die Bildung,- als auch die Lebenszeit einer Wolke beeinflussen können, ist ein Verständnis ihrer Neubildung und ihres Verhaltens in der Atmosphäre wichtig, um das zukünftige Klima korrekt vorherzusagen (Seinfeld und Pandis, 2016; Christensen et al., 2020; IPCC, 2022).

Es wird zwischen primären- und sekundären Aerosolpartikeln unterschieden. Primäre Aerosolpartikel werden direkt in die Atmosphäre eingetragen (Beispiele sind aufgewirbelter Staub, oder Meersalz) (Seinfeld und Pandis, 2016). Sekundäre Aerosole werden dagegen in der Atmosphäre gebildet. Dies geschieht entweder durch Kondensation von Molekülen aus der

Gasphase an primären Aerosolpartikeln oder durch chemische Reaktionen in der Gasphase (Seinfeld und Pandis, 2016). Solche Reaktionen können zu niederflüchtigen Produkten führen (diese werden oft „low volatile compounds“ genannt) (Ehn et al., 2014; Schervish and Donahue, 2020). Durch weitere Reaktionen und Kollisionen wachsen diese anschließend zu thermodynamisch stabilen Clustern an, was als Nukleation bezeichnet wird (Seinfeld und Pandis, 2016). Die neu gebildeten (kleinen) Aerosolpartikel haben eine hohe Diffusivität und gehen durch Kollisionen mit größeren Partikeln entsprechend schnell verloren (Kulmala et al., 2017). Dementsprechend umfasst NPF auch das anfängliche Wachstum dieser Partikel (etwa durch Kondensation) (Friedlander, 1977; Kulmala et al., 2014, 2017).

Sowohl Modelle als auch Laborexperimente zeigen, dass Ammoniak eine wichtige Rolle bei NPF spielen kann (Kurtén et al., 2007a; Kirkby et al., 2011; Kürten et al., 2016a; Kürten, 2019). In die Atmosphäre emittiertes Ammoniak hat verschiedenste Quellterme, wobei häufig landwirtschaftliche Aktivitäten, Massentierhaltung oder Katalysatoren genannt werden (You et al., 2014; Kürten et al., 2016b; Seinfeld und Pandis, 2016; Liu et al., 2021). Hinzukommend hat Ammoniak einen großen Anteil an der Bildung neuer CCN (z.B. Dunne et al., 2016; Höpfner et al., 2019). Messungen in ländlichen Gebieten und in der oberen Troposphäre zeigen, dass Ammoniak auch in Umgebungen ohne direkte Quellterme vorkommt (You et al., 2014; Höpfner et al., 2016; Jokinen et al., 2018; Yan et al., 2018). In der oberen Troposphäre könnte es trotz der dort zu erwartenden geringen Konzentrationen für NPF relevant sein (Bianchi et al., 2016; Wang et al., 2022). Allerdings liegen die Ammoniakkonzentrationen in diesen abgelegenen Gebieten bei den meisten Messmethoden entweder unterhalb der Nachweisgrenze, oder sie erfordern eine lange zeitliche Mittelung (Bell et al., 2009; von Bobrutzki et al., 2010; Wang et al., 2015; Höpfner et al., 2016). Die Entwicklung neuer Messmethoden mit niedrigen Nachweisgrenzen bei gleichzeitig guter zeitlicher Auflösung ist daher von großer Relevanz.

Das erste Projekt dieser Arbeit zeigt die Entwicklung und Charakterisierung eines Instruments zur Messung von Ammoniak an der CLOUD Kammer am CERN. Dabei werden protonierte Wassercluster verwendet, um Ammoniak unter Atmosphärendruck zu ionisieren, weshalb das Instrument „*Water Cluster CI-APi-TOF*“ genannt wird (veröffentlicht in der ersten Publikation dieser Arbeit (Pfeifer et al., 2020)).

Es wird eine neue Kreuzfluss-Ionenquelle („Crossflow-Ionenquelle“) beschrieben, die an einem sogenannten Flugzeit-Massenspektrometer („Time Of Flight Mass Spectrometer“ (*TOF-MS*)) angeschlossen ist (Junninen et al., 2010; Kürten et al., 2011; Gross, 2017; Pfeifer, 2018; Pfeifer et al., 2020). Das Prinzip der Massenspektrometrie beruht dabei auf der Trennung von Ionen nach ihrem Masse-zu-Ladungs-Verhältnis. Dies kann mit einer Vielzahl von Techniken erreicht werden. Beispielsweise werden bei der Quadrupol-Massenspektrometrie Ionen getrennt, indem sie einen oder mehrere Quadrupole passieren (Gross, 2017). Abhängig von der Stabilität ihrer Flugbahn werden Ionen mit unterschiedlichen Masse-zu-Ladungs-Verhältnissen detektiert (Gross, 2017). Im Fall von *TOF-MS* werden Ionen in einem elektrischen Feld unter sehr niedrigem Druck beschleunigt (der Druck im „Time of Flight“ Bereich beträgt üblicherweise etwa $1 \cdot 10^{-7}$ hPa) (Junninen et al., 2010). Je nach Masse-zu-Ladungs-Verhältnis variiert die Flugzeit der Ionen. Am Ende treffen die Ionen auf einen

Detektor, der typischerweise ein Sekundärelektronenvervielfacher ist. Der gemessene Strom wird schließlich mit Hilfe von Analog-to-Digital Convertern in ein digitales Signal umgewandelt (Junninen et al., 2010; Gross, 2017). Flugzeit-Massenspektrometer ermöglichen die parallele Messung von hunderten bis tausenden verschiedener Verbindungen, während Quadrupol-Massenspektrometer einzelne Masse-zu-Ladungs-Verhältnisse nacheinander scannen (Wollnik, 1993; Satoh et al., 2005; Gross, 2017; Wei et al., 2021).

Im Fall der in dieser Arbeit gezeigten Crossflow-Ionenquelle werden zuvor unter Atmosphärendruck erzeugte Reagenzionen (Primärionen) orthogonal zum Probenluftstrom eingebracht. Dabei werden protonierte Wassercluster als Primärionen verwendet (z.B. Sunner et al., 1988). Der Einlass zum Flugzeit-Massenspektrometer befindet sich ebenfalls orthogonal (leicht versetzt) zum Probenluftstrom auf der gegenüberliegenden Seite der Ionenquelle. Die Erzeugung von Primärionen erfolgt durch eine Coronaentladung (z.B. Kürten et al., 2011). Im Fall vom Water-Cluster CI-APi-TOF passieren Argon (95%) und Sauerstoff (5%) zunächst ein Wasserbad. Die Primärionen (protonierte Wassercluster) werden dann erzeugt, indem die gesättigte Mischung um eine Coronanadel geleitet wird, die unter (positive) Hochspannung gesetzt wird (Kürten et al., 2011; Pfeifer et al., 2020). Die Vorzüge zur Verwendung von protonierten Wasserclustern zur Messung von Ammoniak und Aminen sind detailliert in der ersten Publikation dieser Thesis und in der englischen Zusammenfassung erläutert (Pfeifer et al., 2020). Das Prinzip einer Crossflow-Ionenquelle wurde erstmals von Eisele und Hanson (2000) zur Messung von molekularen Schwefelsäureclustern eingesetzt (Eisele und Hanson, 2000). Die Grundidee der in dieser Arbeit gezeigten Ionenquelle stammt dabei von Hanson et al. (2011), die eine Crossflow-Ionenquelle zur Messung von Ammoniak und Aminen verwendeten. Dabei wurde gezeigt, dass dieses Design die Reaktionszeiten für die Bildung von Produktionen signifikant verkürzen kann (Hanson et al., 2011).

Die in dieser Arbeit gezeigte Ionenquelle wurde im Rahmen von Experimenten bei CLOUD am CERN im Jahr 2018 charakterisiert. Bei 80 % relativer Luftfeuchtigkeit und 278 K wurden Ammoniak-Hintergrundwerte von etwa 4 Teilchen pro Billionen („parts per trillion“ (pptv)) gemessen. Die Nachweisgrenze wurde mit 0,5 pptv bestimmt. Dies liegt weit unter der Nachweisgrenze früherer Veröffentlichungen (z. B. Norman et al., 2009; Benson et al., 2010; Yu und Lee, 2012; You et al., 2014; Dong et al., 2022). Mischungsverhältnisse von mehr als 10 Teilchen pro Milliarden („parts per billion“ (ppbv)) können ohne signifikanten Abbau von Primärionen gemessen werden. Außerdem zeigte sich, dass das Water Cluster CI-APi-TOF eine sehr schnelle Reaktionszeit von wenigen Sekunden hat. In Kombination mit den niedrigen Hintergrundkonzentrationen ermöglicht das Instrument die Messung von Ammoniak auch unter sich schnell ändernden Bedingungen, wie beispielsweise im Fall von schneller Ammoniak-Salpetersäure-Kondensation (Wang et al., 2020; Marten et al., 2022). Neben Ammoniak konnte zudem Dimethylamin mit einer Nachweisgrenze von etwa 0,05 pptv gemessen werden (+/- 350%). Weiterhin konnte gezeigt werden, dass das Instrument zahlreiche Jodkomponenten messen kann. Ein Vergleich mit einem sogenannten Nitrat-CI-APi-TOF (das im negativen Modus ionisiert (z.B. Simon et al., 2016) zeigte, dass Jodsäure auch in geringen Konzentrationen zuverlässig nachgewiesen werden kann. Dementsprechend ist das Water Cluster CI-APi-TOF zur Messung verschiedenster Gase geeignet und kann auch in abgelegenen Regionen verwendet werden (Pfeifer et al., 2020).

Unter Verwendung des Water Cluster CI-APi-TOF lässt sich unter Laborbedingungen experimentell zeigen, wie neu gebildete Partikel durch Salpetersäure-Ammoniak-Kondensation unter atmosphärisch relevanten Bedingungen rapide wachsen können (Wang et al., 2020; Marten et al., 2022). Die Experimente wurden im Jahr 2018 während der CLOUD 13 Kampagne durchgeführt. Die schnelle Reaktionszeit des Water Cluster CI-APi-TOF erlaubte es dabei, zu zeigen, dass Ammoniak aus der Gasphase entfernt wird, sobald neu gebildete Partikel einen bestimmten Aktivierungsdurchmesser (etwa 4–5 nm) erreichen (Wang et al., 2020). Dabei wachsen die Partikel rapide an (mit Wachstumsraten von etwa 100 Nanometern pro Stunde). Dies wird in den Coautor-Publikationen dieser Dissertation beschrieben (Publikationen 2 und 3 (Wang et al., 2020; Marten et al., 2022)).

Das zweite Projekt beschreibt die Entwicklung und Charakterisierung eines Instruments zur Produktion mehrfach (elektrisch auf-) geladener Aerosolpartikel an der CLOUD-Kammer am CERN (dem sogenannten CHarged AeRosol GEnerator (CHARGE)).

Mehrfach geladene Aerosolpartikel spielen in zahlreichen Instrumentenaufbauten eine Schlüsselrolle. Sie sind besonders wichtig bei der Messung atmosphärischer (elektrisch geladener) Aerosolpartikel (Hoppel und Frick, 1990; Flagan, 1998; Mirme und Mirme, 2013; Kwan et al., 2019). Um Aerosolverteilungen gemäß ihrer elektrischen Mobilität zu messen, passieren atmosphärische Partikel häufig Ionisatoren (z. B. in DMA- oder EAA-Instrumenten; beispielsweise radioaktive Quellen) (z.B. Birmili et al., 1999; Manninen et al., 2016; Kangasluoma et al., 2020; Stolzenburg et al., 2022). Weichen Analytionen oder geladene Teilchen beispielsweise durch Coulomb-Kräfte von der erwarteten Flugbahn ab, so kann dies die Auflösung und die Sensitivität der Messung beeinträchtigen (Mirme, 1994; Flagan, 1998). Mehrfach geladene Teilchen haben zudem eine höhere elektrische Beweglichkeit, als einfach geladene Teilchen gleicher Größe (Flagan, 1998). Zusätzlich können erhöhte Kollisionsraten mehrfach geladener Aerosolpartikel (und insbesondere auch von Wolkentröpfchen) in Wolken nicht vernachlässigbare Auswirkungen auf die Lebensdauer einer Wolke haben (z. B. Stolzenburg et al., 1998; Harrison et al., 2015; Guo und Xue, 2021).

CHARGE ist ein Instrument, welches auf Elektrospray-Ionisation (ESI) basiert (z.B. Smith et al., 2002). Hierbei wird eine flüssige Lösung durch eine Kapillare geleitet, wobei ein sehr starkes elektrisches Feld an der Spitze der Kapillare angelegt wird. Wird eine positive Spannung angelegt („positiver Modus“), sammeln sich positive Ionen an der Oberfläche der Lösung an (Kebarle, 2000). Das elektrische Feld bewirkt, dass negative Ionen ins Innere der Kapillare wandern. Die positiven Ionen erfahren dabei untereinander eine elektrische (Coulomb-) Abstoßungskraft. Außerdem werden sie durch das elektrische Feld aus der Kapillare herausgezogen, wobei sie eine sogenannte „Taylor Cone“ formen (Kebarle, 2000; Smith et al., 2002). Das Anlegen von negativer Spannung („negativer Modus“) erfolgt äquivalent zum „positiven Modus“ (Kebarle, 2000).

Ziel des CHARGE ist es, durch ESI eine hohe Konzentration mehrfach geladener Aerosolpartikel zu erzeugen. Diese sollen anschließend in die CLOUD-Kammer geleitet werden. Die Konzentration soll ausreichen, um Experimente zur Wirkung mehrfach geladener Aerosolpartikel unter atmosphärisch relevanten Bedingungen durchzuführen. Die Experimente wurden im Jahr 2019 durchgeführt und zeigten, dass diese Ziele erreicht werden und

erfolgreich mehrfach geladene Aerosolpartikel in die CLOUD-Kammer geleitet werden können (Pfeifer et al., 2022 (eingereicht)).

Die mit CHARGE entwickelten Experimente (die sogenannten „CHARGE-Experimente“) eröffnen dabei vielfältige Möglichkeiten zur Erforschung der Auswirkungen mehrfach geladener Aerosolpartikel unter atmosphärisch relevanten Bedingungen (Guo und Xue, 2021; Pfeifer et al., 2022 (eingereicht)). Bei allen Experimenten ist eine Röntgenquelle vor dem CHARGE installiert. Die Röntgenquelle wird während einiger Experimente eingeschaltet, um einen Vergleich zwischen mehrfach geladenen und neutralisierten Aerosolpartikeln vergleichbarer Größe (und chemischer Zusammensetzung) zu ermöglichen. Während aller Experimente messen mehrere Massenspektrometer und Differential Mobility Analyzer (DMA) die Gas- und Partikelphase. Zusätzlich wird ein sogenannter „Electrical Aerosol Analyzer“ (EAA) verwendet, um atmosphärische Ionen, sowie die mehrfach geladenen Aerosolpartikel messen zu können (im Falle der in dieser Arbeit gezeigten CHARGE-Experimente ist dies ein „Neutral Cluster and Air Ion Spectrometer“ (NAIS); z. B. Manninen et al., 2016). Die Daten erlauben so einen Vergleich des Mobilitätsspektrums zwischen mehrfach geladenen Aerosolpartikeln mit solchen, die zuvor neutralisiert wurden.

Bei allen Experimenten wird nach der Injektion der Gasfluss von CHARGE (und die Hochspannungen an CHARGE) abgeschaltet. Darauffolgend lassen sich die Aerosolpartikel ohne unbekannte Quellterme unter kontrollierten Bedingungen in der CLOUD-Kammer beobachten. Durch die Bestimmung der Verlustraten der Partikel wurde ein Verfahren zur Berechnung der Kollisionsratenkoeffizienten mehrfach geladener Partikel mit kleinen Ionen als Funktion der Ladungszahl entwickelt. Die Daten basieren auf Messungen eines DMA (eines sogenannten nano Scanning Mobility Particle Sizer (nSMPS); z.B. Tritscher et al., 2013; Lehtipalo et al., 2014) und eines NAIS (z. B. Manninen et al., 2016). Die Koeffizienten wurden anschließend mit etablierten Modellen verglichen (D’yachkov et al., 2007; Gatti und Kortshagen, 2008; Gopalakrishnan und Hogan, 2012; López-Yglesias und Flagan, 2013; Tamadate et al., 2020b). Die Messungen stimmen gut mit mehreren Modellen überein, insbesondere mit dem Modell von Gatti und Kortshagen (2008). Derzeit gibt es keine vergleichbaren Experimente und diese neuartigen Ergebnisse werden in Zukunft helfen, beispielsweise um Modelle zur Berechnung von Kollisionsratenkoeffizienten zwischen geladenen Partikeln mit Ionen zu verifizieren (Pfeifer et al., 2022 (eingereicht)).

Hinzukommend werden in dieser Arbeit zwei weitere mit CHARGE bei CLOUD durchgeführte Experimente qualitativ vorgestellt (in der englischen Zusammenfassung dieser Arbeit; ohne Publikation). Das zweite Experiment ermöglicht es, die Kollision von (mehrfach geladenen) Aerosolpartikeln, die durch CHARGE erzeugt wurden mit größeren Aerosolpartikeln zu untersuchen. Diese Aerosolpartikel werden durch Verdampfen von reiner Schwefelsäure (in einem beheizten Bad) erzeugt und sind etwa so groß, wie CCN (zwischen 50 und 400 nm). Neben dem NAIS und dem nSMPS werden während dieser Experimente zwei weitere DMA-Instrumente (zwei Scanning Mobility Particle Sizer (SMPS)) verwendet. Diese wurden bereitgestellt vom Paul-Scherrer-Institut („PSI SMPS“; verwendet z.B. in Xiao et al., 2021) und vom Leibniz-Institut für Troposphärenforschung („TROPOS SMPS“; Birmili et al., 1999). Eines der beiden Instrumente hat dabei eine radioaktive Quelle vorgeschaltet, um die

Partikel zu neutralisieren (z.B. Wiedensohler, 1988; Flagan, 1998; Birmili et al., 1999; Amanatidis et al., 2021). Beim Instrument ohne radioaktive Quelle (dem TROPOS SMPS) wird eine Verschiebung des gemessenen Mobilitätsspektrums der Aerosolpartikel beobachtet. Dieses bleibt beim zweiten SMPS mit radioaktiver Quelle (dem PSI SMPS) konstant. Dieses Experiment ermöglicht es, den Ladungstransfer von kleinen (mehrfach geladenen) Aerosolpartikeln zu großen Aerosolpartikeln (im Größenbereich von CCN) während der Kollisionen untereinander zu zeigen. Anschließend werden die großen Aerosolpartikel wiederum durch Kollision mit negativen Ionen neutralisiert (Fuchs und Sutugin, 1965; Hoppel und Frick, 1986; López-Yglesias und Flagan, 2013; Seinfeld und Pandis, 2016).

Das dritte Experiment demonstriert qualitativ mögliche Effekte mehrfach geladener Aerosolpartikel in Wolken. Dazu wurden Expansionsexperimente bei CLOUD durchgeführt. Erneut werden die Effekte mehrfach geladener Aerosolpartikel, mit denen von neutralisierten Aerosolpartikeln verglichen. Zwar werden bei diesem Experiment deutliche Unterschiede in der Partikelanzahlkonzentration nach Expansionen festgestellt, jedoch können in dieser Arbeit keine quantitativen Aussagen getroffen werden, da einige Geräte nicht bei Überdruck messen konnten und für einige Minuten von der CLOUD-Kammer getrennt werden mussten.

1.6 References (Introduction Part)

Aitken, J.: III.— *On some Nuclei of Cloudy Condensation*, Trans. R. Soc. Edinb., 39, 15–25, https://doi.org/10.1017/S0080456800034025, 1900.

Albrecht, B. A.: Aerosols, Cloud Microphysics, and Fractional Cloudiness, Science, 245, 1227–1230, https://doi.org/10.1126/science.245.4923.1227, 1989.

Aljawhary, D., Lee, A. K. Y., and Abbatt, J. P. D.: High-resolution chemical ionization mass spectrometry (ToF-CIMS): application to study SOA composition and processing, Atmos. Meas. Tech., 6, 3211–3224, https://doi.org/10.5194/amt-6-3211-2013, 2013.

Almeida, J., Schobesberger, S., Kürten, A., Ortega, I. K., Kupiainen-Määttä, O., Praplan, A. P., Adamov, A., Amorim, A., Bianchi, F., Breitenlechner, M., David, A., Dommen, J., Donahue, N. M., Downard, A., Dunne, E., Duplissy, J., Ehrhart, S., Flagan, R. C., Franchin, A., Guida, R., Hakala, J., Hansel, A., Heinritzi, M., Henschel, H., Jokinen, T., Junninen, H., Kajos, M., Kangasluoma, J., Keskinen, H., Kupc, A., Kurtén, T., Kvashin, A. N., Laaksonen, A., Lehtipalo, K., Leiminger, M., Leppä, J., Loukonen, V., Makhmutov, V., Mathot, S., McGrath, M. J., Nieminen, T., Olenius, T., Onnela, A., Petäjä, T., Riccobono, F., Riipinen, I., Rissanen, M., Rondo, L., Ruuskanen, T., Santos, F. D., Sarnela, N., Schallhart, S., Schnitzhofer, R., Seinfeld, J. H., Simon, M., Sipilä, M., Stozhkov, Y., Stratmann, F., Tomé, A., Tröstl, J., Tsagkogeorgas, G., Vaattovaara, P., Viisanen, Y., Virtanen, A., Vrtala, A., Wagner, P. E., Weingartner, E., Wex, H., Williamson, C., Wimmer, D., Ye, P., Yli-Juuti, T., Carslaw, K. S., Kulmala, M., Curtius, J., Baltensperger, U., Worsnop, D. R., Vehkamäki, H., and Kirkby, J.: Molecular understanding of sulphuric acid–amine particle nucleation in the atmosphere, Nature, 502, 359–363, https://doi.org/10.1038/nature12663, 2013.

Amanatidis, S., Huang, Y., Pushpawela, B., Schulze, B. C., Kenseth, C. M., Ward, R. X., Seinfeld, J. H., Hering, S. V., and Flagan, R. C.: Efficacy of a portable, moderate-resolution, fast-scanning differential mobility analyzer for ambient aerosol size distribution measurements, Atmos. Meas. Tech., 14, 4507–4516, https://doi.org/10.5194/amt-14-4507-2021, 2021.

Andreae, M. O., Jones, C. D., and Cox, P. M.: Strong present-day aerosol cooling implies a hot future, Nature, 435, 1187–1190, https://doi.org/10.1038/nature03671, 2005.

Andrianova, A. A., DiProspero, T., Geib, C., Smoliakova, I. P., Kozliak, E. I., and Kubátová, A.: Electrospray Ionization with High-Resolution Mass Spectrometry as a Tool for Lignomics: Lignin Mass Spectrum Deconvolution, J. Am. Soc. Mass Spectrom., 29, 1044–1059, https://doi.org/10.1007/s13361-018-1916-z, 2018.

Beck, L. J., Schobesberger, S., Sipilä, M., Kerminen, V.-M., and Kulmala, M.: Estimation of sulfuric acid concentration using ambient ion composition and concentration data obtained with atmospheric pressure interface time-of-flight ion mass spectrometer, Atmos. Meas. Tech., 15, 1957–1965, https://doi.org/10.5194/amt-15-1957-2022, 2022.

Bell, C. L., Dhib, M., Hancock, G., Ritchie, G. A. D., van Helden, J. H., and van Leeuwen, N. J.: Cavity enhanced absorption spectroscopy measurements of pressure-induced broadening and shift coefficients in the υ 1+υ 3 combination band of ammonia, Appl. Phys. B, 94, 327–336, https://doi.org/10.1007/s00340-008-3238-5, 2009.

Bellouin, N., Quaas, J., Gryspeerdt, E., Kinne, S., Stier, P., Watson-Parris, D., Boucher, O., Carslaw, K. S., Christensen, M., Daniau, A. -L., Dufresne, J. -L., Feingold, G., Fiedler, S., Forster, P., Gettelman, A., Haywood, J. M., Lohmann, U., Malavelle, F., Mauritsen, T., McCoy, D. T., Myhre, G., Mülmenstädt, J.,

Neubauer, D., Possner, A., Rugenstein, M., Sato, Y., Schulz, M., Schwartz, S. E., Sourdeval, O., Storelvmo, T., Toll, V., Winker, D., and Stevens, B.: Bounding Global Aerosol Radiative Forcing of Climate Change, Rev. Geophys., 58, e2019RG000660, https://doi.org/10.1029/2019RG000660, 2020.

Bender, F. A.-M., Frey, L., McCoy, D. T., Grosvenor, D. P., and Mohrmann, J. K.: Assessment of aerosol–cloud–radiation correlations in satellite observations, climate models and reanalysis, Clim Dyn, 52, 4371–4392, https://doi.org/10.1007/s00382-018-4384-z, 2019.

Benson, D. R., Young, L.-H., Kameel, F. R., and Lee, S.-H.: Laboratory-measured nucleation rates of sulfuric acid and water binary homogeneous nucleation from the SO_2 + OH reaction, Geophys. Res. Lett., 35, L11801, https://doi.org/10.1029/2008GL033387, 2008.

Benson, D. R., Markovich, A., Al-Refai, M., and Lee, S.-H.: A Chemical Ionization Mass Spectrometer for ambient measurements of Ammonia, Atmos. Meas. Tech., 3, 1075–1087, https://doi.org/10.5194/amt-3-1075-2010, 2010.

Bianchi, F., Tröstl, J., Junninen, H., Frege, C., Henne, S., Hoyle, C. R., Molteni, U., Herrmann, E., Adamov, A., Bukowiecki, N., Chen, X., Duplissy, J., Gysel, M., Hutterli, M., Kangasluoma, J., Kontkanen, J., Kürten, A., Manninen, H. E., Münch, S., Peräkylä, O., Petäjä, T., Rondo, L., Williamson, C., Weingartner, E., Curtius, J., Worsnop, D. R., Kulmala, M., Dommen, J., and Baltensperger, U.: New particle formation in the free troposphere: A question of chemistry and timing, Science, 352, 1109–1112, https://doi.org/10.1126/science.aad5456, 2016.

Birmili, W., Stratmann, F., and Wiedensohler, A.: DESIGN OF A DMA-BASED SIZE SPECTROMETER FOR A LARGE PARTICLE SIZE RANGE AND STABLE OPERATION, Journal of Aerosol Science, 30, 549–553, https://doi.org/10.1016/S0021-8502(98)00047-0, 1999.

Birmili, W., Berresheim, H., Plass-Dülmer, C., Elste, T., Gilge, S., Wiedensohler, A., and Uhrner, U.: The Hohenpeissenberg aerosol formation experiment (HAFEX): a long-term study including size-resolved aerosol, H2SO4, OH, and monoterpenes measurements, Atmos. Chem. Phys., 3, 361–376, https://doi.org/10.5194/acp-3-361-2003, 2003.

Blades, A. T., Ikonomou, M. G., and Kebarle, P.: Mechanism of electrospray mass spectrometry. Electrospray as an electrolysis cell, Anal. Chem., 63, 2109–2114, https://doi.org/10.1021/ac00019a009, 1991.

Blake, R. S., Monks, P. S., and Ellis, A. M.: Proton-Transfer Reaction Mass Spectrometry, Chem. Rev., 109, 861–896, https://doi.org/10.1021/cr800364q, 2009.

von Bobrutzki, K., Braban, C. F., Famulari, D., Jones, S. K., Blackall, T., Smith, T. E. L., Blom, M., Coe, H., Gallagher, M., Ghalaieny, M., McGillen, M. R., Percival, C. J., Whitehead, J. D., Ellis, R., Murphy, J., Mohacsi, A., Pogany, A., Junninen, H., Rantanen, S., Sutton, M. A., and Nemitz, E.: Field inter-comparison of eleven atmospheric ammonia measurement techniques, Atmos. Meas. Tech., 3, 91–112, https://doi.org/10.5194/amt-3-91-2010, 2010.

Breitenlechner, M., Fischer, L., Hainer, M., Heinritzi, M., Curtius, J., and Hansel, A.: PTR3: An Instrument for Studying the Lifecycle of Reactive Organic Carbon in the Atmosphere, Anal. Chem., 89, 5824–5831, https://doi.org/10.1021/acs.analchem.6b05110, 2017.

Burgess, A. B., Dudhia, A., Grainger, R. G., and Stevenson, D.: Progress in tropospheric ammonia retrieval from the MIPAS satellite instrument, Advances in Space Research, 37, 2218–2221, https://doi.org/10.1016/j.asr.2005.06.073, 2006.

Cai, R., Yan, C., Yang, D., Yin, R., Lu, Y., Deng, C., Fu, Y., Ruan, J., Li, X., Kontkanen, J., Zhang, Q., Kangasluoma, J., Ma, Y., Hao, J., Worsnop, D. R., Bianchi, F., Paasonen, P., Kerminen, V.-M., Liu, Y., Wang, L., Zheng, J., Kulmala, M., and Jiang, J.: Sulfuric acid–amine nucleation in urban Beijing, Atmos. Chem. Phys., 21, 2457–2468, https://doi.org/10.5194/acp-21-2457-2021, 2021.

CERN (Official Webpage): Topic: CLOUD Experiment, Article: From cosmic rays to clouds, last visited: Oct 2022: https://home.cern/news/news/experiments/cosmic-rays-clouds, last access: 24 October 2022.

Cess, R. D., Potter, G. L., Blanchet, J. P., Boer, G. J., Del Genio, A. D., Déqué, M., Dymnikov, V., Galin, V., Gates, W. L., Ghan, S. J., Kiehl, J. T., Lacis, A. A., Le Treut, H., Li, Z.-X., Liang, X.-Z., McAvaney, B. J., Meleshko, V. P., Mitchell, J. F. B., Morcrette, J.-J., Randall, D. A., Rikus, L., Roeckner, E., Royer, J. F., Schlese, U., Sheinin, D. A., Slingo, A., Sokolov, A. P., Taylor, K. E., Washington, W. M., Wetherald, R. T., Yagai, I., and Zhang, M.-H.: Intercomparison and interpretation of climate feedback processes in 19 atmospheric general circulation models, J. Geophys. Res., 95, 16601–16615, https://doi.org/10.1029/JD095iD10p16601, 1990.

Chalmers, J. A.: Modern theories of thunderstorm electrification, Geofisica Pura e Applicata, 41, 189–193, https://doi.org/10.1007/BF01981872, 1958.

Chan, T. W. and Mozurkewich, M.: Measurement of the coagulation rate constant for sulfuric acid particles as a function of particle size using tandem di!erential mobility analysis, Aerosol Science, 32, 321–339, https://doi.org/10.1016/S0021-8502(00)00081-1, 2001.

Christensen, M. W., Jones, W. K., and Stier, P.: Aerosols enhance cloud lifetime and brightness along the stratus-to-cumulus transition, Proc. Natl. Acad. Sci. U.S.A., 117, 17591–17598, https://doi.org/10.1073/pnas.1921231117, 2020.

Coulomb, C. A.: Mémoires sur l'électricité et la magnétisme, Chez Bachelier, libraire, https://doi.org/10.5479/sil.304245.39088000647479, 1789.

CP Lab Safety (Official Webpage): Polyetherether Ketone (PEEK) Chemical Compatibility Chart.: https://www.calpaclab.com/polyetherether-ketone-peek-chemical-compatibility-chart/, last access: 28 November 2022.

Crounse, J. D., Nielsen, L. B., Jørgensen, S., Kjaergaard, H. G., and Wennberg, P. O.: Autoxidation of Organic Compounds in the Atmosphere, J. Phys. Chem. Lett., 4, 3513–3520, https://doi.org/10.1021/jz4019207, 2013.

Curtius, J.: Nucleation of atmospheric aerosol particles, Comptes Rendus Physique, 7, 1027–1045, https://doi.org/10.1016/j.crhy.2006.10.018, 2006.

Curtius, J., Sierau, B., Arnold, F., de Reus, M., Ström, J., Scheeren, H. A., and Lelieveld, J.: Measurement of aerosol sulfuric acid: 2. Pronounced layering in the free troposphere during the second Aerosol Characterization Experiment (ACE 2), J. Geophys. Res., 106, 31975–31990, https://doi.org/10.1029/2001JD000605, 2001.

De La Mora, J. F. and Loscertales, I. G.: The current emitted by highly conducting Taylor cones, J. Fluid Mech., 260, 155–184, https://doi.org/10.1017/S0022112094003472, 1994.

DeBitetto, D. J.: Electrometer Fluctuation Compensation Device, Review of Scientific Instruments, 26, 986–986, https://doi.org/10.1063/1.1715171, 1955.

Dépée, A., Lemaitre, P., Gelain, T., Monier, M., and Flossmann, A.: Laboratory study of the collection efficiency of submicron aerosol particles by cloud droplets – Part II: Influence of electric charges, Atmos. Chem. Phys., 21, 6963–6984, https://doi.org/10.5194/acp-21-6963-2021, 2021.

Dias, A., Ehrhart, S., Vogel, A., Williamson, C., Almeida, J., Kirkby, J., Mathot, S., Mumford, S., and Onnela, A.: Temperature uniformity in the CERN CLOUD chamber, Atmos. Meas. Tech., 10, 5075–5088, https://doi.org/10.5194/amt-10-5075-2017, 2017.

Dong, F., Li, H., Liu, B., Liu, R., and Hou, K.: Protonated acetone ion chemical ionization time-of-flight mass spectrometry for real-time measurement of atmospheric ammonia, Journal of Environmental Sciences, 114, 66–74, https://doi.org/10.1016/j.jes.2021.07.023, 2022.

Dunne, E. M., Gordon, H., Kürten, A., Almeida, J., Duplissy, J., Williamson, C., Ortega, I. K., Pringle, K. J., Adamov, A., Baltensperger, U., Barmet, P., Benduhn, F., Bianchi, F., Breitenlechner, M., Clarke, A., Curtius, J., Dommen, J., Donahue, N. M., Ehrhart, S., Flagan, R. C., Franchin, A., Guida, R., Hakala, J., Hansel, A., Heinritzi, M., Jokinen, T., Kangasluoma, J., Kirkby, J., Kulmala, M., Kupc, A., Lawler, M. J., Lehtipalo, K., Makhmutov, V., Mann, G., Mathot, S., Merikanto, J., Miettinen, P., Nenes, A., Onnela, A., Rap, A., Reddington, C. L. S., Riccobono, F., Richards, N. A. D., Rissanen, M. P., Rondo, L., Sarnela, N., Schobesberger, S., Sengupta, K., Simon, M., Sipilä, M., Smith, J. N., Stozkhov, Y., Tomé, A., Tröstl, J., Wagner, P. E., Wimmer, D., Winkler, P. M., Worsnop, D. R., and Carslaw, K. S.: Global atmospheric particle formation from CERN CLOUD measurements, Science, 354, 1119–1124, https://doi.org/10.1126/science.aaf2649, 2016.

Duplissy, J., Merikanto, J., Franchin, A., Tsagkogeorgas, G., Kangasluoma, J., Wimmer, D., Vuollekoski, H., Schobesberger, S., Lehtipalo, K., Flagan, R. C., Brus, D., Donahue, N. M., Vehkamäki, H., Almeida, J., Amorim, A., Barmet, P., Bianchi, F., Breitenlechner, M., Dunne, E. M., Guida, R., Henschel, H., Junninen, H., Kirkby, J., Kürten, A., Kupc, A., Määttänen, A., Makhmutov, V., Mathot, S., Nieminen, T., Onnela, A., Praplan, A. P., Riccobono, F., Rondo, L., Steiner, G., Tome, A., Walther, H., Baltensperger, U., Carslaw, K. S., Dommen, J., Hansel, A., Petäjä, T., Sipilä, M., Stratmann, F., Vrtala, A., Wagner, P. E., Worsnop, D. R., Curtius, J., and Kulmala, M.: Effect of ions on sulfuric acid-water binary particle formation: 2. Experimental data and comparison with QC-normalized classical nucleation theory: BINARY PARTICLE FORMATION EXPERIMENTS, J. Geophys. Res. Atmos., 121, 1752–1775, https://doi.org/10.1002/2015JD023539, 2016.

D'yachkov, L. G., Khrapak, A. G., Khrapak, S. A., and Morfill, G. E.: Model of grain charging in collisional plasmas accounting for collisionless layer, Physics of Plasmas, 14, 042102, https://doi.org/10.1063/1.2713719, 2007.

Ehn, M., Thornton, J. A., Kleist, E., Sipilä, M., Junninen, H., Pullinen, I., Springer, M., Rubach, F., Tillmann, R., Lee, B., Lopez-Hilfiker, F., Andres, S., Acir, I.-H., Rissanen, M., Jokinen, T., Schobesberger, S., Kangasluoma, J., Kontkanen, J., Nieminen, T., Kurtén, T., Nielsen, L. B., Jørgensen, S., Kjaergaard, H. G., Canagaratna, M., Maso, M. D., Berndt, T., Petäjä, T., Wahner, A., Kerminen, V.-M., Kulmala, M., Worsnop, D. R., Wildt, J., and Mentel, T. F.: A large source of low-volatility secondary organic aerosol, Nature, 506, 476–479, https://doi.org/10.1038/nature13032, 2014.

Eisele, F. L. and Hanson, D. R.: First Measurement of Prenucleation Molecular Clusters, J. Phys. Chem. A, 104, 830–836, https://doi.org/10.1021/jp9930651, 2000.

Eisele, F. L. and Tanner, D. J.: Measurement of the gas phase concentration of H_2SO_4 and methane sulfonic acid and estimates of H_2SO_4 production and loss in the atmosphere, J. Geophys. Res., 98, 9001–9010, https://doi.org/10.1029/93JD00031, 1993.

Ellis, A. M. and Mayhew, C. A.: Proton Transfer Reaction Mass Spectrometry: Principles and Applications, John Wiley & Sons, Ltd, Chichester, UK, ISBN: 9781118682883, https://doi.org/10.1002/9781118682883, 2014.

Fehsenfeld, F. C., Huey, L. G., Leibrock, E., Dissly, R., Williams, E., Ryerson, T. B., Norton, R., Sueper, D. T., and Hartsell, B.: Results from an informal intercomparison of ammonia measurement techniques, J.-Geophys.-Res., 107, ACH 28-1-ACH 28-14, https://doi.org/10.1029/2001JD001327, 2002.

Fischer, H., Birk, M., Blom, C., Carli, B., Carlotti, M., von Clarmann, T., Delbouille, L., Dudhia, A., Ehhalt, D., Endemann, M., Flaud, J. M., Gessner, R., Kleinert, A., Koopman, R., Langen, J., López-Puertas, M., Mosner, P., Nett, H., Oelhaf, H., Perron, G., Remedios, J., Ridolfi, M., Stiller, G., and Zander, R.: MIPAS: an instrument for atmospheric and climate research, Atmos. Chem. Phys., 8, 2151–2188, https://doi.org/10.5194/acp-8-2151-2008, 2008.

Flagan, R. C.: History of Electrical Aerosol Measurements, Aerosol Science and Technology, 28, 301–380, https://doi.org/10.1080/02786829808965530, 1998.

Forster, P. M. F. and Gregory, J. M.: The Climate Sensitivity and Its Components Diagnosed from Earth Radiation Budget Data, Journal of Climate, 19, 39–52, https://doi.org/10.1175/JCLI3611.1, 2006.

Franklin, B.: XLIV. A letter from Mr. Franklin to Mr. Peter Collinson, F. R. S. concerning the effects of lightning, Phil. Trans. R. Soc., 47, 289–291, https://doi.org/10.1098/rstl.1751.0045, 1752.

Friedlander, S. K.: Smoke, dust, and haze: fundamentals of aerosol behavior, Wiley, New York, ISBN: 978-0-471-01468-3, 1977.

Fu, H., Patel, A. C., Holtzman, M. J., and Chen, D.-R.: A New Electrospray Aerosol Generator with High Particle Transmission Efficiency, Aerosol Science and Technology, 45, 1176–1183, https://doi.org/10.1080/02786826.2011.582899, 2011.

Fuchs, N. A.: On the stationary charge distribution on aerosol particles in a bipolar ionic atmosphere, Geofisica Pura e Applicata, 56, 185–193, https://doi.org/10.1007/BF01993343, 1963.

Fuchs, N. A.: The Mechanics of Aerosols, Pergamon Press, Oxford, ISBN: 978-0-08-010066-1, 1964.

Fuchs, N. A. and Sutugin, A. G.: Coagulation rate of highly dispersed aerosols, Journal of Colloid Science, 20, 492–500, https://doi.org/10.1016/0095-8522(65)90031-0, 1965.

Fuchs, N. A. and Sutugin, A. G.: HIGH-DISPERSED AEROSOLS, in: Topics in Current Aerosol Research, Elsevier, 1, https://doi.org/10.1016/B978-0-08-016674-2.50006-6, 1971.

Gatti, M. and Kortshagen, U.: Analytical model of particle charging in plasmas over a wide range of collisionality, Phys. Rev. E, 78, 046402, https://doi.org/10.1103/PhysRevE.78.046402, 2008.

Gomez, A. and Tang, K.: Charge and fission of droplets in electrostatic sprays, Physics of Fluids, 6, 404–414, https://doi.org/10.1063/1.868037, 1994.

Gopalakrishnan, R. and Hogan, C. J.: Coulomb-influenced collisions in aerosols and dusty plasmas, Phys. Rev. E, 85, 026410, https://doi.org/10.1103/PhysRevE.85.026410, 2012.

Gross, J. H.: Mass spectrometry: a textbook, 3rd edition., Springer Berlin Heidelberg, New York, NY, ISBN: 978-3-319-54397-0, 2017.

Guenther, A. B., Jiang, X., Heald, C. L., Sakulyanontvittaya, T., Duhl, T., Emmons, L. K., and Wang, X.: The Model of Emissions of Gases and Aerosols from Nature version 2.1 (MEGAN2.1): an extended and updated framework for modeling biogenic emissions, Geosci. Model Dev., 5, 1471–1492, https://doi.org/10.5194/gmd-5-1471-2012, 2012.

Guo, S. and Xue, H.: The enhancement of droplet collision by electric charges and atmospheric electric fields, Atmos. Chem. Phys., 21, 69–85, https://doi.org/10.5194/acp-21-69-2021, 2021.

Guo, S., Hu, M., Peng, J., Wu, Z., Zamora, M. L., Shang, D., Du, Z., Zheng, J., Fang, X., Tang, R., Wu, Y., Zeng, L., Shuai, S., Zhang, W., Wang, Y., Ji, Y., Li, Y., Zhang, A. L., Wang, W., Zhang, F., Zhao, J., Gong, X., Wang, C., Molina, M. J., and Zhang, R.: Remarkable nucleation and growth of ultrafine particles from vehicular exhaust, Proc. Natl. Acad. Sci. U.S.A., 117, 3427–3432, https://doi.org/10.1073/pnas.1916366117, 2020.

Hansel, A., Scholz, W., Mentler, B., Fischer, L., and Berndt, T.: Detection of RO2 radicals and other products from cyclohexene ozonolysis with NH4+ and acetate chemical ionization mass spectrometry, Atmospheric Environment, 186, 248–255, https://doi.org/10.1016/j.atmosenv.2018.04.023, 2018.

Hansen, J., Sato, M., Lacis, A., and Ruedy, R.: The missing climate forcing, Phil. Trans. R. Soc. Lond. B, 352, 231–240, https://doi.org/10.1098/rstb.1997.0018, 1997.

Hanson, D. R., McMurry, P. H., Jiang, J., Tanner, D., and Huey, L. G.: Ambient Pressure Proton Transfer Mass Spectrometry: Detection of Amines and Ammonia, Environ. Sci. Technol., 45, 8881–8888, https://doi.org/10.1021/es201819a, 2011.

Harrison, Alex. G.: The gas-phase basicities and proton affinities of amino acids and peptides, Mass Spectrom. Rev., 16, 201–217, https://doi.org/10.1002/(SICI)1098-2787(1997)16:4<201::AID-MAS3>3.0.CO;2-L, 1997.

Harrison, R. G., Nicoll, K. A., and Ambaum, M. H. P.: On the microphysical effects of observed cloud edge charging: Layer Cloud Electricity, Q.J.R. Meteorol. Soc., 141, 2690–2699, https://doi.org/10.1002/qj.2554, 2015.

Haywood, J. and Boucher, O.: Estimates of the direct and indirect radiative forcing due to tropospheric aerosols: A review, Rev. Geophys., 38, 513–543, https://doi.org/10.1029/1999RG000078, 2000.

He, X.-C., Iyer, S., Sipilä, M., Ylisirniö, A., Peltola, M., Kontkanen, J., Baalbaki, R., Simon, M., Kürten, A., Tham, Y. J., Pesonen, J., Ahonen, L. R., Amanatidis, S., Amorim, A., Baccarini, A., Beck, L., Bianchi, F., Brilke, S., Chen, D., Chiu, R., Curtius, J., Dada, L., Dias, A., Dommen, J., Donahue, N. M., Duplissy, J., El Haddad, I., Finkenzeller, H., Fischer, L., Heinritzi, M., Hofbauer, V., Kangasluoma, J., Kim, C., Koenig, T. K., Kubečka, J., Kvashnin, A., Lamkaddam, H., Lee, C. P., Leiminger, M., Li, Z., Makhmutov, V., Xiao, M., Marten, R., Nie, W., Onnela, A., Partoll, E., Petäjä, T., Salo, V.-T., Schuchmann, S., Steiner, G., Stolzenburg, D., Stozhkov, Y., Tauber, C., Tomé, A., Väisänen, O., Vazquez-Pufleau, M., Volkamer, R., Wagner, A. C., Wang, M., Wang, Y., Wimmer, D., Winkler, P. M., Worsnop, D. R., Wu, Y., Yan, C., Ye, Q., Lehtinen, K., Nieminen, T., Manninen, H. E., Rissanen, M., Schobesberger, S., Lehtipalo, K., Baltensperger, U., Hansel, A., Kerminen, V.-M., Flagan, R. C., Kirkby, J., Kurtén, T., and Kulmala, M.: Determination of the collision rate coefficient between charged iodic acid clusters and iodic acid using the appearance time method, Aerosol Science and Technology, 55, 231–242, https://doi.org/10.1080/02786826.2020.1839013, 2021a.

He, X.-C., Tham, Y. J., Dada, L., Wang, M., Finkenzeller, H., Stolzenburg, D., Iyer, S., Simon, M., Kürten, A., Shen, J., Rörup, B., Rissanen, M., Schobesberger, S., Baalbaki, R., Wang, D. S., Koenig, T. K., Jokinen, T., Sarnela, N., Beck, L. J., Almeida, J., Amanatidis, S., Amorim, A., Ataei, F., Baccarini, A., Bertozzi, B.,

Bianchi, F., Brilke, S., Caudillo, L., Chen, D., Chiu, R., Chu, B., Dias, A., Ding, A., Dommen, J., Duplissy, J., El Haddad, I., Gonzalez Carracedo, L., Granzin, M., Hansel, A., Heinritzi, M., Hofbauer, V., Junninen, H., Kangasluoma, J., Kemppainen, D., Kim, C., Kong, W., Krechmer, J. E., Kvashin, A., Laitinen, T., Lamkaddam, H., Lee, C. P., Lehtipalo, K., Leiminger, M., Li, Z., Makhmutov, V., Manninen, H. E., Marie, G., Marten, R., Mathot, S., Mauldin, R. L., Mentler, B., Möhler, O., Müller, T., Nie, W., Onnela, A., Petäjä, T., Pfeifer, J., Philippov, M., Ranjithkumar, A., Saiz-Lopez, A., Salma, I., Scholz, W., Schuchmann, S., Schulze, B., Steiner, G., Stozhkov, Y., Tauber, C., Tomé, A., Thakur, R. C., Väisänen, O., Vazquez-Pufleau, M., Wagner, A. C., Wang, Y., Weber, S. K., Winkler, P. M., Wu, Y., Xiao, M., Yan, C., Ye, Q., Ylisirniö, A., Zauner-Wieczorek, M., Zha, Q., Zhou, P., Flagan, R. C., Curtius, J., Baltensperger, U., Kulmala, M., Kerminen, V.-M., Kurtén, T., et al.: Role of iodine oxoacids in atmospheric aerosol nucleation, Science, 371, 589–595, https://doi.org/10.1126/science.abe0298, 2021b.

Hegg, D. A. and Baker, M. B.: Nucleation in the atmosphere, Rep. Prog. Phys., 72, 056801, https://doi.org/10.1088/0034-4885/72/5/056801, 2009.

Hewitt, G. W.: The charging of small particles for electrostatic precipitation, Trans. AIEE, Part I: Comm. Electron., 76, 300–306, https://doi.org/10.1109/TCE.1957.6372672, 1957.

Hoch, D. J., Buxmann, J., Sihler, H., Pöhler, D., Zetzsch, C., and Platt, U.: An instrument for measurements of BrO with LED-based Cavity-Enhanced Differential Optical Absorption Spectroscopy, Atmos. Meas. Tech., 7, 199–214, https://doi.org/10.5194/amt-7-199-2014, 2014.

Hofmann, D. J., Butler, J. H., Dlugokencky, E. J., Elkins, J. W., Masarie, K., Montzka, S. A., and Tans, P.: The role of carbon dioxide in climate forcing from 1979 to 2004: introduction of the Annual Greenhouse Gas Index, Tellus B: Chemical and Physical Meteorology, 58, 614–619, https://doi.org/10.1111/j.1600-0889.2006.00201.x, 2006.

Hogg, A. R.: Aitken Condensation Nuclei, Nature, 128, 908–908, https://doi.org/10.1038/128908b0, 1931.

Höpfner, M., Volkamer, R., Grabowski, U., Grutter, M., Orphal, J., Stiller, G., von Clarmann, T., and Wetzel, G.: First detection of ammonia (NH3) in the Asian summer monsoon upper troposphere, Atmos. Chem. Phys., 16, 14357–14369, https://doi.org/10.5194/acp-16-14357-2016, 2016.

Höpfner, M., Ungermann, J., Borrmann, S., Wagner, R., Spang, R., Riese, M., Stiller, G., Appel, O., Batenburg, A. M., Bucci, S., Cairo, F., Dragoneas, A., Friedl-Vallon, F., Hünig, A., Johansson, S., Krasauskas, L., Legras, B., Leisner, T., Mahnke, C., Möhler, O., Molleker, S., Müller, R., Neubert, T., Orphal, J., Preusse, P., Rex, M., Saathoff, H., Stroh, F., Weigel, R., and Wohltmann, I.: Ammonium nitrate particles formed in upper troposphere from ground ammonia sources during Asian monsoons, Nat. Geosci., 12, 608–612, https://doi.org/10.1038/s41561-019-0385-8, 2019.

Hoppel, W. A. and Frick, G. M.: Ion—Aerosol Attachment Coefficients and the Steady-State Charge Distribution on Aerosols in a Bipolar Ion Environment, Aerosol Science and Technology, 5, 1–21, https://doi.org/10.1080/02786828608959073, 1986.

Hoppel, W. A. and Frick, G. M.: The Nonequilibrium Character of the Aerosol Charge Distributions Produced by Neutralizes, Aerosol Science and Technology, 12, 471–496, https://doi.org/10.1080/02786829008959363, 1990.

Hurd, F. K. and Mullins, J. C.: Aerosol size distribution from ion mobility, Journal of Colloid Science, 17, 91–100, https://doi.org/10.1016/0095-8522(62)90001-6, 1962.

IPCC (Ed.): Climate Change 2013 – The Physical Science Basis: Working Group I Contribution to the Fifth Assessment Report of the Intergovernmental Panel on Climate Change, 1st ed., Cambridge University Press, https://doi.org/10.1017/CBO9781107415324, 2014.

IPCC: Climate Change 2022: Impacts, Adaptation, and Vulnerability. Contribution of Working Group II to the Sixth Assessment Report of the Intergovernmental Panel on Climate Change [H.-O. Pörtner, D.C. Roberts, M. Tignor, E.S. Poloczanska, K. Mintenbeck, A. Alegría, M. Craig, S. Langsdorf, S. Löschke, V. Möller, A. Okem, B. Rama (eds.)]., Cambridge University Press., Cambridge, UK and New York, NY, USA, 3056 pp., https://doi.org/10.1017/9781009325844, 2022.

Ishizuka, Y., Tokumura, M., Mizukoshi, A., Noguchi, M., and Yanagisawa, Y.: Measurement of Secondary Products During Oxidation Reactions of Terpenes and Ozone Based on the PTR-MS Analysis: Effects of Coexistent Carbonyl Compounds, IJERPH, 7, 3853–3870, https://doi.org/10.3390/ijerph7113853, 2010.

Israël, H.: Instruments and Methods for the Measurement of Atmospheric Electricity, in: Compendium of Meteorology, edited by: Malone, T. F., American Meteorological Society, Boston, MA, 144–154, https://doi.org/10.1007/978-1-940033-70-9_12, 1951.

Israël, H.: Atmospheric electricity: Atmosphärische Elektrizität, Israel Program for Scientific Translations [available from the U.S. Dept. of Commerce, National Technical Information Service, Springfield, Va.], Jerusalem, ISBN: 978-0-7065-1129-1, 1970.

Jimenez, J. L., Canagaratna, M. R., Donahue, N. M., Prevot, A. S. H., Zhang, Q., Kroll, J. H., DeCarlo, P. F., Allan, J. D., Coe, H., Ng, N. L., Aiken, A. C., Docherty, K. S., Ulbrich, I. M., Grieshop, A. P., Robinson, A. L., Duplissy, J., Smith, J. D., Wilson, K. R., Lanz, V. A., Hueglin, C., Sun, Y. L., Tian, J., Laaksonen, A., Raatikainen, T., Rautiainen, J., Vaattovaara, P., Ehn, M., Kulmala, M., Tomlinson, J. M., Collins, D. R., Cubison, M. J., E., Dunlea, J., Huffman, J. A., Onasch, T. B., Alfarra, M. R., Williams, P. I., Bower, K., Kondo, Y., Schneider, J., Drewnick, F., Borrmann, S., Weimer, S., Demerjian, K., Salcedo, D., Cottrell, L., Griffin, R., Takami, A., Miyoshi, T., Hatakeyama, S., Shimono, A., Sun, J. Y., Zhang, Y. M., Dzepina, K., Kimmel, J. R., Sueper, D., Jayne, J. T., Herndon, S. C., Trimborn, A. M., Williams, L. R., Wood, E. C., Middlebrook, A. M., Kolb, C. E., Baltensperger, U., and Worsnop, D. R.: Evolution of Organic Aerosols in the Atmosphere, Science, 326, 1525–1529, https://doi.org/10.1126/science.1180353, 2009.

Jokinen, T., Sipilä, M., Kontkanen, J., Vakkari, V., Tisler, P., Duplissy, E.-M., Junninen, H., Kangasluoma, J., Manninen, H. E., Petäjä, T., Kulmala, M., Worsnop, D. R., Kirkby, J., Virkkula, A., and Kerminen, V.-M.: Ion-induced sulfuric acid–ammonia nucleation drives particle formation in coastal Antarctica, Sci. Adv., 4, eaat9744, https://doi.org/10.1126/sciadv.aat9744, 2018.

Junge, C.: THE SIZE DISTRIBUTION AND AGING OF NATURAL AEROSOLS AS DETERMINED FROM ELECTRICAL AND OPTICAL DATA ON THE ATMOSPHERE, J. Meteor., 12, 13–25, https://doi.org/10.1175/1520-0469(1955)012<0013:TSDAAO>2.0.CO;2, 1955.

Junninen, H., Ehn, M., Petäjä, T., Luosujärvi, L., Kotiaho, T., Kostiainen, R., Rohner, U., Gonin, M., Fuhrer, K., Kulmala, M., and Worsnop, D. R.: A high-resolution mass spectrometer to measure atmospheric ion composition, Atmos. Meas. Tech., 3, 1039–1053, https://doi.org/10.5194/amt-3-1039-2010, 2010.

Kaddis, C. S., Lomeli, S. H., Yin, S., Berhane, B., Apostol, M. I., Kickhoefer, V. A., Rome, L. H., and Loo, J. A.: Sizing large proteins and protein complexes by electrospray ionization mass spectrometry and ion mobility, J. Am. Soc. Mass Spectrom., 18, 1206–1216, https://doi.org/10.1016/j.jasms.2007.02.015, 2007.

Kangasluoma, J., Cai, R., Jiang, J., Deng, C., Stolzenburg, D., Ahonen, L. R., Chan, T., Fu, Y., Kim, C., Laurila, T. M., Zhou, Y., Dada, L., Sulo, J., Flagan, R. C., Kulmala, M., Petäjä, T., and Lehtipalo, K.: Overview of measurements and current instrumentation for 1–10 nm aerosol particle number size distributions, Journal of Aerosol Science, 148, 105584, https://doi.org/10.1016/j.jaerosci.2020.105584, 2020.

Katz, J. L.: Condensation of a Supersaturated Vapor. I. The Homogeneous Nucleation of the *n* -Alkanes, The Journal of Chemical Physics, 52, 4733–4748, https://doi.org/10.1063/1.1673706, 1970.

Kebarle, P.: A brief overview of the present status of the mechanisms involved in electrospray mass spectrometry, J. Mass Spectrom., 35, 804–817, https://doi.org/10.1002/1096-9888(200007)35:7<804::AID-JMS22>3.0.CO;2-Q, 2000.

Kejna, M., Uscka-Kowalkowska, J., and Kejna, P.: The influence of cloudiness and atmospheric circulation on radiation balance and its components, Theor Appl Climatol, 144, 823–838, https://doi.org/10.1007/s00704-021-03570-8, 2021.

Kelvin, L.: On the Necessity for Incessant Recording and for Simultaneous Observations in Different Locations to Investigate Atmospheric Electricity, Macmillan, 227–229, 1859.

Kirkby, J., Curtius, J., Almeida, J., Dunne, E., Duplissy, J., Ehrhart, S., Franchin, A., Gagné, S., Ickes, L., Kürten, A., Kupc, A., Metzger, A., Riccobono, F., Rondo, L., Schobesberger, S., Tsagkogeorgas, G., Wimmer, D., Amorim, A., Bianchi, F., Breitenlechner, M., David, A., Dommen, J., Downard, A., Ehn, M., Flagan, R. C., Haider, S., Hansel, A., Hauser, D., Jud, W., Junninen, H., Kreissl, F., Kvashin, A., Laaksonen, A., Lehtipalo, K., Lima, J., Lovejoy, E. R., Makhmutov, V., Mathot, S., Mikkilä, J., Minginette, P., Mogo, S., Nieminen, T., Onnela, A., Pereira, P., Petäjä, T., Schnitzhofer, R., Seinfeld, J. H., Sipilä, M., Stozhkov, Y., Stratmann, F., Tomé, A., Vanhanen, J., Viisanen, Y., Vrtala, A., Wagner, P. E., Walther, H., Weingartner, E., Wex, H., Winkler, P. M., Carslaw, K. S., Worsnop, D. R., Baltensperger, U., and Kulmala, M.: Role of sulphuric acid, ammonia and galactic cosmic rays in atmospheric aerosol nucleation, Nature, 476, 429–433, https://doi.org/10.1038/nature10343, 2011.

Kirkby, J., Duplissy, J., Sengupta, K., Frege, C., Gordon, H., Williamson, C., Heinritzi, M., Simon, M., Yan, C., Almeida, J., Tröstl, J., Nieminen, T., Ortega, I. K., Wagner, R., Adamov, A., Amorim, A., Bernhammer, A.-K., Bianchi, F., Breitenlechner, M., Brilke, S., Chen, X., Craven, J., Dias, A., Ehrhart, S., Flagan, R. C., Franchin, A., Fuchs, C., Guida, R., Hakala, J., Hoyle, C. R., Jokinen, T., Junninen, H., Kangasluoma, J., Kim, J., Krapf, M., Kürten, A., Laaksonen, A., Lehtipalo, K., Makhmutov, V., Mathot, S., Molteni, U., Onnela, A., Peräkylä, O., Piel, F., Petäjä, T., Praplan, A. P., Pringle, K., Rap, A., Richards, N. A. D., Riipinen, I., Rissanen, M. P., Rondo, L., Sarnela, N., Schobesberger, S., Scott, C. E., Seinfeld, J. H., Sipilä, M., Steiner, G., Stozhkov, Y., Stratmann, F., Tomé, A., Virtanen, A., Vogel, A. L., Wagner, A. C., Wagner, P. E., Weingartner, E., Wimmer, D., Winkler, P. M., Ye, P., Zhang, X., Hansel, A., Dommen, J., Donahue, N. M., Worsnop, D. R., Baltensperger, U., Kulmala, M., Carslaw, K. S., and Curtius, J.: Ion-induced nucleation of pure biogenic particles, Nature, 533, 521–526, https://doi.org/10.1038/nature17953, 2016.

Knutson, E. O. and Whitby, K. T.: Aerosol classification by electric mobility: apparatus, theory, and applications, Journal of Aerosol Science, 6, 443–451, https://doi.org/10.1016/0021-8502(75)90060-9, 1975.

Köhler, H.: Zur Kondensation des Wasserdampfes in der Atmosphäre, Geofysiske publikasjoner, 2 (3), 1921.

Kulmala, M. and Laaksonen, A.: Binary nucleation of water–sulfuric acid system: Comparison of classical theories with different H_2SO_4 saturation vapor pressures, The Journal of Chemical Physics, 93, 696–701, https://doi.org/10.1063/1.459519, 1990.

Kulmala, M., Laaksonen, A., and Pirjola, L.: Parameterizations for sulfuric acid/water nucleation rates, J. Geophys. Res., 103, 8301–8307, https://doi.org/10.1029/97JD03718, 1998.

Kulmala, M., Petäjä, T., Ehn, M., Thornton, J., Sipilä, M., Worsnop, D. R., and Kerminen, V.-M.: Chemistry of Atmospheric Nucleation: On the Recent Advances on Precursor Characterization and Atmospheric Cluster Composition in Connection with Atmospheric New Particle Formation, Annu. Rev. Phys. Chem., 65, 21–37, https://doi.org/10.1146/annurev-physchem-040412-110014, 2014.

Kulmala, M., Kerminen, V.-M., Petäjä, T., Ding, A. J., and Wang, L.: Atmospheric gas-to-particle conversion: why NPF events are observed in megacities?, Faraday Discuss., 200, 271–288, https://doi.org/10.1039/C6FD00257A, 2017.

Kürten, A.: New particle formation from sulfuric acid and ammonia: nucleation and growth model based on thermodynamics derived from CLOUD measurements for a wide range of conditions, Atmos. Chem. Phys., 19, 5033–5050, https://doi.org/10.5194/acp-19-5033-2019, 2019.

Kürten, A., Rondo, L., Ehrhart, S., and Curtius, J.: Performance of a corona ion source for measurement of sulfuric acid by chemical ionization mass spectrometry, Atmos. Meas. Tech., 4, 437–443, https://doi.org/10.5194/amt-4-437-2011, 2011.

Kürten, A., Jokinen, T., Simon, M., Sipilä, M., Sarnela, N., Junninen, H., Adamov, A., Almeida, J., Amorim, A., Bianchi, F., Breitenlechner, M., Dommen, J., Donahue, N. M., Duplissy, J., Ehrhart, S., Flagan, R. C., Franchin, A., Hakala, J., Hansel, A., Heinritzi, M., Hutterli, M., Kangasluoma, J., Kirkby, J., Laaksonen, A., Lehtipalo, K., Leiminger, M., Makhmutov, V., Mathot, S., Onnela, A., Petäjä, T., Praplan, A. P., Riccobono, F., Rissanen, M. P., Rondo, L., Schobesberger, S., Seinfeld, J. H., Steiner, G., Tomé, A., Tröstl, J., Winkler, P. M., Williamson, C., Wimmer, D., Ye, P., Baltensperger, U., Carslaw, K. S., Kulmala, M., Worsnop, D. R., and Curtius, J.: Neutral molecular cluster formation of sulfuric acid–dimethylamine observed in real time under atmospheric conditions, Proc. Natl. Acad. Sci. U.S.A., 111, 15019–15024, https://doi.org/10.1073/pnas.1404853111, 2014.

Kürten, A., Bianchi, F., Almeida, J., Kupiainen-Määttä, O., Dunne, E. M., Duplissy, J., Williamson, C., Barmet, P., Breitenlechner, M., Dommen, J., Donahue, N. M., Flagan, R. C., Franchin, A., Gordon, H., Hakala, J., Hansel, A., Heinritzi, M., Ickes, L., Jokinen, T., Kangasluoma, J., Kim, J., Kirkby, J., Kupc, A., Lehtipalo, K., Leiminger, M., Makhmutov, V., Onnela, A., Ortega, I. K., Petäjä, T., Praplan, A. P., Riccobono, F., Rissanen, M. P., Rondo, L., Schnitzhofer, R., Schobesberger, S., Smith, J. N., Steiner, G., Stozhkov, Y., Tomé, A., Tröstl, J., Tsagkogeorgas, G., Wagner, P. E., Wimmer, D., Ye, P., Baltensperger, U., Carslaw, K., Kulmala, M., and Curtius, J.: Experimental particle formation rates spanning tropospheric sulfuric acid and ammonia abundances, ion production rates, and temperatures, J. Geophys. Res. Atmos., 121, 12377–12400, https://doi.org/10.1002/2015JD023908, 2016a.

Kürten, A., Bergen, A., Heinritzi, M., Leiminger, M., Lorenz, V., Piel, F., Simon, M., Sitals, R., Wagner, A. C., and Curtius, J.: Observation of new particle formation and measurement of sulfuric acid, ammonia, amines and highly oxidized organic molecules at a rural site in central Germany, Atmos. Chem. Phys., 16, 12793–12813, https://doi.org/10.5194/acp-16-12793-2016, 2016b.

Kurtén, T., Torpo, L., Ding, C.-G., Vehkamäki, H., Sundberg, M. R., Laasonen, K., and Kulmala, M.: A density functional study on water-sulfuric acid-ammonia clusters and implications for atmospheric cluster formation, J. Geophys. Res., 112, D04210, https://doi.org/10.1029/2006JD007391, 2007a.

Kurtén, T., Noppel, M., Vehkamäki, H., Salonen, M., and Kulmala, M.: Quantum chemical studies of hydrate formation of H2SO4 and HSO4–, Boreal Environment Research, 12, 431–453, 2007b.

Kusaka, I., Wang, Z. -G., and Seinfeld, J. H.: Ion-induced nucleation. II. Polarizable multipolar molecules, The Journal of Chemical Physics, 103, 8993–9009, https://doi.org/10.1063/1.470089, 1995.

Kwan, V., Malevanets, A., and Consta, S.: Where Do the Ions Reside in a Highly Charged Droplet?, J. Phys. Chem. A, 123, 9298–9310, https://doi.org/10.1021/acs.jpca.9b03368, 2019.

Landrigan, P. J., Fuller, R., Acosta, N. J. R., Adeyi, O., Arnold, R., Basu, N. (Nil), Baldé, A. B., Bertollini, R., Bose-O'Reilly, S., Boufford, J. I., Breysse, P. N., Chiles, T., Mahidol, C., Coll-Seck, A. M., Cropper, M. L., Fobil, J., Fuster, V., Greenstone, M., Haines, A., Hanrahan, D., Hunter, D., Khare, M., Krupnick, A., Lanphear, B., Lohani, B., Martin, K., Mathiasen, K. V., McTeer, M. A., Murray, C. J. L., Ndahimananjara, J. D., Perera, F., Potočnik, J., Preker, A. S., Ramesh, J., Rockström, J., Salinas, C., Samson, L. D., Sandilya, K., Sly, P. D., Smith, K. R., Steiner, A., Stewart, R. B., Suk, W. A., van Schayck, O. C. P., Yadama, G. N., Yumkella, K., and Zhong, M.: The Lancet Commission on pollution and health, The Lancet, 391, 462–512, https://doi.org/10.1016/S0140-6736(17)32345-0, 2018.

Langer, G., Radnik, J., and Templeton, L.: Development of a Simple, High-Resolution Mobility Analyzer for Small, Charged Particles, Review of Scientific Instruments, 33, 83–84, https://doi.org/10.1063/1.1717670, 1962.

Langevin, M.: Recombinaison et diffusion des ions gazeux, J. Phys. Theor. Appl., 4, 322–333, https://doi.org/10.1051/jphystap:019050040032201, 1905.

Lehtipalo, K., Leppä, Johannes, Kontkanen, J., Kangasluoma, J., Franchin, A., Wimmer, D., Schobesberger, S., Junninen, H., Petäjä, T., Sipilä, M., Mikkilä, J., Vanhanen, J., Worsnop, D. R., and Kulmala, M.: Methods for determining particle size distribution and growth rates between 1 and 3 nm using the Particle Size Magnifier, Boreal Environment Research, 19, 215–236, 2014.

Lehtipalo, K., Rondo, L., Kontkanen, J., Schobesberger, S., Jokinen, T., Sarnela, N., Kürten, A., Ehrhart, S., Franchin, A., Nieminen, T., Riccobono, F., Sipilä, M., Yli-Juuti, T., Duplissy, J., Adamov, A., Ahlm, L., Almeida, J., Amorim, A., Bianchi, F., Breitenlechner, M., Dommen, J., Downard, A. J., Dunne, E. M., Flagan, R. C., Guida, R., Hakala, J., Hansel, A., Jud, W., Kangasluoma, J., Kerminen, V.-M., Keskinen, H., Kim, J., Kirkby, J., Kupc, A., Kupiainen-Määttä, O., Laaksonen, A., Lawler, M. J., Leiminger, M., Mathot, S., Olenius, T., Ortega, I. K., Onnela, A., Petäjä, T., Praplan, A., Rissanen, M. P., Ruuskanen, T., Santos, F. D., Schallhart, S., Schnitzhofer, R., Simon, M., Smith, J. N., Tröstl, J., Tsagkogeorgas, G., Tomé, A., Vaattovaara, P., Vehkamäki, H., Vrtala, A. E., Wagner, P. E., Williamson, C., Wimmer, D., Winkler, P. M., Virtanen, A., Donahue, N. M., Carslaw, K. S., Baltensperger, U., Riipinen, I., Curtius, J., Worsnop, D. R., and Kulmala, M.: The effect of acid–base clustering and ions on the growth of atmospheric nano-particles, Nat Commun, 7, 11594, https://doi.org/10.1038/ncomms11594, 2016.

Lehtipalo, K., Yan, C., Dada, L., Bianchi, F., Xiao, M., Wagner, R., Stolzenburg, D., Ahonen, L. R., Amorim, A., Baccarini, A., Bauer, P. S., Baumgartner, B., Bergen, A., Bernhammer, A.-K., Breitenlechner, M., Brilke, S., Buchholz, A., Mazon, S. B., Chen, D., Chen, X., Dias, A., Dommen, J., Draper, D. C., Duplissy, J., Ehn, M., Finkenzeller, H., Fischer, L., Frege, C., Fuchs, C., Garmash, O., Gordon, H., Hakala, J., He, X., Heikkinen, L., Heinritzi, M., Helm, J. C., Hofbauer, V., Hoyle, C. R., Jokinen, T., Kangasluoma, J., Kerminen, V.-M., Kim, C., Kirkby, J., Kontkanen, J., Kürten, A., Lawler, M. J., Mai, H., Mathot, S., Mauldin, R. L., Molteni, U., Nichman, L., Nie, W., Nieminen, T., Ojdanic, A., Onnela, A., Passananti, M., Petäjä, T., Piel, F., Pospisilova, V., Quéléver, L. L. J., Rissanen, M. P., Rose, C., Sarnela, N., Schallhart, S., Schuchmann, S., Sengupta, K., Simon, M., Sipilä, M., Tauber, C., Tomé, A., Tröstl, J., Väisänen, O., Vogel, A. L., Volkamer, R., Wagner, A. C., Wang, M., Weitz, L., Wimmer, D., Ye, P., Ylisirniö, A., Zha, Q., Carslaw,

K. S., Curtius, J., Donahue, N. M., Flagan, R. C., Hansel, A., Riipinen, I., Virtanen, A., Winkler, P. M., Baltensperger, U., Kulmala, M., and Worsnop, D. R.: Multicomponent new particle formation from sulfuric acid, ammonia, and biogenic vapors, Sci. Adv., 4, eaau5363, https://doi.org/10.1126/sciadv.aau5363, 2018.

Lelieveld, J., Evans, J. S., Fnais, M., Giannadaki, D., and Pozzer, A.: The contribution of outdoor air pollution sources to premature mortality on a global scale, Nature, 525, 367–371, https://doi.org/10.1038/nature15371, 2015.

Lelieveld, J., Klingmüller, K., Pozzer, A., Burnett, R. T., Haines, A., and Ramanathan, V.: Effects of fossil fuel and total anthropogenic emission removal on public health and climate, Proc. Natl. Acad. Sci. U.S.A., 116, 7192–7197, https://doi.org/10.1073/pnas.1819989116, 2019.

Li, M., Weschler, C. J., Bekö, G., Wargocki, P., Lucic, G., and Williams, J.: Human Ammonia Emission Rates under Various Indoor Environmental Conditions, Environ. Sci. Technol., 54, 5419–5428, https://doi.org/10.1021/acs.est.0c00094, 2020.

Liu, B. Y. H. and Pui, D. Y. H.: On the performance of the electrical aerosol analyzer, Journal of Aerosol Science, 6, 249–254, https://doi.org/10.1016/0021-8502(75)90093-2, 1975.

Liu, Y., Wang, H., Li, N., Tan, J., and Chen, D.: Research on ammonia emissions from three-way catalytic converters based on small sample test and vehicle test, Science of The Total Environment, 795, 148926, https://doi.org/10.1016/j.scitotenv.2021.148926, 2021.

Lohmann, U. and Feichter, J.: Global indirect aerosol effects: a review, Atmos. Chem. Phys., 5, 715–737, https://doi.org/10.5194/acp-5-715-2005, 2005.

López-Herrera, J. M., Barrero, A., Boucard, A., Loscertales, I. G., and Márquez, M.: An experimental study of the electrospraying of water in air at atmospheric pressure, J. Am. Soc. Mass Spectrom., 15, 253–259, https://doi.org/10.1016/j.jasms.2003.10.018, 2004.

López-Yglesias, X. and Flagan, R. C.: Ion–Aerosol Flux Coefficients and the Steady-State Charge Distribution of Aerosols in a Bipolar Ion Environment, Aerosol Science and Technology, 47, 688–704, https://doi.org/10.1080/02786826.2013.783684, 2013.

Mach, D. M., Blakeslee, R. J., and Bateman, M. G.: Global electric circuit implications of combined aircraft storm electric current measurements and satellite-based diurnal lightning statistics, J. Geophys. Res., 116, D05201, https://doi.org/10.1029/2010JD014462, 2011.

Mahfouz, N. G. A. and Donahue, N. M.: Atmospheric Nanoparticle Survivability Reduction Due to Charge-Induced Coagulation Scavenging Enhancement, Geophys Res Lett, 48, https://doi.org/10.1029/2021GL092758, 2021a.

Mahfouz, N. G. A. and Donahue, N. M.: Technical note: The enhancement limit of coagulation scavenging of small charged particles, Atmos. Chem. Phys., 21, 3827–3832, https://doi.org/10.5194/acp-21-3827-2021, 2021b.

Mamyrin, B. A.: Laser assisted reflectron time-of-flight mass spectrometry, in: Time-of-Flight Mass Spectrometry and its Applications, Elsevier, 1–19, https://doi.org/10.1016/B978-0-444-81875-1.50004-5, 1994.

Manninen, H. E., Petäjä, T., Asmi, E., Riipinen, I., Nieminen, T., Mikkilä, J., Hörrak, U., Mirme, A., Mirme, S., Laakso, L., Kerminen, V.-M., and Kulmala, M.: Long-term field measurements of charged and neutral

clusters using Neutral cluster and Air Ion Spectrometer (NAIS), Boreal Environment Research, 14, 591–605, 2009.

Manninen, H. E., Mirme, S., Mirme, A., Petäjä, T., and Kulmala, M.: How to reliably detect molecular clusters and nucleation mode particles with Neutral cluster and Air Ion Spectrometer (NAIS), Atmos. Meas. Tech., 9, 3577–3605, https://doi.org/10.5194/amt-9-3577-2016, 2016.

Marten, R., Xiao, M., Rörup, B., Wang, M., Kong, W., He, X.-C., Stolzenburg, D., Pfeifer, J., Marie, G., Wang, D. S., Scholz, W., Baccarini, A., Lee, C. P., Amorim, A., Baalbaki, R., Bell, D. M., Bertozzi, B., Caudillo, L., Chu, B., Dada, L., Duplissy, J., Finkenzeller, H., Carracedo, L. G., Granzin, M., Hansel, A., Heinritzi, M., Hofbauer, V., Kemppainen, D., Kürten, A., Lampimäki, M., Lehtipalo, K., Makhmutov, V., Manninen, H. E., Mentler, B., Petäjä, T., Philippov, M., Shen, J., Simon, M., Stozhkov, Y., Tomé, A., Wagner, A. C., Wang, Y., Weber, S. K., Wu, Y., Zauner-Wieczorek, M., Curtius, J., Kulmala, M., Möhler, O., Volkamer, R., Winkler, P. M., Worsnop, D. R., Dommen, J., Flagan, R. C., Kirkby, J., Donahue, N. M., Lamkaddam, H., Baltensperger, U., and El Haddad, I.: Survival of newly formed particles in haze conditions, Environmental Science: Atmospheres, 2, 491–499, https://doi.org/10.5445/IR/1000146549, 2022.

Martin, N. A., Ferracci, V., Cassidy, N., and Hoffnagle, J. A.: The application of a cavity ring-down spectrometer to measurements of ambient ammonia using traceable primary standard gas mixtures, Appl. Phys. B, 122, 219, https://doi.org/10.1007/s00340-016-6486-9, 2016.

Martínez-Botí, M. A., Foster, G. L., Chalk, T. B., Rohling, E. J., Sexton, P. F., Lunt, D. J., Pancost, R. D., Badger, M. P. S., and Schmidt, D. N.: Plio-Pleistocene climate sensitivity evaluated using high-resolution CO2 records, Nature, 518, 49–54, https://doi.org/10.1038/nature14145, 2015.

Massman, W. J.: A review of the molecular diffusivities of H2O, CO2, CH4, CO, O3, SO2, NH3, N2O, NO, and NO2 in air, O2 and N2 near STP, Atmospheric Environment, 32, 1111–1127, https://doi.org/10.1016/S1352-2310(97)00391-9, 1998.

Mauderly, J. L. and Chow, J. C.: Health Effects of Organic Aerosols, Inhalation Toxicology, 20, 257–288, https://doi.org/10.1080/08958370701866008, 2008.

McClelland, J. A.: II. *On the conductivity of the hot gases from flames*, The London, Edinburgh, and Dublin Philosophical Magazine and Journal of Science, 46, 29–42, https://doi.org/10.1080/14786449808621169, 1898.

Medhe, S.: Ionization Techniques in Mass Spectrometry: A Review, Mass Spectrom Purif Tech, 04, https://doi.org/10.4172/2469-9861.1000126, 2018.

Merikanto, J., Spracklen, D. V., Mann, G. W., Pickering, S. J., and Carslaw, K. S.: Impact of nucleation on global CCN, Atmos. Chem. Phys., 9, 8601–8616, https://doi.org/10.5194/acp-9-8601-2009, 2009.

Merikanto, J., Duplissy, J., Määttänen, A., Henschel, H., Donahue, N. M., Brus, D., Schobesberger, S., Kulmala, M., and Vehkamäki, H.: Effect of ions on sulfuric acid-water binary particle formation: 1. Theory for kinetic- and nucleation-type particle formation and atmospheric implications: BINARY PARTICLE FORMATION THEORY, J. Geophys. Res. Atmos., 121, 1736–1751, https://doi.org/10.1002/2015JD023538, 2016.

Meyerson, S. and Haar, R. W. V.: Multiply Charged Organic Ions in Mass Spectra, The Journal of Chemical Physics, 37, 2458–2462, https://doi.org/10.1063/1.1733027, 1962.

Millikan, R. A.: XXII. *A new modification of the cloud method of determining the elementary electrical charge and the most probable value of that charge*, The London, Edinburgh, and Dublin Philosophical Magazine and Journal of Science, 19, 209–228, https://doi.org/10.1080/14786440208636795, 1910.

Mirme, A.: Electrical Aerosol Spectrometry, PhD thesis, University of Tartu, Estonia, 1994.

Mirme, S. and Mirme, A.: The mathematical principles and design of the NAIS – a spectrometer for the measurement of cluster ion and nanometer aerosol size distributions, Atmos. Meas. Tech., 6, 1061–1071, https://doi.org/10.5194/amt-6-1061-2013, 2013.

Misumi, R., Uji, Y., Miura, K., Mori, T., Tobo, Y., and Iwamoto, Y.: Classification of aerosol-cloud interaction regimes over Tokyo, Atmospheric Research, 272, 106150, https://doi.org/10.1016/j.atmosres.2022.106150, 2022.

Möhler, O., Adams, M., Lacher, L., Vogel, F., Nadolny, J., Ullrich, R., Boffo, C., Pfeuffer, T., Hobl, A., Weiß, M., Vepuri, H. S. K., Hiranuma, N., and Murray, B. J.: The Portable Ice Nucleation Experiment (PINE): a new online instrument for laboratory studies and automated long-term field observations of ice-nucleating particles, Atmos. Meas. Tech., 14, 1143–1166, https://doi.org/10.5194/amt-14-1143-2021, 2021.

Mulcahy, J. P., Johnson, C., Jones, C. G., Povey, A. C., Scott, C. E., Sellar, A., Turnock, S. T., Woodhouse, M. T., Abraham, N. L., Andrews, M. B., Bellouin, N., Browse, J., Carslaw, K. S., Dalvi, M., Folberth, G. A., Glover, M., Grosvenor, D. P., Hardacre, C., Hill, R., Johnson, B., Jones, A., Kipling, Z., Mann, G., Mollard, J., O'Connor, F. M., Palmiéri, J., Reddington, C., Rumbold, S. T., Richardson, M., Schutgens, N. A. J., Stier, P., Stringer, M., Tang, Y., Walton, J., Woodward, S., and Yool, A.: Description and evaluation of aerosol in UKESM1 and HadGEM3-GC3.1 CMIP6 historical simulations, Geosci. Model Dev., 13, 6383–6423, https://doi.org/10.5194/gmd-13-6383-2020, 2020.

Mulcahy, J. P., Jones, C. G., Rumbold, S. T., Kuhlbrodt, T., Dittus, A. J., Blockley, E. W., Yool, A., Walton, J., Hardacre, C., Andrews, T., Bodas-Salcedo, A., Stringer, M., de Mora, L., Harris, P., Hill, R., Kelley, D., Robertson, E., and Tang, Y.: UKESM1.1: Development and evaluation of an updated configuration of the UK Earth System Model, Climate and Earth system modeling, https://doi.org/10.5194/gmd-2022-113, 2022.

Munson, M. S. B. and Field, F. H.: Chemical Ionization Mass Spectrometry. I. General Introduction, J. Am. Chem. Soc., 88, 2621–2630, https://doi.org/10.1021/ja00964a001, 1966.

Myhre, C. E. L., Nielsen, C. J., and Saastad, O. W.: Density and Surface Tension of Aqueous H_2SO_4 at Low Temperature, J. Chem. Eng. Data, 43, 617–622, https://doi.org/10.1021/je980013g, 1998.

Myllys, N., Kubečka, J., Besel, V., Alfaouri, D., Olenius, T., Smith, J. N., and Passananti, M.: Role of base strength, cluster structure and charge in sulfuric-acid-driven particle formation, Atmos. Chem. Phys., 19, 9753–9768, https://doi.org/10.5194/acp-19-9753-2019, 2019.

Nansai, K., Tohno, S., Chatani, S., Kanemoto, K., Kagawa, S., Kondo, Y., Takayanagi, W., and Lenzen, M.: Consumption in the G20 nations causes particulate air pollution resulting in two million premature deaths annually, Nat Commun, 12, 6286, https://doi.org/10.1038/s41467-021-26348-y, 2021.

Natanson, G. L.: On the Theory of Charging of a Microscopic Aerosol Particles as a Result of the Capture of Gas Ions, Soviet Physics Technical Physics, 538–551, 1960.

Nault, B. A., Jo, D. S., McDonald, B. C., Campuzano-Jost, P., Day, D. A., Hu, W., Schroder, J. C., Allan, J., Blake, D. R., Canagaratna, M. R., Coe, H., Coggon, M. M., DeCarlo, P. F., Diskin, G. S., Dunmore, R.,

Flocke, F., Fried, A., Gilman, J. B., Gkatzelis, G., Hamilton, J. F., Hanisco, T. F., Hayes, P. L., Henze, D. K., Hodzic, A., Hopkins, J., Hu, M., Huey, L. G., Jobson, B. T., Kuster, W. C., Lewis, A., Li, M., Liao, J., Nawaz, M. O., Pollack, I. B., Peischl, J., Rappenglück, B., Reeves, C. E., Richter, D., Roberts, J. M., Ryerson, T. B., Shao, M., Sommers, J. M., Walega, J., Warneke, C., Weibring, P., Wolfe, G. M., Young, D. E., Yuan, B., Zhang, Q., de Gouw, J. A., and Jimenez, J. L.: Secondary organic aerosols from anthropogenic volatile organic compounds contribute substantially to air pollution mortality, Atmos. Chem. Phys., 21, 11201–11224, https://doi.org/10.5194/acp-21-11201-2021, 2021.

Nicoll, K. A. and Harrison, R. G.: Experimental determination of layer cloud edge charging from cosmic ray ionisation: DETERMINATION OF CLOUD EDGE CHARGING, Geophys. Res. Lett., 37, L13802, https://doi.org/10.1029/2010GL043605, 2010.

Nieminen, T., Lehtinen, K. E. J., and Kulmala, M.: Sub-10 nm particle growth by vapor condensation – effects of vapor molecule size and particle thermal speed, Atmos. Chem. Phys., 10, 9773–9779, https://doi.org/10.5194/acp-10-9773-2010, 2010.

Nolan, J. J.: The Constitution of Gaseous Ions, Phys. Rev., 24, 16–30, https://doi.org/10.1103/PhysRev.24.16, 1924.

Nolan, P. J. and Kennan, E. L.: Condensation Nuclei from Hot Platinum: Size, Coagulation Coefficient and Charge-Distribution, Proceedings of the Royal Irish Academy. Section A: Mathematical and Physical Sciences, 171–190, 1948.

Norman, M., Spirig, C., Wolff, V., Trebs, I., Flechard, C., Wisthaler, A., Schnitzhofer, R., Hansel, A., and Neftel, A.: Intercomparison of ammonia measurement techniques at an intensively managed grassland site (Oensingen, Switzerland), Atmos. Chem. Phys., 9, 2635–2645, https://doi.org/10.5194/acp-9-2635-2009, 2009.

Nowak, J. B., Huey, L. G., Eisele, F. L., Tanner, D. J., Mauldin III, R. L., Cantrell, C., Kosciuch, E., and Davis, D.: Chemical ionization mass spectrometry technique for detection of dimethylsulfoxide and ammonia, J. Geophys. Res., 107, ACH 10-1-ACH 10-8, https://doi.org/10.1029/2001JD001058, 2002.

O'Dowd, C. D., Aalto, P., Hmeri, K., Kulmala, M., and Hoffmann, T.: Atmospheric particles from organic vapours, Nature, 416, 497–498, https://doi.org/10.1038/416497a, 2002a.

O'Dowd, C. D., Jimenez, J. L., Bahreini, R., Flagan, R. C., Seinfeld, J. H., Hämeri, K., Pirjola, L., Kulmala, M., Jennings, S. G., and Hoffmann, T.: Marine aerosol formation from biogenic iodine emissions, Nature, 417, 632–636, https://doi.org/10.1038/nature00775, 2002b.

Paasonen, P., Sihto, S.-L., Nieminen, T., Vuollekoski, H., Riipinen, I., Plaß-Dülmer, C., Berresheim, H., Birmili, W., and Kulmala, M.: Connection between new particle formation and sulphuric acid at Hohenpeissenberg (Germany) including the influence of organic compounds, BOREAL ENVIRONMENT RESEARCH, 14, 619–629, 2009.

Palas, G.: Produktdatenblatt: Promo 2000 digital. URL: https://www.palas.de/product/promo2000 (Stand 2022), 2022.

Passananti, M., Zapadinsky, E., Zanca, T., Kangasluoma, J., Myllys, N., Rissanen, M. P., Kurtén, T., Ehn, M., Attoui, M., and Vehkamäki, H.: How well can we predict cluster fragmentation inside a mass spectrometer?, Chem. Commun., 55, 5946–5949, https://doi.org/10.1039/C9CC02896J, 2019.

Peters, I., Metwally, H., and Konermann, L.: Mechanism of Electrospray Supercharging for Unfolded Proteins: Solvent-Mediated Stabilization of Protonated Sites During Chain Ejection, Anal. Chem., 91, 6943–6952, https://doi.org/10.1021/acs.analchem.9b01470, 2019.

Pfeifer, J.: Messung von Ammoniak, Aminen und Diaminen: Entwicklung, Charakterisierung und erster Feldeinsatz eines Chemischen Ionisations Massenspektrometers mit neu konzipierter Ionenquelle, Masterthesis, Johann Wolfgang Goethe-University Frankfurt, Germany, 2018.

Pfeifer, J., Simon, M., Heinritzi, M., Piel, F., Weitz, L., Wang, D., Granzin, M., Müller, T., Bräkling, S., Kirkby, J., Curtius, J., and Kürten, A.: Measurement of ammonia, amines and iodine compounds using protonated water cluster chemical ionization mass spectrometry, Atmos. Meas. Tech., 13, 2501–2522, https://doi.org/10.5194/amt-13-2501-2020, 2020.

Pfeifer, J., Mahfouz, N. G. A., Schulze, B., Mathot, S., Stolzenburg, D., Baalbaki, R., Brasseur, Z., Caudillo, L., Dada, L., Granzin, M., He, X.-C., Lamkaddam, H., Lopez, B., Makhmutov, V., Marten, R., Mentler, B., Müller, T., Onnela, A., Philippov, M., Piedehierro, A. A., Rörup, B., Schervish, M., Tian, P., Umo, N. S., Wang, D. S., Wang, M., Weber, S. K., Welti, A., Wu, Y., Zauner-Wieczorek, M., Amorim, A., El Haddad, I., Kulmala, M., Lehtipalo, K., Petäjä, T., Tome, A., Mirme, S., Manninen, H. E., Donahue, N. M., Flagan, R. C., Kürten, A., Curtius, J., and Kirkby, J.: Measurement of the rate coefficients between atmospheric ions and multiply charged aerosol particles in the CERN CLOUD chamber, submitted to Atmos. Chem. Phys., 2022.

Pospíšilová, V.: Investigation of Particle-Phase Processes in Biogenic Secondary Organic Aerosol by Novel Extractive Electrospray Ionization Mass Spectrometry, ETH Zurich, Zürich, Switzerland, https://doi.org/10.3929/ethz-b-000352736, 2019.

Pruppacher, H. R. and Klett, J. D.: Microphysics of Clouds and Precipitation, 1st ed., Springer Netherlands Springer e-books, Dordrecht, ISBN: 978-0-306-48100-0, 2010.

Pye, H. O. T., Ward-Caviness, C. K., Murphy, B. N., Appel, K. W., and Seltzer, K. M.: Secondary organic aerosol association with cardiorespiratory disease mortality in the United States, Nat Commun, 12, 7215, https://doi.org/10.1038/s41467-021-27484-1, 2021.

Quaas, J., Arola, A., Cairns, B., Christensen, M., Deneke, H., Ekman, A. M. L., Feingold, G., Fridlind, A., Gryspeerdt, E., Hasekamp, O., Li, Z., Lipponen, A., Ma, P.-L., Mülmenstädt, J., Nenes, A., Penner, J. E., Rosenfeld, D., Schrödner, R., Sinclair, K., Sourdeval, O., Stier, P., Tesche, M., van Diedenhoven, B., and Wendisch, M.: Constraining the Twomey effect from satellite observations: issues and perspectives, Atmos. Chem. Phys., 20, 15079–15099, https://doi.org/10.5194/acp-20-15079-2020, 2020.

Raäisaänen, J.: How reliable are climate models?, Tellus A: Dynamic Meteorology and Oceanography, 59, 2–29, https://doi.org/10.1111/j.1600-0870.2006.00211.x, 2007.

Ramanathan, V., Cess, R. D., Harrison, E. F., Minnis, P., Barkstrom, B. R., Ahmad, E., and Hartmann, D.: Cloud-Radiative Forcing and Climate: Results from the Earth Radiation Budget Experiment, Science, 243, 57–63, https://doi.org/10.1126/science.243.4887.57, 1989.

Rao, Y., Turro, N. J., and Eisenthal, K. B.: Water Structure at Air/Acetonitrile Aqueous Solution Interfaces, J. Phys. Chem. C, 113, 14384–14389, https://doi.org/10.1021/jp902933e, 2009.

Riccobono, F., Rondo, L., Sipilä, M., Barmet, P., Curtius, J., Dommen, J., Ehn, M., Ehrhart, S., Kulmala, M., Kürten, A., Mikkilä, J., Paasonen, P., Petäjä, T., Weingartner, E., and Baltensperger, U.: Contribution of sulfuric acid and oxidized organic compounds to particle formation and growth, Atmos. Chem. Phys., 12, 9427–9439, https://doi.org/10.5194/acp-12-9427-2012, 2012.

Riipinen, I., Yli-Juuti, T., Pierce, J. R., Petäjä, T., Worsnop, D. R., Kulmala, M., and Donahue, N. M.: The contribution of organics to atmospheric nanoparticle growth, Nature Geosci, 5, 453–458, https://doi.org/10.1038/ngeo1499, 2012.

Roscioli, J. R., Zahniser, M. S., Nelson, D. D., Herndon, S. C., and Kolb, C. E.: New Approaches to Measuring Sticky Molecules: Improvement of Instrumental Response Times Using Active Passivation, J. Phys. Chem. A, 120, 1347–1357, https://doi.org/10.1021/acs.jpca.5b04395, 2016.

Rudek, M. M., Katz, J. L., Vidensky, I. V., Ždímal, V., and Smolík, J.: Homogeneous nucleation rates of *n* -pentanol measured in an upward thermal diffusion cloud chamber, The Journal of Chemical Physics, 111, 3623–3629, https://doi.org/10.1063/1.479642, 1999.

Rycroft, M. J. and Harrison, R. G.: Electromagnetic Atmosphere-Plasma Coupling: The Global Atmospheric Electric Circuit, Space Sci Rev, 168, 363–384, https://doi.org/10.1007/s11214-011-9830-8, 2012.

Rycroft, M. J., Harrison, R. G., Nicoll, K. A., and Mareev, E. A.: An Overview of Earth's Global Electric Circuit and Atmospheric Conductivity, Space Sci Rev, 137, 83–105, https://doi.org/10.1007/s11214-008-9368-6, 2008.

Sagalyn, R. C. and Faucher, G. A.: Aircraft investigation of the large ion content and conductivity of the atmosphere and their relation to meteorological factors, Journal of Atmospheric and Terrestrial Physics, 5, 253–272, https://doi.org/10.1016/0021-9169(54)90046-X, 1954.

Sasamori, T., London, J., and Hoyt, D. V.: Radiation Budget of the Southern Hemisphere, in: Meteorology of the Southern Hemisphere, edited by: Newton, C. W., American Meteorological Society, Boston, MA, 9–23, https://doi.org/10.1007/978-1-935704-33-1_2, 1972.

Sassen, K.: Evidence for Liquid-Phase Cirrus Cloud Formation from Volcanic Aerosols: Climatic Implications, Science, 257, 516–519, https://doi.org/10.1126/science.257.5069.516, 1992.

Satoh, T., Tsuno, H., Iwanaga, M., and Kammei, Y.: The design and characteristic features of a new time-of-flight mass spectrometer with a spiral ion trajectory, J. Am. Soc. Mass Spectrom., 16, 1969–1975, https://doi.org/10.1016/j.jasms.2005.08.005, 2005.

Saunders, C. P. R.: A Review of Thunderstorm Electrification Processes, J. Appl. Meteor., 32, 642–655, https://doi.org/10.1175/1520-0450(1993)032<0642:AROTEP>2.0.CO;2, 1993.

Saunders, C. P. R., Keith, W. D., and Mitzeva, R. P.: The effect of liquid water on thunderstorm charging, J. Geophys. Res., 96, 11007, https://doi.org/10.1029/91JD00970, 1991.

Sayers, J.: Ionic recombination in air, Proc. R. Soc. Lond. A, 169, 83–101, https://doi.org/10.1098/rspa.1938.0196, 1938.

Schervish, M. and Donahue, N. M.: Peroxy radical chemistry and the volatility basis set, Atmos. Chem. Phys., 20, 1183–1199, https://doi.org/10.5194/acp-20-1183-2020, 2020.

Schmitt, J. L.: Precision expansion cloud chamber for homogeneous nucleation studies, Review of Scientific Instruments, 52, 1749–1754, https://doi.org/10.1063/1.1136524, 1981.

Schmitt, J. L., Zalabsky, R. A., and Adams, G. W.: Homogeneous nucleation of toluene, The Journal of Chemical Physics, 79, 4496–4501, https://doi.org/10.1063/1.446336, 1983.

Schneider, S. H.: Cloudiness as a Global Climatic Feedback Mechanism: The Effects on the Radiation Balance and Surface Temperature of Variations in Cloudiness, J. Atmos. Sci., 29, 1413–1422, https://doi.org/10.1175/1520-0469(1972)029<1413:CAAGCF>2.0.CO;2, 1972.

Schnitzhofer, R., Metzger, A., Breitenlechner, M., Jud, W., Heinritzi, M., De Menezes, L.-P., Duplissy, J., Guida, R., Haider, S., Kirkby, J., Mathot, S., Minginette, P., Onnela, A., Walther, H., Wasem, A., Hansel, A., and the CLOUD Team: Characterisation of organic contaminants in the CLOUD chamber at CERN, Atmos. Meas. Tech., 7, 2159–2168, https://doi.org/10.5194/amt-7-2159-2014, 2014.

Schobesberger, S., Junninen, H., Bianchi, F., Lönn, G., Ehn, M., Lehtipalo, K., Dommen, J., Ehrhart, S., Ortega, I. K., Franchin, A., Nieminen, T., Riccobono, F., Hutterli, M., Duplissy, J., Almeida, J., Amorim, A., Breitenlechner, M., Downard, A. J., Dunne, E. M., Flagan, R. C., Kajos, M., Keskinen, H., Kirkby, J., Kupc, A., Kürten, A., Kurtén, T., Laaksonen, A., Mathot, S., Onnela, A., Praplan, A. P., Rondo, L., Santos, F. D., Schallhart, S., Schnitzhofer, R., Sipilä, M., Tomé, A., Tsagkogeorgas, G., Vehkamäki, H., Wimmer, D., Baltensperger, U., Carslaw, K. S., Curtius, J., Hansel, A., Petäjä, T., Kulmala, M., Donahue, N. M., and Worsnop, D. R.: Molecular understanding of atmospheric particle formation from sulfuric acid and large oxidized organic molecules, Proc. Natl. Acad. Sci. U.S.A., 110, 17223–17228, https://doi.org/10.1073/pnas.1306973110, 2013.

Schwantes, R. H., Schilling, K. A., McVay, R. C., Lignell, H., Coggon, M. M., Zhang, X., Wennberg, P. O., and Seinfeld, J. H.: Formation of highly oxygenated low-volatility products from cresol oxidation, Atmos. Chem. Phys., 17, 3453–3474, https://doi.org/10.5194/acp-17-3453-2017, 2017.

Schymanski, E. L., Singer, H. P., Slobodnik, J., Ipolyi, I. M., Oswald, P., Krauss, M., Schulze, T., Haglund, P., Letzel, T., Grosse, S., Thomaidis, N. S., Bletsou, A., Zwiener, C., Ibáñez, M., Portolés, T., de Boer, R., Reid, M. J., Onghena, M., Kunkel, U., Schulz, W., Guillon, A., Noyon, N., Leroy, G., Bados, P., Bogialli, S., Stipaničev, D., Rostkowski, P., and Hollender, J.: Non-target screening with high-resolution mass spectrometry: critical review using a collaborative trial on water analysis, Anal Bioanal Chem, 407, 6237–6255, https://doi.org/10.1007/s00216-015-8681-7, 2015.

Seinfeld, J. H. and Pandis, S. N.: Atmospheric chemistry and physics: from air pollution to climate change, Third edition., John Wiley & Sons, Hoboken, New Jersey, ISBN: 978-1-119-22116-6 978-1-119-22117-3, 2016.

Sigurdsson, H.: Evidence of volcanic loading of the atmosphere and climate response, Global and Planetary Change, 3, 277–289, https://doi.org/10.1016/0921-8181(90)90024-7, 1990.

Simon, M., Heinritzi, M., Herzog, S., Leiminger, M., Bianchi, F., Praplan, A., Dommen, J., Curtius, J., and Kürten, A.: Detection of dimethylamine in the low pptv range using nitrate chemical ionization atmospheric pressure interface time-of-flight (CI-APi-TOF) mass spectrometry, Atmos. Meas. Tech., 9, 2135–2145, https://doi.org/10.5194/amt-9-2135-2016, 2016.

Sipilä, M., Sarnela, N., Jokinen, T., Henschel, H., Junninen, H., Kontkanen, J., Richters, S., Kangasluoma, J., Franchin, A., Peräkylä, O., Rissanen, M. P., Ehn, M., Vehkamäki, H., Kurten, T., Berndt, T., Petäjä, T., Worsnop, D., Ceburnis, D., Kerminen, V.-M., Kulmala, M., and O'Dowd, C.: Molecular-scale evidence of aerosol particle formation via sequential addition of HIO3, Nature, 537, 532–534, https://doi.org/10.1038/nature19314, 2016.

Small, J. D., Chuang, P. Y., Feingold, G., and Jiang, H.: Can aerosol decrease cloud lifetime?, Geophys. Res. Lett., 36, L16806, https://doi.org/10.1029/2009GL038888, 2009.

Smith, D. and Spanel, P.: Ions in the terrestrial atmosphere and in interstellar clouds, Mass Spectrom. Rev., 14, 255–278, https://doi.org/10.1002/mas.1280140403, 1995.

Smith, J. N., Flagan, R. C., and Beauchamp, J. L.: Droplet Evaporation and Discharge Dynamics in Electrospray Ionization, J. Phys. Chem. A, 106, 9957–9967, https://doi.org/10.1021/jp025723e, 2002.

Smith, J. N., Moore, K. F., Eisele, F. L., Voisin, D., Ghimire, A. K., Sakurai, H., and McMurry, P. H.: Chemical composition of atmospheric nanoparticles during nucleation events in Atlanta, J. Geophys. Res., 110, D22S03, https://doi.org/10.1029/2005JD005912, 2005.

Stark, H., Yatavelli, R. L. N., Thompson, S. L., Kimmel, J. R., Cubison, M. J., Chhabra, P. S., Canagaratna, M. R., Jayne, J. T., Worsnop, D. R., and Jimenez, J. L.: Methods to extract molecular and bulk chemical information from series of complex mass spectra with limited mass resolution, International Journal of Mass Spectrometry, 389, 26–38, https://doi.org/10.1016/j.ijms.2015.08.011, 2015.

Sterling, H. J., Prell, J. S., Cassou, C. A., and Williams, E. R.: Protein Conformation and Supercharging with DMSO from Aqueous Solution, J. Am. Soc. Mass Spectrom., 22, 1178–1186, https://doi.org/10.1007/s13361-011-0116-x, 2011.

Stolzenburg, D., Steiner, G., and Winkler, P. M.: A DMA-train for precision measurement of sub-10 nm aerosol dynamics, Atmos. Meas. Tech., 10, 1639–1651, https://doi.org/10.5194/amt-10-1639-2017, 2017.

Stolzenburg, D., Ozon, M., Kulmala, M., Lehtinen, K. E. J., Lehtipalo, K., and Kangasluoma, J.: Combining instrument inversions for sub-10 nm aerosol number size-distribution measurements, Journal of Aerosol Science, 159, 105862, https://doi.org/10.1016/j.jaerosci.2021.105862, 2022.

Stolzenburg, M., Rust, W. D., and Marshall, T. C.: Electrical structure in thunderstorm convective regions: 3. Synthesis, J. Geophys. Res., 103, 14097–14108, https://doi.org/10.1029/97JD03545, 1998.

Sunner, J., Nicol, G., and Kebarle, P.: Factors determining relative sensitivity of analytes in positive mode atmospheric pressure ionization mass spectrometry, Anal. Chem., 60, 1300–1307, https://doi.org/10.1021/ac00164a012, 1988.

Surdu, M., Pospisilova, V., Xiao, M., Wang, M., Mentler, B., Simon, M., Stolzenburg, D., Hoyle, C. R., Bell, D. M., Lee, C. P., Lamkaddam, H., Lopez-Hilfiker, F., Ahonen, L. R., Amorim, A., Baccarini, A., Chen, D., Dada, L., Duplissy, J., Finkenzeller, H., He, X.-C., Hofbauer, V., Kim, C., Kürten, A., Kvashnin, A., Lehtipalo, K., Makhmutov, V., Molteni, U., Nie, W., Onnela, A., Petäjä, T., Quéléver, L. L. J., Tauber, C., Tomé, A., Wagner, R., Yan, C., Prevot, A. S. H., Dommen, J., Donahue, N. M., Hansel, A., Curtius, J., Winkler, P. M., Kulmala, M., Volkamer, R., Flagan, R. C., Kirkby, J., Worsnop, D. R., Slowik, J. G., Wang, D. S., Baltensperger, U., and Haddad, I. el: Molecular characterization of ultrafine particles using extractive electrospray time-of-flight mass spectrometry, Environ. Sci.: Atmos., 1, 434–448, https://doi.org/10.1039/D1EA00050K, 2021.

Suresh, V., Li, L., Redmond Go Felipe, J., and Gopalakrishnan, R.: Modeling nanoparticle charge distribution in the afterglow of non-thermal plasmas and comparison with measurements, J. Phys. D: Appl. Phys., 54, 275205, https://doi.org/10.1088/1361-6463/abf70c, 2021.

Taflin, D. C., Ward, T. L., and Davis, E. J.: Electrified droplet fission and the Rayleigh limit, Langmuir, 5, 376–384, https://doi.org/10.1021/la00086a016, 1989.

Takahashi, T.: Riming Electrification as a Charge Generation Mechanism in Thunderstorms, J. Atmos. Sci., 35, 1536–1548, https://doi.org/10.1175/1520-0469(1978)035<1536:REAACG>2.0.CO;2, 1978.

Takemura, T., Nozawa, T., Emori, S., Nakajima, T. Y., and Nakajima, T.: Simulation of climate response to aerosol direct and indirect effects with aerosol transport-radiation model, J. Geophys. Res., 110, D02202, https://doi.org/10.1029/2004JD005029, 2005.

Tamadate, T., Higashi, H., Seto, T., and Hogan, C. J.: Calculation of the ion–ion recombination rate coefficient via a hybrid continuum-molecular dynamics approach, J. Chem. Phys., 152, 094306, https://doi.org/10.1063/1.5144772, 2020a.

Tamadate, T., Higashi, H., Hogan, C. J., and Seto, T.: The charge reduction rate for multiply charged polymer ions *via* ion–ion recombination at atmospheric pressure, Phys. Chem. Chem. Phys., 22, 25215–25226, https://doi.org/10.1039/D0CP03989F, 2020b.

Tani, A., Hayward, S., Hansel, A., and Hewitt, C. N.: Effect of water vapour pressure on monoterpene measurements using proton transfer reaction-mass spectrometry (PTR-MS), International Journal of Mass Spectrometry, 239, 161–169, https://doi.org/10.1016/j.ijms.2004.07.020, 2004.

Thomson, J. J.: LVII. *On the charge of electricity carried by the ions produced by Röntgen rays*, The London, Edinburgh, and Dublin Philosophical Magazine and Journal of Science, 46, 528–545, https://doi.org/10.1080/14786449808621229, 1898.

Timonen, H., Cubison, M., Aurela, M., Brus, D., Lihavainen, H., Hillamo, R., Canagaratna, M., Nekat, B., Weller, R., Worsnop, D., and Saarikoski, S.: Applications and limitations of constrained high-resolution peak fitting onlow resolving power mass spectra from the ToF-ACSM, Atmos. Meas. Tech., 9, 3263–3281, https://doi.org/10.5194/amt-9-3263-2016, 2016.

Tinsley, B. A., Rohrbaugh, R. P., Hei, M., and Beard, K. V.: Effects of Image Charges on the Scavenging of Aerosol Particles by Cloud Droplets and on Droplet Charging and Possible Ice Nucleation Processes, J. Atmos. Sci., 57, 2118–2134, https://doi.org/10.1175/1520-0469(2000)057<2118:EOICOT>2.0.CO;2, 2000.

TOFWERK AG: TOF-CIMS user guide (2013), URL: https://www.tofwerk.com, 2013.

Townsend, J. S. E.: IV. The diffusion of ions into gases, Phil. Trans. R. Soc. Lond. A, 193, 129–158, https://doi.org/10.1098/rsta.1900.0004, 1900.

Townsend, T. M.: An Investigation into the Tropospheric Chemistry of Acidic Aerosols and Ammonia in the laboratory, PhD thesis, University College Cork, Cork, Ireland, 2010.

Tripathi, N. and Sahu, L. K.: Emissions and atmospheric concentrations of α-pinene at an urban site of India: Role of changes in meteorology, Chemosphere, 256, 127071, https://doi.org/10.1016/j.chemosphere.2020.127071, 2020.

Tritscher, T., Beeston, M., Zerrath, A. F., Elzey, S., Krinke, T. J., Filimundi, E., and Bischof, O. F.: NanoScan SMPS – A Novel, Portable Nanoparticle Sizing and Counting Instrument, J. Phys.: Conf. Ser., 429, 012061, https://doi.org/10.1088/1742-6596/429/1/012061, 2013.

Tröstl, J., Chuang, W. K., Gordon, H., Heinritzi, M., Yan, C., Molteni, U., Ahlm, L., Frege, C., Bianchi, F., Wagner, R., Simon, M., Lehtipalo, K., Williamson, C., Craven, J. S., Duplissy, J., Adamov, A., Almeida, J., Bernhammer, A.-K., Breitenlechner, M., Brilke, S., Dias, A., Ehrhart, S., Flagan, R. C., Franchin, A., Fuchs, C., Guida, R., Gysel, M., Hansel, A., Hoyle, C. R., Jokinen, T., Junninen, H., Kangasluoma, J., Keskinen, H., Kim, J., Krapf, M., Kürten, A., Laaksonen, A., Lawler, M., Leiminger, M., Mathot, S., Möhler, O., Nieminen, T., Onnela, A., Petäjä, T., Piel, F. M., Miettinen, P., Rissanen, M. P., Rondo, L., Sarnela, N., Schobesberger, S., Sengupta, K., Sipilä, M., Smith, J. N., Steiner, G., Tomè, A., Virtanen, A., Wagner, A.

C., Weingartner, E., Wimmer, D., Winkler, P. M., Ye, P., Carslaw, K. S., Curtius, J., Dommen, J., Kirkby, J., Kulmala, M., Riipinen, I., Worsnop, D. R., Donahue, N. M., and Baltensperger, U.: The role of low-volatility organic compounds in initial particle growth in the atmosphere, Nature, 533, 527–531, https://doi.org/10.1038/nature18271, 2016.

Twomey, S.: Pollution and the planetary albedo, Atmospheric Environment (1967), 8, 1251–1256, https://doi.org/10.1016/0004-6981(74)90004-3, 1974.

Twomey, S. and Warner, J.: Comparison of Measurements of Cloud Droplets and Cloud Nuclei, J. Atmos. Sci., 24, 702–703, https://doi.org/10.1175/1520-0469(1967)024<0702:COMOCD>2.0.CO;2, 1967.

Veenhof, R.: Garfield, recent developments, Nuclear Instruments and Methods in Physics Research Section A: Accelerators, Spectrometers, Detectors and Associated Equipment, 419, 726–730, https://doi.org/10.1016/S0168-9002(98)00851-1, 1998.

Vehkamäki, H., Kulmala., M., Napari, I., Lehtinen, K. E. J., Timmreck, M., Noppel, M., and Laaksonen, A.: An improved parameterization for sulfuric acid–water nucleation rates for tropospheric and stratospheric conditions, J. Geophys. Res., 107, AAC 3-1-AAC 3-10, https://doi.org/10.1029/2002JD002184, 2002.

Volmer, M. and Weber, A.: Keimbildung in übersättigten Gebilden, Zeitschrift für Physikalische Chemie, 119U, 277–301, https://doi.org/10.1515/zpch-1926-11927, 1926.

Vonnegut, B.: Some Facts and Speculations Concerning the Origin and Role of Thunderstorm Electricity, in: Severe Local Storms, American Meteorological Society, Boston, MA, 224–241, https://doi.org/10.1007/978-1-940033-56-3_11, 1963.

Wang, M., Kong, W., Marten, R., He, X.-C., Chen, D., Pfeifer, J., Heitto, A., Kontkanen, J., Dada, L., Kürten, A., Yli-Juuti, T., Manninen, H. E., Amanatidis, S., Amorim, A., Baalbaki, R., Baccarini, A., Bell, D. M., Bertozzi, B., Bräkling, S., Brilke, S., Murillo, L. C., Chiu, R., Chu, B., De Menezes, L.-P., Duplissy, J., Finkenzeller, H., Carracedo, L. G., Granzin, M., Guida, R., Hansel, A., Hofbauer, V., Krechmer, J., Lehtipalo, K., Lamkaddam, H., Lampimäki, M., Lee, C. P., Makhmutov, V., Marie, G., Mathot, S., Mauldin, R. L., Mentler, B., Müller, T., Onnela, A., Partoll, E., Petäjä, T., Philippov, M., Pospisilova, V., Ranjithkumar, A., Rissanen, M., Rörup, B., Scholz, W., Shen, J., Simon, M., Sipilä, M., Steiner, G., Stolzenburg, D., Tham, Y. J., Tomé, A., Wagner, A. C., Wang, D. S., Wang, Y., Weber, S. K., Winkler, P. M., Wlasits, P. J., Wu, Y., Xiao, M., Ye, Q., Zauner-Wieczorek, M., Zhou, X., Volkamer, R., Riipinen, I., Dommen, J., Curtius, J., Baltensperger, U., Kulmala, M., Worsnop, D. R., Kirkby, J., Seinfeld, J. H., El-Haddad, I., Flagan, R. C., and Donahue, N. M.: Rapid growth of new atmospheric particles by nitric acid and ammonia condensation, Nature, 581, 184–189, https://doi.org/10.1038/s41586-020-2270-4, 2020.

Wang, M., He, X.-C., Finkenzeller, H., Iyer, S., Chen, D., Shen, J., Simon, M., Hofbauer, V., Kirkby, J., Curtius, J., Maier, N., Kurtén, T., Worsnop, D. R., Kulmala, M., Rissanen, M., Volkamer, R., Tham, Y. J., Donahue, N. M., and Sipilä, M.: Measurement of iodine species and sulfuric acid using bromide chemical ionization mass spectrometers, Atmos. Meas. Tech., 14, 4187–4202, https://doi.org/10.5194/amt-14-4187-2021, 2021.

Wang, M., Xiao, M., Bertozzi, B., Marie, G., Rörup, B., Schulze, B., Bardakov, R., He, X.-C., Shen, J., Scholz, W., Marten, R., Dada, L., Baalbaki, R., Lopez, B., Lamkaddam, H., Manninen, H. E., Amorim, A., Ataei, F., Bogert, P., Brasseur, Z., Caudillo, L., De Menezes, L.-P., Duplissy, J., Ekman, A. M. L., Finkenzeller, H., Carracedo, L. G., Granzin, M., Guida, R., Heinritzi, M., Hofbauer, V., Höhler, K.,

Korhonen, K., Krechmer, J. E., Kürten, A., Lehtipalo, K., Mahfouz, N. G. A., Makhmutov, V., Massabò, D., Mathot, S., Mauldin, R. L., Mentler, B., Müller, T., Onnela, A., Petäjä, T., Philippov, M., Piedehierro, A. A., Pozzer, A., Ranjithkumar, A., Schervish, M., Schobesberger, S., Simon, M., Stozhkov, Y., Tomé, A., Umo, N. S., Vogel, F., Wagner, R., Wang, D. S., Weber, S. K., Welti, A., Wu, Y., Zauner-Wieczorek, M., Sipilä, M., Winkler, P. M., Hansel, A., Baltensperger, U., Kulmala, M., Flagan, R. C., Curtius, J., Riipinen, I., Gordon, H., Lelieveld, J., El-Haddad, I., Volkamer, R., Worsnop, D. R., Christoudias, T., Kirkby, J., Möhler, O., and Donahue, N. M.: Synergistic HNO3–H2SO4–NH3 upper tropospheric particle formation, Nature, 605, 483–489, https://doi.org/10.1038/s41586-022-04605-4, 2022.

Wang, S., Nan, J., Shi, C., Fu, Q., Gao, S., Wang, D., Cui, H., Saiz-Lopez, A., and Zhou, B.: Atmospheric ammonia and its impacts on regional air quality over the megacity of Shanghai, China, Sci Rep, 5, 15842, https://doi.org/10.1038/srep15842, 2015.

Watson, W.: An Answer to Dr. Lining's Query Relating to the Death of Professor Richman, Philosophical Transactions (1683-1775), 765–772, https://doi.org/10.1098/rstl.1753.0089, 1753.

Weber, R. J., Marti, J. J., McMurry, P. H., Eisele, F. L., Tanner, D. J., and Jefferson, A.: MEASURED ATMOSPHERIC NEW PARTICLE FORMATION RATES: IMPLICATIONS FOR NUCLEATION MECHANISMS, Chemical Engineering Communications, 151, 53–64, https://doi.org/10.1080/00986449608936541, 1996.

Wei, Y., Varanasi, R. S., Schwarz, T., Gomell, L., Zhao, H., Larson, D. J., Sun, B., Liu, G., Chen, H., Raabe, D., and Gault, B.: Machine-learning-enhanced time-of-flight mass spectrometry analysis, Patterns, 2, 100192, https://doi.org/10.1016/j.patter.2020.100192, 2021.

Went, F. W.: Blue Hazes in the Atmosphere, Nature, 187, 641–643, https://doi.org/10.1038/187641a0, 1960.

Wiedensohler, A.: An approximation of the bipolar charge distribution for particles in the submicron size range, Journal of Aerosol Science, 19, 387–389, https://doi.org/10.1016/0021-8502(88)90278-9, 1988.

Wilson, C. T. R.: On the comparative efficiency as condensation nuclei of posi-tively and negatively charged ions, Proc. R. Soc. Lond., 65, 289–290, https://doi.org/10.1098/rspl.1899.0036, 1900.

Winkler, J. H.: Die Stärke der elektrischen Kraft des Wassers in gläsernen Gefässen, Leipzig : Bey Bernhard Christoph Breitkopf, URN: urn:nbn:de:bvb:12-bsb10135094-8, 1746.

Winklmayr, W., Reischl, G. P., Lindner, A. O., and Berner, A.: A new electromobility spectrometer for the measurement of aerosol size distributions in the size range from 1 to 1000 nm, Journal of Aerosol Science, 22, 289–296, https://doi.org/10.1016/S0021-8502(05)80007-2, 1991.

Wollnik, H.: Time-of-flight mass analyzers, Mass Spectrom. Rev., 12, 89–114, https://doi.org/10.1002/mas.1280120202, 1993.

Wu, Z. J., Poulain, L., Birmili, W., Größ, J., Niedermeier, N., Wang, Z. B., Herrmann, H., and Wiedensohler, A.: Some insights into the condensing vapors driving new particle growth to CCN sizes on the basis of hygroscopicity measurements, Atmos. Chem. Phys., 15, 13071–13083, https://doi.org/10.5194/acp-15-13071-2015, 2015.

Xiao, M., Hoyle, C. R., Dada, L., Stolzenburg, D., Kürten, A., Wang, M., Lamkaddam, H., Garmash, O., Mentler, B., Molteni, U., Baccarini, A., Simon, M., He, X.-C., Lehtipalo, K., Ahonen, L. R., Baalbaki, R., Bauer, P. S., Beck, L., Bell, D., Bianchi, F., Brilke, S., Chen, D., Chiu, R., Dias, A., Duplissy, J., Finkenzeller,

H., Gordon, H., Hofbauer, V., Kim, C., Koenig, T. K., Lampilahti, J., Lee, C. P., Li, Z., Mai, H., Makhmutov, V., Manninen, H. E., Marten, R., Mathot, S., Mauldin, R. L., Nie, W., Onnela, A., Partoll, E., Petäjä, T., Pfeifer, J., Pospisilova, V., Quéléver, L. L. J., Rissanen, M., Schobesberger, S., Schuchmann, S., Stozhkov, Y., Tauber, C., Tham, Y. J., Tomé, A., Vazquez-Pufleau, M., Wagner, A. C., Wagner, R., Wang, Y., Weitz, L., Wimmer, D., Wu, Y., Yan, C., Ye, P., Ye, Q., Zha, Q., Zhou, X., Amorim, A., Carslaw, K., Curtius, J., Hansel, A., Volkamer, R., Winkler, P. M., Flagan, R. C., Kulmala, M., Worsnop, D. R., Kirkby, J., Donahue, N. M., Baltensperger, U., El Haddad, I., and Dommen, J.: The driving factors of new particle formation and growth in the polluted boundary layer, Atmos. Chem. Phys., 21, 14275–14291, https://doi.org/10.5194/acp-21-14275-2021, 2021.

Yan, C., Dada, L., Rose, C., Jokinen, T., Nie, W., Schobesberger, S., Junninen, H., Lehtipalo, K., Sarnela, N., Makkonen, U., Garmash, O., Wang, Y., Zha, Q., Paasonen, P., Bianchi, F., Sipilä, M., Ehn, M., Petäjä, T., Kerminen, V.-M., Worsnop, D. R., and Kulmala, M.: The role of H2SO4-NH3 anion clusters in ion-induced aerosol nucleation mechanisms in the boreal forest, Atmos. Chem. Phys., 18, 13231–13243, https://doi.org/10.5194/acp-18-13231-2018, 2018.

Yao, L., Wang, M.-Y., Wang, X.-K., Liu, Y.-J., Chen, H.-F., Zheng, J., Nie, W., Ding, A.-J., Geng, F.-H., Wang, D.-F., Chen, J.-M., Worsnop, D. R., and Wang, L.: Detection of atmospheric gaseous amines and amides by a high-resolution time-of-flight chemical ionization mass spectrometer with protonated ethanol reagent ions, Atmos. Chem. Phys., 16, 14527–14543, https://doi.org/10.5194/acp-16-14527-2016, 2016.

Yin, R., Yan, C., Cai, R., Li, X., Shen, J., Lu, Y., Schobesberger, S., Fu, Y., Deng, C., Wang, L., Liu, Y., Zheng, J., Xie, H., Bianchi, F., Worsnop, D. R., Kulmala, M., and Jiang, J.: Acid–Base Clusters during Atmospheric New Particle Formation in Urban Beijing, Environ. Sci. Technol., 55, 10994–11005, https://doi.org/10.1021/acs.est.1c02701, 2021.

You, Y., Kanawade, V. P., de Gouw, J. A., Guenther, A. B., Madronich, S., Sierra-Hernández, M. R., Lawler, M., Smith, J. N., Takahama, S., Ruggeri, G., Koss, A., Olson, K., Baumann, K., Weber, R. J., Nenes, A., Guo, H., Edgerton, E. S., Porcelli, L., Brune, W. H., Goldstein, A. H., and Lee, S.-H.: Atmospheric amines and ammonia measured with a chemical ionization mass spectrometer (CIMS), Atmos. Chem. Phys., 14, 12181–12194, https://doi.org/10.5194/acp-14-12181-2014, 2014.

Yu, F. and Turco, R. P.: Ultrafine aerosol formation via ion-mediated nucleation, Geophys. Res. Lett., 27, 883–886, https://doi.org/10.1029/1999GL011151, 2000.

Yu, H. and Lee, S.-H.: Chemical ionisation mass spectrometry for the measurement of atmospheric amines, Environ. Chem., 9, 190–201, https://doi.org/10.1071/EN12020, 2012.

Yue, D. L., Hu, M., Zhang, R. Y., Wang, Z. B., Zheng, J., Wu, Z. J., Wiedensohler, A., He, L. Y., Huang, X. F., and Zhu, T.: The roles of sulfuric acid in new particle formation and growth in the mega-city of Beijing, Atmos. Chem. Phys., 10, 4953–4960, https://doi.org/10.5194/acp-10-4953-2010, 2010.

Zapadinsky, E., Passananti, M., Myllys, N., Kurtén, T., and Vehkamäki, H.: Modeling on Fragmentation of Clusters inside a Mass Spectrometer, J. Phys. Chem. A, 123, 611–624, https://doi.org/10.1021/acs.jpca.8b10744, 2019.

Zauner-Wieczorek, M., Heinritzi, M., Granzin, M., Keber, T., Kürten, A., Kaiser, K., Schneider, J., and Curtius, J.: Mass spectrometric measurements of ambient ions and estimation of gaseous sulfuric acid in the free troposphere and lowermost stratosphere during the CAFE-EU/BLUESKY campaign, Atmos. Chem. Phys., 22, 11781–11794, https://doi.org/10.5194/acp-2022-238, 2022.

Zeleny, J.: The velocity of the ions produced in gases by Röntgen rays, Proc. R. Soc. Lond., 66, 238–241, https://doi.org/10.1098/rspl.1899.0095, 1900.

Zhang, R., Suh, I., Zhao, J., Zhang, D., Fortner, E. C., Tie, X., Molina, L. T., and Molina, M. J.: Atmospheric New Particle Formation Enhanced by Organic Acids, Science, 304, 1487–1490, https://doi.org/10.1126/science.1095139, 2004.

Zhao, J., Ortega, J., Chen, M., McMurry, P. H., and Smith, J. N.: Dependence of particle nucleation and growth on high-molecular-weight gas-phase products during ozonolysis of α-pinene, Atmos. Chem. Phys., 13, 7631–7644, https://doi.org/10.5194/acp-13-7631-2013, 2013.

Zhou, L. and Tinsley, B. A.: Production of space charge at the boundaries of layer clouds, J. Geophys. Res., 112, D11203, https://doi.org/10.1029/2006JD007998, 2007.

2- Cumulative part

Paper 1: Measurement of ammonia, amines and iodine compounds using protonated water cluster chemical ionization mass spectrometry

Atmos. Meas. Tech., 13, 2501–2522, 2020
https://doi.org/10.5194/amt-13-2501-2020

Atmospheric Measurement Techniques
Open Access
EGU

Measurement of ammonia, amines and iodine compounds using protonated water cluster chemical ionization mass spectrometry

Joschka Pfeifer[1,2], Mario Simon[2], Martin Heinritzi[2], Felix Piel[2,a], Lena Weitz[2,b], Dongyu Wang[3], Manuel Granzin[2], Tatjana Müller[2], Steffen Bräkling[4], Jasper Kirkby[1,2], Joachim Curtius[2], and Andreas Kürten[2]

[1]CERN, 1211 Geneva, Switzerland
[2]Institute for Atmospheric and Environmental Sciences, 60438, Goethe University Frakfurt Am Main, Germany
[3]Laboratory of Atmospheric Chemistry, Paul Scherrer Institute, 5232 Villigen, Switzerland
[4]TOFWERK AG, 3600 Thun, Switzerland
[a]now at: Ionicon Analytik GmbH, 6020 Innsbruck, Austria
[b]now at: GSI Helmholtzzentrum für Schwerionenforschung GmbH, 64291 Darmstadt, Germany

Correspondence: Joschka Pfeifer (joschka.pfeifer@cern.ch)

Received: 25 May 2019 – Discussion started: 16 July 2019
Revised: 6 April 2020 – Accepted: 17 April 2020 – Published: 19 May 2020

Abstract. Here we describe the design and performance of a new water cluster chemical ionization–atmospheric pressure interface time-of-flight mass spectrometer (CI-APi-TOF). The instrument selectively measures trace gases with high proton affinity such as ammonia and dimethylamine, which are important for atmospheric new particle formation and growth. Following the instrument description and characterization, we demonstrate successful measurements at the CERN CLOUD (Cosmics Leaving OUtdoor Droplets) chamber where very low ammonia background levels of ~ 4 pptv were achieved (at 278 K and 80 % RH). The limit of detection of the water cluster CI-APi-TOF is estimated to be ~ 0.5 pptv for ammonia. Although no direct calibration was performed for dimethylamine (DMA), we estimate its detection limit is at least 3 times lower. Due to the short ion–molecule reaction time and high reagent ion concentrations, ammonia mixing ratios up to at least 10 ppbv can be measured with the instrument without significant reagent ion depletion. Besides the possibility to measure compounds like ammonia and amines (dimethylamine), we demonstrate that the ionization scheme is also suitable for the measurement of trace gases containing iodine. During CLOUD experiments to investigate the formation of new particles from I_2, many different iodine-containing species were identified with the water cluster CI-APi-TOF. The compounds included iodic acid and neutral molecular clusters containing up to four iodine atoms. However, the molecular structures of the iodine-containing clusters are ambiguous due to the presence of an unknown number of water molecules. The quantification of iodic acid (HIO_3) mixing ratios is performed from an intercomparison with a nitrate CI-APi-TOF. Using this method the detection limit for HIO_3 can be estimated as 0.007 pptv. In addition to presenting our measurements obtained at the CLOUD chamber, we discuss the applicability of the water cluster Ci-APi-TOF for atmospheric measurements.

1 Introduction

Ammonia (NH_3) is an important atmospheric trace gas that is mainly emitted by vehicles in urban environments and by agricultural activity due to animal husbandry and the use of fertilizers. It can partition to the aerosol phase and is one of the most important compounds contributing to secondary aerosol formation (Jimenez et al., 2009). Strong reductions in $PM_{2.5}$ mass and the associated adverse health effects could potentially be achieved by decreasing ammonia emissions (Pozzer et al., 2017). However, ammonia not only partitions to existing particles, but is also a key vapor driving new particle formation due to its stabilization of newly formed clusters in ternary (sulfuric acid–water–ammonia) and multicomponent (sulfuric acid–water–ammonia–highly oxygenated organic molecules) systems (Kirkby et al., 2011; Kürten et al., 2016a; Lehtipalo et al., 2018). On a global scale, a large

fraction of newly formed particles and cloud condensation nuclei involves ammonia (Dunne et al., 2016). The involvement of ammonia in nucleation has recently been measured in the free troposphere, in Antarctica and in the boreal forest (Bianchi et al., 2016; Jokinen et al., 2018; Yan et al., 2018). In the upper troposphere, model calculations suggest that ammonia is important for new particle formation and early growth (Dunne et al., 2016). Recent satellite measurements support this finding by the observation of up to several tens of parts per trillion by volume (pptv) of ammonia over Asia (Höpfner et al., 2016). Ammonia has a very strong effect on nucleation involving sulfuric acid and water; e.g., recent studies have shown that very low amounts of NH_3 in the parts per trillion by volume range, or even below, can enhance nucleation rates by orders of magnitude compared with the pure binary system of sulfuric acid and water (Kirkby et al., 2011; Kürten et al., 2016a; Kürten, 2019). Stronger basic compounds like amines or diamines have been shown to enhance nucleation rates, despite their much lower atmospheric concentrations (Almeida et al., 2013; Kürten et al., 2014; Jen et al., 2016; Yao et al., 2016). The experimental measurements are confirmed by quantum chemical calculations that compare the stabilizing effects of ammonia, amines and diamines (Kurtén et al., 2008; Elm et al., 2017; Yu et al., 2018). For these reasons improved gas-phase measurements of these compounds are required. Sensitive real-time measurements are needed, spanning mixing ratios over a broad atmospheric range between a few parts per trillion by volume to a few parts per billion by volume of ammonia in the boundary layer, as well as around a few parts per trillion by volume of amines (Ge et al., 2011; Hanson et al., 2011; You et al., 2014; Kürten et al., 2016b; Yao et al., 2016).

In some previous studies, ammonia has been measured using optical absorption or chromatographic methods (Norman et al., 2009; von Bobrutzki et al., 2010; Verriele et al., 2012; Bianchi et al., 2012; Pollack et al., 2019; Ellis et al., 2010). These measurement techniques are often specialized for the detection of only a few selected compounds, whereas chemical ionization mass spectrometry (CIMS) can often measure a suite of atmospheric trace gases simultaneously at low concentrations and high time resolution. The use of different reagent ions has been described in the literature for ammonia and amine measurements; e.g., protonated acetone, protonated ethanol, O_2^+ and protonated water clusters have been successfully applied (Nowak et al., 2007; Norman et al., 2007; Benson et al., 2010; Hanson et al., 2011; You et al., 2014; Yao et al., 2016). Nowak et al. (2010) deployed their instrument on an aircraft for measurements at up to ~ 5 km of altitude. The reported limit of detection (LOD) varies between 35 pptv (You et al., 2014) and 270 pptv (Norman et al., 2009) for ammonia, whereas dimethylamine (and other amines) can be detected in the sub-parts per trillion by volume range (You et al., 2014; Sipilä et al., 2015; Simon et al., 2016). In this study we introduce a newly developed chemical ionization mass spectrometer that uses protonated water clusters for the selective ionization of ammonia and dimethylamine. The instrument is a high-resolution chemical ionization–atmospheric pressure interface time-of-flight mass spectrometer (CI-APi-TOF; Aerodyne Inc. and TOFWERK AG) combined with a home-built ion source. The instrument is called a water cluster CI-APi-TOF, naming it in accordance with other established techniques using the same mass spectrometer but different reagent ions, e.g., the nitrate CI-APi-TOF for sulfuric acid, highly oxygenated organic molecules and cluster measurements (Jokinen et al., 2012; Ehn et al., 2014; Kürten et al., 2014). Here we describe and characterize the instrument during experiments performed at the CLOUD (Cosmics Leaving OUtdoor Droplets) chamber at CERN (European Organization for Nuclear Research). We show that the ammonia LOD is below 1 pptv, which is unprecedented to our knowledge. Besides the measurement of basic compounds with high proton affinity, we find that the protonated water clusters are also well-suited to measure iodine-containing species such as iodic acid (HIO_3) and neutral molecular clusters containing up to four iodine atoms. The corresponding signals in the mass spectra were identified during CLOUD experiments on new particle formation from the oxidation of iodine vapor. The relevance of such compounds for nucleation in the atmosphere has recently been reported (Sipilä et al., 2016). Our findings indicate that the water cluster CI-APi-TOF can provide sensitive real-time measurements of several trace gases that are important for atmospheric new particle formation and growth: ammonia, amines (dimethylamine) and iodine species.

2 Methods

2.1 CLOUD chamber

The measurements presented here were carried out at the CLOUD (Cosmics Leaving OUtdoor Droplets) chamber at CERN (European Organization for Nuclear Research) during fall 2017 (CLOUD12 campaign) and fall 2018 (CLOUD13). The CLOUD chamber is used to investigate new particle formation from different trace gas mixtures under controlled atmospheric conditions of temperature, relative humidity, ultraviolet (UV) light intensity and ionization (Kirkby et al., 2011; Kupc et al., 2011; Duplissy et al., 2016). The cylindrical stainless-steel chamber has a volume of 26.1 m^3. It is designed to ensure that trace gas contaminants are low enough to allow for precisely controlled nucleation experiments (Kirkby et al., 2016). The chamber is continuously flushed with synthetic air generated from liquid nitrogen and oxygen. The temperature and relative humidity of the air inside the chamber can be precisely controlled. For the present study, ammonia and dimethylamine from gas bottles were injected by a two-step dilution system (Simon et al., 2016; Kürten et al., 2016a). The calibration of the water cluster CI-

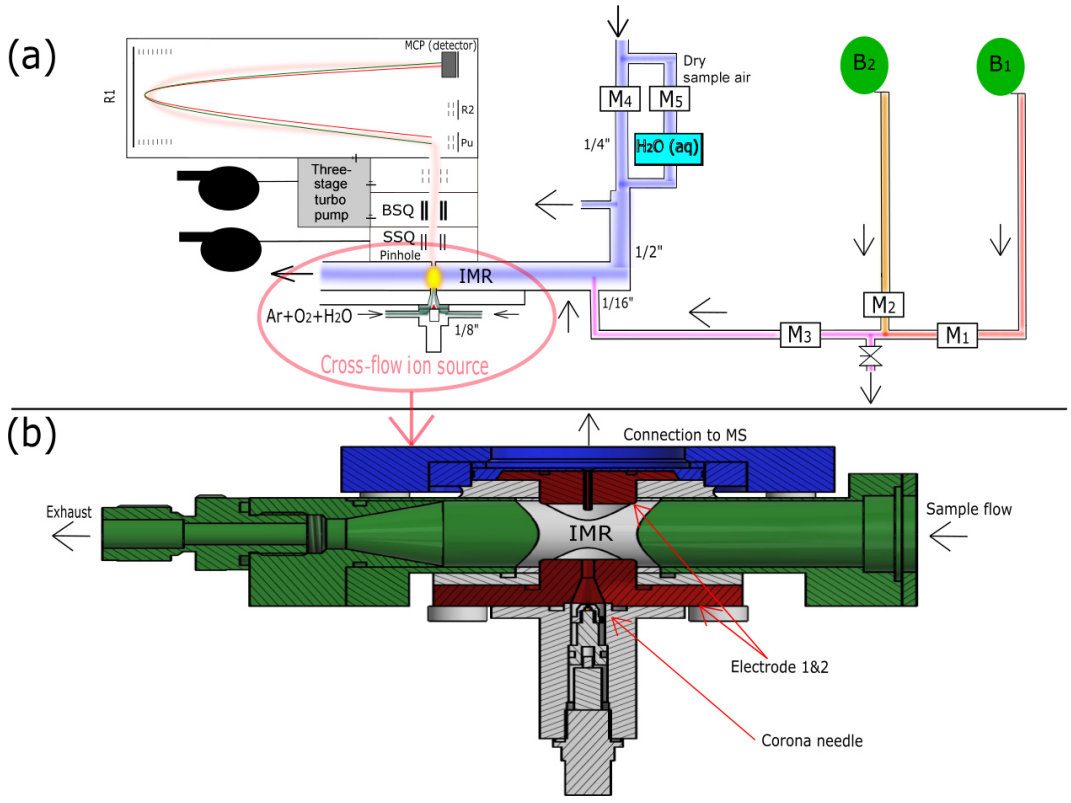

Figure 1. The experimental setup of the water cluster CI-APi-TOF during ammonia calibration is shown in panel **(a)**. Blue indicates the sample flow. It consists of a mixture of 80 % nitrogen and 20 % oxygen. A portion of the sample flow can be humidified with a water bubbler (H_2O_{aq}) to achieve different relative humidities. B_1 represents the ammonia gas bottle, while B_2 represents a gas bottle containing pure nitrogen. There are five mass flow controllers (MFCs; labeled as M_{1-5}) allowing two dilution steps. Three MFCs (M_1, M_2, M_3) control the amount of ammonia that is added through a $1/16''$ capillary into the center of the sample flow, where the second dilution stage occurs. The reagent ions (i.e., protonated water clusters) are produced when the ion source gas (argon, oxygen, water vapor) passes a corona needle at a positive high voltage (detailed in panel **b**). The calibration setup is disconnected during the measurements at the CLOUD chamber to reduce backgrounds (leakage from the $1/16''$ capillary). Details of the ion source used during CLOUD13 are shown in panel **(b)**. The primary ions are guided towards the sample flow using a counter electrode (Electrode 1). Additionally, a funnel is used to accelerate the primary ions towards the sample flow. A second electrode (Electrode 2) is installed directly in front of the pinhole of the mass spectrometer. The ions enter the mass spectrometer through a capillary on the top of Electrode 2.

APi-TOF with ammonia (Fig. 1) was carried out while the instrument was disconnected from the chamber. For the calibration measurements, the two-step dilution system from the CLOUD chamber was replicated (Fig. 1 and Sect. 2.2).

Iodine is introduced into the chamber by nitrogen flowing over solid, molecular iodine (I_2, 99.999 % purity; Sigma-Aldrich) placed in a stainless-steel evaporator immersed in a water bath at 303 K, with a temperature stability near 0.01 K. The generation of iodine-containing species for new particle formation is initiated by the photolysis of I_2 in the CLOUD chamber in the presence of ozone and water. Measurements presented here were carried out at chamber temperatures between 223 and 298 K, with relative humidity (RH) ranging between 10 % and 90 %. A Pt100 sensor string measured the air temperature in the CLOUD chamber (Dias et al., 2017).

A chilled dew-point mirror (Edgetech Instruments) measured the dew point inside the CLOUD chamber. The relative humidity is derived from water vapor pressure formulations published by Murphy and Koop (2005). Additionally, the RH was measured by a tunable diode laser system (TDL) developed by the Karlsruhe Institute for Technology (KIT), which was installed in the midplane of the chamber (Skrotzki, 2012). The relative humidity was derived using the mean value of both instruments, with a combined measurement uncertainty of 5 %.

2.2 Water cluster CI-APi-TOF

The selective detection of ammonia and amines by atmospheric pressure chemical ionization using positively charged water clusters has been demonstrated previously (Hanson et al., 2011). The same ionization technique is used in the present study. The reagent and product ions are measured with an atmospheric pressure interface time-of-

flight mass spectrometer (APi-TOF), which is coupled with a newly designed cross-flow chemical ionization (CI) source operated at ambient pressure (Fig. 1). The reagent ions, i.e., protonated water clusters ($(H_2O)_nH_3O^+$), are generated by positive corona discharge in the presence of argon (95 %), oxygen (5 %) and water vapor. The water vapor is added by bubbling the argon through a stainless steel humidifier (containing about 1 L of Millipore purified water) held at ambient temperature near 20 °C. As suggested by Hanson et al. (2011), a few droplets of sulfuric acid were added to the water in order to minimize potential contamination with ammonia from the water supply. Flow rates of 2.5 standard liters per minute (slm) for argon and 0.1 slm for oxygen were used. All flow rates were controlled by calibrated mass flow controllers (MFCs). A conversion factor for the measured argon flow (provided by the MFC manufacturer) was applied. Initially we used nitrogen instead of argon for the flow that passes the corona needle, but this resulted in much higher ammonia backgrounds. This is likely due to NH_3 production in the corona plasma when nitrogen is present (Haruyama et al., 2016). Furthermore, the addition of oxygen is necessary for the generation of a stable corona discharge in positive mode when using argon as the main ion source gas (Weissler, 1943).

Protonated water is also used in proton-transfer-reaction mass spectrometry (PTR-MS), which has been described in numerous publications (Good et al., 1970; Kebarle, 1972; Zhao and Zhang, 2004; Hansel et al., 2018). A simplified reaction scheme leading to the formation of protonated water clusters is shown as follows (Sunner et al., 1988).

$$e^- + O_2 \rightarrow O_2^+ + 2\,e^- \quad \text{(R1)}$$

$$O_2^+ + (H_2O)_2 \rightarrow O_2^+(H_2O)_2 \rightarrow H_3O^+(OH) + O_2 \quad \text{(R2)}$$

$$H_3O^+(OH) + (H_2O)_n \rightarrow H_3O^+(H_2O)_n + OH \quad \text{(R3)}$$

The PTR-MS operates its ion–molecule reaction (IMR) zone typically at low pressure ($\sim$ 10 hPa) and uses an electric field ($\sim 100\,\mathrm{V\,mm^{-1}}$) to break up water clusters so that mainly non-hydrated H_3O^+ ions remain. The use of charged water clusters ($(H_2O)_{n\geq 1}H_3O^+$ instead of H_3O^+) can increase the selectivity as water clusters have a much higher proton affinity compared to the water monomer (Aljawhary et al., 2013). However, due to their high proton affinity, ammonia and amines can still be detected according to the following reaction scheme:

$$H_3O^+(H_2O)_n + X \rightarrow XH^+(H_2O)_b + (n+1-b)\cdot(H_2O), \quad \text{(R4)}$$

where X represents the target substance that is ionized in the ion–molecule reaction zone (see below) and detected in the mass spectrometer. Since water molecules can evaporate in the atmospheric pressure interface of the mass spectrometer, some of the product ions are detected without water; e.g., ammonia is mainly detected as NH_4^+ (see Fig. 2).

A schematic drawing of the calibration setup and the ion source is shown in Fig. 1. The gas mixture for the ion source is composed of argon, oxygen and water vapor. It is introduced from two lines placed in the opposite direction to each other at an overall flow rate of $\sim$ 2.6 slm (Fig. 1a). The electrodes of the ion source are displayed in red in Fig. 1b. The connection to the mass spectrometer is shown using blue. The 1″ sampling line and the inlet (22 mm inner diameter) consist of stainless steel and are shown in green. Components used for insulation are shown in white. A total sample flow rate of $\sim$ 19.5 slm is maintained by a vacuum pump and a mass flow controller. The overall length of the sampling line connecting the CLOUD chamber and the ion molecule reaction zone is 1.3 m. A voltage of 3600 V is applied to the corona needle, while 500 V is applied to the conically shaped counter electrode (Electrode 1 in Fig. 1b) made of stainless steel. The housing of the ion source is made of polyether ether ketone (PEEK). The ion source gas and the generated reagent ions flow through a funnel (smallest inner diameter 2.5 mm) before they mix with the sample flow. A small capillary (inner diameter of 0.8 mm) is located opposite the funnel (Electrode 2 in Fig. 1b). The electric field between the counter electrode and the capillary (at ground potential) accelerates the ions towards the entrance of the mass spectrometer. The pinhole plate (pinhole inner diameter of 350 µm) and the capillary are in electric contact, and $\sim$ 0.8 slm flows through the capillary and the pinhole into the mass spectrometer. The measured product ions are generated in the ion–molecule reaction zone (IMR, yellow area in Fig. 1a) at atmospheric pressure. The dimension of the IMR is defined by the distance between the counter electrode and the capillary ($\sim$ 16.4 mm). After passing the pinhole, the ions are transported through two quadrupoles (small segmented quadrupole – SSQ, big segmented quadrupole – BSQ) towards the detection region of the mass spectrometer (microchannel plate – MCP; pressure is approx. 1×10^{-6} hPa). The estimated reaction time is < 1 ms. This short reaction time allows for the measurement of high ammonia mixing ratios (up to $\sim$ 10 ppbv) without significant depletion of the reagent ions; this would be the case when using an ion source design for the measurement of sulfuric acid (Eisele and Tanner, 1993; Kürten et al., 2011), which is typically present at much lower concentrations than ammonia. The principle of a cross-flow ion source was introduced by Eisele and Hanson (2000), who used this technique to detect molecular sulfuric acid clusters. In more recent studies, this technique was used for the measurement of ammonia (Nowak et al., 2002, 2006; Hanson et al., 2011).

The measured volume mixing ratio (VMR; pptv) of detected compounds is derived from a calibration factor (C) and the sum of the product ion counts per second (pcs) normalized against the sum of the reagent ion counts per second (rcs) (Kürten et al., 2016b; Simon et al., 2016):

$$\mathrm{VMR} = C \cdot \ln\left(1 + \frac{\sum \mathrm{pcs}}{\sum \mathrm{rcs}}\right) = C \cdot \mathrm{ncps}. \quad (1)$$

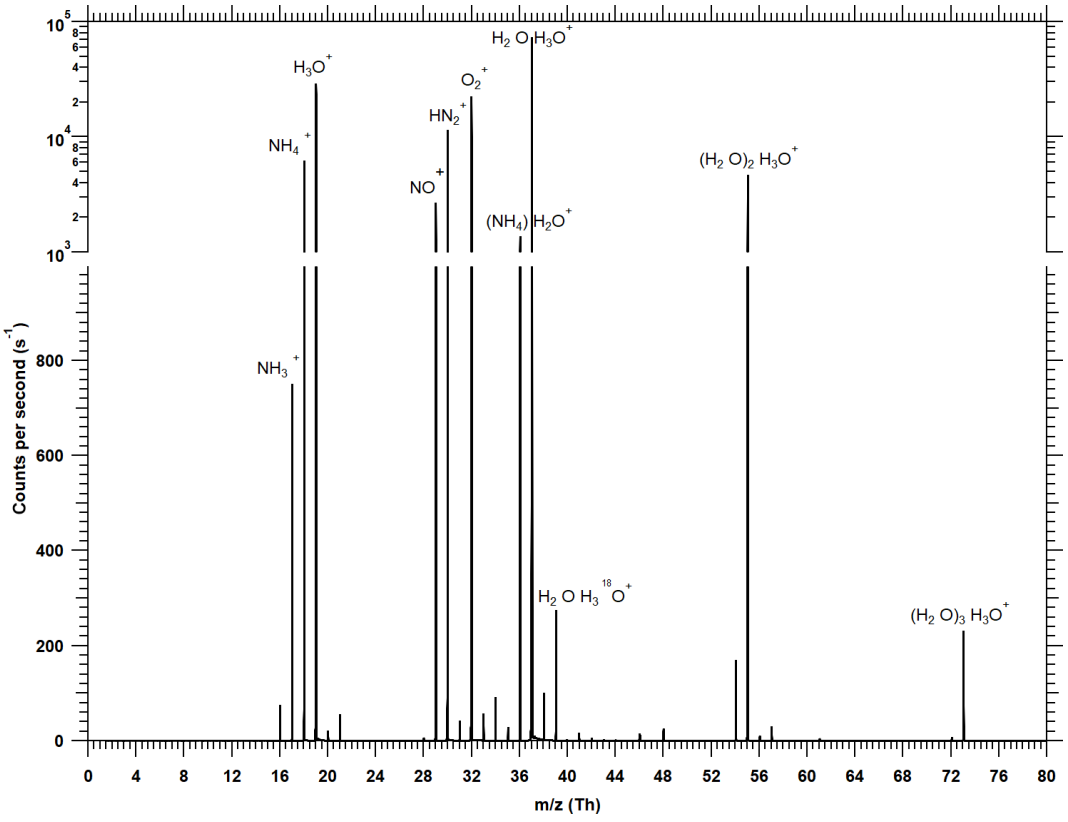

Figure 2. Typical mass spectrum recorded with the water cluster CI-APi-TOF when about 10 ppbv of ammonia is added during a calibration. Signals below 1000 counts per second are shown on a linear scale, while the dominant signals (> 1000 cps) are shown on a logarithmic scale. To calculate the ammonia mixing ratio, the product ion signals (NH_4^+ and $(H_2O)NH_4^+$) are normalized against the most prominent reagent ion signals (H_3O^+, $(H_2O)H_3O^+$, $(H_2O)_2H_3O^+$, $(H_2O)_3H_3O^+$). Larger water clusters are probably also present in the ion–molecule reaction zone, but a significant fraction of water evaporates upon crossing the pinhole at the atmospheric pressure interface of the instrument. Background peaks from N_2H^+, NO^+ and O_2^+ are always present but are neglected in the data evaluation. Due to the short reaction time (< 1 ms) in the ion–molecule reaction zone, the count rates of the reagent ions dominate the spectrum even at high ammonia mixing ratios near 10 ppbv.

Equation (1) yields the VMR measured by the water cluster CI-APi-TOF as a function of the normalized counts per second (ncps). A calibration factor, C, which includes factors like the reaction rate and the effective reaction time, is required to convert the normalized counts per second to a mixing ratio. This factor can be derived from the inverse slope of a calibration curve (see Sect. 3.2). While Hanson et al. (2011) report a maximum for the water cluster distribution at the pentamer, the evaporation of water seems to be stronger in our instrument. The maximum signal in clean spectra is usually found for the water dimer ($(H_2O)H_3O^+$; see Fig. 2), and a strong drop in the reagent ion signals is found beyond the tetramer ($(H_2O)_3H_3O^+$). Therefore, the sample quantification includes, using ammonia as an example, the product ions $(H_2O)_nNH_4^+$ with $n = 0$ and $n = 1$ as well as the reagent ions $(H_2O)_mH_3O^+$ with $m = 0$–3. Possible losses in the sampling line are not taken into account by the calibration factor (see Sect. 3.8 for a discussion of sampling line losses). The only compound for which a direct calibration is performed in the present study is ammonia (Sect. 2.3). When mixing ratios for dimethylamine are presented, the same calibration factor is used. This approach can introduce uncertainty, as the proton affinity and transmission efficiency differ for dimethylamine compared to ammonia. However, previous studies showed that the ionization efficiency from protonated water clusters is collision-limited for both ammonia and dimethylamine (Sunner et al., 1988; Hanson et al., 2011). The applicability of this approach is discussed in Sect. 3.9; it is estimated that the mixing ratios for dimethylamine are correct within a factor of ~ 3.5.

2.3 Calibrations

2.3.1 Ammonia

During calibrations, ammonia was drawn from a gas bottle containing an NH_3 mixing ratio, B, of 100 ppmv diluted in pure nitrogen (Air Liquide, ± 5 % uncertainty for the certi-

fied NH_3 mixing ratio). It was diluted in two steps, whereby MFCs (shown as M_n in Fig. 1a) are used to obtain different set points for the volume mixing ratio (Fig. 1a). During the second dilution step the mixture from the first dilution is injected into the center of the main sample flow (flow rate, Q_{sample}). The theoretical $\text{VMR}_{\text{theor}}$ is given by (Simon et al., 2016):

$$\text{VMR}_{\text{theor}} = \frac{\text{M}_1}{\text{M}_1 + \text{M}_2} \cdot \frac{\text{M}_3}{\text{M}_3 + Q_{\text{sample}}} \cdot \text{B}. \quad (2)$$

The flow of ammonia from the gas bottle is set by M_1 (0.01 slm max.), whereas M_2 (2 slm range) controls the flow of nitrogen for the first dilution step. The flow of diluted ammonia that is introduced into the sample flow is controlled by M_3 (0.1 slm range). The calibration flow consists of the same synthetic air as used for the CLOUD chamber. The flow is provided by two MFCs that control a dry portion (M_4) and a wet portion of the flow that has passed a stainless-steel water bubbler (M_5, see Fig. 1). By adjusting M_4 and M_5 (both 50 slm range) the RH of the sample flow can be controlled in order to test whether a humidity dependence exists for Reaction (R4). Care is taken that the sum of M_4 and M_5 is always somewhat larger than Q_{sample}. To avoid overpressure in the sampling line, the excess flow is vented through an exhaust before the sampling line.

Accordingly, the measured sample air consists of synthetic air (80 % nitrogen, 20 % oxygen) with an adjustable RH and ammonia mixing ratio. Results of the calibrations are discussed in Sect. 3.2.

2.3.2 Iodine oxides

The water cluster chemical ionizer is also effective for iodine-containing species, which were detected in new particle formation experiments from I_2 photolysis during CLOUD13. Prominent signals of iodic acid ($HIO_3 \cdot H^+$ and $HIO_3 \cdot H_3O^+$) were observed among many iodine compounds (Sect. 3.6 and Table 2). These species can be unambiguously identified due to the large negative mass defect of the iodine atom and the high resolution ($> 3000\,\text{Th}\,\text{Th}^{-1}$) of the mass spectrometer. No direct calibration for HIO_3 was performed; however, a second chemical ionization mass spectrometer at CLOUD, using nitrate reagent ions (nitrate CI-APi-TOF), was also measuring HIO_3 simultaneously. Therefore, a calibration factor for HIO_3 has been derived by scaling concentrations measured by the nitrate CI-APi-TOF, which itself had been calibrated for sulfuric acid (Kürten et al., 2012). We further assume that both sulfuric and iodic acid are detected with the same efficiency by the nitrate CI-APi-TOF. This assumption introduces uncertainty when estimating the detection limit of HIO_3. However, as the reaction of sulfuric acid with nitrate ions is at the kinetic limit (Viggiano et al., 1997), the detection limits shown here based on this assumption can be seen as lower limits. Unfortunately, there is currently no direct calibration technique established for iodic acid in the gas phase. The assumption we use in the present study was also applied in a previous study for deriving gas-phase concentrations of iodic acid (Sipilä et al., 2016).

For the instrument intercomparison (and the indirect calibration of the water cluster CI-APi-TOF), 18 different CLOUD experimental runs were selected and mean values were calculated for different steady-state concentrations. We took six steady-state concentrations each at temperatures of 263 K (80 % RH) and 283 K (40 % RH and 80 % RH).

2.4 PICARRO

A PICARRO G1103-t NH_3 analyzer (PICARRO Inc., USA) measuring ammonia mixing ratios based on cavity ring-down spectroscopy was also connected to the CLOUD chamber during CLOUD12 and CLOUD13. The instrument is suitable for real-time monitoring of ammonia in ambient air and has been presented in previous studies (Bell et al., 2009). The G1103-t was installed at the CLOUD chamber with its own sampling line coated with Sulfinert (Restek GmbH, Germany), and the coating reduced the losses of ammonia to the sampling line walls considerably. Since the PICARRO has a rather small sample flow rate (< 1 slm), an additional pump was used to enhance the flow rate to 5 slm just before the instrument inlet. This was done in order to minimize line losses and to shorten the response times. How much these measures helped with the measurements was, however, not quantitatively tested (Sulfinert and increased flow rate). The PICARRO was also independently calibrated with an NH_3 permeation tube (Fine Metrology, Italy) using a multigas calibrator (SONIMIX 6000 C1, LNI Swissgas, Switzerland). The time interval for one measurement of the PICARRO is 5 s for which a lower detection limit of 200 pptv is specified (PICARRO Inc., USA; Martin et al., 2016). By using the same method (at the same time period) as for the water cluster CI-APi-TOF (see Sect. 3.5), we derive a detection limit of 366.2 pptv for the PICARRO unit used in our study during CLOUD13. The detection limit derived for the PICARRO used during the CLOUD12 experiments is 170.1 pptv.

3 Results and discussion

3.1 Main peaks in spectrum

Figure 2 shows a typical spectrum during calibrations, whereby 10 ppbv of ammonia is injected (40 % RH, ∼ 293 K). The most prominent primary ions are H_3O^+, $(H_2O)H_3O^+$ and $(H_2O)_2H_3O^+$. The dominant primary ion is $(H_2O)H_3O^+$. The water tetramer ($(H_2O)_3H_3O^+$) is usually the largest water cluster that can be detected. The addition of ammonia generates NH_4^+ and $(H_2O)NH_4^+$; a small signal from NH_3^+ is also visible. At low ammonia concentrations the signal from NH_4^+ has a similar magnitude as H_2O^+ (which may arise from reactions of O_2^+ and H_2O). Since these ions have the same integer mass, high mass-resolving

Table 1. Estimated limit of detection (LOD) for some compounds with high proton affinity and for iodic acid measured with the water cluster CI-APi-TOF. The LOD is derived by background measurements at the CLOUD chamber, where LOD $= 3 \cdot \sigma$ (You et al., 2014). σ is defined as the standard deviation of the background signal. The detection limits are based on a measurement at 278 K and 80 % RH (1 min averaging time). The measured instrumental background mixing ratios (mean values) during this time period are also indicated.

Detected compound	LOD (pptv)	Instrumental background (pptv)	Measured m/z values (Th)
NH_3 (ammonia)	0.5 ± 0.05	3.73 ± 0.35	18.0338 (NH_4^+); 36.0444 ($(H_2O)NH_4^+$)
$(CH_3)_2NH$ (dimethylamine)[a]	0.047[a]	0.058[a]	46.0651 ($(CH_3)_2NH_2^+$)
HIO_3 (iodic acid)[b]	0.007[b]	<LOD[b]	176.9043 ($(HIO_3)H^+$); 194.9149 ($(HIO_3)H_3O^+$)

[a] Amine mixing ratios are estimated using the same calibration factor derived for ammonia. This can cause uncertainties. The applicability of this assumption is discussed in Sect. 3.9. [b] Iodic acid mixing ratios are derived from an intercomparison with a nitrate CI-APi-TOF, which evaluates HIO_3 based on a calibration factor derived for sulfuric acid. This assumption can lead to uncertainties but is necessary because no direct calibration method exists for such low gas-phase HIO_3 concentrations.

Table 2. Iodine-containing compounds (atomic composition), together with their m/z values, identified in the water cluster CI-APi-TOF spectra during the CLOUD13 campaign.

Detected compound	m/z value (Th)
I^+	126.9039
IO^+	142.8988
HIO^+	143.9067
IO_2^+	158.8938
$H_2IO_2^+$	160.9094
$H_3IO_2^+$	161.9172
$H_4IO_2^+$	162.9251
HIO_3^+	175.8965
$H_2IO_3^+$	176.9043
$H_3IO_3^+$	177.9121
$H_4IO_3^+$	178.9200
$H_4IO_4^+$	194.9149
$H_6IO_5^+$	212.9254
I_2^+	253.8084
$HI_2O_5^+$	334.7908
$H_3I_2O_5^+$	336.8064
$H_3I_2O_6^+$	352.8014
$H_5I_2O_6^+$	354.8170
$H_5I_2O_7^+$	370.8119
$H_2I_3O_7^+$	494.6929
$HI_3O_8^+$	509.6800
$H_2I_3O_8^+$	510.6878
$H_4I_3O_8^+$	512.7035
$H_4I_3O_9^+$	528.6984
$HI_4O_8^+$	636.5845
$HI_4O_9^+$	652.5794
$H_3I_4O_9^+$	654.5950
$H_3I_4O_{10}^+$	670.5900
$H_3I_4O_{11}^+$	686.5849

power is essential to reach low detection limits for ammonia as otherwise the differentiation between the two signals is not possible. At low mass, the APi-TOF used in the present study has a resolving power of $\sim 2000\,\mathrm{Th\,Th^{-1}}$, which is sufficient to separate the two peaks. For the analysis of the spectra, the software TOFWARE is used that allows for analyzing high-resolution spectra (Stark et al., 2015; Cubison and Jimenez, 2015; Timonen et al., 2016). Prominent peaks from N_2H^+, NO^+ and O_2^+ are also seen (Fig. 2). It is not clear how these ions are formed and why they survive the relatively long reaction time of ~ 1 ms since Good et al. (1970) report that O_2^+ reacts rapidly away in moist air. For the analysis the presence of these background peaks is currently ignored and they are not counted as reagent ions (in Eq. 1) as we have no indication that they interact with the target species relevant for the present study. An exception could be NH_3^+ (possibly from the reaction of O_2^+ and NH_3); however, NH_3^+ is not considered and is only a small fraction of NH_4^+.

In contrast to the spectrum shown in Fig. 2 with relatively small water clusters, Hanson et al. (2011) observe the highest signal in the water cluster distribution for the pentamer. We explain this difference with the more pronounced fragmentation and evaporation of ion clusters in the atmospheric pressure interface of our mass spectrometer.

For estimating an ammonia mixing ratio (Eq. 1), the product ion count rates are normalized to the dominating reagent ion count rates. Figure 2 shows that even at 10 ppbv ammonia the reagent ion signals are an order of magnitude higher than the product ion count rates. This indicates that very little reagent ion depletion occurs, and thus the normalized counts per second are linear with the ammonia VMR at least up to 10 ppbv (see Sect. 3.2).

3.2 Ammonia and iodic acid calibration

Figure 3 shows the calibration curves obtained for NH_3 and HIO_3 during the CLOUD13 campaign. Each dot represents the mean value of a steady-state measurement of at least 20 min. The normalized counts per second are based on the two highest signals assigned to the analyzed compound (NH_4^+ and $(H_2O)NH_4^+$ for ammonia and HIO_3H^+ and $HIO_3H_3O^+$ for iodic acid). The total error of the mixing ratios (x axis) is calculated by Gaussian error propagation, taking into account the standard deviation of the flow rates from the mass flow controllers and the uncertainty of the ammonia gas bottle concentration. Since we obtained the mixing

ratio shown in Fig. 3b by scaling the concentrations measured by a nitrate CI-APi-TOF calibrated for sulfuric acid, the error on the x axis equals the uncertainty of these measurements (estimated as a factor of 2 for the iodic acid concentration). The error on the y axis is given by the standard deviation of the normalized counts per second. We derive a calibration curve from a linear regression model using the Wilkinson–Rogers notation (Wilkinson and Rogers, 1973). The fit is forced through the origin; however, even when the fit is not constrained, the resulting slope is essentially the same (the results for the slopes and sensitivities differ by 1.35 %). The derived slopes represent the inverse of the calibration factor, C ($\sim 1.46 \times 10^5$ pptv at 40 % RH), in Eq. (2). Figure 3 shows that all measured mixing ratios lie in the area of the confidence intervals (95 % confidence intervals), and thus the linear model describes the dependency very well. The calibration was performed in September 2018, before the CLOUD13 campaign and also during and after the end of the campaign in December at relative humidities between ~ 3 % and 82 % and at ambient temperatures of the experimental hall near 293 K. The calibrations for ammonia were performed by introducing the highest mixing ratio first. However, it took almost a day to reach stable signals as the tubing and the two MFCs through which the ammonia flowed (M_1 and M_3) needed to equilibrate. The further calibration points were then recorded by reducing the flow rate of M_3. In this way, no change in the ammonia mixing ratio inside the capillary before the main sampling line and in the MFCs was necessary. This allowed for a relatively fast stepping through the calibration set points. However, even when the ammonia flow was shut off there was still significant diffusion of ammonia from the capillary into the sampling line, which resulted in relatively high background values (with nominally zero NH_3). We therefore derived the limit of detection by measuring the ammonia background in the CLOUD chamber with the calibration lines disconnected from our instrument (Sect. 3.5). During the calibrations, the relative humidity was calculated by assuming that the sample flow passing the water reservoir is 100 % saturated (Fig. 1a). For the calibrations carried out after the campaign, the temperature of the total sample flow was measured to derive the absolute humidity. The calibration points in Fig. 3 were taken at measured gas flow temperatures of 288 to 290 K. The relative humidity was set to 40 % RH by adjusting the dry and wet flow rates for the sample flow; these conditions correspond to an absolute humidity of $\sim 0.0057\,\mathrm{kg\,m^{-3}}$. The calibration factor derived for CLOUD12 (for ammonia) differs from the calibration factor shown here. This is due to a different ion source (designed for a 0.5″ sampling line in CLOUD12 compared with a 1″ line in CLOUD13), a different sample flow rate and different tuning of the CI-APi-TOF.

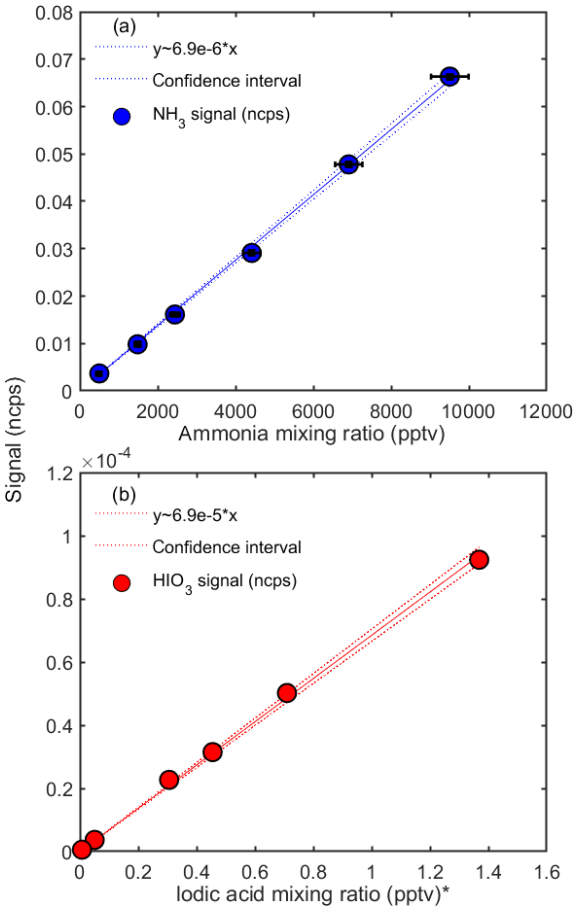

Figure 3. Calibration curves for ammonia **(a)** and iodic acid **(b)** at 40 % relative humidity. The y axes show the normalized counts per second (ncps) measured with the water cluster CI-APi-TOF. The ammonia mixing ratios are determined from the calibration setup, and the iodic acid mixing ratios are taken from simultaneous measurements with a nitrate CI-APi-TOF at the CLOUD chamber. The systematic uncertainty of the iodic acid mixing ratios is estimated as $+100\,\%/-50\,\%$ (Sipilä et al., 2016). The inverse slopes from the linear fits yield the calibration factors (see Eqs. 1 and 2). * Note that the iodic acid mixing ratio is derived by applying a calibration factor for sulfuric acid to the nitrate CI-APi-TOF data.

3.3 Response times

The response time of the water cluster CI-APi-TOF is defined as the characteristic time needed for the instrument to react to changes in the ammonia mixing ratio. We define the response time as the time required for the instrument to reach 95 % of the new mixing ratio being injected. The response time takes into account two processes. It includes both the response time of the instrument ("instrumental response time") and the time for the lines to reach a steady state for ammonia delivery ("line response time"). Figure 4 indicates the typical response times of the water cluster CI-APi-TOF during calibrations (here at 60 % relative humidity). It shows a decay between two calibration steps when the injected ammonia is

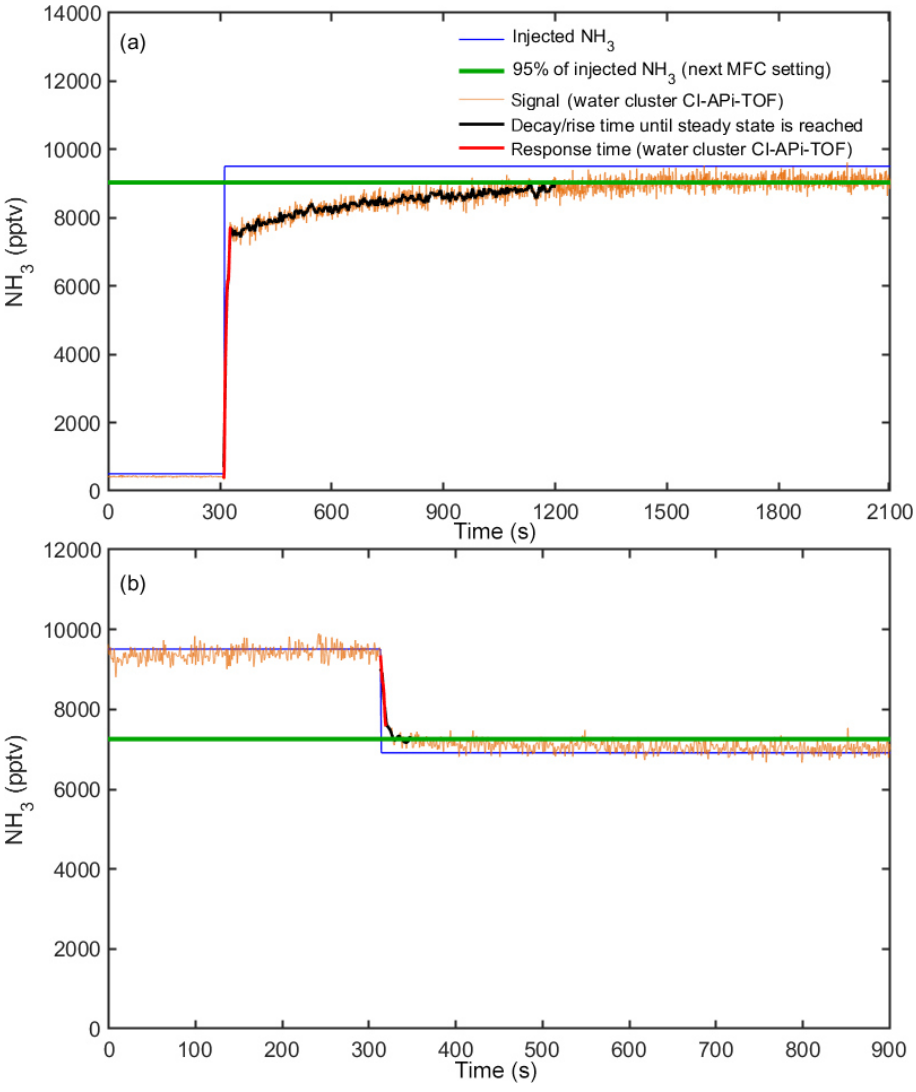

Figure 4. Response time of the water cluster CI-APi-TOF during calibrations at 60 % RH. The injected ammonia mixing ratio from MFC settings is shown by the blue line. The signal of the water cluster CI-APi-TOF is shown by the orange line (here the data are shown with a 1 s time resolution; i.e., no time averaging is applied). The green line represents 95 % of the mixing ratio being applied with the next MFC setting. The black line shows the response time until a steady state **(a)** or 95 % of the final measured concentration is reached **(b)**. The response time is the sum of the response time of the water cluster CI-APi-TOF (red line) and the (slower) response time for the lines to reach a steady state at which the walls are conditioned.

reduced from 9509 to 6911 pptv and a rise in the signal when the ammonia mixing ratio is increased from 500 to 9509 pptv. Panel (a) indicates a clear difference between the fast instrumental response time (red line) and slower line response time (black line). While we expect a similar behavior in instrumental response time for a decay from 9509 to 500 pptv, a longer line response time is expected due to reevaporation of ammonia from the sampling lines. Thus, the mixing ratios were gradually reduced during calibrations. The instrumental response time shown in Fig. 4 is 6 s for a decay in mixing ratio (9509 to 6911 pptv) and 18 s for a rise (500 to 9509 pptv). The line response time is 37 s (decay) and 890 s (rise). The experiments were repeated several times at varying relative humidities. The instrumental response time only varied by a few seconds during our experiments (between 6 and 10 s for decay and 18 to 25 s for a rise). While the variation in instrumental response time is small, the line response time can vary strongly depending on precursor conditions and relative humidity. During our experiments, the line response time varied between 37 and 54 s (decay) and between 535 and 890 s (rise). Interactions of ammonia with the sampling line are discussed in Sect. 3.8.

3.4 Influence of the humidity on the sensitivity

Figure 5 shows the sensitivity of the ammonia measurements to relative humidity. These data are derived from calibration curves similar to that in Fig. 3a. During the calibrations the humidity was changed by adjusting the dry and wet sample flow rates. For all conditions NH_4^+ has the highest product ion count rate. However, the ratio of the signals for $(H_2O)NH_4^+$ and NH_4^+ increases with humidity and sensitivity. A possible explanation for the observed sensitivity dependence could be increased collision rates at high humidity at which larger water clusters are present. In addition, the detection efficiency as a function of the ion mass can vary depending on the voltages applied to the ion source and the APi section, as well as the time-of-flight region of the mass spectrometer. Thus, the mass spectrometer does not have a constant detection efficiency over the full mass range (Heinritzi et al., 2016). A higher detection efficiency at m/z 36 ($(H_2O)NH_4^+$) compared with m/z 18 (NH_4^+), together with the higher fraction of $(H_2O)NH_4^+$ compared with NH_4^+, at high humidity could explain some of the observed effect. However, the observed increase in sensitivity is modest (increase by a factor of ~ 2.5 when the humidity increases by a factor of 10). Nevertheless, the effect is taken into account by using the measured relative humidity inside the CLOUD chamber (see Sect. 2.1) to correct the derived ammonia mixing ratio. The effect of temperature on the sensitivity could not be tested during a dedicated calibration experiment as our calibration setup was not temperature-controlled. However, during a transition from 298 to 248 K in the CLOUD chamber and constant ammonia injection, no significant change in the measured ammonia was observed, which indicates a weak influence of temperature.

For iodic acid measurements, the sensitivity to relative humidity and temperature is different (Fig. 6). While NH_4^+, without any water molecule, is the dominant signal for ammonia, the highest iodic acid signal is $H_4IO_4^+$, which is $H_2O \cdot HIO_3H^+$ or $HIO_3 \cdot H_3O^+$. We observed an increasing sensitivity at lower temperatures, while the humidity dependency appears to be smaller compared to the ammonia measurements (Fig. 5). The higher counting rate of $H_4IO_4^+$ compared to $H_2IO_3^+$ indicates that iodic acid requires additional water in order to be associated with a positively charged ion. However, during the transition from ambient pressure to the vacuum of the mass spectrometer, water molecules can evaporate and leave $H_2IO_3^+$ in a nonequilibrium state. Besides the observation of iodic acid, additional signals from iodine-containing species can be found in the spectra. These compounds are listed in Table 2. Elucidating the exact formation pathways of these ions and the corresponding neutral species is a subject for future work.

3.5 Detection limits and instrumental backgrounds

Determining the limit of detection (LOD) for ammonia is complicated by changes in the observed background signal. During the calibrations a relatively high background was measured, which decreased slowly after the ammonia flow through the capillary was shut off. A typical value reached a couple of minutes after the ammonia flow was turned off is $\sim$ 30–60 pptv. When the water cluster CI-APi-TOF was connected to the CLOUD chamber the NH_3 signals usually fell more rapidly when no ammonia was actively added. However, even under these conditions the ammonia was not zero and the measured signal changed when the RH or temperature of the chamber was adjusted, indicating the release of ammonia from the chamber walls. The ammonia contaminant level of the CLOUD chamber was previously determined to be several parts per trillion by volume at 278 K and 38 % RH (Kürten et al., 2016a). During CLOUD13 the measured ammonia background was 3.7 pptv at 278 K and 80 % RH, which confirms the previous estimate made with less sensitive ammonia instrumentation. The measured background also includes any contamination in the sampling line of the instrument. Another source of background ammonia could be the ion source. During the early stages of our development we used nitrogen instead of argon as the main ion source gas. This led to ammonia backgrounds of several hundred parts per trillion by volume since ammonia can be generated by the nitrogen plasma from the corona tip when it mixes with the humid sample flow (Haruyama et al., 2016). Replacing nitrogen with argon sharply decreased the background ammonia signals. Nevertheless, traces of nitrogen-containing gases in the ion source could potentially contribute to the ammonia background. However, the ammonia background is reduced at lower chamber temperatures, which argues against the ion source being a significant source of ammonia, since it is always at ambient temperature.

The LOD is defined as the additional ammonia mixing ratio that is necessary to exceed 3 standard deviations of the background fluctuations (You et al., 2014). This value corresponds to 0.5 pptv for an averaging time of 1 min. Assuming the same sensitivity as for ammonia and taking into account the background signals for the exact masses, we can estimate LODs for other compounds. Besides the calculated values for ammonia, Table 1 lists the estimated backgrounds and LODs for dimethylamine and iodic acid. High-resolution data are necessary to reach the LODs shown in Table 1 since several species may share the same integer mass. For example, for dimethylamine (exact mass of protonated compound at 46.0651 Th) other species like NO_2^+ (45.9924 Th) or CH_4NO^+ (46.0287 Th) can interfere. For dimethylamine only the peak with the highest count rate is taken into account, since $(C_2H_7N)H_3O^+$ interferes with other compounds measured during the experiments, even with high-resolution data. In principle, the omission of the larger product ions (with one additional water molecule) should lead to a dif-

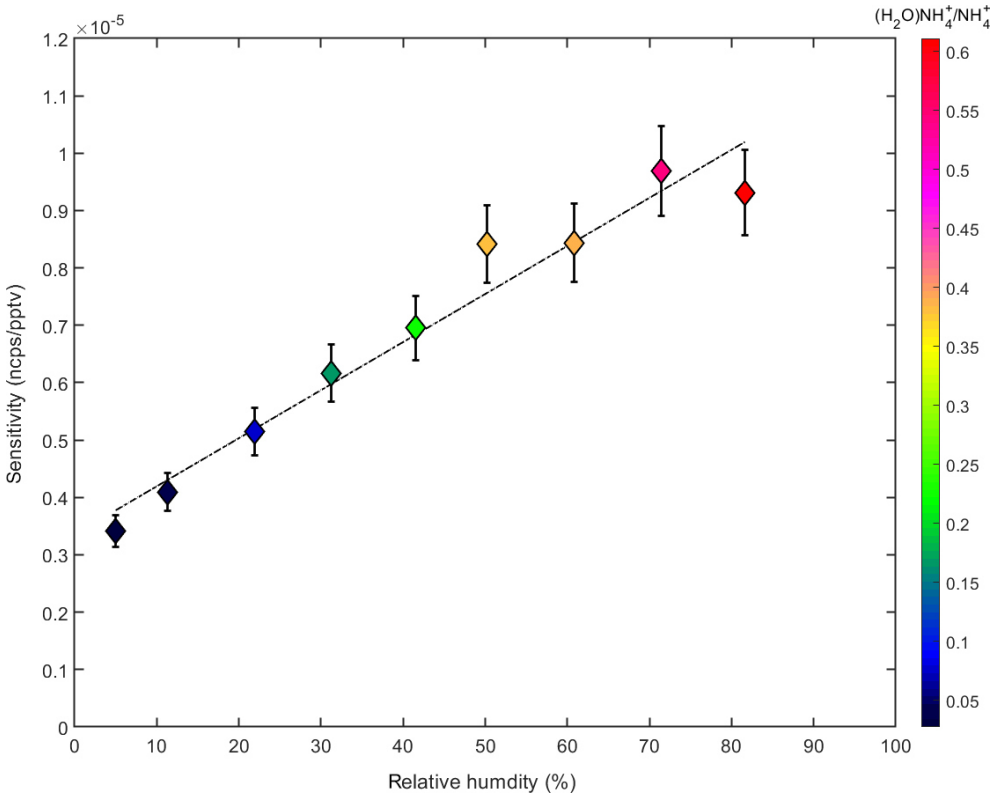

Figure 5. Dependency of the ammonia sensitivity as a function of the relative humidity (%). A linear increase with relative humidity is observed, which tracks an increase in the ratio of the $(H_2O)NH_4^+$ and NH_4^+ ion signals (indicated by the color code).

ferent calibration constant. However, the effect is small since for the measured bases, the ion signals with associated water are smaller than the products without the water molecule. The goodness of the assumption of using the same calibration constant for dimethylamine as that derived for ammonia is discussed in Sect. 3.9.

The instrumental background for NH_3 is higher than the estimated backgrounds for the other compounds shown in Table 1. Ammonia is ubiquitous and hard to remove completely by water purification systems, so it can be introduced into the CLOUD chamber via the air humidification system. Nevertheless, the detection limit derived for ammonia is well below the LOD reported for other measurement techniques and instruments (von Bobrutzki et al., 2010; You et al., 2014; Wang et al., 2015). However, the performance of the water cluster CI-APi-TOF during atmospheric measurements remains to be tested. The dimethylamine level in the CLOUD chamber is mostly below the estimated LOD.

The estimated LOD of iodic acid is well below that of ammonia and dimethylamine (Table 1). We might explain this when looking at signals that could possibly interfere with the measured compounds. All compounds shown in Table 1 have an integer mass at which other signals are also detected, e.g., H_2O^+ at the nominal mass of ammonia or NO_2^+ at the nominal mass of dimethylamine. For the high masses of the iodine-containing species, with their strong negative mass defects, these isobaric compounds are much less crucial. Additionally, iodic acid has a much lower vapor pressure compared with ammonia and is not emitted efficiently from surfaces at temperatures relevant for the present study. Therefore, much lower backgrounds can be expected even if the sampling line and the instrument were exposed to high concentrations before.

3.6 Iodine identified species during CLOUD13

The CI-APi-TOF measurements of HIO_3 with positive water cluster ionization show excellent correlation with negative nitrate ionization (Fig. 3b). Furthermore, we were able to detect iodine-containing species at higher mass-to-charge ratios (e.g., iodine pentoxides) during several experiments. Figure 7 shows the detected iodine species when a high I_2 concentration ($\sim$ 50–100 pptv) was injected into the chamber (mean values over a duration of 120 min). The derived mean iodic acid mixing ratio is $\sim$ 0.98 pptv according to the measurements of the water cluster CI-APi-TOF. During this experiment, we observed compounds containing up to four iodine atoms. The size of the circles in Fig. 7 corresponds to the mean count rate of the signals on a logarithmic scale. For comparison, the intensities of the reagent ions are also

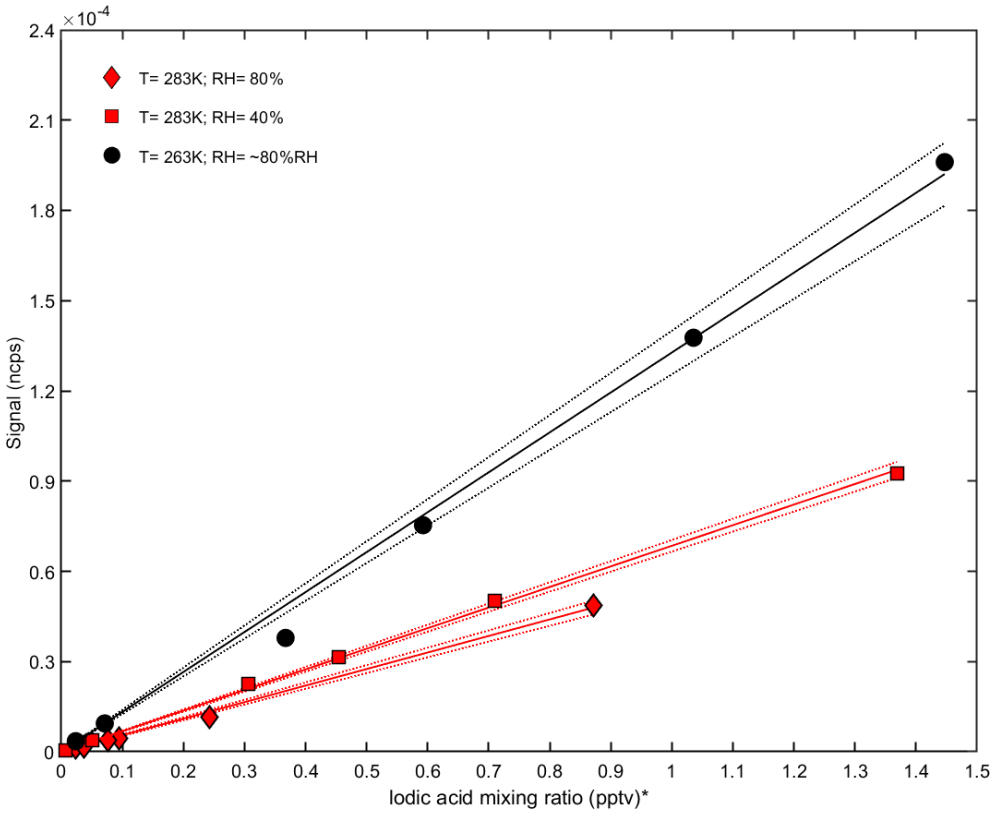

Figure 6. Calibration curves for iodic acid at different relative humidities and temperatures in the CLOUD chamber. The normalized counts per second (y axis) are shown against the iodic acid mixing ratio measured with a nitrate CI-APi-TOF (x axis). The sensitivity increases at lower temperatures (black line), while no strong dependency on relative humidity is found at 283 K (red line). * Note that the iodic acid mixing ratio is derived by applying a calibration factor for sulfuric acid to the nitrate CI-APi-TOF data.

shown. Table 2 lists the sum formulas of some identified iodine species.

During some experiments, an electric field of about 20 kV m^{-1} was applied to the chamber to remove ions and study purely neutral (i.e., uncharged) nucleation. Even during these experiments the same signals as shown in Fig. 7 were present. This indicates that the water cluster CI-APi-TOF measures neutral compounds after ionizing them in the ion–molecule reaction zone. The present study only gives a short overview of the iodine signals measured with the water cluster CI-APi-TOF. Further CLOUD publications will focus on the chemistry of the iodine-containing species and on their role in new particle formation processes.

3.7 CLOUD chamber characterization

The performance of the water cluster CI-APi-TOF during CLOUD12 experiments with ammonia is shown in Fig. 8. We compare the derived mixing ratios with the measurements of the PICARRO. In addition, both can be compared with the range of ammonia mixing ratios expected from the MFC settings for ammonia injected into the CLOUD chamber, the chamber volume and the ammonia lifetime (see, e.g., Simon et al., 2016, and Kürten et al., 2016a, for the equations linking these quantities to the estimated CLOUD mixing ratios). While the injected ammonia can be determined to better than 20 % from the MFC settings, the ammonia lifetime in the chamber can span a wide range. For a very clean chamber or at very low temperatures the chamber walls represent a perfect sink and the ammonia has a short lifetime. A wall loss lifetime of 100 s at 12 % fan speed was previously reported by Kürten et al. (2016a). Measurements with sulfuric acid indicate a factor of 4 increase in the wall loss rate when the fan speed is changed from the nominal setting of 12 % to 100 %. Scaling these measurements to the ammonia measurements yields a wall loss lifetime of 25 s at 100 % fan speed. On the other hand, once the walls have been exposed for sufficient time with ammonia they reach an equilibrium at which condensation and evaporation rates are equal. Under these conditions, the ammonia lifetime is determined by the chamber dilution lifetime alone (6000 s), so the NH_3 increases to higher equilibrium concentrations. Furthermore, the walls can act as a source of ammonia due to the reevaporation of ammonia molecules attached to the surface. This effect can be significant when the concentrations previously injected into the chamber were higher than the current con-

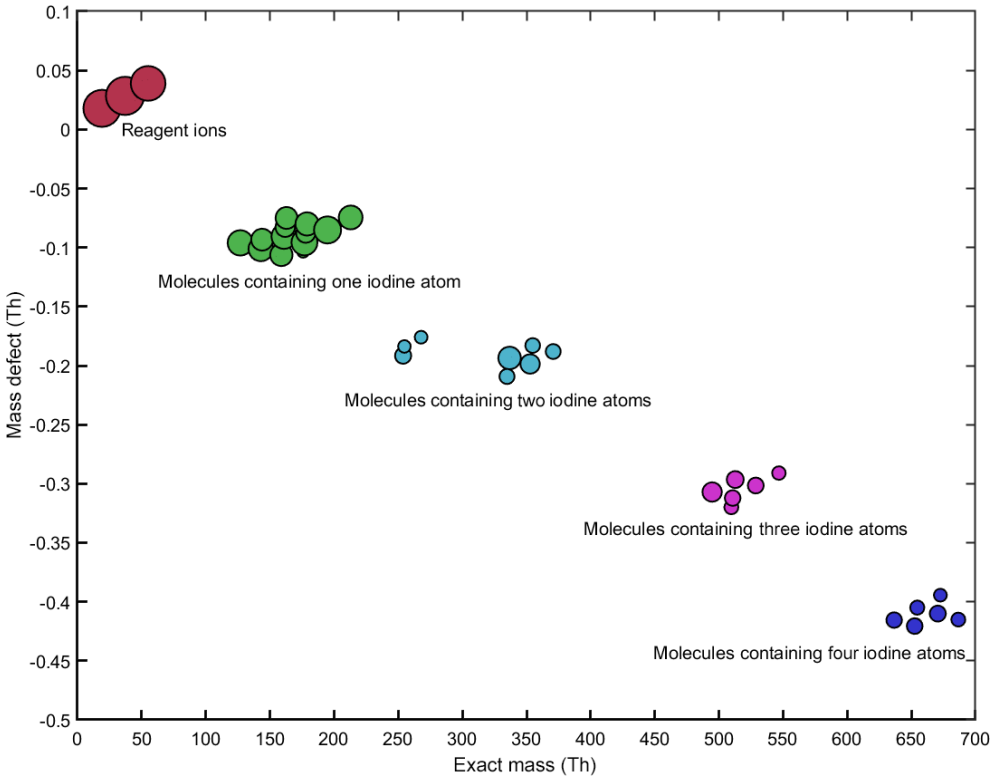

Figure 7. Mass defect plot for the iodine compounds, as well as the most prominent reagent ions, during a CLOUD experiment on new particle formation from iodine. The estimated iodic acid mixing ratio is ~ 0.98 pptv. The y axis shows the mass defects of the compounds (see Table 2 and the text for details), while the x axis shows the absolute masses. The size of the symbols is proportional to the measured signal intensities on a logarithmic scale (from 1.24×10^{-6} to 14.04 ions s^{-1}).

centrations. Thus, the estimated range can vary by a factor of ~ 200 based on the chamber conditions. This wide range is indicated by the shaded areas in Fig. 8 (light blue).

Figure 8a shows the measurements of the water cluster CI-APi-TOF, the PICARRO and the calculated values for ammonia. The PICARRO trace is shown for the time when the detection limit (170.1 pptv during CLOUD12) is exceeded. The signal measured by the water cluster CI-APi-TOF follows the injected ammonia almost instantaneously (the first injection is on 23 October). The slower response time of the PICARRO can be explained by a combination of the longer sampling line (~ 1.8 m compared to 1.3 m for the water cluster CI-APi-TOF) and the lower flow rate (~ 1 slm with a core sampling of 5 slm compared with ~ 20 slm for the water cluster CI-APi-TOF). After the flow of ammonia is shut off, both the mass spectrometer and the PICARRO show almost identical values as the chamber progressively releases ammonia from the walls. Before the first ammonia injection it can also be seen that the water cluster CI-APi-TOF shows progressively lower background ammonia values. Whether this is due to a gradual cleaning of the chamber, the instrument or the sampling line is unclear. Figure 8a also indicates the influence of temperature on the level of contaminant after ammonia had been injected into the chamber. When the chamber temperature falls from 298 to 278 K (shortly before 31 October) the contaminant NH_3 decreases by around a factor of 5 due to the lower evaporation rate of ammonia from the chamber walls.

The influence of changing relative humidity can be seen in Fig. 8 between 29 and 30 October. Part of the change is due to the response of the water cluster CI-APi-TOF (Sect. 3.4). A second contribution arises since water molecules can displace adsorbed ammonia on surfaces (Vaittinen et al., 2014). This effect can be pronounced when the chamber walls have been conditioned with high ammonia concentrations. It is important to note that the instrument was characterized for humidity dependency during the following CLOUD13 campaign. While changes in sensitivity with relative humidity were taken into account during CLOUD13, this was not the case during CLOUD12. The observed increase in mixing ratios at this time is a combination of a change in sensitivity of the instrument and an increase in the gas-phase concentration of ammonia due to reevaporation from the walls of the CLOUD chamber. Here, the PICARRO trace can provide insight into the magnitude of both effects, indicating that the reevaporation from the chamber walls dominates over the change in sensitivity. In Fig. 8 during the early part of 25 October the PICARRO shows a steep increase in am-

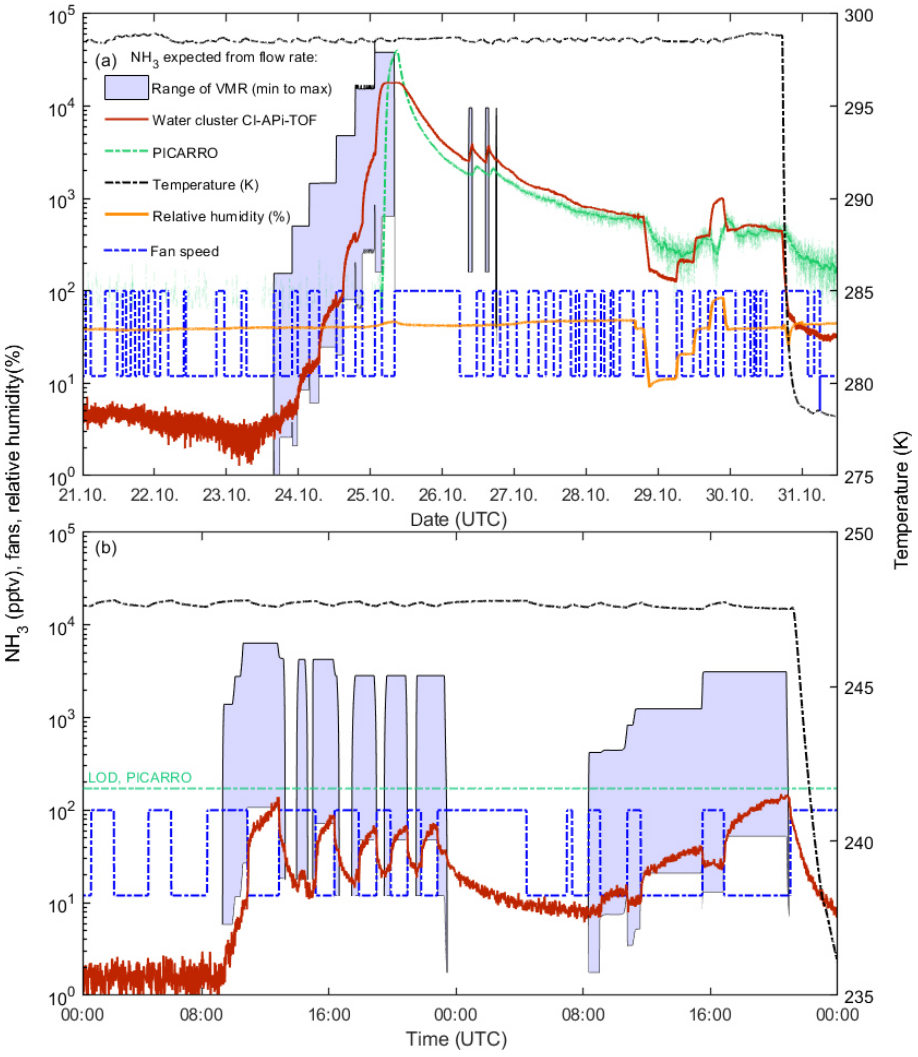

Figure 8. Intercomparison between calculated (shaded blue area) and measured ammonia mixing ratios (PICARRO: solid green line; water cluster CI-APi-TOF: solid red line) at CLOUD. The PICARRO background (∼ 200 pptv) has been subtracted, while no background was subtracted from the water cluster CI-APi-TOF. The temperature inside the chamber is indicated by the dashed black line. The speed (percent of maximum, 397 revolutions per minute) of the two fans that mix the air inside the chamber is shown by the dashed blue line. The calculated ammonia mixing ratios (based on the calculated injection of ammonia into the chamber from the MFC settings) have a wide range due to uncertainties of the ammonia loss rate in the chamber. We display the maximum calculated range assuming, for the lower limit, that the chamber walls act as a perfect sink (wall loss dominated; 25 and 100 s lifetime for fan speeds of 100 % and 12 %, respectively) and, for the upper limit, no net uptake of NH_3 on the walls and a loss rate determined by dilution (6000 s lifetime). For higher fan speeds, the lifetime decreases due to increased turbulence and, in turn, increased wall loss rate. Relative humidity is indicated by the orange line. The water cluster CI-APi-TOF reacts rapidly to changing conditions, such as the ammonia flow into the chamber, relative humidity, temperature or fan speed. At low concentrations, the ammonia lifetime is determined by the wall loss rate (panel **b** and initial stages of panel **a**). However, at high ammonia concentrations, the walls of the CLOUD chamber progressively become conditioned as a source of ammonia, with corresponding increases in the ammonia lifetime and the time to reach new equilibria at lower ammonia flow rates (later stages of panel **a**).

monia, while the water cluster CI-APi-TOF saturates near 20 ppbv due to depletion of the primary ions. It is important to note that other vapor concentrations were also high at this time, which contributed to the depletion of the primary ions. During CLOUD13, wherein an improved version of the ion source was used (Sect. 3.2), significant depletion of primary ions was only observed above 40 ppbv of ammonia.

Figure 8b shows how the ammonia mixing ratios vary with the mixing fan speed in the CLOUD chamber. The fan speed was varied between 12 % (default value) and 100 %. Since the temperature during these experiments was low (248 K), the chamber walls act as a fairly efficient sink for ammonia. Therefore, the measured mixing ratios respond promptly to the changing fan speed, indicating a change of almost a fac-

tor of 4 in ammonia. Moreover, the measurements coincide with the values calculated from the MFC settings, assuming wall loss lifetimes of 100 and 25 s at 12 % and 100 % fan speed, respectively. Due to its higher detection limit, the PICARRO is insensitive at these low mixing ratios (green line in Fig. 8b).

3.8 Ammonia wall loss rates in the sampling line

The largest uncertainty in the ammonia measurement is related to the sampling line losses. At CLOUD, the stainless-steel sampling lines have an inner diameter of 0.5″ or 1″ and 0.75 m total length (a 1″ sampling probe was used for the water cluster CI-APi-TOF, and the instrument has a sampling line of 0.55 m total length). The tips are located 0.35 m from the chamber walls to avoid sampling air from the boundary layer. Thus, after connecting to the CLOUD chamber, the total length of the sampling line of our instrument is 1.3 m. For an ammonia diffusivity of 0.1978 $cm^2\ s^{-1}$ (Massman, 1998) and a sample flow rate of 20 slm, the sample line penetration efficiency is estimated to be 33.7 % for a laminar flow (Dunlop and Bignell, 1997; Baron and Willeke, 2001; Yokelson, 2003). This means that if the walls of the sampling line act as a perfect sink, then the measured NH_3 mixing ratios would need to be corrected with a factor of ~ 3. However, it is quite likely that the sampling line does not always act as a perfect sink for ammonia due to partial reevaporation. Furthermore, interactions of ammonia with the inner walls of the sampling line depend on the humidity of the sampled air. Water on surfaces can affect the uptake or release of ammonia. Vaittinen et al. (2014) showed that increased humidity can displace ammonia from surfaces. Additionally, water on surfaces can allow weak acids and bases to dissociate into their conjugate compounds on the surface, thereby affecting the partitioning to the surface (Coluccia et al., 1987). Vaittinen et al. (2014) studied the adsorption of ammonia on various surfaces and found a value of 1.38×10^{14} molecule cm^{-2} for the surface coverage on stainless steel. For humid conditions this value is, however, significantly smaller and decreases to $\sim 5 \times 10^{12}\ cm^{-2}$ for a water vapor mixing ratio of 3500 ppmv at 278 K. Eventually an equilibrium is reached between the condensation on and evaporation from the walls, depending on the ammonia mixing ratio, RH and temperature. At equilibrium, ammonia losses from the chamber are due to dilution alone, and ammonia losses in the sampling line are negligible. Furthermore, ammonia may reevaporate from the inlet line walls if saturation happened previously at higher concentrations. At CLOUD, the sampling lines are attached to the chamber and cannot easily be removed during the experiments. Thus, it is not possible to quantitatively distinguish between interactions with the surface of the sampling line and the surface of the CLOUD chamber. This complicates the evaluation of the influence of the sampling line regarding the measured ammonia. One practical solution would be to report averages of the values considering the wall loss correction factor and neglecting the factor.

Sampling line losses introduce up to a factor of 3 uncertainty in the ammonia measurement, corresponding to transmission efficiencies between 33.7 % and 100 % for walls that are a perfect sink and zero sink, respectively. Variable sampling efficiency is a general problem encountered for most ammonia measurements (e.g., Leifer et al., 2017). The uncertainty is smaller for larger molecules; e.g., the sampling efficiency for triethylamine (diffusivity of 0.067 $cm^2\ s^{-1}$; Tang et al., 2015) is 61 %. For atmospheric measurements, we suggest using an inlet system in which a short piece of the 1″ sampling line only takes the core sample flow from a large-diameter inlet. A blower can generate a fast flow in the large inlet to essentially reduce the losses for the core flow to zero before it enters the actual sampling line (Berresheim et al., 2000).

3.9 Measurement of dimethylamine

The same calibration factor as derived for ammonia was used to determine the mixing ratio of dimethylamine (Sect. 3.5 and Table 1). This assumption can lead to uncertainties as the sensitivity of the instrument is expected to depend on the proton affinity of the measured substance (Hanson et al., 2011). To estimate the validity of this assumption, we compared the mixing ratios measured by the water cluster CI-APi-TOF with the calculated mixing ratios for a period when dimethylamine was actively injected into the CLOUD chamber. A chamber characterization for dimethylamine was already conducted by Simon et al. (2016), wherein the wall loss lifetime was determined as 432 s for conditions in which the chamber walls acted as a perfect sink (12 % fan speed). Additionally, as discussed in Sect. 3.7, we use a lifetime of 108 s at 100 % fan speed (change of a factor of 4 when the fan speed is changed from 12 % to 100 %). The chamber dilution lifetime represents the maximum possible lifetime when wall loss would be negligible (Sect. 3.7). Thus, the wall loss lifetime used in this study gives a lower limit for dimethylamine mixing ratios in the CLOUD chamber. Figure 9a shows a period when dimethylamine was added to the chamber. Since it takes a certain time until the stainless-steel pipes of the gas dilution system are saturated with dimethylamine there is a short time delay between the switching of a valve that allows dimethylamine to enter the chamber and the rise in the measured dimethylamine mixing ratio. Once the lines are conditioned and the dimethylamine is homogenously mixed into the chamber, the measured and estimated mixing ratios are generally in good agreement with each other. The response to changes in fan speed is initially sharp but gradually weakens as the walls progressively adsorb more dimethylamine. To estimate the consistency of the approach of scaling the calibration factor derived for ammonia to estimate dimethylamine mixing ratios, we use the ratio between the mixing ratio calculated for the water cluster CI-

APi-TOF and the calculated mixing ratios based on the wall loss lifetime for the CLOUD chamber. For these measurements, we estimated a wall loss rate in the sampling lines of ~ 1.96 for dimethylamine, and a diffusivity of $0.1\,\mathrm{cm^2\,s^{-1}}$ was used (Freshour et al., 2014; Simon et al., 2016). The mean deviation between the estimated dimethylamine mixing ratio and the calculated mixing ratio is 3.48, indicating that the approach of scaling the calibration factor derived for ammonia introduces uncertainties within a factor of ~ 3.5. The deviations at the end of the time series shown in Fig. 9a are caused by nucleation experiments in which high concentrations of other vapors are used. During these stages a significant uptake of dimethylamine on particles can explain the discrepancy between measured and expected dimethylamine. Figure 9b shows a measurement of the background dimethylamine in the chamber, measured over 5 d during CLOUD13. The mean background is ~ 0.14 pptv at 50 % RH to 60 % RH and temperatures of 278 to 290 K. These are similar to the backgrounds measured at 80 % RH and 278 K (Table 1). The observed variations are in a range of ~ 0.1 to 0.3 pptv provided that the measurement is not interrupted, e.g., due to the replenishment of the water source that humidifies the flow for generating the reagent ions (which explains the first drop of the background measurement in Fig. 9b). The estimated detection limits shown here are below or at similar levels compared to those reported in previous publications (You et al., 2014; Simon et al., 2016).

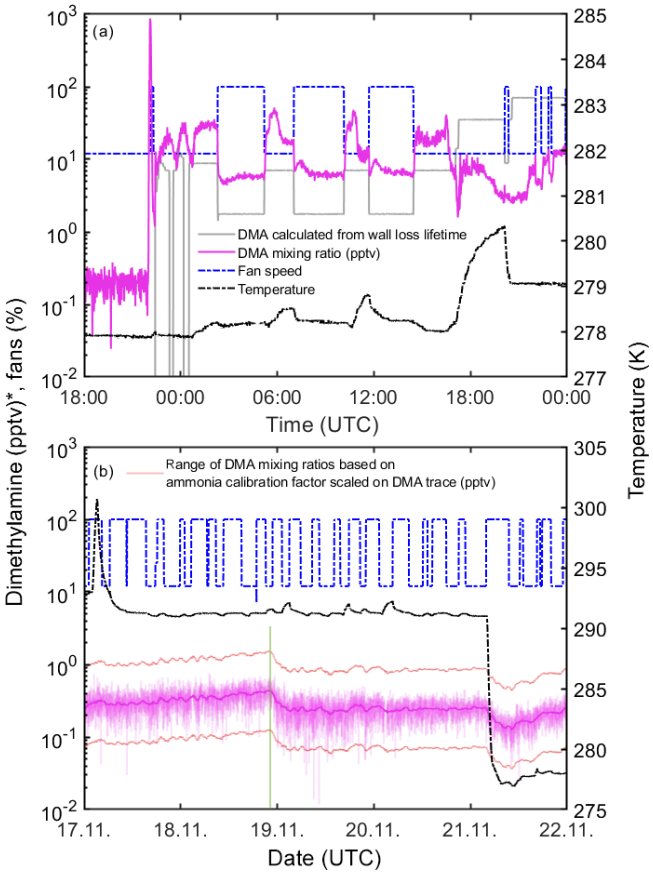

Figure 9. Dimethylamine mixing ratios (magenta line) during the CLOUD13 experiment. The dashed black line shows the temperature inside the CLOUD chamber. The dashed blue line shows the fan speed. Panel **(a)** shows the dimethylamine signal during active injection into the chamber. The grey line indicates the dimethylamine mixing ratio in the chamber calculated from the MFC settings and the wall loss lifetime. The upper limit for the uncertainty in the dimethylamine mixing ratio is a factor of ~ 3.5 (see the text for details). Panel **(b)** shows a measurement of background dimethylamine in the chamber over a period of 5 d, when there was zero dimethylamine flow. We consider this to be due to instrumental background and not to an actual dimethylamine background in the chamber. The thin red lines show the possible range of dimethylamine based on the scaled calibration factor (factor of 3.48, 95 % CI). The thick magenta line indicates a moving average of the dimethylamine background measurement. The water source was replenished during the period shown (green line). The mean instrumental background of dimethylamine over this period is ~ 0.14 pptv. * Note that the dimethylamine mixing ratio is determined with the calibration factor for ammonia.

4 Discussion and application to ambient measurements

The present study demonstrates the successful application of a water cluster CI-APi-TOF during controlled chamber experiments to measure ammonia, dimethylamine and iodic acid. During experiments involving iodide, neutral clusters containing up to four iodine atoms were detected. The instrument has demonstrated unrivalled low detection limits for ammonia, as well as a fast time response and time resolution. We believe this instrument can readily be applied to atmospheric measurements. The amount of clean gas required for the corona tip (2 slm of argon and some oxygen) is rather small and can easily be supplied with gas bottles (one argon gas bottle of 50 L at 200 bar should last about 3 d). At CLOUD there is a restriction regarding the maximum sample flow that can be drawn from the chamber. During atmospheric measurements much higher flow rates can easily be realized. Therefore, the suggested design of the inlet system using a blower and a core sample inlet should be used (Sect. 3.8). Furthermore, the use of an internal calibration standard would be beneficial. We have tried to add a defined mixing ratio of ND_3 to the sample flow. However, besides the expected signal at (ND_3H^+, m/z 21) further signals corresponding to NH_4^+, NDH_3+ and $ND_2H_2^+$ were also present due to deuterium–hydrogen exchange, which makes this method unsuitable. The use of $^{15}NH_3$ for calibration is also unsuitable since the $^{15}NH_4^+$ signal is hard to distinguish from the comparatively high H_3O^+ signal at the same integer mass even for a high-resolution mass spectrometer.

Roscioli et al. (2016) demonstrated that the addition of 1H,1H-perfluorooctylamine to the sample flow can be used to passivate an inlet, which reduces sampling line losses

and sharpens the time response for ammonia measurements. Recently, Pollack et al. (2019) implemented this passivation technique for ambient measurements on an aircraft. For these measurements, a tunable infrared laser was used (TILDAS-CS, Aerodyne Inc.). We tested this passivation technique but found it unsuitable for our instrument; the high mixing ratio of 1H,1H-perfluorooctylamine (~ 100 ppm to 0.1 % injection into the sample flow) that is required led to excessive consumption of the reagent ions since 1H,1H-perfluorooctylamine has a high proton affinity and is therefore also efficiently ionized by the protonated water clusters. For this reason, the passivation technique for the measurement of ammonia can in our opinion only be used with spectroscopic techniques as was the case in the studies by Rosciolli et al. (2016) and Pollack et al. (2019).

5 Summary and conclusion

We have described the design and performance of a novel water cluster chemical ionization–atmospheric pressure interface time-of-flight mass spectrometer (CI-APi-TOF) for measurements of ammonia, amines (dimethylamine) and iodine compounds. The instrument includes a new home-built cross-flow ion source operated at atmospheric pressure. The protonated water clusters ($(H_2O)_{n\geq 1}H_3O^+$) selectively ionize compounds of high proton affinity at short reaction times. The instrument's response is linear up to a mixing ratio of at least 10 ppbv for ammonia when the derived calibration factor is applied to the normalized counts per second. The water cluster CI-APi-TOF was operated at the CLOUD chamber where very low background ammonia mixing ratios were measured (ca. 4 pptv at 278 K). The limit of detection (LOD) was estimated as 0.5 pptv for NH_3. To our knowledge, such a low detection limit for ammonia measurements is unprecedented. We attribute the low LOD mainly to the use of ultraclean argon (5.0 purity) as the main ion source gas for the reagent ion generation. Much higher background NH_3 was observed when nitrogen was used instead of argon. The instrument shows some sensitivity to the relative humidity of the sample flow (factor of 3 increase in the signal from 5 % to 80 % RH). However, this can readily be measured and corrected. We did not explicitly demonstrate the quantitative measurement of diamines (and amines other than dimethylamine) in the present study but the instrument should also be well-suited for such measurements.

During experiments involving iodine, it was observed that the protonated water clusters can also be used to detect various iodine compounds. A total of 29 different iodine-containing compounds were identified, including iodic acid (HIO_3) and neutral clusters containing up to four iodine atoms. The water cluster CI-APi-TOF was cross-calibrated against a nitrate CI-APi-TOF measuring iodic acid. The two instruments showed exactly the same time-dependent trends. As there is no established calibration method for iodic acid, detection limits have been derived under the assumption that HIO_3 is measured with the same efficiency as sulfuric acid, for which the nitrate CI-APi-TOF was calibrated. In this way, we estimated the LOD for iodic acid in the water cluster CI-APi-TOF to be 0.007 pptv.

Future studies will focus on the evaluation of the iodine signals and also on further signal identification in the mass spectra. Laboratory and ambient measurements indicate the increased importance of ammonia for new particle formation and growth in both pristine and polluted environments. Due to the instrument characteristics, we plan to apply the method to ambient atmospheric measurements to study the influence of ammonia, amines, diamines and iodic acid on new particle formation.

The water cluster CI-APi-TOF technique is also well-suited for airborne measurements in the upper troposphere, where fast response times and low detection limits are vital (Höpfner et al., 2016).

Data availability. Data for Figs. 2–9 and for Table 1 are available at https://doi.org/10.5281/zenodo.3831469 (Pfeifer et al., 2020). Further data are available upon request.

Author contributions. All authors contributed to the scientific discussion and interpretation of the results. JP, AK, LW and FP contributed to the design of the ion source presented in this study. JP, AK, MS, MH, MG, TM and SB collected the data at the CLOUD chamber. DW installed and operated the PICARRO unit used at the CLOUD chamber. AK and JC led the composition of the paper. JK contributed to the scientific discussion and interpretation of the results.

Competing interests. The authors declare that they have no conflict of interest.

Special issue statement. This article is part of the special issue "The CERN CLOUD experiment (ACP/AMT inter-journal SI)". It is not associated with a conference.

Acknowledgements. We would like to thank CERN for the support of CLOUD with financial and technical resources. We thank the PS/SPS team from CERN for providing the CLOUD experiment with a particle beam from the proton synchroton. We also want to thank Louis-Philippe De Menezes for providing us with a mass flow controller used during the calibrations. In addition to this, we would like to thank Robert Sitals, Timo Keber, Serge Mathot, Hanna Elina Manninen, Antti Onnela, Stefan Karl Weber and Robert Kristic for their contributions to the experiment. The discussion with Xucheng He during the creation of the paper is gratefully acknowledged. We thank Christoph Hüglin for providing us with the PIARRCO and its calibration unit. This work was funded by the German Federal Ministry of Education and Research under

CLOUD-16 (no. 01LK1601A), EC Horizon 2020 MSCA-ITN under CLOUD-MOTION (no. 764991), and the EC Seventh Framework Programme MC-ITN under CLOUD-TRAIN (no. 316662).

Financial support. This research has been supported by CLOUD-MOTION (grant no. 764991), CLOUD-16 (grant no. 01LK1601A), and CLOUD-TRAIN (grant no. 316662).

Review statement. This paper was edited by Jonathan Abbatt and reviewed by two anonymous referees.

References

Aljawhary, D., Lee, A. K. Y., and Abbatt, J. P. D.: High-resolution chemical ionization mass spectrometry (ToF-CIMS): application to study SOA composition and processing, Atmos. Meas. Tech., 6, 3211–3224, https://doi.org/10.5194/amt-6-3211-2013, 2013.

Almeida, J., Schobesberger, S., Kürten, A., Ortega, I. K., Kupiainen-Määttä, O., Praplan, A. P., Adamov, A., Amorim, A., Bianchi, F., Breitenlechner, M., David, A., Dommen, J., Donahue, N. M., Downard, A., Dunne, E., Duplissy, J., Ehrhart, S., Flagan, R. C., Franchin, A., Guida, R., Hakala, J., Hansel, A., Heinritzi, M., Henschel, H., Jokinen, T., Junninen, H., Kajos, M., Kangasluoma, J., Keskinen, H., Kupc, A., Kurtén, T., Kvashin, A. N., Laaksonen, A., Lehtipalo, K., Leiminger, M., Leppä, J., Loukonen, V., Makhmutov, V., Mathot, S., McGrath, M. J., Nieminen, T., Olenius, T., Onnela, A., Petäjä, T., Riccobono, F., Riipinen, I., Rissanen, M., Rondo, L., Ruuskanen, T., Santos, F. D., Sarnela, N., Schallhart, S., Schnitzhofer, R., Seinfeld, J. H., Simon, M., Sipilä, M., Stozhkov, Y., Stratmann, F., Tomé, A., Tröstl, J., Tsagkogeorgas, G., Vaattovaara, P., Viisanen, Y., Virtanen, A., Vrtala, A., Wagner, P. E., Weingartner, E., Wex, H., Williamson, C., Wimmer, D., Ye, P., Yli-Juuti, T., Carslaw, K. S., Kulmala, M., Curtius, J., Baltensperger, U., Worsnop, D. R., Vehkamäki, H., and Kirkby, J.: Molecular understanding of sulphuric acid-amine particle nucleation in the atmosphere, Nature, 502, 359–363, https://doi.org/10.1038/nature12663, 2013.

Baron, P. A. and Willeke, K.: Aerosol measurement: Principles, techniques, and applications, 2nd ed., Wiley, New York, xxiii, 1131, 2001.

Bell, C. L., Dhib, M., Hancock, G., Ritchie, G. A. D., van Helden, J. H., and van Leeuwen, N. J.: Cavity enhanced absorption spectroscopy measurements of pressure-induced broadening and shift coefficients in the υ 1+υ 3 combination band of ammonia, Appl. Phys. B, 94, 327–336, https://doi.org/10.1007/s00340-008-3238-5, 2009.

Benson, D. R., Markovich, A., Al-Refai, M., and Lee, S.-H.: A Chemical Ionization Mass Spectrometer for ambient measurements of Ammonia, Atmos. Meas. Tech., 3, 1075–1087, https://doi.org/10.5194/amt-3-1075-2010, 2010.

Berresheim, H., Elste, T., Plass-Dülmer, C., Eiseleb, F. L., and Tannerb, D. J.: Chemical ionization mass spectrometer for long-term measurements of atmospheric OH and H_2SO_4, Int. J. Mass Spectrom., 202, 91–109, https://doi.org/10.1016/S1387-3806(00)00233-5, 2000.

Bianchi, F., Dommen, J., Mathot, S., and Baltensperger, U.: Online determination of ammonia at low pptv mixing ratios in the CLOUD chamber, Atmos. Meas. Tech., 5, 1719–1725, https://doi.org/10.5194/amt-5-1719-2012, 2012.

Bianchi, F., Tröstl, J., Junninen, H., Frege, C., Henne, S., Hoyle, C. R., Molteni, U., Herrmann, E., Adamov, A., Bukowiecki, N., Chen, X., Duplissy, J., Gysel, M., Hutterli, M., Kangasluoma, J., Kontkanen, J., Kürten, A., Manninen, H. E., Münch, S., Peräkylä, O., Petäjä, T., Rondo, L., Williamson, C., Weingartner, E., Curtius, J., Worsnop, D. R., Kulmala, M., Dommen, J., and Baltensperger, U.: New particle formation in the free troposphere: A question of chemistry and timing, Science, 352, 1109–1112, https://doi.org/10.1126/science.aad5456, 2016.

Coluccia, S., Lavagnino, S., and Marchese, L.: Adsorption and dissociation of Ammonia on the hydroxylated surface of magnesium oxide powders, J. Chem. Soc., Faraday Trans. 1, 83, 477–486, https://doi.org/10.1039/F19878300477, 1987.

Cubison, M. J. and Jimenez, J. L.: Statistical precision of the intensities retrieved from constrained fitting of overlapping peaks in high-resolution mass spectra, Atmos. Meas. Tech., 8, 2333–2345, https://doi.org/10.5194/amt-8-2333-2015, 2015.

Dias, A., Ehrhart, S., Vogel, A., Williamson, C., Almeida, J., Kirkby, J., Mathot, S., Mumford, S., and Onnela, A.: Temperature uniformity in the CERN CLOUD chamber, Atmos. Meas. Tech., 10, 5075–5088, https://doi.org/10.5194/amt-10-5075-2017, 2017.

Dunlop, P. J. and Bignell, C. M.: Prediction of the temperature dependence of binary diffusion coefficients of gaseous systems from thermal diffusion factors and diffusion coefficients at 300 K, Int. J. Thermophys., 18, 939–945, https://doi.org/10.1007/BF02575239, 1997.

Dunne, E. M., Gordon, H., Kürten, A., Almeida, J., Duplissy, J., Williamson, C., Ortega, I. K., Pringle, K. J., Adamov, A., Baltensperger, U., Barmet, P., Benduhn, F., Bianchi, F., Breitenlechner, M., Clarke, A., Curtius, J., Dommen, J., Donahue, N. M., Ehrhart, S., Flagan, R. C., Franchin, A., Guida, R., Hakala, J., Hansel, A., Heinritzi, M., Jokinen, T., Kangasluoma, J., Kirkby, J., Kulmala, M., Kupc, A., Lawler, M. J., Lehtipalo, K., Makhmutov, V., Mann, G., Mathot, S., Merikanto, J., Miettinen, P., Nenes, A., Onnela, A., Rap, A., Reddington, C. L. S., Riccobono, F., Richards, N. A. D., Rissanen, M. P., Rondo, L., Sarnela, N., Schobesberger, S., Sengupta, K., Simon, M., Sipilä, M., Smith, J. N., Stozkhov, Y., Tomé, A., Tröstl, J., Wagner, P. E., Wimmer, D., Winkler, P. M., Worsnop, D. R., and Carslaw, K. S.: Global atmospheric particle formation from CERN CLOUD measurements, Science, 354, 1119–1124, https://doi.org/10.1126/science.aaf2649, 2016.

Duplissy, J., Merikanto, J., Franchin, A., Tsagkogeorgas, G., Kangasluoma, J., Wimmer, D., Vuollekoski, H.,Schobesberger, S., Lehtipalo, K., Flagan, R. C., Brus, D., Donahue, N. M., Vehkamäki, H., Almeida, J., Amorim, A., Barmet, P., Bianchi, F., Breitenlechner, M., Dunne, E. M., Guida, R., Henschel, H., Junninen, H., Kirkby, J., Kürten, A., Kupc, A., Määttänen, A., Makhmutov, V., Mathot, S., Nieminen, T., Onnela, A., Praplan, A. P., Riccobono, F., Rondo, L., Steiner, G., Tome, A., Walther, H., Baltensperger, U., Carslaw, K. S., Dommen, J., Hansel, A., Petäjä, T., Sipilä, M., Stratmann, F., Vrtala, A., Wagner, P. E., Worsnop, D. R, Curtius, J., and Kulmala, M.: Effect of ions on sulfuric acid-water binary particle formation: 2. Ex-

perimental data and comparison with QC-normalized classical nucleation theory, J. Geophys. Res.-Atmos., 121, 1752–1775, https://doi.org/10.1002/2015JD023539, 2016.

Ehn, M., Thornton, J. A., Kleist, E., Sipilä, M., Junninen, H., Pullinen, I., Springer, M., Rubach, F., Tillmann, R., Lee, B., Lopez-Hilfiker, F., Andres, S., Acir, I.-H., Rissanen, M., Jokinen, T., Schobesberger, S., Kangasluoma, J., Kontkanen, J., Nieminen, T., Kurtén, T., Nielsen, L. B., Jørgensen, S., Kjaergaard, H. G., Canagaratna, M., Maso, M. D., Berndt, T., Petäjä, T., Wahner, A., Kerminen, V.-M., Kulmala, M., Worsnop, D. R., Wildt, J., and Mentel, T. F.: A large source of low-volatility secondary organic aerosol, Nature, 506, 476–479, https://doi.org/10.1038/nature13032, 2014.

Eisele, F. L. and Hanson, D. R.: First Measurement of Prenucleation Molecular Clusters, J. Phys. Chem. A, 104, 830–836, https://doi.org/10.1021/jp9930651, 2000.

Eisele, F. L. and Tanner, D. J.: Measurement of the gas phase concentration of H_2SO_4 and methane sulfonic acid and estimates of H_2SO_4 production and loss in the atmosphere, J. Geophys. Res.-Atmos., 98, 9001–9010, https://doi.org/10.1029/93JD00031, 1993.

Ellis, R. A., Murphy, J. G., Pattey, E., van Haarlem, R., O'Brien, J. M., and Herndon, S. C.: Characterizing a Quantum Cascade Tunable Infrared Laser Differential Absorption Spectrometer (QC-TILDAS) for measurements of atmospheric ammonia, Atmos. Meas. Tech., 3, 397–406, https://doi.org/10.5194/amt-3-397-2010, 2010.

Elm, J., Passananti, M., Kurtén, T., and Vehkamäki, H.: Diamines Can Initiate New Particle Formation in the Atmosphere, J. Phys. Chem. A, 121, 6155–6164, https://doi.org/10.1021/acs.jpca.7b05658, 2017.

Freshour, N. A., Carlson, K. K., Melka, Y. A., Hinz, S., Panta, B., and Hanson, D. R.: Amine permeation sources characterized with acid neutralization and sensitivities of an amine mass spectrometer, Atmos. Meas. Tech., 7, 3611–3621, https://doi.org/10.5194/amt-7-3611-2014, 2014.

Ge, X., Wexler, S., and Clegg, S. L.: Atmospheric amines-Part I. A review, Atmos. Environ., 45, 524–546, https://doi.org/10.1016/j.atmosenv.2010.10.012, 2011.

Good, A., Durden, D. A., and Kebarle, P.: Mechanism and Rate Constants of Ion–Molecule Reactions Leading to Formation of $H + (H_2O)$ n in Moist Oxygen and Air, J. Chem. Phys., 52, 222–229, https://doi.org/10.1063/1.1672668, 1970.

Hansel, A., Scholz, W., Mentler, B., Fischer, L., and Berndt, T.: Detection of RO_2 radicals and other products from cyclohexene ozonolysis with NH_4^+ and acetate chemical ionization mass spectrometry, Atmos. Environ., 186, 248–255, https://doi.org/10.1016/j.atmosenv.2018.04.023, 2018.

Hanson, D. R., McMurry, P. H., Jiang, J., Tanner, D., and Huey, L. G.: Ambient pressure proton transfer mass spectrometry: detection of amines and ammonia, Environ. Sci. Technol., 45, 8881–8888, https://doi.org/10.1021/es201819a, 2011.

Haruyama, T., Namise, T., Shimoshimizu, N., Uemura, S., Takatsuji, Y., Hino, M., Yamasaki, R., Kamachi, T., and Kohno, M.: Non-catalyzed one-step synthesis of ammonia from atmospheric air and water, Green Chem., 18, 4536–4541, https://doi.org/10.1039/C6GC01560C, 2016.

Heinritzi, M., Simon, M., Steiner, G., Wagner, A. C., Kürten, A., Hansel, A., and Curtius, J.: Characterization of the mass-dependent transmission efficiency of a CIMS, Atmos. Meas. Tech., 9, 1449–1460, https://doi.org/10.5194/amt-9-1449-2016, 2016.

Höpfner, M., Volkamer, R., Grabowski, U., Grutter, M., Orphal, J., Stiller, G., von Clarmann, T., and Wetzel, G.: First detection of ammonia (NH_3) in the Asian summer monsoon upper troposphere, Atmos. Chem. Phys., 16, 14357–14369, https://doi.org/10.5194/acp-16-14357-2016, 2016.

Jen, C. N., Bachman, R., Zhao, J., McMurry, P. H., and Hanson, D. R.: Diamine-sulfuric acid reactions are a potent source of new particle formation, Geophys. Res. Lett., 43, 867–873, https://doi.org/10.1002/2015GL066958, 2016.

Jimenez, J. L., Canagaratna, M. R., Donahue, N. M., Prevot, A. S. H., Zhang, Q., Kroll, J. H., DeCarlo, P. F., Allan, J. D., Coe, H., Ng, N. L., Aiken, A. C., Docherty, K. S., Ulbrich, I. M., Grieshop, A. P., Robinson, A. L., Duplissy, J., Smith, J. D., Wilson, K. R., Lanz, V. A., Hueglin, C., Sun, Y. L., Tian, J., Laaksonen, A., Raatikainen, T., Rautiainen, J., Vaattovaara, P., Ehn, M., Kulmala, M., Tomlinson, J. M., Collins, D. R., Cubison, M. J., Dunlea, J., Huffman, J. A., Onasch, T. B., Alfarra, M. R., Williams, P. I., Bower, K., Kondo, Y., Schneider, J., Drewnick, F., Borrmann, S., Weimer, S., Demerjian, K., Salcedo, D., Cottrell, L., Griffin, R., Takami, A., Miyoshi, T., Hatakeyama, S., Shimono, A., Sun, J. Y., Zhang, Y. M., Dzepina, K., Kimmel, J. R., Sueper, D., Jayne, J. T., Herndon, S. C., Trimborn, A. M., Williams, L. R., Wood, E. C., Middlebrook, A. M., Kolb, C. E., Baltensperger, U., and Worsnop, D. R.: Evolution of Organic Aerosols in the Atmosphere, Science, 326, 1525–1529, https://doi.org/10.1126/science.1180353, 2009.

Jokinen, T., Sipilä, M., Junninen, H., Ehn, M., Lönn, G., Hakala, J., Petäjä, T., Mauldin III, R. L., Kulmala, M., and Worsnop, D. R.: Atmospheric sulphuric acid and neutral cluster measurements using CI-APi-TOF, Atmos. Chem. Phys., 12, 4117–4125, https://doi.org/10.5194/acp-12-4117-2012, 2012.

Jokinen, T., Sipilä, M., Kontkanen, J., Vakkari, V., Tisler, P., Duplissy, E.-M., Junninen, H., Kangasluoma, J., Manninen, H. E., Petäjä, T., Kulmala, M., Worsnop, D. R., Kirkby, J., Virkkula, A., and Kerminen, V.-M.: Ion-induced sulfuric acid–ammonia nucleation drives particle formation in coastal Antarctica, Sci. Adv., 4, eaat 9744, https://doi.org/10.1126/sciadv.aat9744, 2018.

Kebarle, P.: Higher-Order Reactions–Ion Clusters and Ion Solvation, in: Ion-Molecule Reactions: Volume 1, edited by: Franklin, J. L., Springer US, Boston, MA, 315–362, 1972.

Kirkby, J., Curtius, J., Almeida, J., Dunne, E., Duplissy, J., Ehrhart, S., Franchin, A., Gagné, S., Ickes, L., Kürten, A., Kupc, A., Metzger, A., Riccobono, F., Rondo, L., Schobesberger, S., Tsagkogeorgas, G., Wimmer, D., Amorim, A., Bianchi, F., Breitenlechner, M., David, A., Dommen, J., Downard, A., Ehn, M., Flagan, R. C., Haider, S., Hansel, A., Hauser, D., Jud, W., Junninen, H., Kreissl, F., Kvashin, A., Laaksonen, A., Lehtipalo, K., Lima, J., Lovejoy, E. R., Makhmutov, V., Mathot, S., Mikkilä, J., Minginette, P., Mogo, S., Nieminen, T., Onnela, A., Pereira, P., Petäjä, T., Schnitzhofer, R., Seinfeld, J. H., Sipilä, M., Stozhkov, Y., Stratmann, F., Tomé, A., Vanhanen, J., Viisanen, Y., Vrtala, A., Wagner, P. E., Walther, H., Weingartner, E., Wex, H., Winkler, P. M., Carslaw, K. S., Worsnop, D. R., Baltensperger, U., and Kulmala, M.: Role of sulphuric acid, ammonia and galactic cosmic rays in atmospheric aerosol nucleation, Nature, 476, 429–433, https://doi.org/10.1038/nature10343, 2011.

Kirkby, J., Duplissy, J., Sengupta, K., Frege, C., Gordon, H., Williamson, C., Heinritzi, M., Simon, M., Yan, C., Almeida, J., Tröstl, J., Nieminen, T., Ortega, I. K., Wagner, R., Adamov, A., Amorim, A., Bernhammer, A.-K., Bianchi, F., Breitenlechner, M., Brilke, S., Chen, X., Craven, J., Dias, A., Ehrhart, S., Flagan, R. C., Franchin, A., Fuchs, C., Guida, R., Hakala, J., Hoyle, C. R., Jokinen, T., Junninen, H., Kangasluoma, J., Kim, J., Krapf, M., Kürten, A., Laaksonen, A., Lehtipalo, K., Makhmutov, V., Mathot, S., Molteni, U., Onnela, A., Peräkylä, O., Piel, F., Petäjä, T., Praplan, A. P., Pringle, K., Rap, A., Richards, N. A. D., Riipinen, I., Rissanen, M. P., Rondo, L., Sarnela, N., Schobesberger, S., Scott, C. E., Seinfeld, J. H., Sipilä, M., Steiner, G., Stozhkov, Y., Stratmann, F., Tomé, A., Virtanen, A., Vogel, A. L., Wagner, A. C., Wagner, P. E., Weingartner, E., Wimmer, D., Winkler, P. M., Ye, P., Zhang, X., Hansel, A., Dommen, J., Donahue, N. M., Worsnop, D. R., Baltensperger, U., Kulmala, M., Carslaw, K. S., and Curtius, J.: Ion-induced nucleation of pure biogenic particles, Nature, 533, 521–526, https://doi.org/10.1038/nature17953, 2016.

Kupc, A., Amorim, A., Curtius, J., Danielczok, A., Duplissy, J., Ehrhart, S., Walther, H., Ickes, L., Kirkby, J., Kürten, A., Lima, J. M., Mathot, S., Minginette, P., Onnela, A., Rondo, and Rondo, L.: A fibre-optic UV system for H_2SO_4 production in aerosol chambers causing minimal thermal effects, J. Aerosol Sci., 42, 532–543, https://doi.org/10.1016/j.jaerosci.2011.05.001, 2011.

Kurtén, T., Loukonen, V., Vehkamäki, H., and Kulmala, M.: Amines are likely to enhance neutral and ion-induced sulfuric acid-water nucleation in the atmosphere more effectively than ammonia, Atmos. Chem. Phys., 8, 4095–4103, https://doi.org/10.5194/acp-8-4095-2008, 2008.

Kürten, A., Rondo, L., Ehrhart, S., and Curtius, J.: Performance of a corona ion source for measurement of sulfuric acid by chemical ionization mass spectrometry, Atmos. Meas. Tech., 4, 437–443, https://doi.org/10.5194/amt-4-437-2011, 2011.

Kürten, A., Rondo, L., Ehrhart, S., and Curtius, J.: Calibration of a Chemical Ionization Mass Spectrometer for the Measurement of Gaseous Sulfuric Acid, J. Phys. Chem. A, 116, 6375–6386, https://doi.org/10.1021/jp212123n, 2012.

Kürten, A., Jokinen, T., Simon, M., Sipilä, M., Sarnela, N., Junninen, H., Adamov, A., Almeida, J., Amorim, A., Bianchi, F., Breitenlechner, M., Dommen, J., Donahue, N. M., Duplissy, J., Ehrhart, S., Flagan, R. C., Franchin, A., Hakala, J., Hansel, A., Heinritzi, M., Hutterli, M., Kangasluoma, J., Kirkby, J., Laaksonen, A., Lehtipalo, K., Leiminger, M., Makhmutov, V., Mathot, S., Onnela, A., Petäjä, T., Praplan, A. P., Riccobono, F., Rissanen, M. P., Rondo, L., Schobesberger, S., Seinfeld, J. H., Steiner, G., Tomé, A., Tröstl, J., Winkler, P. M., Williamson, C., Wimmer, D., Ye, P., Baltensperger, U., Carslaw, K. S., Kulmala, M., Worsnop, D. R., and Curtius, J.: Neutral molecular cluster formation of sulfuric acid-dimethylamine observed in real time under atmospheric conditions, P. Natl. Acad. Sci. USA, 111, 15019–15024, https://doi.org/10.1073/pnas.1404853111, 2014.

Kürten, A., Bianchi, F., Almeida, J., Kupiainen-Määttä, O., Dunne, E. M., Duplissy, J., Williamson, C., Barmet, P., Breitenlechner, M., Dommen, J., Donahue, N. M., Flagan, R. C., Franchin, A., Gordon, H., Hakala, J., Hansel, A., Heinritzi, M., Ickes, L., Jokinen, T., Kangasluoma, J., Kim, J., Kirkby, J., Kupc, A., Lehtipalo, K., Leiminger, M., Makhmutov, V., Onnela, A., Ortega, I. K., Petäjä, T., Praplan, A. P., Riccobono, F., Rissanen, M. P., Rondo, L., Schnitzhofer, R., Schobesberger, S., Smith, J. N., Steiner, G., Stozhkov, Y., Tomé, A., Tröstl, J., Tsagkogeorgas, G., Wagner, P. E., Wimmer, D., Ye, P., Baltensperger, U., Carslaw, K., Kulmala, M., and Curtius, J.: Experimental particle formation rates spanning tropospheric sulfuric acid and ammonia abundances, ion production rates, and temperatures, J. Geophys. Res.-Atmos., 121, 12377–12400, https://doi.org/10.1002/2015JD023908, 2016a.

Kürten, A., Bergen, A., Heinritzi, M., Leiminger, M., Lorenz, V., Piel, F., Simon, M., Sitals, R., Wagner, A. C., and Curtius, J.: Observation of new particle formation and measurement of sulfuric acid, ammonia, amines and highly oxidized organic molecules at a rural site in central Germany, Atmos. Chem. Phys., 16, 12793–12813, https://doi.org/10.5194/acp-16-12793-2016, 2016b.

Kürten, A.: New particle formation from sulfuric acid and ammonia: nucleation and growth model based on thermodynamics derived from CLOUD measurements for a wide range of conditions, Atmos. Chem. Phys., 19, 5033–5050, https://doi.org/10.5194/acp-19-5033-2019, 2019.

Lehtipalo, K., Yan, C., Dada, L., Bianchi, F., Xiao, M., Wagner, R., Stolzenburg, D., Ahonen, L. R., Amorim, A., Baccarini, A., Bauer, P. S., Baumgartner, B., Bergen, A., Bernhammer, A.-K., Breitenlechner, M., Brilke, S., Buchholz, A., Mazon, S. B., Chen, D., Chen, X., Dias, A., Dommen, J., Draper, D. C., Duplissy, J., Ehn, M., Finkenzeller, H., Fischer, L., Frege, C., Fuchs, C., Garmash, O., Gordon, H., Hakala, J., He, X., Heikkinen, L., Heinritzi, M., Helm, J. C., Hofbauer, V., Hoyle, C. R., Jokinen, T., Kangasluoma, J., Kerminen, V.-M., Kim, C., Kirkby, J., Kontkanen, J., Kürten, A., Lawler, M. J., Mai, H., Mathot, S., Mauldin, R. L., Molteni, U., Nichman, L., Nie, W., Nieminen, T., Ojdanic, A., Onnela, A., Passananti, M., Petäjä, T., Piel, F., Pospisilova, V., Quéléver, L. L. J., Rissanen, M. P., Rose, C., Sarnela, N., Schallhart, S., Schuchmann, S., Sengupta, K., Simon, M., Sipilä, M., Tauber, C., Tomé, A., Tröstl, J., Väisänen, O., Vogel, A. L., Volkamer, R., Wagner, A. C., Wang, M., Weitz, L., Wimmer, D., Ye, P., Ylisirniö, A., Zha, Q., Carslaw, K. S., Curtius, J., Donahue, N. M., Flagan, R. C., Hansel, A., Riipinen, I., Virtanen, A., Winkler, P. M., Baltensperger, U., Kulmala, M., and Worsnop, D. R.: Multicomponent new particle formation from sulfuric acid, ammonia, and biogenic vapors, Sci. Adv., 4, eaau5363, https://doi.org/10.1126/sciadv.aau5363, 2018.

Leifer, I., Melton, C., Tratt, D. M., Buckland, K. N., Clarisse, L., Coheur, P., Frash, J., Gupta, M., Johnson, P. D., Leen, J. B., van Damme, M., Whitburn, S., and Yurganov, L.: Remote sensing and in situ measurements of methane and ammonia emissions from a megacity dairy complex: Chino, CA, Environ. Pollut., 221, 37–51, https://doi.org/10.1016/j.envpol.2016.09.083, 2017.

Martin, N. A., Ferracci, V., Cassidy, N., and Hoffnagle, J. A.: The application of a cavity ring-down spectrometer to measurements of ambient ammonia using traceable primary standard gas mixtures, Appl. Phys. B, 122, 219, https://doi.org/10.1007/s00340-016-6486-9, 2016.

Massman, W. J.: A review of the molecular diffusivities of H_2O, CO_2, CH_4, CO, O_3, SO_2, NH_3, N_2O, NO, and NO_2 in air, O_2 and N_2 near STP, Atmos. Environ., 32, 1111–1127, https://doi.org/10.1016/S1352-2310(97)00391-9, 1998.

Murphy, D. M. and Koop, T.: Review of the vapour pressures of ice and supercooled water for atmospheric applications, Q. J. Roy.

Meteor. Soc., 131, 1539–1565, https://doi.org/10.1256/qj.04.94, 2005.

Norman, M., Hansel, A., and Wisthaler, A.: O2+ as reagent ion in the PTR-MS instrument: Detection of gas-phase ammonia, Int. J. Mass Spectrom., 265, 382–387, https://doi.org/10.1016/j.ijms.2007.06.010, 2007.

Norman, M., Spirig, C., Wolff, V., Trebs, I., Flechard, C., Wisthaler, A., Schnitzhofer, R., Hansel, A., and Neftel, A.: Intercomparison of ammonia measurement techniques at an intensively managed grassland site (Oensingen, Switzerland), Atmos. Chem. Phys., 9, 2635–2645, https://doi.org/10.5194/acp-9-2635-2009, 2009.

Nowak, J. B., Huey, L. G., Eisele, F. L., Tanner, D. J., Mauldin, R. L., Cantrell, C., Kosciuch, E., and Davis, D.: Chemical ionization mass spectrometry technique for the detection of dimethylsulfoxide and ammonia, J. Geophys. Res., 107, 4363, https://doi.org/10.1029/2001JD001058, 2002.

Nowak, J. B., Huey, L. G., Russel, A. G., Tian D., Neuman, J. A., Orsini, D., Sjostedt, S. J., Sullivan, A. P., Tanner, D. J., Weber, R. J., Nenes, A.,Edgerton, E., and Fehsenfeld, F. C.: Analysis of urban gas phase ammonia measurements from the 2002 Atlanta Aerosol Nucleation and Real-Time Characterization Experiment (ANARChE), J. Geophys. Res., 111, D17308, https://doi.org/10.1029/2006JD007113, 2006.

Nowak, J., Neuman, J., Kozai, K., G. Huey, L., Tanner, D., Holloway, J., B. Ryerson, T., Frost, G., McKeen, S., and Fehsenfeld, F.: A chemical ionization mass spectrometry technique for airborne measurements of ammonia, J. Geophys. Res., 112, D10S02, https://doi.org/10.1029/2006JD007589, 2007.

Nowak, J., Neuman, J., Bahreini, R., A. Brock, C., M. Middlebrook, A., G. Wollny, A., Holloway, J., Peischl, J., Ryerson, T. B., and Fehsenfeld, F.: Airborne observations of ammonia and ammonium nitrate formation over Houston, Texas, J. Geophys. Res., 115, D22304, https://doi.org/10.1029/2010JD014195, 2010.

Pfeifer, J., Simon, M., Kürten, A., Kirkby, J., Curtius, J., Heinritzi, M., and Bräkling, S.: Measurement of ammonia, amines and iodine compounds using protonated water cluster chemical ionization mass spectrometry (Version Published data), Zenodo, https://doi.org/10.5281/zenodo.3831469, 2020.

Pollack, I. B., Lindaas, J., Roscioli, J. R., Agnese, M., Permar, W., Hu, L., and Fischer, E. V.: Evaluation of ambient ammonia measurements from a research aircraft using a closed-path QC-TILDAS operated with active continuous passivation, Atmos. Meas. Tech., 12, 3717–3742, https://doi.org/10.5194/amt-12-3717-2019, 2019.

Pozzer, A., Tsimpidi, A. P., Karydis, V. A., de Meij, A., and Lelieveld, J.: Impact of agricultural emission reductions on fine-particulate matter and public health, Atmos. Chem. Phys., 17, 12813–12826, https://doi.org/10.5194/acp-17-12813-2017, 2017.

Roscioli, J. R., Zahniser, M. S., Nelson, D. D., Herndon, S. C., and Kolb, C. E.: New Approaches to Measuring Sticky Molecules: Improvement of Instrumental Response Times Using Active Passivation, J. Phys. Chem. A, 120, 1347–1357, https://doi.org/10.1021/acs.jpca.5b04395, 2016.

Simon, M., Heinritzi, M., Herzog, S., Leiminger, M., Bianchi, F., Praplan, A., Dommen, J., Curtius, J., and Kürten, A.: Detection of dimethylamine in the low pptv range using nitrate chemical ionization atmospheric pressure interface time-of-flight (CI-APi-TOF) mass spectrometry, Atmos. Meas. Tech., 9, 2135–2145, https://doi.org/10.5194/amt-9-2135-2016, 2016.

Sipilä, M., Sarnela, N., Jokinen, T., Junninen, H., Hakala, J., Rissanen, M. P., Praplan, A., Simon, M., Kürten, A., Bianchi, F., Dommen, J., Curtius, J., Petäjä, T., and Worsnop, D. R.: Bisulfate – cluster based atmospheric pressure chemical ionization mass spectrometer for high-sensitivity (< 100 ppqV) detection of atmospheric dimethyl amine: proof-of-concept and first ambient data from boreal forest, Atmos. Meas. Tech., 8, 4001–4011, https://doi.org/10.5194/amt-8-4001-2015, 2015.

Sipilä, M., Sarnela, N., Jokinen, T., Henschel, H., Junninen, H., Kontkanen, J., Richters, S., Kangasluoma, J., Franchin, A., Peräkylä, O., Rissanen, M. P., Ehn, M., Vehkamäki, H., Kurten, T., Berndt, T., Petäjä, T., Worsnop, D., Ceburnis, D., Kerminen, V.-M., Kulmala, M., and O'Dowd, C.: Molecular-scale evidence of aerosol particle formation via sequential addition of HIO_3, Nature, 537, 532–534, https://doi.org/10.1038/nature19314, 2016.

Skrotzki, J.: High-accuracy multiphase humidity measurements using TDLAS: application to the investigation of ice growth in simulated cirrus clouds, Ruperto-Carola University of Heidelberg, Heidelberg, 2012.

Stark, H., Yatavelli, R. L. N., Thompson, S. L., Kimmel, J. R., Cubison, M. J., Chhabra, P. S., Canagaratna, M. R., Jayne, J. T., Worsnop, D. R., and Jimenez, J. L.: Methods to extract molecular and bulk chemical information from series of complex mass spectra with limited mass resolution, Int. J. Mass Spectrom., 389, 26–38, https://doi.org/10.1016/j.ijms.2015.08.011, 2015.

Sunner, J., Nicol, G., and Kebarle, P.: Factors determining relative sensitivity of analytes in positive mode atmospheric pressure ionization mass spectrometry, Anal. Chem., 60, 1300–1307, https://doi.org/10.1021/ac00164a012, 1988.

Tang, M. J., Shiraiwa, M., Pöschl, U., Cox, R. A., and Kalberer, M.: Compilation and evaluation of gas phase diffusion coefficients of reactive trace gases in the atmosphere: Volume 2. Diffusivities of organic compounds, pressure-normalised mean free paths, and average Knudsen numbers for gas uptake calculations, Atmos. Chem. Phys., 15, 5585–5598, https://doi.org/10.5194/acp-15-5585-2015, 2015.

Timonen, H., Cubison, M., Aurela, M., Brus, D., Lihavainen, H., Hillamo, R., Canagaratna, M., Nekat, B., Weller, R., Worsnop, D., and Saarikoski, S.: Applications and limitations of constrained high-resolution peak fitting on low resolving power mass spectra from the ToF-ACSM, Atmos. Meas. Tech., 9, 3263–3281, https://doi.org/10.5194/amt-9-3263-2016, 2016.

Vaittinen, O., Metsälä, M., Persijn, S., Vainio, M., and Halonen, L.: Adsorption of ammonia on treated stainless steel and polymer surfaces, Appl. Phys. B, 115, 185–196, https://doi.org/10.1007/s00340-013-5590-3, 2014.

Verriele, M., Plaisance, H., Depelchin, L., Benchabane, S., Locoge, N., and Meunier, G.: Determination of 14 amines in air samples using midget impingers sampling followed by analysis with ion chromatography in tandem with mass spectrometry, J. Environ. Monitor., 14, 402–408, https://doi.org/10.1039/c2em10636a, 2012.

Viggiano, A. A., Seeley, J. V., Mundis, P. L., Williamson, J. S., and Morris, R. A.: Rate constants for the reactions of $XO_3^-(H_2O)_n$ (X = C, HC, and N) and $NO_3^-(H_3O)_n$ with H_2SO_4: implica-

tions for atmospheric detection of H_2SO_4, J. Chem. Phys. A, 101, 8275–8278, https://doi.org/10.1021/jp971768h, 1997.

von Bobrutzki, K., Braban, C. F., Famulari, D., Jones, S. K., Blackall, T., Smith, T. E. L., Blom, M., Coe, H., Gallagher, M., Ghalaieny, M., McGillen, M. R., Percival, C. J., Whitehead, J. D., Ellis, R., Murphy, J., Mohacsi, A., Pogany, A., Junninen, H., Rantanen, S., Sutton, M. A., and Nemitz, E.: Field inter-comparison of eleven atmospheric ammonia measurement techniques, Atmos. Meas. Tech., 3, 91–112, https://doi.org/10.5194/amt-3-91-2010, 2010.

Wang, S., Nan, J., Shi, C., Fu, Q., Gao, S., Wang, D., Cui, H., Saiz-Lopez, A., and Zhou, B.: Atmospheric ammonia and its impacts on regional air quality over the megacity of Shanghai, China, Sci. Rep.-UK, 5, 15842, https://doi.org/10.1038/srep15842, 2015.

Weissler, G. L.: Positive and Negative Point-to-Plane Corona in Pure and Impure Hydrogen, Nitrogen, and Argon, Phys. Rev., 63, 96–107, https://doi.org/10.1103/PhysRev.63.96, 1943.

Wilkinson, G. N. and Rogers, C. E.: Symbolic Description of Factorial Models for Analysis of Variance, J. R. Stat. Soc. C-Appl., 22, 392–399, https://doi.org/10.2307/2346786, 1973.

Yan, C., Dada, L., Rose, C., Jokinen, T., Nie, W., Schobesberger, S., Junninen, H., Lehtipalo, K., Sarnela, N., Makkonen, U., Garmash, O., Wang, Y., Zha, Q., Paasonen, P., Bianchi, F., Sipilä, M., Ehn, M., Petäjä, T., Kerminen, V.-M., Worsnop, D. R., and Kulmala, M.: The role of H_2SO_4-NH_3 anion clusters in ion-induced aerosol nucleation mechanisms in the boreal forest, Atmos. Chem. Phys., 18, 13231–13243, https://doi.org/10.5194/acp-18-13231-2018, 2018.

Yao, L., Wang, M.-Y., Wang, X.-K., Liu, Y.-J., Chen, H.-F., Zheng, J., Nie, W., Ding, A.-J., Geng, F.-H., Wang, D.-F., Chen, J.-M., Worsnop, D. R., and Wang, L.: Detection of atmospheric gaseous amines and amides by a high-resolution time-of-flight chemical ionization mass spectrometer with protonated ethanol reagent ions, Atmos. Chem. Phys., 16, 14527–14543, https://doi.org/10.5194/acp-16-14527-2016, 2016.

Yokelson, R. J.: Evaluation of adsorption effects on measurements of ammonia, acetic acid, and methanol, J. Geophys. Res., 108, 4649, https://doi.org/10.1029/2003JD003549, 2003.

You, Y., Kanawade, V. P., de Gouw, J. A., Guenther, A. B., Madronich, S., Sierra-Hernández, M. R., Lawler, M., Smith, J. N., Takahama, S., Ruggeri, G., Koss, A., Olson, K., Baumann, K., Weber, R. J., Nenes, A., Guo, H., Edgerton, E. S., Porcelli, L., Brune, W. H., Goldstein, A. H., and Lee, S.-H.: Atmospheric amines and ammonia measured with a chemical ionization mass spectrometer (CIMS), Atmos. Chem. Phys., 14, 12181–12194, https://doi.org/10.5194/acp-14-12181-2014, 2014.

Yu, F., Nadykto, A. B., Herb, J., Luo, G., Nazarenko, K. M., and Uvarova, L. A.: $H_2SO_4-H_2O-NH_3$ ternary ion-mediated nucleation (TIMN): kinetic-based model and comparison with CLOUD measurements, Atmos. Chem. Phys., 18, 17451–17474, https://doi.org/10.5194/acp-18-17451-2018, 2018.

Zhao, J. and Zhang, R.: Proton transfer reaction rate constants between hydronium ion (H_3O^+) and volatile organic compounds, Atmos. Environ., 38, 2177–2185, https://doi.org/10.1016/j.atmosenv.2004.01.019, 2004.

Paper 2: Rapid growth of new atmospheric particles by nitric acid and ammonia condensation

Rapid growth of new atmospheric particles by nitric acid and ammonia condensation

https://doi.org/10.1038/s41586-020-2270-4

Received: 26 September 2019

Accepted: 17 March 2020

Published online: 13 May 2020

Open access

Check for updates

A list of authors and their affiliations appears at the end of the paper

New-particle formation is a major contributor to urban smog[1,2], but how it occurs in cities is often puzzling[3]. If the growth rates of urban particles are similar to those found in cleaner environments (1–10 nanometres per hour), then existing understanding suggests that new urban particles should be rapidly scavenged by the high concentration of pre-existing particles. Here we show, through experiments performed under atmospheric conditions in the CLOUD chamber at CERN, that below about +5 degrees Celsius, nitric acid and ammonia vapours can condense onto freshly nucleated particles as small as a few nanometres in diameter. Moreover, when it is cold enough (below −15 degrees Celsius), nitric acid and ammonia can nucleate directly through an acid–base stabilization mechanism to form ammonium nitrate particles. Given that these vapours are often one thousand times more abundant than sulfuric acid, the resulting particle growth rates can be extremely high, reaching well above 100 nanometres per hour. However, these high growth rates require the gas-particle ammonium nitrate system to be out of equilibrium in order to sustain gas-phase supersaturations. In view of the strong temperature dependence that we measure for the gas-phase supersaturations, we expect such transient conditions to occur in inhomogeneous urban settings, especially in wintertime, driven by vertical mixing and by strong local sources such as traffic. Even though rapid growth from nitric acid and ammonia condensation may last for only a few minutes, it is nonetheless fast enough to shepherd freshly nucleated particles through the smallest size range where they are most vulnerable to scavenging loss, thus greatly increasing their survival probability. We also expect nitric acid and ammonia nucleation and rapid growth to be important in the relatively clean and cold upper free troposphere, where ammonia can be convected from the continental boundary layer and nitric acid is abundant from electrical storms[4,5].

The formation of new particles may mask up to half of the radiative forcing caused since the industrial revolution by carbon dioxide and other long-lived greenhouse gases[6]. Present-day particle formation is thought to predominantly involve sulfuric acid vapours globally[7–9]. Subsequent particle growth is richer, often involving organic molecules[10]. Often growth is the limiting step for the survival of particles from freshly nucleated clusters to diameters of 50 or 100 nm, where they become large enough to directly scatter light and also to seed cloud formation[11,12].

New-particle formation in megacities is especially important[2], in part because air pollution in megacities constitutes a public health crisis[13], but also because the regional climate forcing associated with megacity urban haze can be large[14]. However, new-particle formation in highly polluted megacities is often perplexing, because the apparent particle growth rates are only modestly faster (by a factor of roughly three) than growth rates in remote areas, whereas the vapour condensation sink (to background particles) is up to two orders of magnitude larger (Extended Data Fig. 1). This implies a very low survival probability in the 'valley of death', where particles with diameters (d_p) of 10 nm or less have high Brownian diffusivities and will be lost by coagulational scavenging unless they grow rapidly[7,15].

Ammonium nitrate has long been recognized as an important yet semivolatile constituent of atmospheric aerosols[16]. Especially in winter and in agricultural areas, particulate nitrate can be a substantial air-quality problem[17]. However, the partitioning of nitric acid and ammonia vapours with particulate ammonium nitrate is thought to rapidly reach an equilibrium, often favouring the gas phase when it is warm.

Because ammonium nitrate is semivolatile, nitric acid has not been thought to play an important role in new-particle formation and growth, where very low vapour pressures are required for constituents to be important. Such constituents would include sulfuric acid[18] but also very low vapour pressure organics[19,20] and iodine oxides[21]. However, it is saturation ratio and not vapour pressure per se that determines the thermodynamic driving force for condensation, and nitric acid can be three or four orders of magnitude more abundant than sulfuric acid in urban environments. Thus, even a small fractional supersaturation of nitric acid and ammonia vapours with respect to ammonium nitrate has the potential to drive very rapid particle growth, carrying very small, freshly nucleated particles through the valley of death in a few minutes. These rapid growth events can exceed 100 nm h^{-1} under urban conditions—an order of magnitude higher than previous observations—and the growth will continue until the vapours are exhausted and conditions return to equilibrium. Such transients will be difficult to identify in inhomogeneous urban environments, yet have the potential

to explain the puzzling observations of new-particle formation in highly polluted megacities.

Nucleation measurements in CLOUD at CERN

Here we report experiments performed with mixtures of nitric acid, sulfuric acid and ammonia vapours under atmospheric conditions in the CERN CLOUD chamber (Cosmics Leaving OUtdoor Droplets[22]; see Methods for experimental details) from 21 September to 7 December 2018 (CLOUD 13). We varied the temperature from +20 °C to −10 °C, in one case cooling progressively from −15 °C to −25 °C. We adjusted levels of sulfuric acid (H_2SO_4), ammonia (NH_3) and nitric acid (HNO_3), as well as aromatic precursors, to span the ranges typical of polluted megacities. In Fig. 1 we show two representative events at −10 °C. For Fig. 1a we oxidized SO_2 with OH to form H_2SO_4 in the presence of 1,915 parts per trillion volume (pptv) ammonia. The resulting 'banana' is typical of such experiments and of ambient observations under relatively clean conditions, with a single nucleation mode that appears shortly after the onset of nucleation and grows at roughly 20 nm h^{-1}. In Fig. 1b we repeated this experiment but also with 5.8 parts per billion volume (ppbv) NO_2, which was oxidized by OH to produce 24 pptv of HNO_3 vapour. The resulting size distribution initially resembles the first case, but when the particles reach about 5 nm, their growth rate accelerates to roughly 45 nm h^{-1}. This activation is reminiscent of cloud-droplet activation and thus suggestive of 'nano-Köhler' behaviour and the Kelvin curvature effect[23].

We repeated these experiments over a range of conditions, either forming HNO_3 from NO_2 oxidation or injecting it directly into the CLOUD chamber from an ultrapure evaporation source. We observed this activation and rapid growth behaviour consistently. In Fig. 1c we show the resulting rapid growth rates after activation at −10 °C (green) and +5 °C (purple), plotted against the product of the measured gas-phase HNO_3 and NH_3 mixing ratios. Growth rates are based on the 50% appearance time—the time at which particle number concentrations in each size bin of the rapid growth regime reach 50% of their maximum. Both a strong correlation and a clear temperature dependence are evident; when it is colder, the particles grow at the same rate for a much lower product of vapour concentrations. This is consistent with semivolatile uptake of both species, rate limited by the formation of ammonium nitrate.

To confirm this, we measured the composition of the particles using a filter inlet for gases and aerosols (FIGAERO) iodide (I^-) chemical ionization mass spectrometer (CIMS), along with the gas-phase vapour concentrations via several CIMS methods. In Fig. 2 we show another rapid growth event, this one at +5 °C (indicated in Fig. 1c with a black outlined purple square). We started with an almost perfectly clean chamber and only vapours present (SO_2, HNO_3 and NH_3) at constant levels (Fig. 2a). Here we injected the HNO_3 without photochemical production so we could independently control HNO_3 and sulfuric acid. The FIGAERO showed no measurable signal in the absence of particles, indicating negligible crosstalk from vapours. We then turned on ultraviolet lights in order to form OH radicals and to initiate SO_2 oxidation to H_2SO_4. Fig. 2b shows the resulting number distribution; as in Fig. 1b, particles appear, grow slowly, and then activate and grow at 700 nm h^{-1}. We again show the 50% appearance time of both modes. In Fig. 2c we show the associated volume distribution. Within 15 min of the onset of particle formation, the volume is dominated by the upper mode near 200 nm. Finally, in Fig. 2d we show a FIGAERO thermogram (signal versus desorption temperature) for particles collected between 10 min and 40 min after the onset of photochemistry. Their composition is dominated by nitrate, with a much smaller but notable sulfate contribution; the semivolatile nitrate desorbs at a much lower temperature than the sulfate. The I^- chemical ionization is not sensitive to NH_3, but both nitrate and sulfate exist presumably as ammonium salts in the particles.

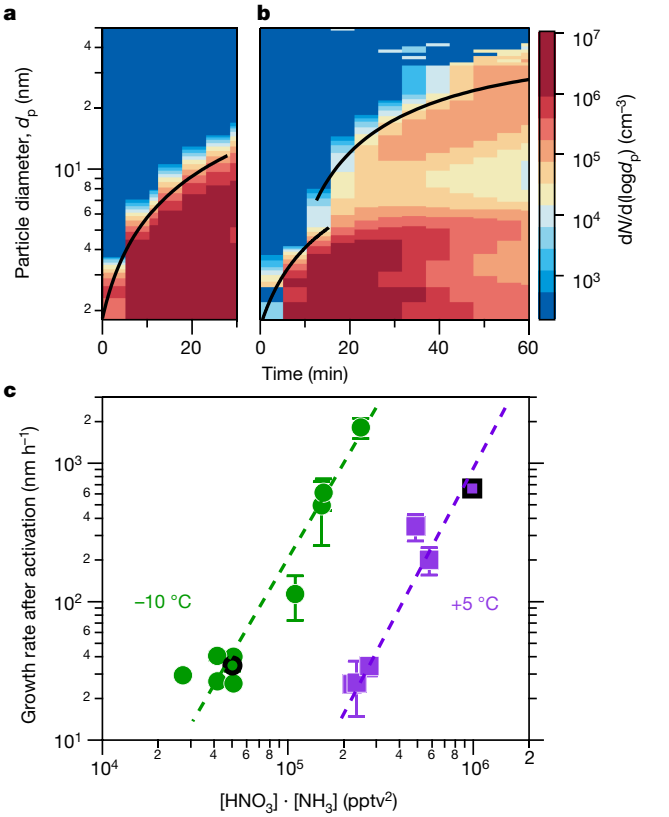

Fig. 1 | Rapid growth events observed in the CERN CLOUD chamber. **a**, Particle nucleation and growth (particle growth rate, dd_p/dt) at −10 °C from a mixture of 0.44 pptv sulfuric acid and 1,915 pptv ammonia at 60% relative humidity. Particles form and grow to roughly 10 nm in 30 min. The black curve shows the linear fit to the 50% appearance times. **b**, Particle formation and growth under identical conditions to those in **a**, but with the addition of 24 pptv of nitric acid vapour formed via NO_2 oxidation. Once particles reach roughly 5 nm, they experience rapid growth to much larger sizes, reaching more than 30 nm in 45 min. **c**, Observed growth rates after activation versus the product of measured nitric acid and ammonia levels at +5 °C and −10 °C. The point corresponding to the rapid growth regime for $d_p > 6$ nm in **b** is a black-outlined green circle, and the point corresponding to Fig. 2 is a black-outlined purple square. Growth rates at a given vapour product are substantially faster at −10 °C than at +5 °C, consistent with semivolatile condensation that is rate limited by ammonium nitrate formation. Error bars are 95% confidence limits on the fitting coefficients used to determine growth rates. The overall systematic scale uncertainties of ±10% on the NH_3 mixing ratio and ±25% on the HNO_3 mixing ratio are not shown.

In addition to the correlation of activated particle growth rates with the product of HNO_3 and NH_3 at a given temperature, the observed activation diameter (d_{act}) shows a strong dependence on this product. The activation diameter is evident as a clear kink in the 50% appearance curve, as well as a notable absence of particles in the slower-growth mode above d_{act}. In Extended Data Fig. 2a we show an example of how we determine d_{act}, using the emergence of a bimodal size distribution as the defining feature. In Fig. 3a we plot the observed activation diameter at each temperature in a phase space, with [HNO_3] on the log$x$ axis and [NH_3] on the log$y$ axis (both in pptv). The number within each symbol is the observed activation diameter for that experiment. We show the saturation ratio (S) of ammonium nitrate at each temperature via a series of diagonal lines in this log–log space (slope = −1); specifically, we show $S = 1$, 5 and 25, emphasizing $S = 1$ as a thick solid line. We also indicate 1:1 [HNO_3]:[NH_3] with a dashed grey line (slope +1); points to the upper left (most of the values) are

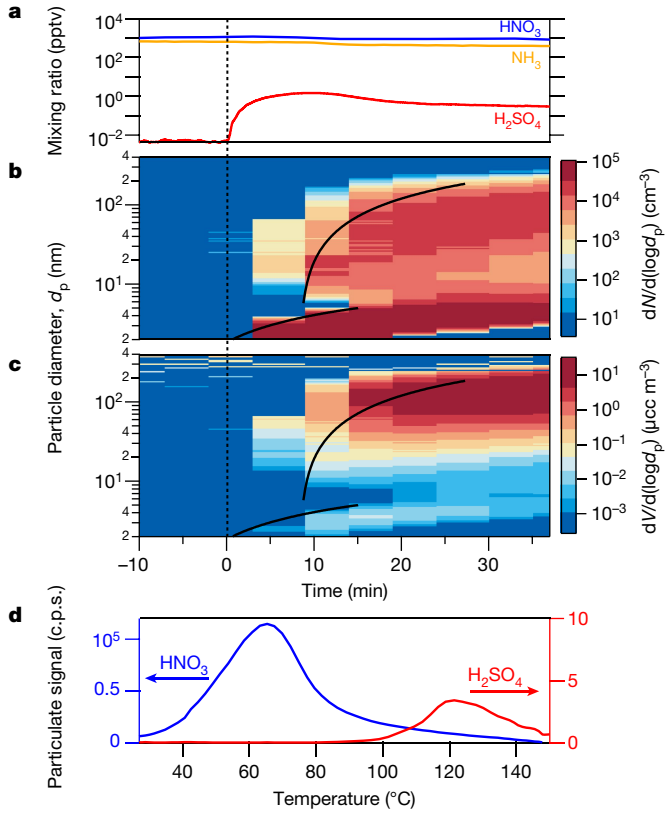

Fig. 2 | Chemical composition during a rapid growth event at +5 °C and 60% relative humidity. This growth event is indicated in Fig. 1c with a black-outlined purple square. **a**, Gas-phase nitric acid (NO_3), ammonia (NH_3) and sulfuric acid (H_2SO_4) mixing ratios versus time in an event initiated by SO_2 oxidation, with constant nitric acid and ammonia. **b**, Particle diameters and number distributions versus time, showing a clean chamber (to the left of the vertical dotted line), then nucleation after sulfuric acid formation and rapid growth once particles reach 2.3 nm. Black curves are linear fits to the 50% appearance times. **c**, Particle volume distributions from the same data, showing that 200-nm particles dominate the mass after 15 min. 1 μcc = 1 cm^{-6}. **d**, FIGAERO thermogram from a 30-min filter sample after rapid growth (c.p.s., counts per second). The particle composition is dominated by nitrate with a core of sulfate, consistent with rapid growth by ammonium nitrate condensation on an ammonium sulfate (or bisulfate) core (note the different *y*-axis scales; the instrument is not sensitive to ammonia). A thermogram from just before the formation event shows no signal from either nitrate or sulfate, indicating that vapour adsorption did not interfere with the analysis.

'nitric acid limited', with more ammonia than nitric acid. All of these concentrations are well within the ranges typically observed in wintertime megacity conditions[24].

For both +5 °C and −10 °C, we consistently observe a relationship between *S* and d_{act} (we never achieved saturation at +20 °C and did not observe rapid growth). We observe no activation for *S* values of less than 1, and activation for *S* values greater than 1, with logd_{act} being inversely proportional to log([HNO_3]·[NH_3]) at each temperature (Extended Data Fig. 2b). Notably, d_{act} can be well under 10 nm and as low as 1.6 nm. This suggests that nitric acid and ammonia (ammonium nitrate) condensation may play a role in new-particle formation and growth within the valley of death, where very small particles are most vulnerable to loss by coagulation[8].

We also performed experiments with only nitric acid, ammonia and water vapour added to the chamber (sulfuric acid contamination was measured to be less than 2×10^{-3} pptv). For temperatures of less than −15 °C and *S* values of more than 10^3, we observed nucleation and growth of pure ammonium nitrate particles (Fig. 3c). We progressively cooled the chamber to −24 °C, while holding the vapours at a constant level (Fig. 3b). The particle-formation rate ($J_{1.7}$) rose steadily from 0.006 cm^{-3} s^{-1} to 0.06 cm^{-3} s^{-1} at −24 °C. In Extended Data Fig. 3 we show a pure ammonium nitrate nucleation experiment performed at −25 °C under vapour conditions reported for the tropical upper troposphere[4] (30–50 pptv nitric acid and 1.8 ppbv ammonia), showing that this mechanism can produce several 100 cm^{-3} particles per hour.

Our experiments show that semivolatile ammonium nitrate can condense on tiny nanoparticles, consistent with nano-Köhler theory[23]. To confirm this we conducted a series of simulations using the monodisperse thermodynamic model MABNAG (model for acid-base chemistry in nanoparticle growth)[25], which treats known thermodynamics, including curvature (Kelvin) effects for a single evolving particle size. We show the points of the MABNAG simulations as triangles in Fig. 3a. MABNAG consistently and quantitatively confirms our experimental findings: there is little ammonium nitrate formation at *S* values of less than 1.0, as expected; and activation behaviour with ammonium nitrate condensation ultimately dominating the particle composition occurs at progressively smaller d_{act} values as *S* rises well above 1.0. The calculated and observed d_{act} values are broadly consistent. In Fig. 4 we show two representative MABNAG growth simulations for the two points indicated with open and filled diamonds in Fig. 3a; the simulations show no ammonium nitrate formation when conditions are undersaturated, but substantial formation when conditions are saturated, with activation behaviour near the observed d_{act} = 4.7 nm. We show the calculated composition as well as diameter versus time for these and other cases in Extended Data Fig. 4.

We also conducted nano-Köhler simulations[23], shown in Extended Data Fig. 2c, which confirm the activation of ammonium nitrate condensation at diameters less than 4 nm, depending on the size of an assumed ammonium sulfate core. For a given core size the critical supersaturation required for activation at −10 °C is a factor of two to three higher than at +5 °C, consistent with the observed behaviour shown in Fig. 3a. While particles of 1–2 nm contain only a handful of acid and base molecules, the MABNAG and nano-Köhler simulations based on bulk thermodynamics—with only a Kelvin term to represent the unique behaviour of the nanoparticles—capture the activation and growth behaviours we observe.

Atmospheric implications

Our findings suggest that the condensation of nitric acid and ammonia onto nanoparticles to form ammonium nitrate (or, by extension, aminium nitrates in the presence of amines) may be important in the atmosphere. This process may contribute to urban new-particle formation during wintertime via rapid growth. It may also play a role in free-tropospheric particle formation, where sufficient vapours may exist to allow nucleation and growth of pure ammonium nitrate particles. We observe these behaviours in CLOUD for vapour concentrations well within those typical of the atmosphere.

Rapid growth may contribute to the often puzzling survival of newly formed particles in megacities, where particles form at rates consistent with sulfuric-acid–base nucleation and appear to grow at typical rates (roughly 10 nm h^{-1}) in the presence of extremely high condensation sinks that seemingly should scavenge all of the tiny nucleated particles. As shown in Extended Data Fig. 1, the ratio of 10^4 × condensation sink (CS; in units of s^{-1}) to growth rate (GR; in nm h^{-1}) during nucleation events in Asian megacities typically ranges between 20 and 50, where the survival probability of particles with sizes of between 1.5 nm and 3 nm should drop precipitously[3]. However, the observed growth rates are based on appearance times in

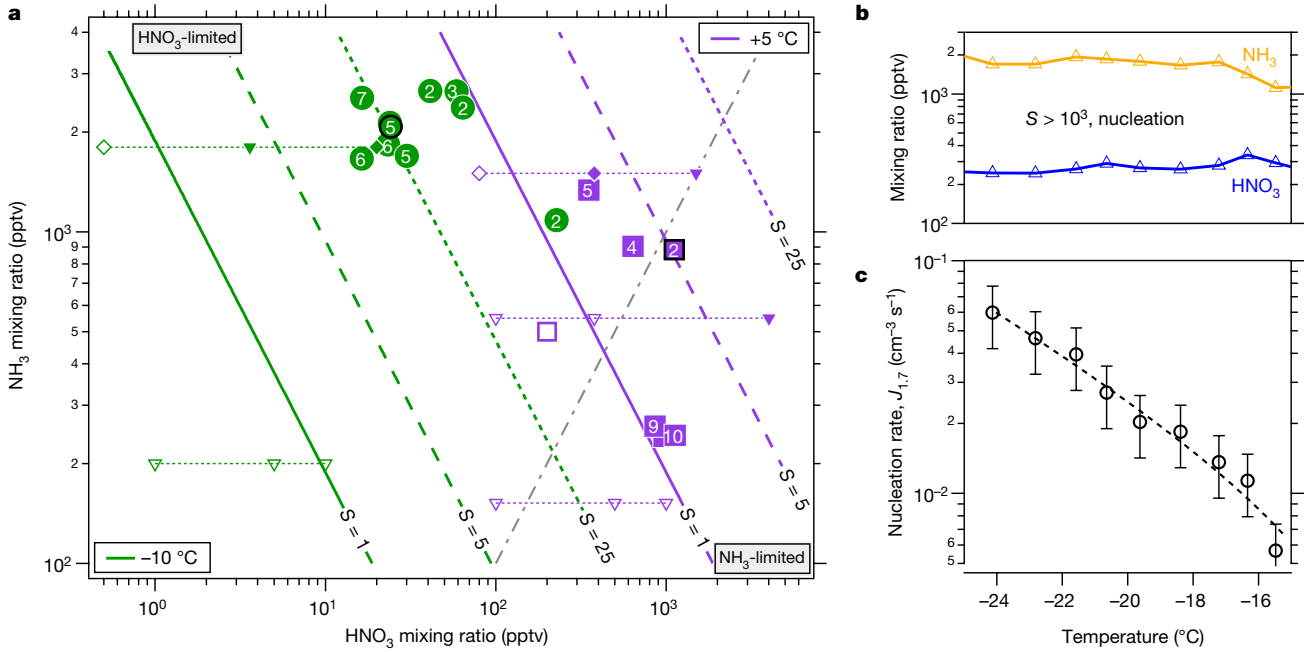

Fig. 3 | Phase space for rapid growth and nucleation. a, Ammonium nitrate saturation ratios versus gas-phase nitric acid and ammonia mixing ratios at 60% relative humidity. The coloured lines (slope = −1) represent $S = 1$ (bold), $S = 5$ (dashed) and $S = 25$ (dotted), at −10 °C (green) and +5 °C (purple). The slope = +1 dot-dashed grey line indicates a 1:1 ammonia:nitric-acid stoichiometry; the phase space to the upper left of this line is nitric-acid limited. Observed activation diameters (in nm) for measured nitric-acid–ammonia pairs are plotted as numbers inside solid circles and squares; open symbols show no activation. Activation occurs only for S values of more than 1, and the activation diameter decreases as S increases. Points from MABNAG simulations are shown with open triangles for no activation and filled triangles for activation; simulations indicated with diamonds are shown in detail in Fig. 4 and Extended Data Fig. 4. Points from runs shown in Figs. 1, 2 are emphasized with a thick black outline. **b**, Mixing ratios for ammonia and nitric acid vapour during a pure ammonium nitrate nucleation scan from −16 °C to −24 °C. **c**, Particle-formation (nucleation) rates ($J_{1.7}$) during the nucleation scan, showing a strong inverse relationship with temperature at constant HNO_3 and NH_3, with H_2SO_4 concentrations of less than 0.002 pptv and relative humidity starting at 60% and ending at 40%. The bars indicate 30% estimated total errors on the nucleation rates, although the overall systematic scale uncertainties of ±10% on the NH_3 mixing ratio and ±25% on the HNO_3 mixing ratio are not shown.

measured ambient size distributions—just as in Figs. 1, 2—and thus reflect a spatial and temporal average of air masses passing over a sampling site during the course of a day. Rapid growth rates can reduce CS:GR by a factor of ten or more, effectively displacing urban ratios into a range characteristic of remote regions (Extended Data Fig. 1b). The empirically derived nucleation rates in Extended Data Fig. 1b correlate positively with high CS:GR, consistent with high production rates of condensable vapours; however, the complicated microphysics of particles smaller than 10 nm make a simple determination of the growth rate difficult. Urban conditions are however far less homogeneous than those of CLOUD, or even of remote boreal forests such as Hyytiälä. Because survival probability depends exponentially on CS:GR (refs. [3,7]), but spatial (and temporal) averaging as well as ambient mixing are linear, real urban conditions may contain pockets conducive to transient rapid growth and thus unusually high survival probability that are blurred in the (averaged) observations.

The key here is that nitric acid vapour and ammonia are often at least one thousand times more abundant than sulfuric acid vapour. Thus, although they tend towards equilibrium with ammonium nitrate in the particle phase, even a modest perturbation above saturation can unleash a tremendous thermodynamic driving force for condensational growth, nominally up to one thousand times faster than growth by sulfuric acid condensation. This may be brief, but because of the disparity in concentrations, even a small deviation in saturation ratio above 1.0 may drive rapid growth for a short period at several nanometres per minute, as opposed to several nanometres per hour. The particles will not experience rapid growth for long, but they may grow fast enough to escape the valley of death.

We illustrate rapid growth in Fig. 4. Under most urban conditions, nucleation and early growth up to the activation size are likely to be controlled by sulfuric acid and a base (ammonia or an amine), shown by the red 'cores' in Fig. 4b. During the day (even in wintertime)—when NO_2 is oxidized by OH in the gas phase to produce nitric acid at rates of up to 3 ppbv h^{-1}, and ammonia from traffic, other combustion emissions and agriculture can reach 8 ppbv (ref. [24])—nitric acid and ammonia will not equilibrate, but rather will approach a modest steady-state supersaturation that drives ammonium nitrate formation to balance the production and emissions. However, this steady state will only be reached after several e-folding time periods set by the particle condensation sink. Typically, new-particle formation occurs at the lower end of the condensation-sink distribution (even under urban conditions)[2,7], so this timescale will be several minutes, or a length scale of hundreds of metres in the horizontal and tens of metres in the vertical. There are ample sources of inhomogeneity on this timescale, including inhomogeneous sources such as traffic on major roadways and vertical mixing (with an adiabatic lapse rate of −9 °C km^{-1})[24]. Further, large eddy simulations of a megacity (Hong Kong) confirm widespread eddies with spatial scales of tens to hundreds of metres and velocity perturbations of the order 1 m s^{-1} (ref. [26]). This is consistent with the sustained inhomogeneity required for the rapid growth we demonstrate here, shown conceptually in Fig. 4a. It is thus likely that dense urban conditions will typically include persistent inhomogeneities that maintain supersaturation of nitric acid and ammonia with sufficient magnitude to drive rapid growth, as indicated by the blue 'shell' in Fig. 4b. Our thermodynamic models support the phenomenology of Fig. 4b, as shown in Fig. 4c, d, although the composition is likely to be an amorphous mixture of salts (Extended Data Fig. 4).

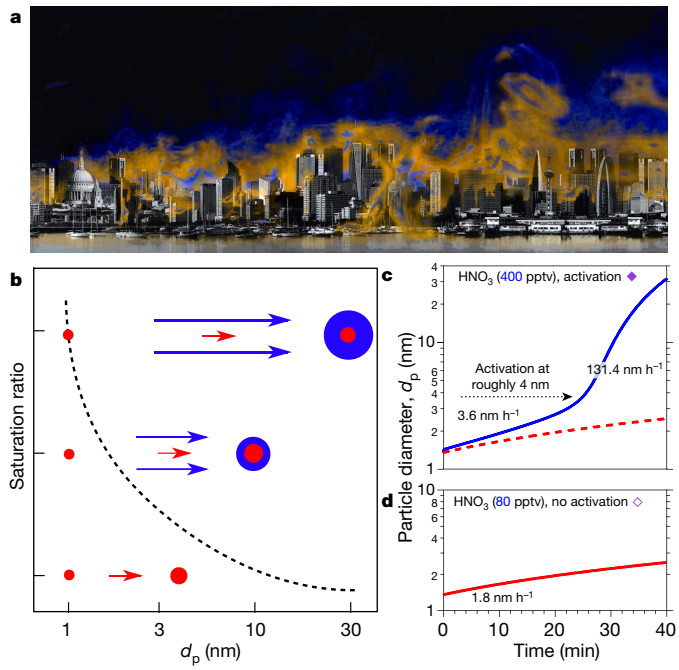

Fig. 4 | Conditions for rapid growth. Persistent supersaturations of ammonia and nitric acid with respect to ammonium nitrate will be sustained by inhomogeneity in urban conditions with high source strength. This will be sufficient to accelerate particle growth in the range 1–10 nm, where survival is threatened by the high coagulation sink of pre-existing particles from pollution. **a**, Conceptual image of urban conditions, where inhomogeneities in the concentrations of ammonia and nitric acid vapour and in temperatures are caused by non-uniform sources and large-scale eddies. **b**, Particles nucleate and grow slowly as (base-stabilized) sulfate (red). The activation size (shown with d_p on the *x*-axis) correlates inversely with the ammonium nitrate saturation ratio (shown qualitatively on the *y*-axis), as indicated by the dashed curve. Available concentrations of gas-phase nitric acid can exceed those of sulfuric acid by a factor of 1,000, so modest supersaturation drives rapid growth (blue) above an activation diameter determined by particle curvature (the Kelvin term). **c**, **d**, Monodisperse thermodynamic growth calculations (from MABNAG simulations) for high (**c**) and low (**d**) saturation ratios of ammonium nitrate, corresponding to **b** and to the closed and open diamonds towards the upper right in Fig. 3a. For a saturation ratio near 4, activation is predicted to occur near 4 nm, consistent with our observations.

Rapid growth may be sufficient for particles to grow from vulnerable sizes near 2.5 nm to more robust sizes larger than 10 nm. For example, repeated nucleation bursts with very rapid growth were observed in the ammonia- and nitric-acid-rich Cabauw site in the Netherlands during the EUCAARI campaign[27].

It is common for chemical transport models to use an equilibrium assumption for ammonium nitrate partitioning, because—on the time-scale of the coarse spatial grids and long time steps characteristic of large-scale models—the ammonium nitrate aerosol system should equilibrate with respect to the bulk submicrometre-size particles. Further, because rapid growth appears to be rate limited by the formation of ammonium nitrate, the covariance of base and nitric acid sources and concentrations may be essential. Even typical megacity steady-state vapour concentrations fall somewhat above the green points in Fig. 3a (towards larger mixing ratios). For constant production rates, as the temperature falls the ammonium nitrate saturation lines shown in Fig. 3a will sweep from the upper right towards the lower left, moving the system from rough equilibrium for typical urban production and emission rates when it is warmer than about +5 °C, to a sustained supersaturation when it is colder. Just as equilibrium organic condensation and partitioning results in underestimated growth rates from organics in the boreal forest[28], equilibrium treatments of ammonium nitrate condensation will underestimate the role of nitric acid in nanoparticle growth, especially for inhomogeneous urban environments.

Although the pure ammonium nitrate nucleation rates in Fig. 3c are too slow to compete in urban new-particle formation, this mechanism may provide an important source of new particles in the relatively clean and cold upper free troposphere, where ammonia can be convected from the continental boundary layer[29] and abundant nitric acid is produced by electrical storms[4]. Theoretical studies have also suggested that nitric acid may serve as a chaperone to facilitate sulfuric-acid–ammonia nucleation[30]. Larger (60–1,000 nm) particles consisting largely of ammonium nitrate, along with more than 1 ppbv of ammonia, have been observed by satellite in the upper troposphere during the Asian monsoon anticyclone[4], and abundant 3–7-nm particles have been observed in situ in the tropical convective region at low temperature and condensation sink[5]. Although these particles are probably formed via nucleation, the mechanism is not yet known. However, our experiment under similar conditions (Extended Data Fig. 3) shows that it is plausible that pure ammonium nitrate nucleation and/or rapid growth by ammonium nitrate condensation contributes to these particles in the upper troposphere.

Our results indicate that the condensation of nitric acid and ammonia is likely to be an important new mechanism for particle formation and growth in the cold upper free troposphere, as supported by recent observations[4,5]. Furthermore, this process could help to explain how newly formed particles survive scavenging losses in highly polluted urban environments[3]. As worldwide pollution controls continue to reduce SO_2 emissions sharply, the importance of NO_x and nitric acid for new-particle formation is likely to increase. In turn, controls on NO_x and ammonia emissions may become increasingly important, especially for the reduction of urban smog.

Online content

Any methods, additional references, Nature Research reporting summaries, source data, extended data, supplementary information, acknowledgements, peer review information; details of author contributions and competing interests; and statements of data and code availability are available at https://doi.org/10.1038/s41586-020-2270-4.

1. Stanier, C. O., Khlystov, A. Y. & Pandis, S. N. Nucleation events during the Pittsburgh Air Quality Study: description and relation to key meteorological, gas phase, and aerosol parameters. *Aerosol Sci. Technol.* **38**, 253–264 (2004).
2. Yao, L. et al. Atmospheric new particle formation from sulfuric acid and amines in a Chinese megacity. *Science* **361**, 278–281 (2018).
3. Kulmala, M., Kerminen, V.-M., Petäjä, T., Ding, A. J. & Wang, L. Atmospheric gas-to-particle conversion: why NPF events are observed in megacities? *Faraday Discuss.* **200**, 271–288 (2017).
4. Höpfner, M. et al. Ammonium nitrate particles formed in upper troposphere from ground ammonia sources during Asian monsoons. *Nat. Geosci.* **12**, 608–612 (2019).
5. Williamson, C. J. et al. A large source of cloud condensation nuclei from new particle formation in the tropics. *Nature* **574**, 399–403 (2019).
6. Intergovernmental Panel on Climate Change (IPCC). *Climate Change 2013: The Physical Science Basis* (Cambridge Univ. Press, 2013).
7. McMurry, P. H. et al. A criterion for new particle formation in the sulfur-rich Atlanta atmosphere. *J. Geophys. Res. D* **110**, D22S02 (2005).
8. Kulmala, M. et al. Direct observations of atmospheric aerosol nucleation. *Science* **339**, 943–946 (2013).
9. Gordon, H. et al. Causes and importance of new particle formation in the present-day and pre-industrial atmospheres. *J. Geophys. Res. D* **122**, 8739–8760 (2017).
10. Riipinen, I. et al. Contribution of organics to atmospheric nanoparticle growth. *Nat. Geosci.* **5**, 453–458 (2012).
11. Pierce, J. R. & Adams, P. J. Efficiency of cloud condensation nuclei formation from ultrafine particles. *Atmos. Chem. Phys.* **7**, 1367–1379 (2007).
12. Kuang, C., McMurry, P. H. & McCormick, A. V. Determination of cloud condensation nuclei production from measured new particle formation events. *Geophys. Res. Lett.* **36**, L09822 (2009).
13. Apte, J. S., Brauer, M., Cohen, A. J., Ezzati, M. & Pope, C. A. Ambient $PM_{2.5}$ reduces global and regional life expectancy. *Environ. Sci. Technol. Lett.* **5**, 546–551 (2018).
14. Chen, G., Wang, W.-C. & Chen, J.-P. Circulation responses to regional aerosol climate forcing in summer over East Asia. *Clim. Dyn.* **51**, 3973–3984 (2018).

15. Kerminen, V.-M. & Kulmala, M. Analytical formulae connecting the "real" and the "apparent" nucleation rate and the nuclei number concentration for atmospheric nucleation events. *J. Aerosol Sci.* **33**, 609–622 (2002).
16. Takahama, S., Wittig, A. E., Vayenas, D. V., Davidson, C. I. & Pandis, S. N. Modeling the diurnal variation of nitrate during the Pittsburgh Air Quality Study. *J. Geophys. Res. D* **109**, D16S06 (2004).
17. Xu, W. et al. Changes in aerosol chemistry from 2014 to 2016 in winter in Beijing: insights from high-resolution aerosol mass spectrometry. *J. Geophys. Res. D* **124**, 1132–1147 (2019).
18. McMurry, P. H. Photochemical aerosol formation from SO_2: a theoretical analysis of smog chamber data. *J. Colloid Interface Sci.* **78**, 513–527 (1980).
19. Kirkby, J. et al. Ion-induced nucleation of pure biogenic particles. *Nature* **533**, 521–526 (2016).
20. Stolzenburg, D. et al. Rapid growth of organic aerosol nanoparticles over a wide tropospheric temperature range. *Proc. Natl Acad. Sci. USA* **115**, 9122–9127 (2018).
21. O'Dowd, C. D. et al. Marine aerosol formation from biogenic iodine emissions. *Nature* **417**, 632–636 (2002).
22. Kirkby, J. et al. Role of sulphuric acid, ammonia and galactic cosmic rays in atmospheric aerosol nucleation. *Nature* **476**, 429–433 (2011).
23. Kontkanen, J., Olenius, T., Kulmala, M. & Riipinen, I. Exploring the potential of nano-köhler theory to describe the growth of atmospheric molecular clusters by organic vapors using cluster kinetics simulations. *Atmos. Chem. Phys.* **18**, 13733–13754 (2018).
24. Lu, K. et al. Fast photochemistry in wintertime haze: consequences for pollution mitigation strategies. *Environ. Sci. Technol.* **53**, 10676–10684 (2019).
25. Yli-Juuti, T. et al. Model for acid-base chemistry in nanoparticle growth (MABNAG). *Atmos. Chem. Phys.* **13**, 12507–12524 (2013).
26. Letzel, M. O. et al. LES case study on pedestrian level ventilation in two neighbourhoods in Hong Kong. *Meteorol. Z. (Berl.)* **21**, 575–589 (2012).
27. Manninen, H. E. et al. EUCAARI ion spectrometer measurements at 12 European sites – analysis of new particle formation events. *Atmos. Chem. Phys.* **10**, 7907–7927 (2010).
28. Pierce, J. R. et al. Quantification of the volatility of secondary organic compounds in ultrafine particles during nucleation events. *Atmos. Chem. Phys.* **11**, 9019–9036 (2011).
29. Ge, C., Zhu, C., Francisco, J. S., Zeng, X. C. & Wang, J. A molecular perspective for global modeling of upper atmospheric NH_3 from freezing clouds. *Proc. Natl Acad. Sci. USA* **115**, 6147–6152 (2018).
30. Liu, L. et al. The role of nitric acid in atmospheric new particle formation. *Phys. Chem. Chem. Phys.* **20**, 17406–17414 (2018).

Mingyi Wang[1,2,30], Weimeng Kong[3,30], Ruby Marten[4], Xu-Cheng He[5], Dexian Chen[1,6], Joschka Pfeifer[7], Arto Heitto[8], Jenni Kontkanen[5], Lubna Dada[5], Andreas Kürten[9], Taina Yli-Juuti[8], Hanna E. Manninen[7], Stavros Amanatidis[3], António Amorim[10], Rima Baalbaki[5], Andrea Baccarini[4], David M. Bell[4], Barbara Bertozzi[11], Steffen Bräkling[12], Sophia Brilke[13], Lucía Caudillo Murillo[9], Randall Chiu[14], Biwu Chu[5], Louis-Philippe De Menezes[7], Jonathan Duplissy[5,15], Henning Finkenzeller[14], Loic Gonzalez Carracedo[13], Manuel Granzin[9], Roberto Guida[7], Armin Hansel[16,17], Victoria Hofbauer[1,2], Jordan Krechmer[18], Katrianne Lehtipalo[5,19], Houssni Lamkaddam[4], Markus Lampimäki[5], Chuan Ping Lee[4], Vladimir Makhmutov[20], Guillaume Marie[9], Serge Mathot[7], Roy L. Mauldin[1,2,21], Bernhard Mentler[16], Tatjana Müller[9], Antti Onnela[7], Eva Partoll[16], Tuukka Petäjä[5], Maxim Philippov[20], Veronika Pospisilova[4], Ananth Ranjithkumar[22], Matti Rissanen[5,23], Birte Rörup[5], Wiebke Scholz[16,17], Jiali Shen[5], Mario Simon[9], Mikko Sipilä[5], Gerhard Steiner[16,24], Dominik Stolzenburg[5,13], Yee Jun Tham[5], António Tomé[25], Andrea C. Wagner[9,14], Dongyu S. Wang[4], Yonghong Wang[5], Stefan K. Weber[7], Paul M. Winkler[13], Peter J. Wlasits[13], Yusheng Wu[5], Mao Xiao[4], Qing Ye[1,2,26], Marcel Zauner-Wieczorek[9], Xueqin Zhou[4], Rainer Volkamer[14], Ilona Riipinen[27], Josef Dommen[4], Joachim Curtius[9], Urs Baltensperger[4], Markku Kulmala[5,15,28,29], Douglas R. Worsnop[5,18], Jasper Kirkby[7,9], John H. Seinfeld[3], Imad El-Haddad[4], Richard C. Flagan[3] & Neil M. Donahue[1,6,2,26]✉

[1]Center for Atmospheric Particle Studies, Carnegie Mellon University, Pittsburgh, PA, USA. [2]Department of Chemistry, Carnegie Mellon University, Pittsburgh, PA, USA. [3]Division of Chemistry and Chemical Engineering, California Institute of Technology, Pasadena, CA, USA. [4]Laboratory of Atmospheric Chemistry, Paul Scherrer Institute, Villigen, Switzerland. [5]Institute for Atmospheric and Earth System Research (INAR), University of Helsinki, Helsinki, Finland. [6]Department of Chemical Engineering, Carnegie Mellon University, Pittsburgh, PA, USA. [7]CERN, the European Organization for Nuclear Research, Geneva, Switzerland. [8]Department of Applied Physics, University of Eastern Finland, Kuopio, Finland. [9]Institute for Atmospheric and Environmental Sciences, Goethe University Frankfurt, Frankfurt am Main, Germany. [10]CENTRA and Faculdade de Ciências da Universidade de Lisboa, Campo Grande, Lisbon, Portugal. [11]Institute of Meteorology and Climate Research, Karlsruhe Institute of Technology, Karlsruhe, Germany. [12]Tofwerk, Thun, Switzerland. [13]Faculty of Physics, University of Vienna, Vienna, Austria. [14]Department of Chemistry and CIRES, University of Colorado at Boulder, Boulder, CO, USA. [15]Helsinki Institute of Physics, University of Helsinki, Helsinki, Finland. [16]Institute for Ion Physics and Applied Physics, University of Innsbruck, Innsbruck, Austria. [17]Ionicon Analytik, Innsbruck, Austria. [18]Aerodyne Research, Billerica, MA, USA. [19]Finnish Meteorological Institute, Helsinki, Finland. [20]P.N. Lebedev Physical Institute of the Russian Academy of Sciences, Moscow, Russia. [21]Department of Atmospheric and Oceanic Sciences, University of Colorado at Boulder, Boulder, CO, USA. [22]School of Earth and Environment, University of Leeds, Leeds, UK. [23]Aerosol Physics Laboratory, Physics Unit, Faculty of Engineering and Natural Sciences, Tampere University, Tampere, Finland. [24]Grimm Aerosol Technik Ainring, Ainring, Germany. [25]Institute Infante Dom Luíz, University of Beira Interior, Covilhã, Portugal. [26]Department of Engineering and Public Policy, Carnegie Mellon University, Pittsburgh, PA, USA. [27]Department of Applied Environmental Science, University of Stockholm, Stockholm, Sweden. [28]Joint International Research Laboratory of Atmospheric and Earth System Sciences, Nanjing University, Nanjing, China. [29]Aerosol and Haze Laboratory, Beijing Advanced Innovation Center for Soft Matter Science and Engineering, Beijing University of Chemical Technology, Beijing, China. [30]These authors contributed equally: Mingyi Wang, Weimeng Kong. ✉e-mail: nmd@andrew.cmu.edu

Methods

The CLOUD facility

We conducted our measurements at the CERN CLOUD facility, a 26.1 m^3 electropolished stainless-steel chamber that enables new-particle-formation experiments under the full range of tropospheric conditions with scrupulous cleanliness and minimal contamination[22,31]. The CLOUD chamber is mounted in a thermal housing, capable of keeping temperature constant in a range between −65 °C and +100 °C with ±0.1 °C precision[32], and relative humidity between 0.5% and 101%. Photochemical processes are initiated by homogeneous illumination with a built-in ultraviolet fibre-optic system, including four 200-W Hamamatsu Hg–Xe lamps at wavelengths between 250 nm and 450 nm and a 4-W KrF excimer ultraviolet laser at 248 nm with adjustable power. Ion-induced nucleation under different ionization levels is simulated with a combination of electric fields (±30 kV) and a high-flux beam of 3.6-GeV pions (π^+), which can artificially scavenge or enhance small ions. Uniform spatial mixing is achieved with magnetically coupled stainless-steel fans mounted at the top and bottom of the chamber. The characteristic gas mixing time in the chamber during experiments is a few minutes. The loss rate of condensable vapours and particles onto the chamber walls is comparable to the ambient condensation sink. To avoid contamination, the chamber is periodically cleaned by rinsing the walls with ultrapure water and heating to 100 °C for at least 24 h, ensuring extremely low contaminant levels of sulfuric acid (less than 5×10^4 cm^{-3}) and total organics (less than 50 pptv)[19,33]. The CLOUD gas system is also built to the highest technical standards of cleanliness and performance. The dry air supply for the chamber is provided by boil-off oxygen (Messer, 99.999%) and boil-off nitrogen (Messer, 99.999%) mixed at the atmospheric ratio of 79:21. Highly pure water vapour, ozone and other trace gases can be precisely added at the pptv level.

Typical experimental sequence

To investigate the role of nitric acid in new-particle formation, we performed particle growth experiments at $T = -10$ °C, +5 °C and +20 °C, and (for the most part) at relative humidities of approximately 60%. A typical experiment started with illumination of the chamber at constant ozone (O_3) to photochemically produce •OH radicals. The subsequent oxidation of premixed SO_2, NO_2 and anthropogenic volatile organic compounds (VOCs; that is, toluene or cresol) led to the production of H_2SO_4, HNO_3 and highly oxygenated organic molecules (HOMs), respectively. As a result, nucleation was induced, followed (once the particles reached an activation diameter, d_{act}) by rapid growth via condensation of nitric acid and ammonia. In some experiments, we also injected nitric acid vapour directly into the CLOUD chamber from an ultrapure source to cover a wide range of conditions. In addition, to prove consistency we also carried out experiments with a biogenic precursor, α-pinene, replacing anthropogenic VOCs, as well as experiments without any organic vapours. For the experiments we focus on here, the HOM concentrations were either zero or small enough to have a minor effect on the experiment. In one case, we cooled the particle-free chamber (with fewer than 1 particle per cm^{-3}) continuously from −10 °C to −25 °C, while holding nitric acid and ammonia at a constant level, but with no sulfuric acid (less than 5×10^4 cm^{-3} or 2×10^{-3} pptv). We observed new-particle formation purely from nitric acid and ammonia at temperatures of −15 °C and lower. The nucleation rate grew as the temperature dropped. Moreover, as shown in Extended Data Fig. 3, at −25 °C new-particle formation events appeared to be quenched when we swept out primary ions with the electric field, and did not return until the field was turned off to allow primary ion production by galactic cosmic rays to again accumulate (roughly 700 cm^{-3}). We list the chamber conditions and key parameters for all the experiments here in Extended Data Table 1.

Instrumentation

To measure gas-phase nitric acid, we deployed a bromide chemical ionization atmospheric pressure interface time-of-flight (CI-APi-TOF) mass spectrometer[34,35] equipped with a commercial inlet (Airmodus) to minimize wall contact of the sample[36]. We flowed dibromomethane (CH_2Br_2) into the ion-molecule reaction inlet to produce the primary reagent ion Br^-. During its collision with HNO_3, Br^- reacts either to form a cluster or via a proton transfer from the HNO_3 to form NO_3^-:

$$Br^- + HNO_3 \rightarrow HNO_3 \cdot Br^-$$

$$Br^- + HNO_3 \rightarrow HBr + NO_3^-$$

To take the variation in the total reagent ions into account, we quantified nitric acid concentrations according to:

$$[HNO_3] = \frac{[NO_3^-]}{[Br^-] + [H_2O \cdot Br^-]} \times C$$

where C (in units of pptv) is a calibration coefficient obtained by measuring HNO_3/N_2 mixtures with known nitric acid concentrations. The nitric acid source was a portable permeation tube, kept constantly at 40 °C. An N_2 flow of 2 litres per minute was introduced into the permeation device to carry out the nitric acid vapour. To determine the permeation rate of nitric acid, we passed the outflow of the permeation tube through an impinger containing deionized water, and analysed the resulting nitric acid solution by spectrophotometry. Line losses during experiments and calibration procedures were calculated separately. We determined the corrected calibration coefficient to be 7,364 pptv.

Gas-phase ammonia was measured by a water cluster CI-APi-TOF mass spectrometer (described elsewhere[37]). The crossflow ion source coupled to a TOF mass spectrometer enables the selective measurement of basic compounds (for example, ammonia) by using positively charged water clusters as primary ions. Owing to the low reaction times (less than 1 ms), the instrument responds rapidly to changing chamber conditions with a detection limit of ammonia of 0.5 pptv.

Gas-phase sulfuric acid and HOMs were routinely measured with a detection limit of approximately 5×10^4 cm^{-3} by two nitrate CI-APi-TOF mass spectrometers. One instrument was equipped with the Airmodus inlet and an X-ray generator as the ion source; the other deployed a home-made inlet and a corona discharge for ion generation[38]. An electrostatic filter was installed in front of each instrument to remove ions and charged clusters formed in the chamber. Sulfuric acid and HOMs were quantified following calibration and loss correction procedures described previously[19,22,39].

VOCs were monitored by a proton transfer reaction time-of-flight mass spectrometer (PTR-TOF-MS; Ionicon Analytik); this also provides information about the overall cleanliness regarding VOCs in the chamber. The technique has been extensively described previously[40]. Direct calibration using diffusion sources allows us to determine VOC mixing ratios with an accuracy of 5% and a typical detection limit of 25 pptv (ref. [41]).

Gas monitors were used to measure ozone (O_3; Thermo Environmental Instruments TEI 49C), sulfur dioxide (SO_2; Thermo Fisher Scientific 42i-TLE) and nitric oxide (NO; ECO Physics, CLD 780TR). Nitrogen dioxide (NO_2) was measured using a cavity-attenuated phase-shift NO_2 monitor (CAPS NO_2, Aerodyne Research) and a homemade cavity-enhanced differential optical absorption spectroscopy (CE-DOAS) instrument. The relative humidity of the chamber was determined using dew point mirrors (EdgeTech).

We measured the particle-phase composition via thermal desorption using an iodide-adduct chemical ionization time-of-flight mass spectrometer equipped with a filter inlet for gases and aerosols (FIGAERO-CIMS)[42,43]. FIGAERO is a manifold inlet for a CIMS with

two operating modes. In one mode, gases are directly sampled into a 100-mbar turbulent flow ion-molecule reactor while particles are concurrently collected on a polytetrafluorethylene (PTFE) filter via a separate dedicated port. In the other mode, the filter is automatically moved into a pure N_2 gas stream flowing into the ion-molecule reactor while the N_2 is progressively heated to evaporate the particles via temperature-programmed desorption. Analytes are then chemically ionized and extracted into a TOF-MS, achieving a detection limit below 10^6 cm^{-3}.

Particle-size distributions between 1.8 nm and 500 nm were monitored continuously by a differential mobility analyser train (DMA-Train), a nano-scanning electrical mobility spectrometer (nSEMS), a nano-scanning mobility particle sizer (nano-SMPS), and a long-SMPS. The DMA-Train was constructed with six identical DMAs operating at different, but fixed, voltages. Particles transmitted through the DMAs were then detected by either a particle-size magnifier (PSM) or a CPC, depending on the size ranges. An approximation of the size distribution with 15 size bins was acquired by logarithmic interpolation between the six channels[44]. The nSEMS used a new, radial opposed migration ion and aerosol classifier (ROMIAC), which is less sensitive to diffusional resolution degradation than the DMAs[45], and a soft X-ray charge conditioner. After leaving the classifier, particles were first activated in a fast-mixing diethylene glycol stage[46], and then counted with a butanol-CPC. The nSEMS transfer function that was used to invert the data to obtain the particle-size distribution was derived using three-dimensional finite-element modelling of the flows, electric field and particle trajectories[47,48]. The two commercial mobility particle-size spectrometers, nano-SMPS and long-SMPS, have been fully characterized, calibrated and validated in several previous studies[49–51].

Determination of growth rate

The combined particle-size distribution was reconstructed using measurement data from DMA-Train at 1.8–4.3 nm, nSEMS at 4.3–18.1 nm, nano-SMPS at 18.1–55.2 nm and long-SMPS at 55.2–500 nm, and synchronized with long-SMPS measurement time. We list the sizing and resolution information of these instruments in Extended Data Table 2. As depicted in Extended Data Fig. 5a, the four instruments showed excellent agreement in their overlapping regions of the size ranges. The total number concentration obtained by integrating the combined size distribution agreed well with measurement by an Airmodus A11 nano-condensation nucleus counter (nCNC) and a TSI 3776 ultrafine condensation particle counter (UCPC) (Extended Data Fig. 5b). Particle growth rate, dd_p/dt, was then determined from the combined size distributions using the 50% appearance time method[20], as a clear front of a growing particle population could be identified during most rapid growth events (Extended Data Fig. 6). For the rapid growth rates, which are the principal focus here, the SMPS measurements provided the major constraint.

Determination of activation diameter

The activation diameter (d_{act}) was interpreted as the size at which growth accelerated from the slow, initial rate to the rapid, post-activation rate. The activation diameter was determined using the particle-size distribution acquired from DMA-Train or nSEMS at small sizes (less than 15 nm). At the activation diameter, the growth rate calculated from the 50% appearance time usually experienced a sharp change, from below 10 nm h^{-1} to (often) over 100 nm h^{-1}, depending on concentrations of supersaturated HNO_3 and NH_3 vapours. A fast growth rate leads to a relatively low steady-state concentration of particles just above the activation diameter; the activation event often resulted in a notable gap in the particle-number size distribution. In some cases, a clear bimodal distribution was observed, with the number concentration in one size bin plunging below 10 counts cm^{-3}, while the counts at larger sizes rose to more than 100 counts cm^{-3}; the centroid diameter of the size bin at which the number concentration dropped was then defined as the activation diameter (Extended Data Fig. 2a).

Calculation of saturation ratio

We model the ammonium nitrate formed in the particle phase as solid in our particle growth experiments, given that the relative humidity (roughly 60%) was less than the deliquescence relative humidity (DRH), given by[52]:

$$\ln(\mathrm{DRH}) = \frac{723.7}{T} + 1.6954$$

The dissociation constant, K_p, is defined as the product of the equilibrium partial pressures of HNO_3 and NH_3. K_p can be estimated by integrating the van't Hoff equation[53]. The resulting equation for K_p in units of ppb^2 (assuming 1 atm of total pressure)[54] is:

$$\ln K_p = 118.87 - \frac{24{,}084}{T} - 6.025 \ln T$$

The saturation ratio, S, is thus calculated by dividing the product of measured mixing ratios of HNO_3 and NH_3 by the dissociation constant. The dissociation constant is quite sensitive to temperature changes, varying over more than two orders of magnitude for typical ambient conditions. Several degrees of temperature drop can lead to a much higher saturation ratio, shifting the equilibrium of the system towards the particle phase drastically. As illustrated in Extended Data Fig. 7, with an adiabatic lapse rate of −9 °C km^{-1} during fast vertical mixing, upward transport of a few hundred metres alone is sufficient for a saturated nitric acid and ammonia air parcel to reach the saturation ratio capable of triggering rapid growth at a few nanometres.

Determination of nucleation rate

The nucleation rate, $J_{1.7}$, is determined here at a mobility diameter of 1.7 nm (a physical diameter of 1.4 nm) using particle size magnifier (PSM). At 1.7 nm, a particle is normally considered to be above its critical size and, therefore, thermodynamically stable. $J_{1.7}$ is calculated using the flux of the total concentration of particles growing past a specific diameter (here at 1.7 nm), as well as correction terms accounting for aerosol losses due to dilution in the chamber, wall losses and coagulation. Details can be found in our previous work[55].

The MABNAG model

To compare our measurements to thermodynamic predictions (including the Kelvin term for curved surfaces), we used the model for acid-base chemistry in nanoparticle growth (MABNAG)[25]. MABNAG is a monodisperse particle population growth model that calculates the time evolution of particle composition and size on the basis of concentrations of condensing gases, relative humidity and ambient temperature, considering also the dissociation and protonation between acids and bases in the particle phase. In the model, water and bases are assumed always to be in equilibrium state between the gas and particle phases. Mass fluxes of acids to and from the particles are determined on the basis of their gas phase concentrations and their equilibrium vapour concentrations. In order to solve for the dissociation- and composition-dependent equilibrium concentrations, MABNAG couples a particle growth model to the extended aerosol inorganics model (E-AIM)[56,57]. Here, we assumed particles in MABNAG to be liquid droplets at +5 °C and −10 °C, at 60% relative humidity. The simulation system consisted of four compounds: water, ammonia, sulfuric acid and nitric acid. The initial particle composition in each simulation was 40 sulfuric acid molecules and a corresponding amount of water and ammonia according to gas-particle equilibrium on the basis of their gas concentrations. With this setting, the initial diameter was approximately 2 nm. Particle density and surface tension were set to 1,500 kg m^{-3} and

0.03 N m^{-1}, respectively. In Extended Data Fig. 4, we show that MAGNAG computations confirm that nitric acid and ammonia at the measured concentrations can activate small particles and cause rapid growth, and also confirm that the activation diameter depends on the ammonium nitrate saturation ratio, consistent with our measured diameter (diamonds in Fig. 3a).

Nano-Köhler theory

To prove consistency, we also calculated the equilibrium saturation ratios of ammonium nitrate above curved particle surfaces according to nano-Köhler theory[23]. This theory describes the activation of nanometre-sized inorganic clusters to growth by vapour condensation, which is analogous to Köhler theory describing the activation of cloud condensation nuclei (CCN) to cloud droplets. Here, we assumed seed particles of ammonium sulfate, and performed calculations for three seed-particle diameters (d_s = 1.4 nm, 2.0 nm and 2.9 nm) at +5 °C and −10 °C, and at 60% relative humidity. The equilibrium vapour pressures of HNO_3 and NH_3 over the liquid phase, and the surface tension and density of the liquid phase, were obtained from an E-AIM[56,57]. The equilibrium saturation ratios of ammonium nitrate were calculated as described in the Methods section 'Calculation of saturation ratio', also including the Kelvin term. The resulting Köhler curves, showing the equilibrium saturation ratio as a function of particle diameter, are presented in Extended Data Fig. 2c. The maxima of each curve corresponds to the activation diameter (d_{act}); saturation ratios of 10–50 lead to d_{act} values of 3–5 nm, consistent with our measurements in Fig. 3a. We summarize detailed results in Extended Data Table 1.

Ambient nucleation and growth

In Extended Data Table 3 we compile ambient observations of nucleation rates, growth rates and the ambient condensation sink. In most cases these are derived from evolving particle-size distributions. We summarize these observations in Extended Data Fig. 1.

Data availability

The full dataset shown in the figures and tables is publicly available[58]. All data shown in the figures and tables and additional raw data are available upon request from the corresponding author. Source data for Figs. 1–4 and Extended Data Figs. 1–7 are provided with the paper.

Code availability

Codes for the MABNAG and nano-Köhler simulations and for conducting the analysis presented here can be obtained upon request from the corresponding author.

31. Duplissy, J. et al. Effect of ions on sulfuric acid-water binary particle formation: 2. Experimental data and comparison with QC-normalized classical nucleation theory. *J. Geophys. Res. D* **121**, 1752–1775 (2016).
32. Dias, A. et al. Temperature uniformity in the CERN CLOUD chamber. Aerosol *Meas. Tech.* **10**, 5075–5088 (2017).
33. Schnitzhofer, R. et al. Characterisation of organic contaminants in the CLOUD chamber at CERN. *Aerosol Meas. Techn.* **7**, 2159–2168 (2014).
34. Jokinen, T. et al. Atmospheric sulphuric acid and neutral cluster measurements using CI-APi-TOF. *Atmos. Chem. Phys.* **12**, 4117–4125 (2012).
35. Junninen, H. et al. A high-resolution mass spectrometer to measure atmospheric ion composition. *Atmos. Meas. Tech.* **3**, 1039–1053 (2010).
36. Eisele, F. & Tanner, D. Measurement of the gas phase concentration of H_2SO_4 and methane sulfonic acid and estimates of H_2SO_4 production and loss in the atmosphere. *J. Geophys. Res. D* **98**, 9001–9010 (1993).
37. Pfeifer, J. et al. Measurement of ammonia, amines and iodine species using protonated water cluster chemical ionization mass spectrometry. *Atmos. Meas. Tech.* https://doi.org/10.5194/amt-2019-215 (2019).
38. Kürten, A., Rondo, L., Ehrhart, S. & Curtius, J. Performance of a corona ion source for measurement of sulfuric acid by chemical ionization mass spectrometry. *Atmos. Meas. Tech.* **4**, 437–443 (2011).
39. Tröstl, J. et al. The role of low-volatility organic compounds in initial particle growth in the atmosphere. *Nature* **533**, 527–531 (2016).
40. Breitenlechner, M. et al. PTR3: an instrument for studying the lifecycle of reactive organic carbon in the atmosphere. *Anal. Chem.* **89**, 5824–5831 (2017).
41. Gautrois, M. & Koppmann, R. Diffusion technique for the production of gas standards for atmospheric measurements. *J. Chromatogr. A* **848**, 239–249 (1999).
42. Wang, M. et al. Reactions of atmospheric particulate stabilized Criegee intermediates lead to high molecular weight aerosol components. *Environ. Sci. Technol.* **50**, 5702–5710 (2016).
43. Lopez-Hilfiker, F. D. et al. A novel method for online analysis of gas and particle composition: description and evaluation of a Filter Inlet for Gases and AEROsols (FIGAERO). *Atmos. Meas. Tech.* **7**, 983–1001 (2014).
44. Stolzenburg, D., Steiner, G. & Winkler, P. M. A DMA-train for precision measurement of sub-10 nm aerosol dynamics. *Atmos. Meas. Tech.* **10**, 1639–1651 (2017).
45. Mui, W., Mai, H., Downard, A. J., Seinfeld, J. H. & Flagan, R. C. Design, simulation, and characterization of a radial opposed migration ion and aerosol classifier (ROMIAC). *Aerosol Sci. Technol.* **51**, 801–823 (2017).
46. Wimmer, D. et al. Performance of diethylene glycol-based particle counters in the sub-3 nm size range. *Atmos. Meas. Tech.* **6**, 1793–1804 (2013).
47. Mai, H. & Flagan, R. C. Scanning DMA data analysis I. Classification transfer function. *Aerosol Sci. Technol.* **52**, 1382–1399 (2018).
48. Mai, H., Kong, W., Seinfeld, J. H. & Flagan, R. C. Scanning DMA data analysis II. Integrated DMA-CPC instrument response and data inversion. *Aerosol Sci. Technol.* **52**, 1400–1414 (2018).
49. Jurányi, Z. et al. A 17 month climatology of the cloud condensation nuclei number concentration at the high alpine site Jungfraujoch. *J. Geophys. Res. D* **116**, D10204 (2011).
50. Tröstl, J. et al. Fast and precise measurement in the sub-20 nm size range using a scanning mobility particle sizer. *J. Aerosol Sci.* **87**, 75–87 (2015).
51. Wiedensohler, A. et al. Mobility particle size spectrometers: harmonization of technical standards and data structure to facilitate high quality long-term observations of atmospheric particle number size distributions. *Atmos. Meas. Tech.* **5**, 657–685 (2012).
52. Seinfeld, J. H. & Pandis, S. N. *Atmospheric Chemistry and Physics* 2nd edn (John Wiley & Sons, 2006).
53. Denbigh, K. G. & Denbigh, K. G. *The Principles of Chemical Equilibrium: With Applications in Chemistry and Chemical Eengineering* (Cambridge Univ. Press, 1981).
54. Mozurkewich, M. The dissociation constant of ammonium nitrate and its dependence on temperature, relative humidity and particle size. *Atmos. Environ. A* **27**, 261–270 (1993).
55. Lehtipalo, K. et al. Multi-component new particle formation from sulfuric acid, ammonia and biogenic vapors. *Sci. Adv.* **4**, eaau5363 (2018).
56. Clegg, S. L. & Seinfeld, J. H. Thermodynamic models of aqueous solutions containing inorganic electrolytes and dicarboxylic acids at 298.15 K. 1. The acids as nondissociating components. *J. Phys. Chem. A* **110**, 5692–5717 (2006).
57. Clegg, S. L. & Seinfeld, J. H. Thermodynamic models of aqueous solutions containing inorganic electrolytes and dicarboxylic acids at 298.15 K. 2. Systems including dissociation equilibria. *J. Phys. Chem. A* **110**, 5718–5734 (2006).
58. Wang, M. et al. Rapid growth of new atmospheric particles by nitric acid and ammonia condensation: data resources. https://doi.org/10.5281/zenodo.3653377 (2020).
59. Xiao, S. et al. Strong atmospheric new particle formation in winter in urban Shanghai, China. *Atmos. Chem. Phys.* **15**, 1769–1781 (2015).
60. Iida, K., Stolzenburg, M. R., McMurry, P. H. & Smith, J. N. Estimating nanoparticle growth rates from size-dependent charged fractions: Analysis of new particle formation events in Mexico City. *J. Geophys. Res. D Atmospheres* **113**, D05207 (2008).
61. Mordas, G. et al. On operation of the ultra-fine water-based CPC TSI 3786 and comparison with other TSI models (TSI 3776, TSI 3772, TSI 3025, TSI 3010, TSI 3007). *Aerosol Sci. Technol.* **42**, 152–158 (2008).
62. Lehtipalo, K. et al. The effect of acid-base clustering and ions on the growth of atmospheric nano-particles. *Nat. Commun.* **7**, 11594 (2016).
63. Dal Maso, M. et al. Aerosol size distribution measurements at four Nordic field stations: identification, analysis and trajectory analysis of new particle formation bursts. *Tellus B Chem. Phys. Meterol.* **59**, 350–361 (2007).
64. Dal Maso, M. et al. Formation and growth of fresh atmospheric aerosols: eight years of aerosol size distribution data from SMEAR II, Hyytiälä, Finland. *Boreal Environ. Res.* **10**, 323–326 (2005).
65. Komppula, M. et al. Observations of new particle formation and size distributions at two different heights and surroundings in subarctic area in northern finland. *J. Geophys. Res. D Atmospheres* **108** (D9), 4295 (2003).
66. Vehkamäki, H. et al. Atmospheric particle formation events at Värriö measurement station in Finnish Lapland 1998-2002. *Atmos. Chem. Phys.* **4**, 2015–2023 (2004).
67. Dal Maso, M. et al. Aerosol particle formation events at two Siberian stations inside the boreal forest. *Boreal Environ. Res.* **13**, 81–92 (2008).
68. Hussein, T. et al. Observation of regional new particle formation in the urban atmosphere. *Tellus B Chem. Phys. Meterol.* **60**, 509–521 (2008).
69. Pikridas, M. et al. In situ formation and spatial variability of particle number concentration in a European megacity. *Atmos. Chem. Phys.* **15**, 10219–10237 (2015).
70. Hamed, A. et al. Nucleation and growth of new particles in Po Valley, Italy. *Atmos. Chem. Phys.* **7**, 355–376 (2007).
71. Hama, S. M., Cordell, R. L., Kos, G. P., Weijers, E. & Monks, P. S. Sub-micron particle number size distribution characteristics at two urban locations in leicester. *Atmos. Res.* **194**, 1–16 (2017).
72. Gao, J., Chai, F., Wang, T., Wang, S. & Wang, W. Particle number size distribution and new particle formation: new characteristics during the special pollution control period in Beijing. *J. Environ. Sci.* **24**, 14–21 (2012).
73. Wang, Z. et al. Characteristics of regional new particle formation in urban and regional background environments in the North China Plain. *Atmos. Chem. Phys.* **13**, 12495–12506 (2013).
74. Yue, D. et al. Characteristics of aerosol size distributions and new particle formation in the summer in Beijing. *J. Geophys. Res. D Atmospheres* **114**, D00G12 (2009).
75. Zhang, Y. et al. Characterization of new particle and secondary aerosol formation during summertime in Beijing, *China. Tellus B Chem. Phys. Meterol.* **63**, 382–394 (2011).
76. Man, H. et al. Comparison of daytime and nighttime new particle growth at the HKUST supersite in Hong Kong. *Environ. Sci. Technol.* **49**, 7170–7178 (2015).

77. An, J. et al. Characteristics of new particle formation events in Nanjing, China: effect of water-soluble ions. *Atmos. Environ.* **108**, 32–40 (2015).
78. Herrmann, E. et al. Aerosols and nucleation in eastern China: first insights from the new SORPES-NJU station. *Atmos. Chem. Phys.* **14**, 2169–2183 (2014).
79. Yu, H. et al. Nucleation and growth of sub-3 nm particles in the polluted urban atmosphere of a megacity in China. *Atmos. Chem. Phys.* **16**, 2641–2657 (2016).
80. Peng, J. et al. Submicron aerosols at thirteen diversified sites in China: size distribution, new particle formation and corresponding contribution to cloud condensation nuclei production. *Atmos. Chem. Phys.* **14**, 10249–10265 (2014).
81. Kanawade, V. et al. Infrequent occurrence of new particle formation at a semi-rural location, Gadanki, in tropical Southern India. *Atmos. Environ.* **94**, 264–273 (2014).
82. Mönkkönen, P. et al. Measurements in a highly polluted Asian mega city: observations of aerosol number size distribution, modal parameters and nucleation events. *Atmos. Chem. Phys.* **5**, 57–66 (2005).
83. Kuang, C. et al. An improved criterion for new particle formation in diverse atmospheric environments. *Atmos. Chem. Phys.* **10**, 8469–8480 (2010).
84. Iida, K. et al. Contribution of ion-induced nucleation to new particle formation: Methodology and its application to atmospheric observations in Boulder, Colorado. *J. Geophys. Res. D Atmospheres* **111**, D23201 (2006).

Acknowledgements We thank the European Organization for Nuclear Research (CERN) for supporting CLOUD with technical and financial resources and for providing a particle beam from the CERN Proton Synchrotron. This research has received funding from the US National Science Foundation (NSF; grant numbers AGS1602086, AGS1801329 and AGS-1801280); a NASA graduate fellowship (grant number NASA-NNX16AP36H); a Carnegie Mellon University Scott Institute Visiting Fellows grant; the Swiss National Science Foundation (grant numbers 200021_169090, 200020_172602 and 20FI20_172622); the European Community (EC) Seventh Framework Programme and the European Union (EU) H2020 programme (Marie Skłodowska Curie ITN CLOUD-TRAIN grant number 316662 and CLOUD-MOTION grant number 764991); a European Research Council (ERC) Advanced Grant (number ATM-GP 227463); an ERC Consolidator Grant (NANODYNAMITE 616075); an ERC Starting Grant (GASPARCON 714621), the Academy of Finland (grants 306853, 296628, 316114 and 299544); the Academy of Finland Center of Excellence programme (grant 307331); the German Federal Ministry of Education and Research (CLOUD-12 number 01LK1222A and CLOUD-16 number 01LK1601A); the Knut and Alice Wallenberg Foundation Wallenberg Academy Fellow project AtmoRemove (grant number 2015.0162); the Austrian Science Fund (grant number P 27295-N20); the Portuguese Foundation for Science and Technology (grant number CERN/FIS-COM/0014/2017); and the Presidium of the Russian Academy of Sciences ('High energy physics and neutrino astrophysics' 2015). The FIGAERO-CIMS was supported by a Major Research Instrumentation (MRI) grant for the US NSF (AGS-1531284), and by the Wallace Research Foundation. We thank H. Cawley for producing Fig. 4a.

Author contributions M.W., R.M., J. Dommen, U.B., J. Kirkby, I.E-H. and N.M.D. planned the experiments. M.W., W.K., R.M., X-C.H., D.C., J.P., A.K., H.E.M., S.A., A.B., S. Bräkling, S. Brilke, L.C.M., B.C., L-P.D.M., J. Duplissy, H.F., L.G.C., M.G., R.G., A. Hansel, V.H., J.K., K.L., H.L., C.P.L., V.M., G.M., S.M., B.M., T.M., A.O., E.P., T.P., M.P., V.P., M.R., B.R., W.S., J.S., M. Simon, M. Sipilä, G.S., D.S., Y.J.T., A.T., R.V., A.C.W., D.S.W., Y. Wang, S.K.W., P.M.W., P.J.W., Y. Wu, Q.Y., M.Z.-W., X.Z., J. Kirkby, I.E.-H. and R.C.F. prepared the CLOUD facility or measuring instruments. M.W., W.K., R.M., X.-C.H., D.C., J.P., L.D., H.E.M., S.A., A.A., R.B., A.B., D.M.B., B.B., S. Bräkling, S. Brilke, R.C., H.F., L.G.C., M.G., V.H., J.S., J. Duplissy, H.L., M.L., C.P.L., V.M., G.M., R.L.M., B.M., T.M., E.P., V.P., A.R., M.R., B.R., W.S., M. Simon, G.S., D.S., Y.J.T., A.T., A.C.W., D.S.W., Y. Wang, S.K.W., P.M.W., P.J.W., Y. Wu, M.X., M.Z.-W., X.Z., J. Kirkby and I.E.-H. collected the data. M.W., W.K., R.M., X.-C.H., D.C., J.P., A. Heitto, J. Kontkanen, L.D., A.K., T.Y.-J., H.E.M., S.A., L.G.C., J.S., W.S., M. Simon, D.S., D.S.W., S.K.W., P.M.W., I.E.-H., R.C.F. and N.M.D. analysed the data. M.W., W.K., R.M., X.-C.H., D.C., A. Heitto, J. Kontkanen, T.Y.-J., H.E.M., D.M.B., H.L., D.S., R.V., M.X., I.R., J. Dommen, J.C., U.B., M.K., D.R.W., J. Kirkby, J.H.S., I.E.-H., R.C.F. and N.M.D. contributed to the scientific discussion. M.W., W.K., R.M., X.-C.H., D.C., J.P., A. Heitto, J. Kontkanen, T.Y.-J., I.R., J. Dommen, U.B., M.K., D.R.W., J. Kirkby, J.H.S., I.E.-H., R.C.F. and N.M.D. wrote the manuscript.

Competing interests The authors declare no competing interests.

Additional information
Correspondence and requests for materials should be addressed to N.M.D.
Peer review information *Nature* thanks Hugh Coe and the other, anonymous, reviewer(s) for their contribution to the peer review of this work.
Reprints and permissions information is available at http://www.nature.com/reprints.

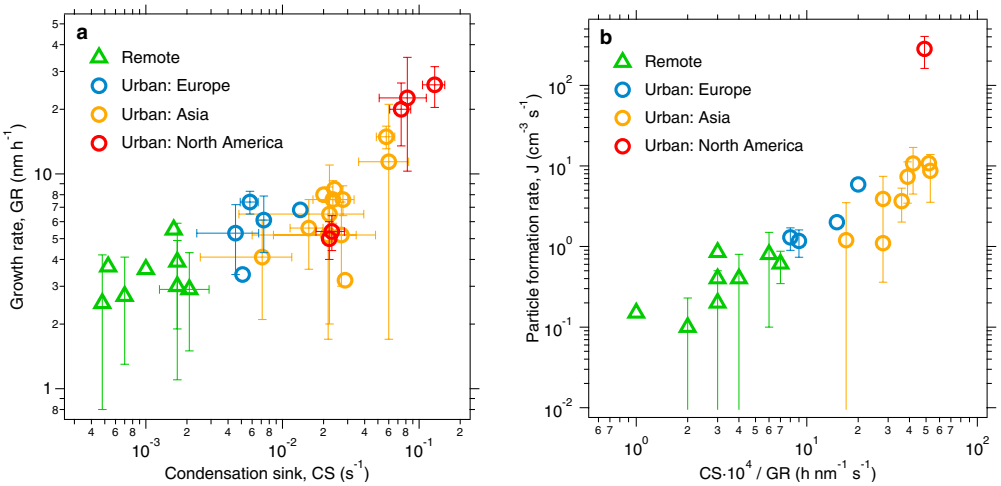

Extended Data Fig. 1 | New-particle-formation events observed in various remote and urban environments (see Extended Data Table 3 for a complete set of references). a, Growth rates (GR) versus condensation sinks (CS), showing that both are higher in polluted urban environments than in other environments. **b**, Particle-formation rates (J) versus a measure of particle loss via coagulation (CS × 10^4/GR, similar to the the McMurry L parameter), showing high new-particle-formation rates in urban conditions where the condensation sinks were so high compared to the growth rate that survival of nucleated particles should be very low. J and GR were calculated over the size range from a few nanometres to over 20 nm, except for J at Shanghai[59] and Tecamac[60], which were calculated from 3 nm to 6 nm. The bars indicate 1σ total errors.

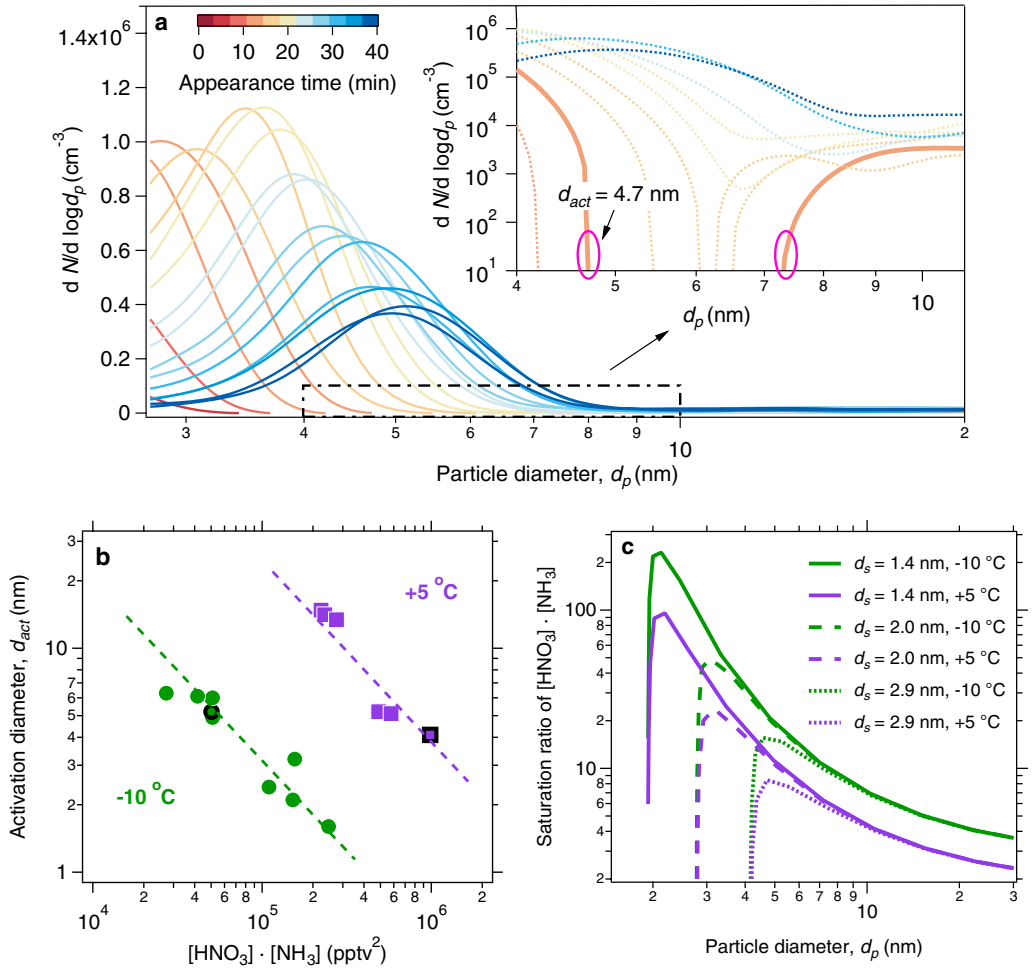

Extended Data Fig. 2 | Activation diameter of newly formed particles. **a**, Determination of the activation diameter, d_{act}, from a rapid growth event at +5 °C, in the presence of nitric acid, ammonia and sulfuric acid. The solid orange trace in the insert indicates the first size distribution curve that exhibited a clear bimodal distribution, which appeared roughly 7 min after nucleation. We define the activation diameter as the largest observed size of the smaller mode. In this case, d_{act} = 4.7 nm, which agrees well with the value obtained from MABNAG simulations (roughly 4 nm) under the same conditions as in Fig. 4. **b**, Activation diameter versus vapour product. Measured activation diameters at a given temperature correlate inversely with the product of nitric acid and ammonia vapours, in a log-log space. An amount of vapour product that is approximately one order of magnitude higher is required for the same d_{act} at +5 °C than at −10 °C, because of the higher vapour pressure (faster dissociation) of ammonium nitrate when it is warmer. **c**, Equilibrium particle diameter (d_p) at different saturation ratios of ammonium nitrate, calculated according to nano-Köhler theory. Purple curves are for +5 °C and green curves are for −10 °C (as throughout this work). The line type shows the diameter of the seed particle (d_s). The maximum of each curve corresponds to the activation diameter (d_{act}). A higher supersaturation is required for activation at lower temperature.

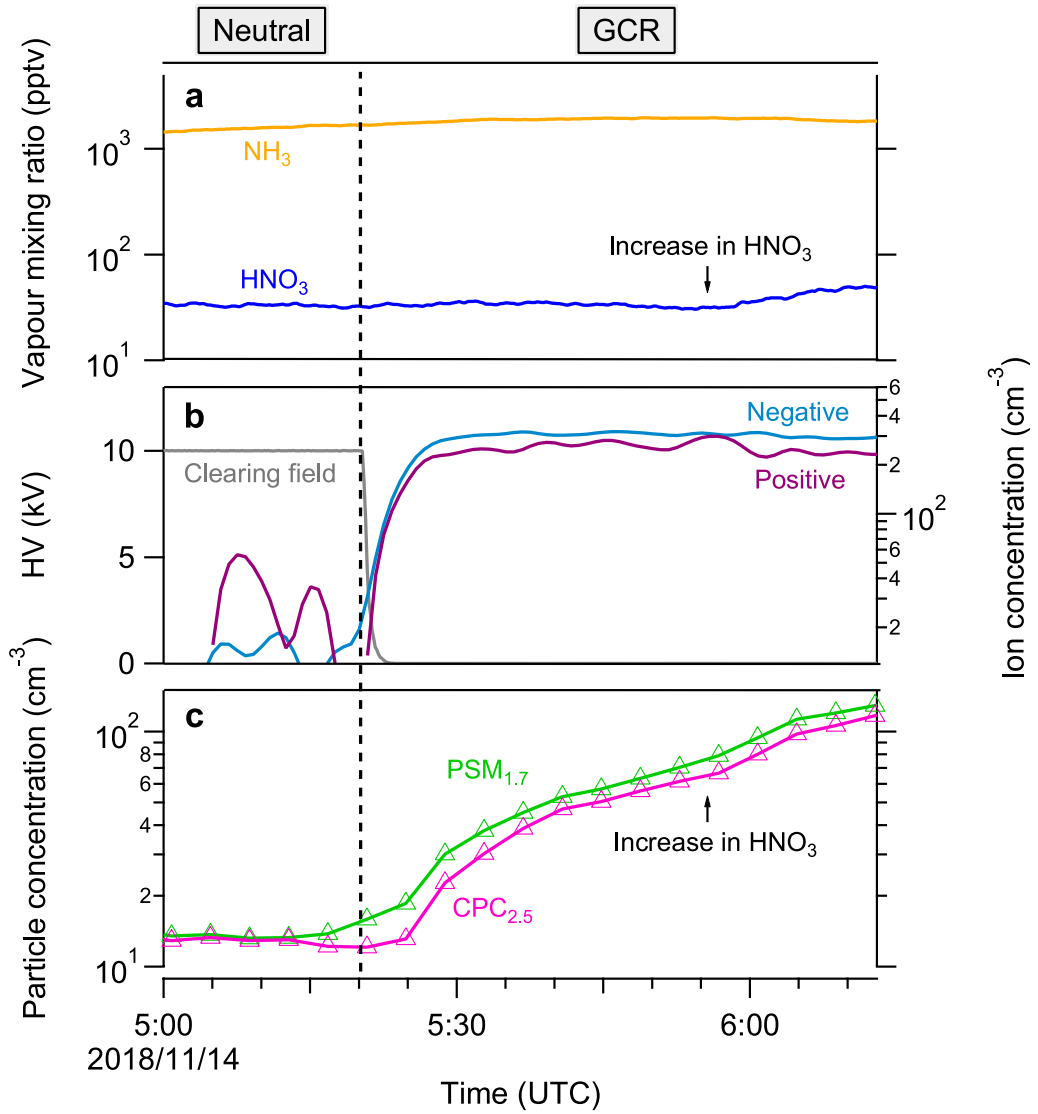

Extended Data Fig. 3 | A typical measurement sequence. Nucleation was carried out purely from nitric acid and ammonia, with no sulfuric acid (measured to less than 5×10^4 cm^{-3} or 2×10^{-3} pptv), as a function of coordinated universal time (UTC), at 60% relative humidity and −25 °C. **a**, Gas-phase ammonia and nitric acid mixing ratios. The run started with injection of the nitric acid and ammonia flow into the chamber to reach chosen steady-state values near 30 pptv and 1,500 pptv, respectively. The nitric acid flow was increased at 5:53 on 14 November 2018 to prove consistency. **b**, Clearing-field voltage and ion concentrations. Primary ions were formed from galactic cosmic rays (GCR). The clearing-field high voltage (HV) was used to sweep out small ions at the beginning of the run, and turned off at 05:21 on 14 November 2018 to allow the ion concentration to build up to a steady state between GCR production and wall deposition. **c**, Particle concentrations at two cut-off sizes (1.7 nm and 2.5 nm). Particles formed slowly in the chamber under 'neutral' conditions with the HV clearing field on and thus without ions present. The presence of ions ('GCR' condition) caused a sharp increase in the particle-number concentration by about one order of magnitude, with a slower approach to steady state because of the longer wall-deposition time constant for the larger particles. Particle numbers rose again with rising nitric acid.

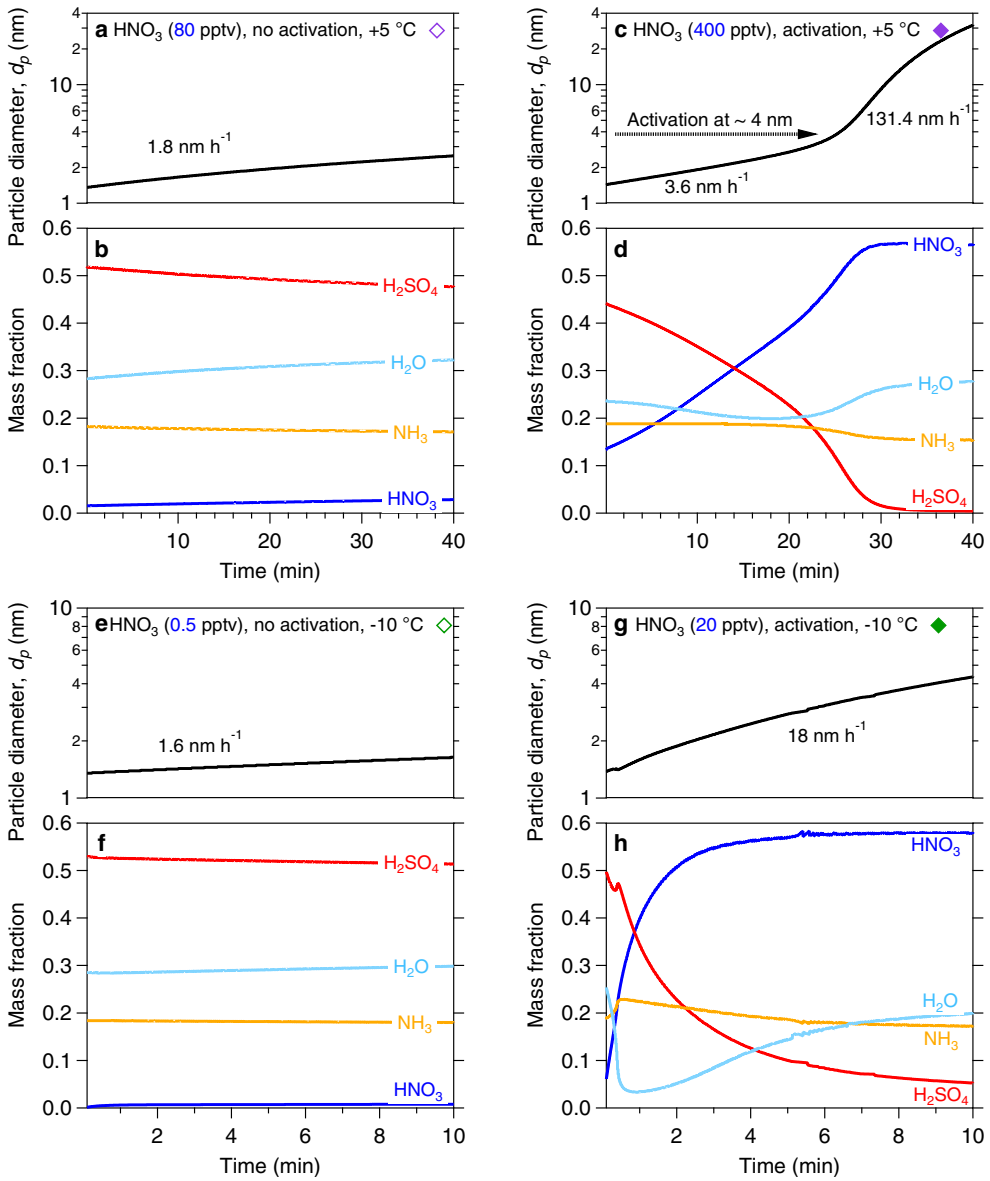

Extended Data Fig. 4 | Comparison of growth rates and chemical composition in four simulations at +5 °C and −10 °C with the thermodynamic model MABNAG. The simulation points are shown in Fig. 3a (filed diamonds, with activation; open diamonds, without activation). **a**, **c**, **e**, **g**, Temporal evolution of the particle diameter. **b**, **d**, **f**, **h**, Temporal evolution of the particle-phase chemical composition. The left-hand column (**a**, **b**, **e**, **f**) shows simulations without activation. The right-hand column (**c**, **d**, **g**, **h**) shows simulations with activation. We set the HNO_3 mixing ratios at 80 pptv and 400 pptv with 1,500 pptv NH_3 at +5 °C, and set the HNO_3 mixing ratios at 20 pptv and 0.5 pptv with 1,500 pptv NH_3 at −10 °C, to simulate unsaturated (**a**, **b**, **e**, **f**) and supersaturated (**c**, **d**, **g**, **h**) conditions, respectively. All other conditions were held constant for the simulations, with the $[H_2SO_4]$ at 2×10^7 cm^{-3} and relative humidity at 60%. Activation corresponds to a rapid increase in the nitric acid (nitrate) mass fraction; the simulations for activation conditions suggest that water activity may be an interesting variable influencing activation behaviour. The activated model results (**c**, **d**, **g**, **h**) confirm that supersaturated nitric acid and ammonia lead to rapid growth of nanoparticles. The simulated activation diameter at +5 °C is roughly 4 nm, similar to that from the chamber experiment (4.7 nm, Fig. 3a); at −10 °C the simulated activation diameter is less than 2 nm, smaller than observed.

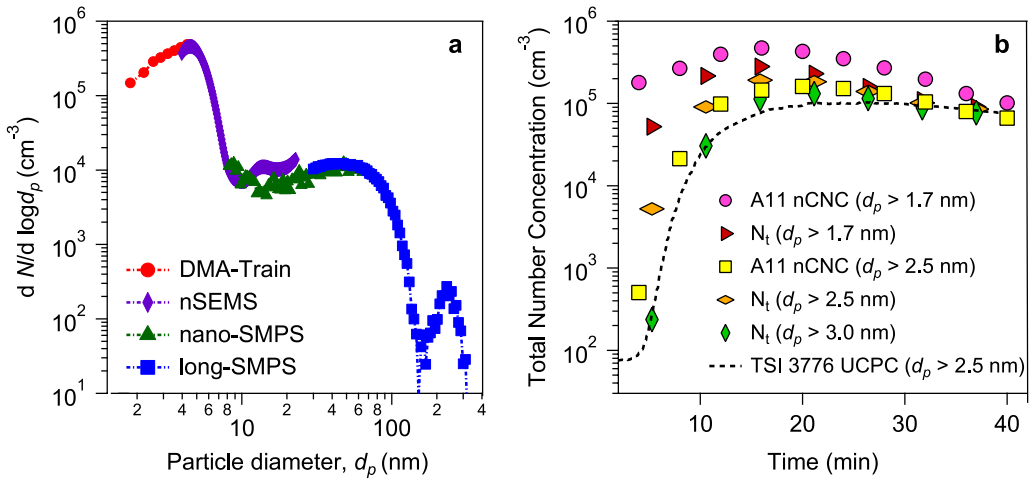

Extended Data Fig. 5 | Combined particle-size distribution and total concentrations from four particle characterization instruments. **a**, Combined size distributions, $n_N^{\circ}(d_p) = dN/d(\log d_p)$, from four electrical mobility particle-size spectrometers of different, but overlapping, detection ranges. The DMA-Train, nSEMS and nano-SMPS data were averaged every five minutes to coordinate with the long-SMPS scanning time resolution. The tail of the size distribution of large particles outside the detection range was extrapolated by fitting a lognormal distribution. **b**, Comparison of the integrated number concentrations from the combined size distributions in **a** with total number counts obtained from fixed-cutoff-size condensation particle counters. We obtained the total number concentration of particles, $N_t(d_{p0})$, above a cutoff size, d_{p0}, by integrating the particle-size distribution using[52]: $N_t = \int_{d_{p0}}^{\infty} \{n_N(d_p) \times \eta_{UCPC}\} dd_p$, applying the size-dependent detection efficiency, η_{UCPC}[61], to adjust the integrated total number concentration. We plot the total number concentrations for three different cutoff sizes (d_{p0}) of 1.7 nm, 2.5 nm and 3.0 nm, obtained every 5 min, with coloured symbols as shown in the legend. We also plot measured total number concentrations from two instruments: the Airmodus A11 nCNC-system at nominal cutoff sizes of 1.7 nm and 2.5 nm, and a TSI 3776 UCPC with a nominal cutoff size of 2.5 nm. The Airmodus A11 nCNC-system consists of an A10 PSM and an A20 CPC, which determined both the size distribution of 1–4-nm aerosol particles and the total number concentration of particles smaller than 1 µm (ref. [62]). The TSI 3776 UCPC has a rapid response time and so, rather than the 5-min basis for the other points, we plot the values from this instrument with a dashed curve.

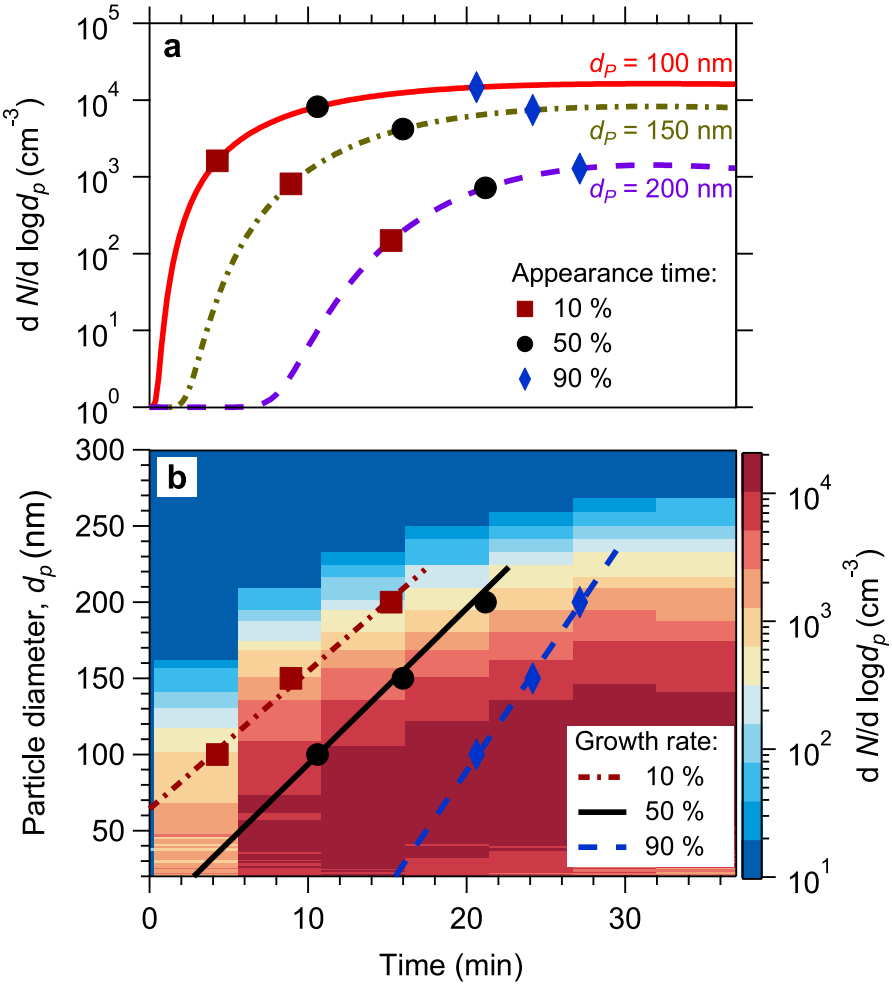

Extended Data Fig. 6 | Determination of growth rate using the appearance-time method. a, Logarithmic interpolated time-dependent growth profiles for particles with diameters of 100 nm, 150 nm and 200 nm. Three appearance times, when particle number concentrations reached 10%, 50%, and 90% of their maximum, are labelled with different symbols for the three different diameters. **b**, Growth-rate calculation for a rapid growth event (as in Fig. 2) above the activation diameter. The growth rates, in nm h^{-1}, that we report here are the slopes of linear fits to the 50% (among 10%, 50% and 90%) appearance times calculated from all sizes above the activation diameter (the slope of the solid black line and the black circles in **b**).

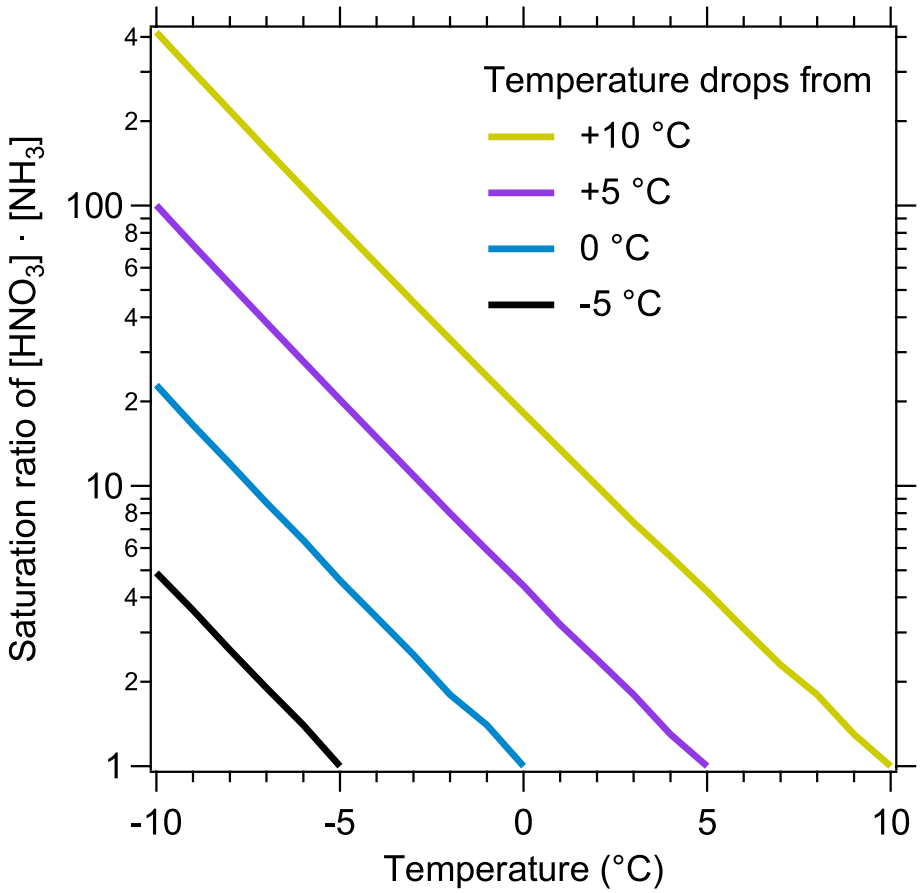

Extended Data Fig. 7 | Saturation ratio as a function of temperature. At constant nitric acid and ammonia, a decline in temperature leads to an exponential increase in the saturation ratio of ammonium nitrate, shown as the product of nitric acid and ammonia vapour concentration. With an adiabatic lapse rate of −9 °C km^{-1} during adiabatic vertical mixing, upward transport of a few hundred metres alone is enough for a saturated nitric acid and ammonia air parcel to reach the saturation ratio capable of triggering rapid growth at a few nanometres.

Extended Data Table 1 | Conditions for all nucleation and growth experiments and nano-Köhler simulations discussed here

Run	T (°C)	HNO_3 (pptv)	NH_3 (pptv)	H_2SO_4 (pptv)	HOMs (pptv)	RH %	Saturation ratio of $[HNO_3]\cdot[NH_3]$	d_{act} (nm)
2163.01	+20	150	2400	3.60	n/a	60	0.03	n/a
2140.06	+5	860	259	0.96	5.18	60	1.18	9.4
2140.08	+5	971	242	0.84	5.29	60	1.25	10.4
2140.10	+5	1130	244	0.88	5.25	60	1.46	10.0
2170.05	+5	292	370	3.00	n/a	60	0.57	n/a
2170.15	+5	1117	883	1.48	n/a	60	5.24	2.3
2170.20	+5	352	1387	1.48	n/a	60	2.59	4.7
2174.06	+5	640 [a]	904	0.46	12.01	60	3.07	3.9
2156.13	-10	228	1085	0.16	n/a	60	131.44	1.6
2156.15	-10	64	2371	0.06	n/a	60	80.90	2.1
2156.17	-10	41	2659	0.07	n/a	60	58.31	2.4
2157.06	-10	n/a	1915	0.44	0.32	60	n/a	n/a
2158.02	-10	59 [a]	2654	0.38	0.26	60	82.97	2.9
2158.04	-10	24 [a]	2131	0.46	0.28	60	27.06	4.6
2158.06	-10	24 [a]	2077	0.36	0.29	60	26.72	4.5
2159.02	-10	23 [a]	1835	0.72	0.67	60	22.15	4.5
2159.04	-10	30 [a]	1694	1.04	0.78	60	27.07	4.9
2160.02	-10	16 [a]	1663	0.60	0.25	60	14.44	5.9
2160.06	-10	16 [a]	2535	0.30	0.23	60	22.11	6.5
2162.01	-15 → -24	272	1647	< 0.002	n/a	60 → 40	1252.22	Nucleation
d_s = 1.4 nm	+5	n/a	n/a	n/a	n/a	60	96	2.2
d_s = 2.0 nm	+5	n/a	n/a	n/a	n/a	60	24	3.2
d_s = 2.9 nm	+5	n/a	n/a	n/a	n/a	60	8	4.7
d_s = 1.4 nm	-10	n/a	n/a	n/a	n/a	60	231	2.1
d_s = 2.0 nm	-10	n/a	n/a	n/a	n/a	60	49	3.1
d_s = 2.9 nm	-10	n/a	n/a	n/a	n/a	60	16	4.6

[a] HNO_3 production via NO_2 photo-oxidation.
n/a, not applicable; RH, relative humidity.

Extended Data Table 2 | Specifications of the four particle-sizing instruments used here

Instrument	Components	Size Range	Size Resolution	Time Resolution
DMA-Train	TSI 3776 UCPC TSI 3776 nanoEnhancer Airmodus A10 PSM	1.8 nm - 8.0 nm	15 bins (interpolated)	5 s
nSEMS	ROMIAC TSI 3760A CPC	1.5 nm - 23 nm	240 bins	1 min
nano-SMPS	TSI 3938 SMPS TSI 3776 UCPC	2 nm - 64 nm	96 bins	1 min
long-SMPS	TSI 3071 DMA TSI 3010 CPC	20 nm - 500 nm	84 bins	5 min

Extended Data Table 3 | Ambient particle-formation rates (*J*), growth rates (GR) and condensation sinks (CS) in various remote and urban environments

City/Region (Country)	J [a] ($cm^{-3} \cdot s^{-1}$)	GR [a] ($nm \cdot h^{-1}$)	CS (s^{-1})	$CS \cdot 10^4/GR$ ($h \cdot nm^{-1} \cdot s^{-1}$)	Ref.
Hyytiälä (Finland)	0.8 ± 0.7	3.0 ± 1.9	1.7×10^{-3}	6	63
Hyytiälä (Finland)	0.6 ± 0.3	2.9 ± 1.4	$2.1 \times 10^{-3} \pm 8.2 \times 10^{-4}$	7	64
Pallas (Finland)	0.1 ± 0.1	2.5 ± 1.7	4.8×10^{-4}	2	63
Pallas (Finland)	0.2	3.7	5.3×10^{-4}	1	65
Värriö (Finland)	0.9	3.6	1.0×10^{-3}	3	66
Värriö (Finland)	0.2 ± 0.3	2.7 ± 1.4	7.0×10^{-4}	3	63
Tomsk (Russia)	0.4	5.5	1.6×10^{-3}	3	67
Sörmland (Sweden)	0.4 ± 0.4	3.9 ± 2.0	1.7×10^{-3}	4	63
Helsinki (Finland)	2.0	3.4	5.1×10^{-3}	15	68
Paris (France)	n/a	6.1 ± 1.8	$7.3 \times 10^{-3} \pm 8.0 \times 10^{-4}$	12	69
Po Valley (Italy)	5.9	6.8	1.4×10^{-2}	20	70
Brookfield (UK)	1.2 ± 0.4	5.3 ± 1.9	$4.5 \times 10^{-3} \pm 2.2 \times 10^{-3}$	9	71
Leicester (UK)	1.3 ± 0.4	7.4 ± 0.9	$5.8 \times 10^{-3} \pm 8.7 \times 10^{-4}$	8	71
Beijing (China)	n/a	3.2	2.9×10^{-2}	90	72
Beijing (China)	10.8	5.2 ± 2.2	$2.7 \times 10^{-2} \pm 2.1 \times 10^{-2}$	52	73
Beijing (China)	10.7 ± 6.2	5.2 ± 3.5	$2.2 \times 10^{-2} \pm 1.3 \times 10^{-2}$	42	74
Beijing (China)	n/a	6.5 ± 4.5	$2.2 \times 10^{-2} \pm 1.7 \times 10^{-2}$	34	75
Hong Kong (China)	3.9 ± 3.5	5.6 ± 2.0	$1.6 \times 10^{-2} \pm 4.2 \times 10^{-3}$	28	76
Nanjing (China)	3.7 ± 1.6	7.6 ± 1.2	$2.8 \times 10^{-2} \pm 5.7 \times 10^{-3}$	36	77
Nanjing (China)	1.1	8.5	2.4×10^{-2}	28	78
Nanjing (China)	n/a	7.6 ± 1.7	$2.3 \times 10^{-2} \pm 6.7 \times 10^{-3}$	31	79
Shanghai (China)	8.7 ± 5.2 [b]	11.4 ± 9.7	$6.0 \times 10^{-2} \pm 2.4 \times 10^{-2}$	53	59
Shanghai (China)	n/a	8.0	2.0×10^{-2}	25	80
Gadanki (India)	1.2 ± 2.3	4.1 ± 2.0	$7.1 \times 10^{-3} \pm 4.6 \times 10^{-3}$	17	81
New Delhi (India)	7.3 ± 3.9	14.9 ± 1.8	$5.8 \times 10^{-2} \pm 8.9 \times 10^{-3}$	39	82
Tecamac (Mexico)	283.0 ± 121.0 [b]	26.0 ± 5.6	$1.3 \times 10^{-1} \pm 2.4 \times 10^{-2}$	49	60
Tecamac (Mexico)	n/a	22.6 ± 12.3	$8.2 \times 10^{-2} \pm 3.1 \times 10^{-2}$	36	60
Atlanta (US)	n/a	20.0 ± 6.5	$7.4 \times 10^{-2} \pm 1.3 \times 10^{-2}$	37	7, 83
Boulder (US)	n/a	5.4 ± 1.0	$2.3 \times 10^{-2} \pm 5.4 \times 10^{-3}$	42	84
Boulder (US)	n/a	5.0 ± 1.0	2.2×10^{-2}	43	60

[a] *J* and GR were mostly calculated over a size range from a few nanometres to more than 20 nm.

[b] *J* calculated from 3 nm to 6 nm.

Uncertainties indicate 1σ errors. From refs. [7,59,60,63–84].

Paper 3: Survival of newly formed particles in haze conditions

Environmental Science: Atmospheres

ROYAL SOCIETY OF CHEMISTRY

PAPER

View Article Online
View Journal | View Issue

Cite this: *Environ. Sci.: Atmos.*, 2022, **2**, 491

Survival of newly formed particles in haze conditions†

Ruby Marten, [a] Mao Xiao,[a] Birte Rörup, [b] Mingyi Wang,[c] Weimeng Kong,[d] Xu-Cheng He,[b] Dominik Stolzenburg,[b] Joschka Pfeifer,[ef] Guillaume Marie, [f] Dongyu S. Wang,[a] Wiebke Scholz, [g] Andrea Baccarini, [ah] Chuan Ping Lee, [a] Antonio Amorim,[i] Rima Baalbaki,[b] David M. Bell, [a] Barbara Bertozzi,[j] Lucía Caudillo,[f] Biwu Chu,[b] Lubna Dada, [a] Jonathan Duplissy, [dk] Henning Finkenzeller, [l] Loïc Gonzalez Carracedo,[m] Manuel Granzin,[f] Armin Hansel, [g] Martin Heinritzi,[f] Victoria Hofbauer,[c] Deniz Kemppainen,[b] Andreas Kürten, [f] Markus Lampimäki, [b] Katrianne Lehtipalo,[bn] Vladimir Makhmutov, [o] Hanna E. Manninen, [e] Bernhard Mentler, [g] Tuukka Petäjä, [b] Maxim Philippov, [o] Jiali Shen,[b] Mario Simon, [f] Yuri Stozhkov,[o] António Tomé,[p] Andrea C. Wagner, [f] Yonghong Wang,[b] Stefan K. Weber, [e] Yusheng Wu,[b] Marcel Zauner-Wieczorek, [f] Joachim Curtius, [f] Markku Kulmala, [b] Ottmar Möhler,[j] Rainer Volkamer, [l] Paul M. Winkler,[m] Douglas R. Worsnop,[q] Josef Dommen, [a] Richard C. Flagan, [d] Jasper Kirkby,[ef] Neil M. Donahue, [c] Houssni Lamkaddam,*[a] Urs Baltensperger[a] and Imad El Haddad *[a]

Intense new particle formation events are regularly observed under highly polluted conditions, despite the high loss rates of nucleated clusters. Higher than expected cluster survival probability implies either ineffective scavenging by pre-existing particles or missing growth mechanisms. Here we present experiments performed in the CLOUD chamber at CERN showing particle formation from a mixture of anthropogenic vapours, under condensation sinks typical of haze conditions, up to 0.1 s^{-1}. We find that new particle formation rates substantially decrease at higher concentrations of pre-existing particles, demonstrating experimentally for the first time that molecular clusters are efficiently scavenged by larger sized particles. Additionally, we demonstrate that in the presence of supersaturated gas-phase nitric acid (HNO_3) and ammonia (NH_3), freshly nucleated particles can grow extremely rapidly, maintaining a high particle number concentration, even in the presence of a high condensation sink. Such high growth rates may explain the high survival probability of freshly formed particles under haze conditions. We identify under what typical urban conditions HNO_3 and NH_3 can be expected to contribute to particle survival during haze.

Received 23rd January 2022
Accepted 24th March 2022

DOI: 10.1039/d2ea00007e

rsc.li/esatmospheres

[a]*Laboratory of Atmospheric Chemistry, Paul Scherrer Institute, 5232 Villigen, Switzerland. E-mail: houssni.lamkaddam@psi.ch; imad.el-haddad@psi.ch*

[b]*Institute for Atmospheric and Earth System Research (INAR)/Physics, Faculty of Science, University of Helsinki, 00014 Helsinki, Finland*

[c]*Center for Atmospheric Particle Studies, Carnegie Mellon University, 15213 Pittsburgh, PA, USA*

[d]*California Institute of Technology, Division of Chemistry and Chemical Engineering 210-41, Pasadena, CA 91125, USA*

[e]*CERN, CH-1211 Geneva, Switzerland*

[f]*Institute for Atmospheric and Environmental Sciences, Goethe University Frankfurt, 60438 Frankfurt am Main, Germany*

[g]*Institute of Ion Physics and Applied Physics, University of Innsbruck, 6020 Innsbruck, Austria*

[h]*Extreme Environments Research Laboratory (EERL), École Polytechnique Fédérale de Lausanne, Sion, CH, Switzerland*

[i]*CENTRA, FCUL, University of Lisbon, 1749-016 Lisbon, Portugal*

[j]*Institute of Meteorology and Climate Research, Karlsruhe Institute of Technology, 76021 Karlsruhe, Germany*

[k]*Helsinki Institute of Physics (HIP)/Physics, Faculty of Science, University of Helsinki, 00014 Helsinki, Finland*

[l]*Department of Chemistry & CIRES, University of Colorado Boulder, 215 UCB, Boulder, 80309, CO, USA*

[m]*Faculty of Physics, University of Vienna, Boltzmanngasse 5, A-1090 Vienna, Austria*

[n]*Finnish Meteorological Institute, Helsinki, Finland*

[o]*Lebedev Physical Institute of the Russian Academy of Sciences, Leninsky Prospekt, 53, Moscow, 119991, Russian Federation*

[p]*IDL-Universidade da Beira Interior, 6201-001 Covilhã, Portugal*

[q]*Aerodyne Research, 01821 Billerica, MA, USA*

† Electronic supplementary information (ESI) available. See DOI: 10.1039/d2ea00007e

Environmental significance

Haze and pollution affect visibility, local climate, and human health. Current understanding of new particle formation and growth mechanisms cannot explain how high number concentrations of nucleated particles are sustained during haze events, as the loss processes for new clusters seem to outcompete growth. It has been proposed that either scavenging of small particles is overestimated, or that there is a missing growth mechanism. We present measurements, and supporting model calculations, showing efficient scavenging of clusters involving unit sticking probability. Furthermore, we show that rapid growth from ammonium nitrate formation increases survival of clusters in the presence of haze. Ammonium nitrate formation may be a missing growth mechanism which contributes to sustaining high particle numbers during haze in urban environments.

Introduction

Aerosols play a key role in cloud formation and climate,[1–3] substantially offsetting the warming by greenhouse gases.[4] It is therefore important to understand what mechanisms are driving the formation and growth of aerosols, so that climate models can include them. Of equal importance, nucleation and growth of aerosols leads to persistent pollution in megacities, which can also be responsible for changes in local weather systems and local climate forcing.[5,6] In addition, particulate pollution causes millions of premature deaths annually, and is one of the leading causes of deaths globally.[7–9]

Once new particles have been formed, they are able to grow *via* condensation of vapours. The growth must be fast enough to rival coagulation with larger particles, referred to as the coagulation sink. Particles smaller than 10 nm have high Brownian diffusivity and are therefore most vulnerable to coagulation loss.[10] The likelihood of a particle's survival is dependent on a balance between growth rate and coagulation sink. Previous understanding was that growth rates in cities are only up to a few times greater than those in clean environments.[11] Therefore, under highly polluted conditions seen in cities, newly formed particles are not expected to survive very long before sticking to larger particles. However, intense new particle formation events are regularly observed under these conditions, with particle formation rates up to hundreds of times higher than in clean environments,[12–16] despite the high loss rates of nucleated clusters. Currently, there is a major gap in our understanding as to how the particle number concentration can be sustained under such highly polluted conditions. Higher than expected cluster survival through the most critical size range (the so-called "valley of death" between nucleated particles and ~10 nm) implies either ineffective scavenging by pre-existing particles or a missing growth mechanism.[17]

Recently, Wang *et al.* (2020)[18] presented a new mechanism of rapid particle growth, affecting particles as small as a few nanometers, *via* condensation of HNO_3 and NH_3. Ammonium nitrate is an important semi-volatile constituent of large particles, previously thought to be too volatile to contribute to early growth. However, Wang *et al.* (2020) demonstrated that in conditions of excess NH_3 and HNO_3 mixing ratios, with respect to ammonium nitrate saturation ratios, particles as small as a few nanometers can be activated to rapidly grow to much larger sizes, analogous to CCN activation. Ammonium nitrate growth affects particles once they reach a critical diameter, referred to as the activation diameter. This growth mechanism could play a key role in high survival of small particles and therefore explain the maintenance of high particle number concentration under highly polluted conditions. An alternative mechanism that has been also suggested would be that our current understanding of loss rates is incomplete, and clusters are not efficiently lost to large particles.[17] However, neither theory has been experimentally tested or verified to date. In this work, we present the first combined experimental and model results of survival of small particles in the presence of a high coagulation sink, analogous to haze.

Methods

The CLOUD chamber at CERN

The experiments presented were undertaken at the CLOUD (Cosmics Leaving OUtdoor Droplets) chamber at CERN (European Organization for Nuclear Research). The conditions in the chamber were controlled to 5 °C and 60% relative humidity (RH). Further details on the CLOUD chamber experiments can be found in the ESI.†

Nucleation experiments. We begin the nucleation experiments with a clean chamber and constant gas concentrations. The experiments start by injecting several precursor gases which would be expected in a city, namely NO, SO_2, toluene, α-pinene, HONO, NH_3, O_3, and dimethylamine. Through photolysis of HONO (UVA generated at 385 nm by a 400 W UVA LED saber, LS3) and/or O_3 (170 W quartz-clad high intensity Hg lamp, saber, LS1) OH radicals were produced, and subsequently condensable gases, leading to nucleation and growth of particles. HNO_3 was formed through reaction of $^{\bullet}OH$ with NO_2; organic oxidation products through reaction of $^{\bullet}OH$ with volatile organic compounds (VOCs); and H_2SO_4 through reaction of $^{\bullet}OH$ with SO_2. In certain experiments, HNO_3 was also injected directly into the chamber. We then monitor the nucleation and growth, and when the stage is deemed finished, the lights are turned off and cleaning and preparation for the next stage begins.

High condensation sink experiments. In the high condensation sink experiments, before nucleation attempts began, we generated a high condensation sink, consisting of particles around 100 nm and larger. This was achieved by rapidly growing particles with a high amount of condensable gases (H_2SO_4, HNO_3, NH_3, DMA, and toluene organic oxidation products). Once the condensation sink reached values above 0.06 s^{-1}, the lights were turned off to halt further gas production, and the fan speed in the chamber was increased, to remove small particles and condensable gases. After the cleaning step, the experimental run was undertaken as described previously (see Nucleation experiments).

Modelling ammonium sulfate

The sulfuric acid and ammonia nucleation and growth model is based on the model described in detail in Xiao *et al.* (2021)[11] which is developed from the general dynamic equation.[19] Briefly, the model calculates particle and gas concentrations for each time step *via* a sum of production and losses for each gas, cluster or particle size bin. When organic oxidation products were present in the experiments, nucleation and growth were parameterised in the model to that of the experiment. This was achieved by increasing the H_2SO_4 concentration used in the model to account for enhanced growth rates since this model does not include organic oxidation products.

Particle loss rates

For the particle loss rates in the chamber, we consider wall loss, dilution loss, and coagulation loss (or gain). We calculate the coagulation change in each size bin using the coagulation coefficient and the general dynamic equation from Seinfeld and Pandis (2006)[19] and solving for the change in particle number for each size bin for each time step.[11,20]

Modelling ammonium nitrate

We developed an ammonium nitrate growth model addition to the ammonium sulfate model. It is a polydisperse growth model, with 150 bins ranging from one ammonium sulfate cluster to 1000 nm, which also provides the time evolution of particle size and composition. We predict condensation of ammonium nitrate based on the equilibrium of NH_3 and HNO_3 in the gas phase. NH_3 and HNO_3 concentrations are also calculated by summing up production and losses at each time step (injection, photolysis, wall loss, dilution loss, condensation, *etc.*). For some experiments, gas phase concentration or formation rates were constrained from measurements. As shown in Wang *et al.* (2020)[18] ammonium nitrate condensation behaves much like CCN activation, and the behaviour is consistent with the nano-Köhler theory. A mass flux is established, based on whether the ammonium nitrate is in supersaturation or not. The supersaturation was calculated based on the dissociation constant K_p,[21] defined as the equilibrium product of gas phase NH_3 and HNO_3. Supersaturation of ammonium nitrate is equal to $([NH_3]_g \times [HNO_3]_g)/K_p$. The fluxes of HNO_3 and NH_3 are considered to be equal and dependent on the limiting gas, since formation of ammonium nitrate is equimolar. Therefore, we calculate the net flux of NH_3 and HNO_3 at every time step and include a Kelvin term and activity term in order to calculate the different fluxes for different particle sizes (see eqn (S.3) ESI† – Modelling ammonium nitrate).

Results

Modelling rapid growth from ammonium nitrate condensation

Experiments were undertaken at the CLOUD chamber at CERN under various concentrations of H_2SO_4, NH_3 and HNO_3 at 5 °C

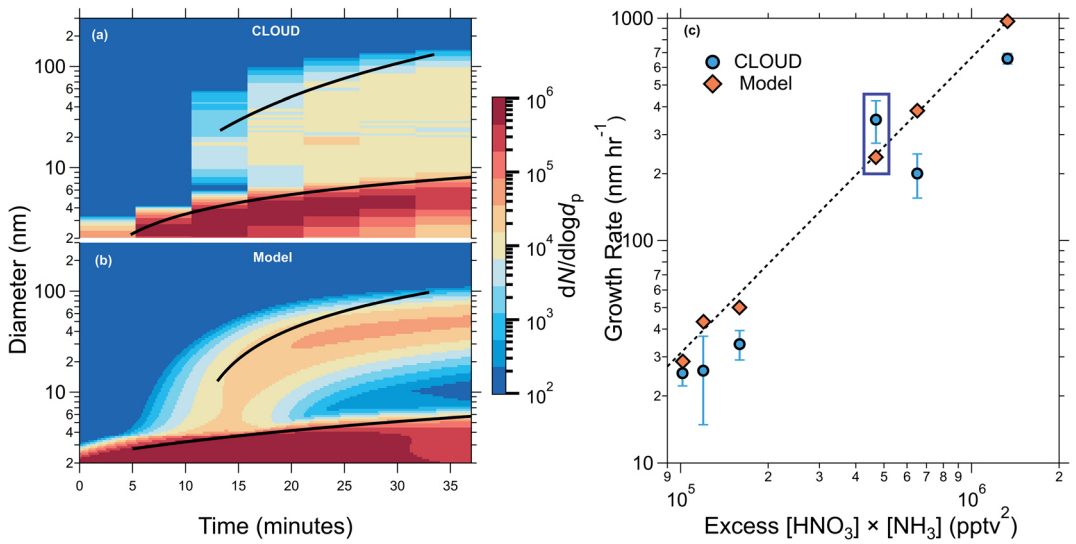

Fig. 1 Comparison of measured and modelled growth rates. (a) Particle size distribution from an example CLOUD experiment showing rapid growth from NH_4NO_3 formation once the activation diameter (vapour supersaturation including the Kelvin effect) is reached. (b) Model prediction for the experiment in (a). The black traces in (a) and (b) show the 50% appearance time. The initial experimental conditions are 1891 pptv NH_3, 352 pptv HNO_3, and 3.9×10^7 molecules per cm^3 H_2SO_4. The inputs to the model are the production rates of HNO_3, NH_3, and H_2SO_4, and the Kelvin diameter determined from other CLOUD experiments (see ESI† – Modelling ammonium nitrate). (c) Measured particle growth rates after activation *versus* excess $[HNO_3] \times [NH_3]$ vapour product (round points, previously shown in Wang *et al.* (2020)[18]). The excess vapour product is the supersaturation for the formation of ammonium nitrate, and is determined by subtracting the calculated equilibrium vapour product from the measured value. The round points were determined using the 50% appearance time method (see ESI† – growth rates). The diamond points show the growth rates obtained by fitting modelled data for each experiment. The growth rates corresponding to panels a and b are indicated by a blue box. The dashed black curve shows a power law fit through the model values of the form $y = kx^p$, with $p = 1.33$ and $k = 7 \times 10^{-6}$. All experiments were performed at 5 °C and 60% relative humidity.

and 60% relative humidity, and in some instances in the presence of dimethyl amine and/or organic oxidation products formed from α-pinene or toluene. Fig. 1(c) shows experimental CLOUD (2018) and kinetic model results and the dependence of the growth rate of particles after activation by ammonium nitrate on the excess ammonium nitrate concentration. The excess ammonium nitrate is calculated by subtracting the dissociation constant K_p from the product of the gas phase NH_3 and HNO_3 concentrations, this represents the amount of gas available for condensational growth, once the particles have grown as large as the activation diameter. In the majority of CLOUD experiments presented, the limiting gas for condensation was HNO_3, as the experimental design was intended to be comparable to ambient conditions where NH_3 is usually in excess. The modelled growth rates are in good agreement with measured growth rates from CLOUD, and the model replicates qualitatively and quantitatively the evolution of the entire size distribution with particles rapidly growing by ammonium nitrate condensation once they reach a critical diameter of ~4 nm for the experiment shown.

The effect of high growth rates in the presence of high coagulation sink

We generated a high condensation sink (CS), with loss rates comparable to those found during haze, in order to verify experimentally the loss rates of small clusters, and to test the effect of high growth rates on the survival of small particles. Condensation is a sink for condensable gases and depends on

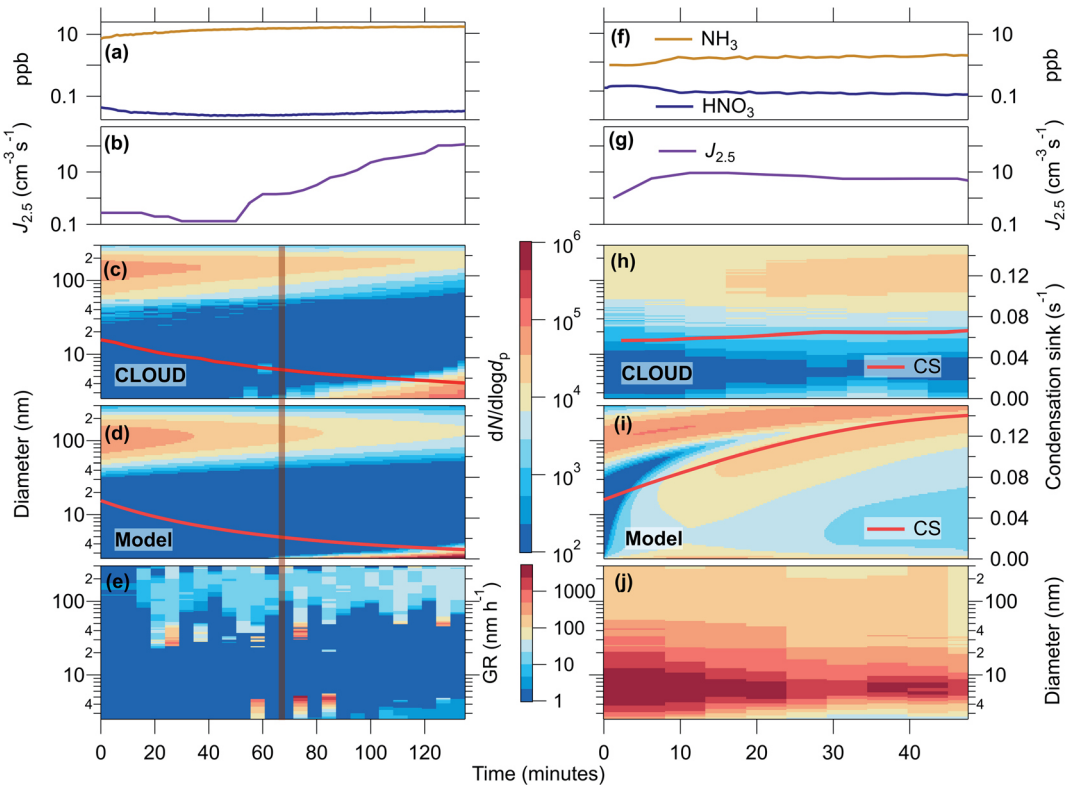

Fig. 2 Nucleation experiments and model simulations with a high condensation sink in the CLOUD chamber. (a–c) A CLOUD experiment with low HNO_3 (~0.03 ppbv) and high initial condensation sink (CS) (0.06 s^{-1}) from pre-existing particles around 100 nm size. The experimental conditions are ~2.5 × 10^6 molecules per cm^3 [H_2SO_4], ~0.03 ppbv [HNO_3], ~5–20 ppbv [NH_3], 60% RH, and 5 °C. The initial vapour product [HNO_3] × [NH_3] gives an activation diameter of ~30 nm, *i.e.* particles less than 29.8 nm are in sub-saturated conditions. The CS gradually falls as the particles are flushed from the chamber (diluted) by fresh makeup gas. At 65 minutes, the CS reaches ~0.033 s^{-1} (indicated by an orange line) and new particles begin to appear above 2.5 nm (b and c) and grow steadily at a rate of 6.4 ± 1.0 nm h^{-1}, in the size range 3.2–4.9 nm. The formation rate, $J_{2.5}$, continues to increase as the CS falls further. (d) Model simulation using the measured initial HNO_3 and NH_3 concentrations and H_2SO_4 production rates, and an initial lognormal particle size distribution centred around 100 nm. The model closely reproduces the onset of new particle formation near 65 minutes (orange line). (e) Size and time dependent growth rates calculated using the INSIDE method. (f–h) A second CLOUD experiment with higher HNO_3 (0.1–0.2 ppbv) and high initial CS (0.06 s^{-1}) from pre-existing particles around 100 nm size. The experimental conditions are ~6 × 10^6 cm^{-3} [H_2SO_4], ~1.7 ppbv [NH_3], 60% RH, and 5 °C. The initial vapour product [HNO_3] × [NH_3] gives an activation diameter of ~7.5 nm, *i.e.* particles larger than 7.5 nm are in supersaturated conditions. Under these conditions, we measure steady new particle formation ($J_{2.5}$ = 5–10 cm^{-3} s^{-1}; panel f) and rapid growth of both the newly formed and the pre-existing particles, which maintains a high CS despite dilution of the chamber contents (panel g). (i) Model simulation of the second CLOUD experiment. The initial vapour product for the simulation has an activation diameter of 2.5 nm, *i.e.* particles larger than 2.5 nm are in supersaturated conditions. The model predicts continuous new particle formation as well as rapid growth of both the new particles and the pre-existing particles. The reason for the different appearance of the measured (h) and simulated (i) size distributions is due to varying experimental conditions (see text). (j) Size and time dependent growth rates calculated using the INSIDE method.

the surface area, and coagulation is a sink for particles that depends on the diameter of the colliding particles. In Fig. 2 we present two CLOUD experiments (one longer than the other) at 5 °C and 60% relative humidity, summarising the observations (panels a–c, e and f–h, j) and our kinetic model results (panels d and i).

Run 1 of the CLOUD measurements shown in Fig. 2(a–c and e) presents results of an experiment in which we observed no nucleation under the initial high CS. The initial concentrations of this experiment were $\sim 2.5 \times 10^6$ molecules per cm^3 H_2SO_4, $\sim$0.03 ppbv HNO_3, $\sim$6 ppbv NH_3 and an initial CS of $\sim 0.06\ s^{-1}$. During the experiment the CS steadily decayed due to dilution in the CLOUD chamber, as well as evaporation of NH_4NO_3 due to sub-saturated conditions of gas phase NH_3 and HNO_3. The gas phase NH_3 was constantly increasing, although the injection rate was constant, most likely due to increased production rate of NH_3 by evaporation, combined with a decreasing loss rate to the CS resulting in a higher steady state concentration. HNO_3 should experience the same changes in loss and production rates, but the increase in concentration in Fig. 2(a) is delayed. This is probably due to its higher wall loss rate (*i.e.* the walls are not an effective source and act as a sink), and the fact that HNO_3 is not in steady state at the beginning of the experiment, as each run starts with the onset of lights and therefore HNO_3 production. Nucleation of particles commenced once the CS dropped to approximately 0.03 s^{-1} (indicated with a vertical orange line). As the condensation sink decreased further, the nucleation rate continued to increase and the particles continued to grow, although at relatively slow rates. In this experiment, neither particle formation and growth nor condensation to the larger mode was sufficient to sustain the particle number and the CS.

Run 2 of the CLOUD measurements in Fig. 2(f–h and j) shows a second experiment, with similar initial conditions but higher HNO_3 concentration ($\sim 6 \times 10^6$ cm^{-3} H_2SO_4, $\sim$0.2 ppbv HNO_3, $\sim$1.7 ppbv NH_3, and an initial CS of $\sim 0.06\ s^{-1}$). We observe that not only were the condensation sink and particle number sustained, but small particles were present from the beginning of the experiment, with measurable and continuous formation of 2.5 nm particles ($J_{2.5}$) as well as high growth rates. Since loss rates of particles to dilution are the same between the two runs, comparing the progression of the large particle mode in Fig. 2(c and h) can elucidate much about the growth of particles. Although growth does not manifest as a typical new particle formation (NPF) and growth event in Fig. 2(h), it is clear from comparing to Fig. 2(c) that rapid and continuous growth is occurring. In Fig. 2(c), the lower end of the large pre-existing particle mode increases in diameter due to slow growth of the particles, while the CS and particle number decreases. However, in Fig. 2(h) there are continuous particle concentrations around 10 nm and a steady CS, which can only be explained by new particle formation and rapid growth. Furthermore, as time progresses in Fig. 2(h), the particle number concentration at large sizes (indicated by colour) increases, whereas for Fig. 2(c) it is decreasing. These results indicate that, with sufficient HNO_3 and NH_3, higher growth rates at small particle sizes can shepherd small particles to larger sizes through the so-called "valley of death", and thus sustain particle number concentration and CS during haze events.

Panels e and j present size and time dependent growth rates calculated using the INSIDE method.[22,23] Panel e shows that initially, before the onset of nucleation, the only measured growth is slow growth of large particles, most likely caused by condensable gases present other than NH_3 and HNO_3. While there are relatively low growth rates for the newly formed particles (<4 nm) in panel j, as soon as the activation diameter is reached the particles experience extremely rapid and continuous growth just above the activation diameter, leading to rapid condensational loss, resulting in the apparent gap in the particle-number size distribution. Similar observations of apparent gaps in the particle size distribution, due to ammonium nitrate growth, were also reported in Wang *et al.* (2020).[18] The activation diameter is increasing during the first 20 minutes of run 2; this is visible as the leading edge of the nucleation mode is increasing in diameter (Fig. 2(h)), concurrent with lower growth rates (Fig. 2(j)). As the gas phase NH_3 and HNO_3 concentrations stabilise (Fig. 2(f)) the activation diameter also stabilises.

Panels d and i of Fig. 2 show the kinetic modelling results of these runs. Each model run had initial and boundary conditions consistent with the corresponding experimental run. We initialized both simulations with a condensation sink of $\sim 0.06\ s^{-1}$, comprising particles with a 100 nm modal diameter. We constrained $J_{2.5}$ and the concentrations of NH_3 and HNO_3 to the experimental values and the production rate of H_2SO_4. For run 1 (a–e), the model agrees qualitatively and quantitatively with the observations. For run 2 (f–j) the model agrees qualitatively but with evident differences that we shall discuss. In run 1, even with the rise in $J_{2.5}$ after $\sim$65 min, the particles only grow a few nm before being lost, and the CS declines steadily due to ventilation without being counterbalanced by newly formed growing particles. A second simulation with $J_{2.5}$ constrained to 10 cm^{-3} s^{-1} throughout the run shows very similar results, with essentially no growth before 65 min and only feeble growth afterwards (Fig. S1(a and b)†). Sensitivity tests show that the differences in H_2SO_4 and NH_3 between the experiments also do not have a strong influence on the particle size distribution (Fig. S1(c and d)†). With these experiments, we demonstrate that our current understanding of coagulation loss rates of small particles, which we use in the model, is correct as the results match well with the experiments, *i.e.* clusters and small particles are efficiently lost to large particles, and inefficient coagulation is not the explanation for measured J rates in polluted conditions.

For run 2 (f–j) model simulation we found the lower limit where we could reproduce this experiment was at concentrations of $\sim$0.3 ppbv HNO_3 and $\sim$3.8 ppbv NH_3, around two times larger than the estimated concentrations in the chamber. This discrepancy is within the estimated errors of gas concentrations for these runs (see ESI†). The model reproduces the observed "smear" of particles across the size distribution, with an indistinct minimum near 5 nm. However, the "CS mode" at 100 nm also grows rapidly, in contrast to the observations. The rapidly increasing diameter of the gap in between the

nucleation and Aitken modes in panel (i) is most likely an artefact of the initial conditions. We thus confirm the high particle survival as well as the persistent CS, which is sustained against losses as the result of ammonium nitrate-enabled particle activation. The model-measurement differences likely arise from multiple factors, predominantly because experimental conditions were changing dynamically, making it more difficult to constrain the model accurately. As seen in Fig. S2–S4 (ESI†) the activation diameter and especially the growth rate are very sensitive to the experimental, or ambient, conditions. Specifically, the growth rate depends on the diameter, and close to the activation diameter, d_{act}, the growth rate rapidly increases with increasing diameter. The sensitivity is especially high when HNO_3 and NH_3 are near stoichiometric equivalence, such as in this case (Fig. S4†). The activation diameter is then also sensitive to the saturation concentration, S where a small change in S can result in a large change in activation diameter. Finally, certain data limitations (lack of particle composition measurements, lack of HNO_3 measurements *etc.*) meant that the model could not be constrained to all experimental conditions. The result of these effects is that, in a dynamic situation such as in the CLOUD experiments or ambient environments, we expect to observe a size distribution as we have observed, due to changes in sinks and sources resulting in rapid changes in growth rate and activation. The differences in Fig. 2(h and i) indicate that ammonium nitrate growth would not necessarily be classified as a NPF event, and thus could be overlooked in ambient data. We also do not yet include the effect of van der Waals forces, which for sulfuric acid – NH_3 growth can enhance sub-10 nm growth by up to a factor of 2.[20] While van der Waals forces have a small effect on the overall results, they might contribute to high growth rates in the smallest particles without causing a higher growth at larger sizes (see ESI† – Modelling ammonium nitrate).

Effect of NH_3 and HNO_3 concentrations on particle survival

Results from Fig. 1 and 2 indicate that the model accurately captures the growth by ammonium nitrate, as well as particle

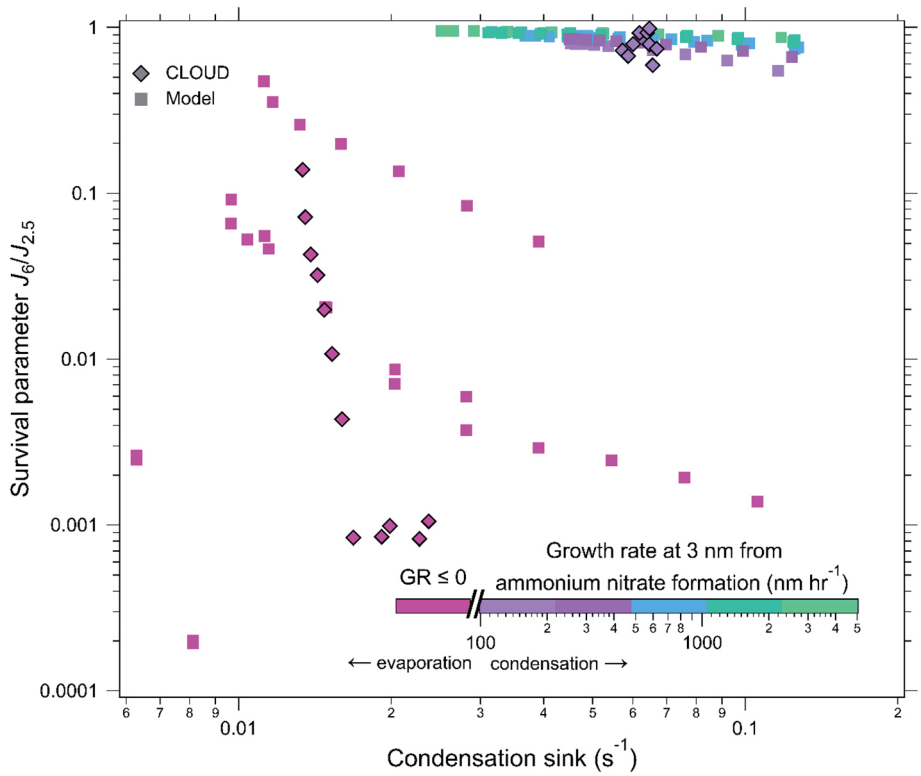

Fig. 3 Survival parameter of newly formed particles *versus* condensation sink: the survival parameter is defined as the particle formation rate at 6 nm divided by the formation rate at 2.5 nm, *i.e.* $J_6/J_{2.5}$. CLOUD measurements are indicated by diamond symbols and model simulations by square symbols without outlines. The points are coloured according to the particle growth rate at 3 nm, calculated from the measured HNO_3 and NH_3 concentrations (Fig. 1), the fuchsia colour indicates conditions of either no growth (GR = 0) or evaporation of NH_4NO_3 (GR < 0). The CLOUD experiments are those shown in Fig. 2, the experimental conditions are listed in its caption. All the model simulations assume kinetic nucleation (zero evaporation), and ~10 nm h^{-1} early growth (from H_2SO_4) for non-activated particles, in the absence of any particle condensation sink. The model assumes a constant $J_{2.5}$ of 10 cm^{-3} s^{-1}. The model conditions are 5 °C, HNO_3 and NH_3 between 400 pptv and 4 ppbv, and a condensation sink between 0.01 and 0.13 s^{-1}. Experiments where the activation diameter is sufficiently low that the non-activated growth surpasses it result in activation of particles. Activated particles grow rapidly enough to survive loss in the presence of high condensation sinks whereas non-activated particles have very low survival probabilities. The experimental measurements show that the rapid particle growth rates from ammonium nitrate formation are sufficient to overcome losses of newly formed particles in high condensation sink environments. The good agreement of the model with the experimental data confirms that particle scavenging involves unit sticking probability, as expected from previous measurements in low condensation sink environments.

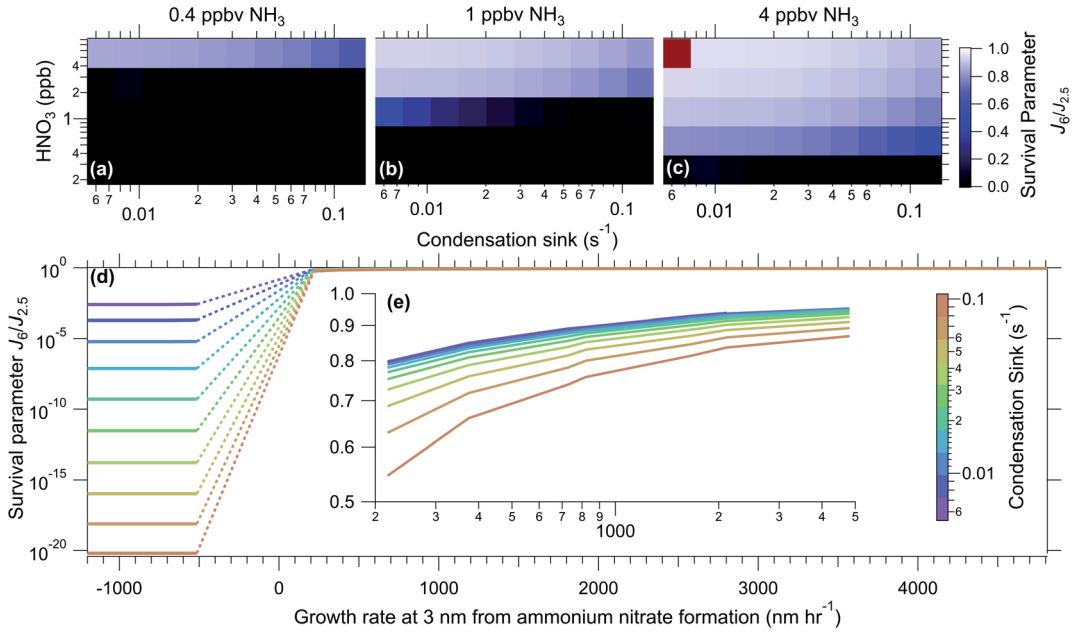

Fig. 4 Illustration of the binary behaviour of modelled survival of newly formed particles due to ammonium nitrate formation: (a–c) modelled particle survival parameter as a function of condensation sink and concentrations of HNO_3 and NH_3 at 5 °C. The model assumes constant HNO_3 and NH_3 concentrations and H_2SO_4 production rate, and simulates a variable CS at 300 nm. The red square in panel c is a model where the CS and J rates did not stabilise within the time of the model. (d) Particle survival parameter *versus* the calculated growth rate at 3 nm for different condensation sinks. When the growth is not positive, *i.e.* no condensation, the particle survival parameter, $J_6/J_{2.5}$, is extremely low and around 5×10^{-4} for CS = 0.005 s^{-1}. However, above the activation diameter, the total particle growth rates increase by up to a factor of 100 or more and the survival parameter approaches unity, even for condensation sinks as high as 0.1 s^{-1}. The dashed line in between positive and negative growth rates represents a range with no data points. (e) An inset of (d) with only growth rates above 0.

loss rates; therefore, the model most likely accurately represents the underlying physics and chemistry of particle growth associated with ammonium nitrate activation. We now use the model to explore under which atmospherically relevant conditions ammonium nitrate condensation could enhance the survival of newly formed particles.

The model was run at 5 °C with NH_3 and HNO_3 concentrations ranging from 400 pptv to 4 ppbv and the condensation sink ranging from 0.01 to 0.13 s^{-1} covering a range of low particle surface area to extremely high limits. We define the survival parameter as the ratio of the formation rate of 6 nm (J_6) particles to that of 2.5 nm ($J_{2.5}$) particles at steady state, *i.e.* the proportion of how many particles survived between 2.5 and 6 nm. We feed the model with 2.5 nm particles ($J_{2.5} = 10$ cm^{-3} s^{-1}) and assume no evaporation of clusters of H_2SO_4 (kinetic nucleation). All model runs have the same production rate of H_2SO_4, which, in the absence of a condensation sink, leads to ~10 nm h^{-1} early growth (1.8–3.2 nm) for non-activated particles.

Fig. 3 indicates the calculated ammonium-nitrate-driven growth rate at 3 nm of model and CLOUD experiments *via* symbol colour, with points plotted as survival parameter against condensation sink. The fuchsia diamond symbols represent a CLOUD run with low amounts of HNO_3, as in Fig. 2, panels a–c. We can see that as the CS decayed and particles began to grow that the survival significantly increased compared to at higher CS. The purple diamond symbols represent the run with higher HNO_3 (Fig. 2 panels f–h and j), and these points along with the model points show us that at high growth rates, the condensation sink has little effect on the survival, and these points even approach unity. Although there is relatively high survival at low condensation sinks (~0.01 s^{-1}), even with slower growth rates, at high condensation sinks the only experiments that saw high survival were those with activation and high growth rates. This confirms our theory that high growth rates are able to "shepherd" small particles through size ranges where they are most vulnerable to loss.

Discussion and conclusions

Fig. 4 illustrates results from model runs over the selected concentration ranges. As can be seen, the results are almost binary, with a sharp transition from a region of no survival to a region of high survival, showing how crucial activation is for survival. In parts b and c, at high HNO_3 concentrations, the effect of the condensation sink is very small. This can also be seen in part d of the Fig. 4, but with the calculated growth rate caused by ammonium nitrate formation (at 3 nm) on the x-axis. Growth rates from ammonium nitrate formation directly scale with the flux of HNO_3 and NH_3. The ammonium nitrate flux is dependent on the concentration of gas phase NH_3 and HNO_3, as well as on which gas is limiting, and the size of the particle, the full equations are found in the ESI.† The region between negative and positive growth rates (evaporation and condensation, respectively) is where we see a step in survival, and above this region the condensation sink has a smaller effect. In panel

d, it is also more visible that at calculated negative growth rates the survival is highly dependent on the condensation sink (though it is always low). In this region, the survival is controlled by H_2SO_4 and NH_3 growth, as without activation HNO_3 does not contribute to nucleation and growth. Although the calculated flux, and therefore growth rate, of ammonium nitrate is negative, when there is no ammonium nitrate in the particles evaporation will not occur.

Survival of particles will depend on not only the growth rate, but also the activation diameter, since if particles are not large enough for NH_3 and HNO_3 to condense on there will be no activation. Therefore the contribution of activation to survival of particles will also depend on the pre-existing particle distribution. Since we constrain $J_{2.5}$ in our model, and the experiments with positive flux shown in Fig. 4(d and e) have activation diameters under 2.5 nm, all of the particles can be activated.

The observed differences in Fig. 2 parts (h) and (i) give a strong indication that although these processes may happen under ambient conditions, they are most probably masked to researchers as they do not appear as typical NPF events. This is especially the case because deviations from equilibrium are expected to be brief in the ambient atmosphere, and vapour concentrations of NH_3 and HNO_3 tend rapidly towards equilibrium. However, even short perturbations above saturation may drive the rapid growth of nucleating particles at rates up to one thousand times faster than growth by H_2SO_4 condensation, given the disparity between HNO_3 and H_2SO_4 concentrations. Particles may not experience rapid growth for long, but they can grow sufficiently fast to escape the valley of death and continue to grow *via* other condensable gases. In ambient conditions, transient deviations from equilibrium are expected to occur, especially in inhomogeneous urban settings with strong local sources of ammonia (*e.g.* from traffic or urban geometry). Since HNO_3 is usually the limiting gas, inhomogeneities in HNO_3 could have a larger impact on particle size distributions, however since NH_3 is directly emitted by a multitude of sources, it is more likely to be variable and therefore will likely have a larger impact in typical urban environments. Wang *et al.* (2020)[18] show the strong temperature dependence of ammonium nitrate formation, therefore we also expect temperature changes characteristic of vertical convection to drive the vapour concentrations of NH_3 and HNO_3 out of equilibrium. Future analysis should investigate the effect of urban and vertical mixing on the rapid growth of nucleating particles by NH_3 and HNO_3 condensation.

While Wang *et al.* (2020)[18] presented the first evidence of rapid growth by ammonium nitrate condensation, we have additionally provided the first experimental data and supporting modelling calculations demonstrating efficient scavenging of nucleating molecular clusters by larger sized particles under haze conditions. We also present experimental results of high survival of freshly nucleated particles even in the presence of a high condensation sink, confirming the hypothesis from Wang *et al.* (2020)[18] that rapid growth caused by NH_4NO_3 formation can aid in particle survival through the valley of death. These results strongly support the hypothesis that the unexplained survival of particles is due to a missing growth mechanism, and that under typical ambient conditions of a megacity at 5 °C, rapid ammonium nitrate condensation could be that missing mechanism, increasing survival of nucleated particles, and thus sustaining particle number and poor visibility during haze.

Author contributions

Conceptualization: R. M., M. X., M. W., J. Dommen, J. K., N. M. D., H. L., U. B. and I. E. H. Resources, prepared the CLOUD facility or measuring instruments: R. M., B. R., M. W., W. K., X.-C. H., D. S., J. P., G. M., D. S. W., W. S., A. B., C. P. L., R. B., L. C., B. C., J. C., L. D., J. Duplissy, H. F., L. G. C., M. G., A. H., M. H., V. H., D. K., A. K., M. K., K. L., V. M., H. E. M., B. M., O. M., T. P., M. P., J. S., M. S., Y. S., A. T., R. V., A. W., Y. Wang, S. K. W., P. M. W., Y. Wu, M. Z.-W., R. C. F., J. K., H. L., and I. E. H. Investigation: R. M., M. X., B. R., M. W., W. K., X.-C. H., D. S., J. P., G. M., D. S. W., W. S., A. B., C. P. L., A. A., R. B., D. B., B. B., L. C., L. D., J. Duplissy, H. F., L. G. C., M. G., M. H., V. H., D. K., M. L., V. M., B. M., J. S., M. S., A. T., A. W., S. K. W., Y. Wu, M. Z.-W., J. K., H. L., and I. E. H. Formal analysis: R. M., B. R., M. W., W. K., X. H., D. S., J. P., G. M., D. S. W., W. S., C. P. L., L. C., L. D., M. S., S. K. W., P. M. W., R. C. F., N. M. D., H. L., and I. E. H. Scientific discussion: R. M., M. X., B. R., M. W., W. K., X.-C. H., D. S., W. S., C. P. L., D. B., J. C., L. D., H. F., K. L., J. Dommen, R. C. F., J. K., N. M. D., H. L., U. B., and I. E. H. Writing: R. M., B. R., M. W., W. K., X.-C. H., D. S., J. P., D. S. W., J. Dommen, J. K., N. M. D., H. L., U. B., and I. E. H.

Conflicts of interest

There are no conflicts to declare.

Acknowledgements

We thank the European Organization for Nuclear Research (CERN) for supporting CLOUD with technical and financial resources and for providing a particle beam from the CERN Proton Synchrotron. This research has received funding from the European Community (EC) Seventh Framework Programme and the European Union (EU) H2020 programme (Marie Skłodowska Curie ITN CLOUD-TRAIN grant number 316662 and CLOUD-MOTION grant number 764991); European Union's Horizon 2020 research and innovation programme under the Marie Sklodowska-Curie grant agreement no. 895875 ("NPF-PANDA"); the Swiss National Science Foundation (no. 200021_169090, 200020_172602, 20FI20_172622); the US National Science Foundation (NSF; grant numbers AGS1602086, AGS1801329 and AGS-1801280); NASA graduate fellowship (NASA-NNX16AP36H); Project CLOUD-16 (project number 01LK1601C) funded by the German Bundesministerium für Bildung und Forschung (BMBF); ERC Advanced 'ATM-GP' grant no. 227463; The Portuguese Foundation for Science and Technology (project no. CERN/FIS-COM/0028/2019); ERC Consolidator grant NANODYNAMITE, 616075; the Austrian Science Fund (FWF; project no. P27295-N20); the Presidium of the Russian Academy of Sciences, the Program "Physics of

Fundamental Interactions" 2017–2020; Ministry of Science and High education of the Russian Federation; VM acknowledges the Grant No. PCF IRN BR10965191.

References

1 E. M. Dunne, *et al.*, Global atmospheric particle formation from CERN CLOUD measurements, *Science*, 2016, **354**, 1119–1124.
2 J. Merikanto, D. V. Spracklen, G. W. Mann, S. J. Pickering and K. S. Carslaw, Impact of nucleation on global CCN, *Atmos. Chem. Phys.*, 2009, **9**, 8601–8616.
3 Intergovernmental Panel on Climate Change (IPCC), *Climate Change 2013: the Physical Science Basis*, 2013.
4 U. Lohmann and J. Feichter, Global indirect aerosol effects: a review, *Atmos. Chem. Phys.*, 2005, **5**, 715–737.
5 G. Chen, W.-C. Wang and J.-P. Chen, Circulation responses to regional aerosol climate forcing in summer over East Asia, *Clim. Dyn.*, 2018, **51**, 3973–3984.
6 S. Guo, *et al.*, Elucidating severe urban haze formation in China, *Proc. Natl. Acad. Sci. U. S. A.*, 2014, **111**, 17373–17378.
7 J. S. Apte, M. Brauer, A. J. Cohen, M. Ezzati and C. A. Pope, Ambient $PM_{2.5}$ Reduces Global and Regional Life Expectancy, *Environ. Sci. Technol. Lett.*, 2018, **5**, 546–551.
8 WHO, *WHO Methods and Data Sources for Global Burden of Disease Estimates 2000–2019*, 2014.
9 WHO, *WHO Methods and Data Sources for Country-Level Causes of Death 2000–2019*, 2014.
10 V.-M. Kerminen and M. Kulmala, Analytical formulae connecting the "real" and the "apparent" nucleation rate and the nuclei number concentration for atmospheric nucleation events, *J. Aerosol Sci.*, 2002, **33**, 609–622.
11 M. Xiao, *et al.*, The driving factors of new particle formation and growth in the polluted boundary layer, *Atmos. Chem. Phys.*, 2021, **21**, 14275–14291.
12 D. Bousiotis, M. Dall'Osto, D. C. S. Beddows, F. D. Pope and R. M. Harrison, Analysis of new particle formation (NPF) events at nearby rural, urban background and urban roadside sites, *Atmos. Chem. Phys.*, 2019, **19**, 5679–5694.
13 Z. B. Wang, *et al.*, Characteristics of regional new particle formation in urban and regional background environments in the North China Plain, *Atmos. Chem. Phys.*, 2013, **13**, 12495–12506.
14 Z. Wang, *et al.*, New particle formation in China: current knowledge and further directions, *Sci. Total Environ.*, 2017, **577**, 258–266.
15 L. Yao, Atmospheric new particle formation from sulfuric acid and amines in a Chinese megacity, *Science*, 2018, **361**, 278–281.
16 S. Xiao, *et al.*, Strong atmospheric new particle formation in winter in urban Shanghai, China, *Atmos. Chem. Phys.*, 2015, **15**, 1769–1781.
17 M. Kulmala, V.-M. Kerminen, T. Petäjä, A. J. Ding and L. Wang, Atmospheric gas-to-particle conversion: why NPF events are observed in megacities?, *Faraday Discuss.*, 2017, **200**, 271–288.
18 M. Wang, *et al.*, Rapid growth of new atmospheric particles by nitric acid and ammonia condensation, *Nature*, 2020, **581**, 184–189.
19 J. H. Seinfeld and S. N. Pandis, *Atmospheric Chemistry and Physics*, John Wiley & Sons, 2nd edn, 2006.
20 D. Stolzenburg, *et al.*, Enhanced growth rate of atmospheric particles from sulfuric acid, *Atmos. Chem. Phys.*, 2020, **20**, 7359–7372.
21 M. Mozurkewich, The dissociation constant of ammonium nitrate and its dependence on temperature, relative humidity and particle size, *Atmos. Environ., Part A*, 1993, **27**, 261–270.
22 L. Pichelstorfer, *et al.*, Resolving nanoparticle growth mechanisms from size- and time-dependent growth rate analysis, *Atmos. Chem. Phys.*, 2018, **18**, 1307–1323.
23 M. Ozon, D. Stolzenburg, L. Dada, A. Seppänen and K. E. J. Lehtinen, Aerosol formation and growth rates from chamber experiments using Kalman smoothing, *Atmos. Chem. Phys.*, 2021, **21**, 12595–12611.

Electronic supplementary information

Survival of newly formed particles in haze conditions

Ruby Marten[1], Mao Xiao[1], Birte Rörup[2], Mingyi Wang[3], Weimeng Kong[4], Xu-cheng He[2], Dominik Stolzenburg[2], Joschka Pfeifer[5,6], Guillaume Marie[6], Dongyu S. Wang[1], Wiebke Scholz[7], Andrea Baccarini[1,8], Chuan Ping Lee[1], Antonio Amorim[9], Rima Baalbaki[2], David M. Bell[1], Barbara Bertozzi[10], Lucia Caudillo[6], Biwu Chu[2], Lubna Dada[1], Jonathan Duplissy[2], Henning Finkenzeller[11], Loïc Gonzalez Carracedo[12], Manuel Granzin[6], Armin Hansel[7], Martin Heinritzi[6], Victoria Hofbauer[3], Deniz Kemppainen[2], Andreas Kürten[6], Markus Lampimäki[2], Katrianne Lehtipalo[2,13], Vladimir Makhmutov[14], Hanna E. Manninen[5], Bernhard Mentler[7], Tuukka Petäjä[2], Maxim Philippov[14], Jiali Shen[2], Mario Simon[6], Yuri Stozhkov[14], António Tomé[15], Andrea Wagner[6], Yonghong Wang[2], Stefan K. Weber[5], Yusheng Wu[2], Marcel Zauner-Wieczorek[6], Joachim Curtius[6], Markku Kulmala[2], Ottmar Möhler[10], Rainer Volkamer[11], Paul M. Winkler[12], Douglas R. Worsnop, Josef Dommen[1], Richard C. Flagan[4], Jasper Kirkby[5,6], Neil M. Donahue[3], Houssni Lamkaddam[1,@], Urs Baltensperger[1], Imad El Haddad[1,@]

[1]Laboratory of Atmospheric Chemistry, Paul Scherrer Institute, 5232 Villigen, Switzerland.
[2]Institute for Atmospheric and Earth System Research (INAR)/ Physics, Faculty of Science, University of Helsinki, 00014 Helsinki, Finland.
[3]Center for Atmospheric Particle Studies, Carnegie Mellon University, 15213 Pittsburgh, PA, USA.
[4]California Institute of Technology, Division of Chemistry and Chemical Engineering 210-41, Pasadena, CA 91125, USA.
[5]CERN, CH-1211 Geneva, Switzerland.
[6]Institute for Atmospheric and Environmental Sciences, Goethe University Frankfurt, 60438 Frankfurt am Main, Germany.
[7]Institute of Ion Physics and Applied Physics, University of Innsbruck, 6020 Innsbruck, Austria
[8]Extreme Environments Research Laboratory (EERL), École Polytechnique Fédérale de Lausanne, Sion, CH.
[9]CENTRA and FCUL, University of Lisbon, 1749-016 Lisbon, Portugal.
[10]Institute of Meteorology and Climate Research, Karlsruhe Institute of Technology, 76021 Karlsruhe, Germany.
[11]Department of Chemistry & CIRES, University of Colorado Boulder, 215 UCB, Boulder, 80309, CO, USA.
[12]Faculty of Physics, University of Vienna, Boltzmanngasse 5, A-1090 Vienna, Austria.
[13]Finnish Meteorological Institute, Helsinki, Finland.
[14]Lebedev Physical Institute of the Russian Academy of Sciences, 119991, Moscow, Leninsky prospekt, 53, Russian Federation.
[15]IDL-Universidade da Beira Interior, 6201-001 Covilhã, Portugal.
[16]Aerodyne Research, 01821 Billerica, MA, USA.
[@]Corresponding authors e-mails: houssni.lamkaddam@psi.ch, imad.el-haddad@psi.ch.

Summary

This electronic supplementary information (ESI) document describes the CLOUD chamber and details of experimentation and instrumentation used at CLOUD, CERN. Details of the parameters calculated from CLOUD results (such as growth rates) and details of the kinetic model set up and equations used are also presented.

Methods

The CLOUD chamber at CERN

The CLOUD chamber is 26.1 cubic meters, is made of stainless steel, and the inside surface is electro-polished [1,2]. The chamber concentrations are kept homogeneous via turbulence created by two magnetically coupled stainless steel fans at the top and bottom of the chamber [3], with mixing times typically on the order of a few minutes. The dilution (ventilation) lifetime is 1.3 hours. Wall loss rates of gases and different sized particles are also well characterised [4]. Precursor gases are injected via a state-of-the-art gas system that allows us to control dilution and injection flows to control the gas concentrations with great accuracy. The trace gases are injected into the chamber along with dry air, formed by mixing 79% boil-off nitrogen and 21% boil-off oxygen (both Messer, 99.999%) and water is added from an evaporator using ultrapure water (18 MΩ cm, Millipore Corporation) in order to control the relative humidity. Note that in this study experiments were done without use of the 3.5 GeV/c secondary pion beam (π beam) from the CERN PS.

The experiments presented in this paper involved varying mixtures of gases capable of nucleation and growth; sulfuric acid, ammonia, dimethylamine, nitric acid, and HOMs generated from toluene and α-pinene. Experiments started when lights were turned on and condensable gases were formed by photolysis (and further reactions). The various lights used in these experiments resulted in a homogeneous illumination of the chamber. These different sources were: three UV sources including four 200 W Hamamatsu Hg-Xe lamps (UVH), a 170 W quartz-clad high intensity Hg lamp (saber, LS1), and a 4 W KrF 248 nm excimer UV laser (UVX); further, UVA was generated at 385 nm by a 400 W UVA LED saber (LS3). LS1, UVH, and UVX were used to photolyse ozone, and LS3 was used to photolyse HONO, both in order to generate OH radicals. After each experiment, the particles and condensable gases were cleaned from the chamber by increasing the fan speed and thus the loss rates of particles, and gas concentrations were set up for the subsequent experiment.

The high condensation sink runs were extremely challenging to perform. For example, in instances where the condensation sink was decreasing over time, the gas phase NH_3 was constantly increasing, although the injection rate was constant. The large amount of HNO_3 generated in building up the condensation sink was also the cause of depletion of reagent ions in the Br^- CIMS, and so the HNO_3 was modelled for certain experiments (see modelling nitric acid).

Instrumentation

To measure gas-phase nitric acid, a Br^- chemical ionisation atmospheric pressure interface time of flight mass spectrometer (CI-API-TOF-MS) was deployed in the CLOUD chamber at CERN. We used a commercially available inlet from Airmodus for the mass spectrometer, which is optimised for minimum wall loss. The details of measurements can be found in the Methods section of Wang *et al*. (2020). During some experiments, the Br^- ion was depleted in the Br- CIMS due to high levels of HNO_3, and so HNO_3 was modelled from other time-series (see modelling nitric acid).

H_2SO_4 and HOMs were also measured by a CI-API-TOF-MS but with nitrate reagent ions. There were two NO_3^- CIMS present, one was equipped with an inlet from Airmodus, and the other used a home-made inlet and corona discharge for ion generation[5]. Both instruments were equipped with an electrostatic filter so as not to measure naturally formed ions from the CLOUD chamber. The detection limit of the condensable gases measured by the NO_3^- CIMS was approximately 5 x 10^4 cm^{-3}. Calibration techniques for H_2SO_4 and HOMs have been described previously [6,7].

Volatile organic compounds (VOCs) were measured by two different custom built proton transfer reaction time of flight mass spectrometers, a selective reagent ionization time of flight mass spectrometer (SRI-ToF-MS) described in Canaval *et al.* (2019)[8] and the PTR3-ToF-MS described in Breitenlechner *et al.* (2017)[9]. Both instruments used H_3O^+ ions to charge compounds of the sample gas. Humidity dependent calibrations of toluene were performed by directly measuring a gas standard (Apel Riemer Environmental Inc) at specific conditions of the respective experiments. These instruments were also used to analyze the cleanliness of the chamber in between experiments.

Ammonia and DMA were measured by a water cluster CI-API-TOF-MS, this instrument is described in detail in Pfeifer *et al*. (2020)[10]. The instrument introduced a newly designed cross-flow ion source. The authors report the limit of detection of ammonia to be ~ 0.5 pptv and predict the detection limit of DMA to be lower.

A suite of instruments covering different size ranges measured the particle number and size distribution between 1.5 nm and 487 nm. Starting with the smallest size, the instruments used were: a nano condensation nucleus counter (nCNC) [11]; a differential mobility analyser train (DMA-Train) [12]; a nano-scanning electrical mobility spectrometer (nSEMS) [13]; a nano-scanning mobility particle sizer (nano-SMPS); and a long SMPS.

The A11 nano Condensation Nucleus Counter is composed of a particle size magnifier (PSM) connected in series with a condensation particle counter (CPC). The PSM is an aerosol pre-conditioner that uses diethylene glycol (DEG) to grow aerosol particles to a size that is easily detected by the CPC. The saturator flow rate inside the PSM can be adjusted so aerosol particles of different sizes are activated. During CLOUD13, the PSM saturator flow was set to scanning, meaning it measured the particle size distribution between 1.5 and 2.5 nm [14,15].

The DMA train is built up of 6 different DMAs in parallel, measuring the range 1.8 - 4.3 nm each with different fixed voltages, to allow different size ranges, and the particles are counted by either a PSM or CPC depending on the size [12]; Stolzenburg *et al*. (2017) describe the instrument in detail.

The nSEMS is a newly developed instrument that operates in the range of 1.5 – 25 nm. For classification of particle size, the nSEMS uses a radial opposed migration ion and aerosol classifier (ROMIAC), which is capable of measuring particle diameters down to the nanometer level with less degradation and less sensitivity to diffusional resolution degradation than the DMAs. A full description of the instrument can be found in Kong *et al*. (2021)[13].

The nano and long SMPS are commercially available instruments and have been fully characterised and described in previous studies [16–18]. Together, the nano-SMPS and long-SMPS scan range spanned from 4 to 487 nm. Particles larger than 487 nm were formed during runs with high condensation

sinks. For these experiments, a multi-peak fitting routine was applied to deconvolve the observable size distribution into component modes, which were assumed to be lognormal in shape. The fitting results were then used to estimate the particle size distribution from 487 nm to 1036 nm. This was necessary for us to better calculate the condensation sinks and *J* rates, since the existence of larger particles will influence these parameters.

Ozone (O_3, Thermo Environmental Instruments, TEI 49C), sulfur dioxide (SO_2 Thermo Fischer Scientific Inc. 42i-TLE), and nitric oxide (NO, ECO Physics, CLD 780TR) were measured by gas monitors. Nitrogen dioxide was also measured but by a cavity attenuated phase shift NO_2 monitor (CAPS NO_2, Aerodyne Research Inc.). A custom-made cavity-enhanced differential optical absorption spectrometry instrument (CE-DOAS) was also used to measure NO_2 and HONO. Relative humidity of the chamber was measured by two instruments, dew point mirrors (EdgeTech) and an in situ-TDL-Hygrometer (KIT, CERN). Temperature was measured by mid-plane internal PT100 temperature sensors placed at 5 different distances from the chamber wall. The sensor that was closest to the midpoint of the chamber, 1.2 m from the wall, was used as the chamber's reference temperature.

Growth rates

Growth rates were calculated using the 50 % appearance time method [19]. This method works best in chamber or flow tube experiments, as it relies on the identification of a growing particle distribution easily differentiated from other particles. Since the CLOUD chamber is cleaned before each experiment, and new particles are nucleated from gases rather than injected, it is easy to differentiate the growing particles. This was more difficult in the case of the high condensation sink runs, as there were many pre-existing particles of different sizes, and thus the reason why growth rates are not reported for these runs. The model was set up to give output of different size bin concentrations at every time step (0.1 s) and so growth rates could be calculated in the same way as experimental data, where the sizing instrument output also gives size-distributed particle concentrations. Each size bin concentration over time is fit to the following function using a least-squares solver:

$$S_{d_p}(t) = \frac{a - b}{1 + (t / t_{app})^d} + b \qquad \text{(S.1)}$$

Size and time dependent growth rates calculated using the INSIDE method were presented in Figure 2.[20] This method is based on the adapted, size-integrated GDE, where the growth rate is solved for using experimental inputs for other variables. Full details of this method can be found in Pichelstorfer *et al*. (2018). [20] GDE-based GR methods might suffer from statistical fluctuations in the size-distribution measurement that may cause significant error. However, Ozon *et al.* (2021) [21] showed that for well-controlled chamber experiments, the INSIDE method agrees well with a fixed interval Kalman smoother which estimates the GR error for similar experiments to those in Figure 2a-e) to be roughly 1 nm hr^{-1}, or at maximum 50% for more dynamic situations such as in Figure 2f-j).

Where S_{dp} is the signal or concentration of a particular diameter (d_p) bin, *a* and *b* are the background and plateau concentrations respectively, *d* is a free parameter which relates to the steepness of the sigmoidal increasing curve, and t_{app} is the 50 % appearance time, which is equal to the time at which 50% of the concentration (in between background and plateau) has been reached. The appearance time for each bin is then plotted against the particle diameter and a linear fit is made to present

growth rates in nm hr^{-1}. For a full description see the Supporting Information of Stolzenburg *et al*. (2018)[19].

Formation rates

Formation rates were determined using the balance equation between the particle sources and sinks as per Dada et al. (2020)[22] shown in equation (S.2):

$$J_x = \frac{dN_{\geq x}}{dt} + S_{dil} + S_{wall} + S_{coag} \quad \text{(S.2)}$$

Where the units of J are (particles) cm^{-3} s^{-1} and S_{dil}, S_{wall}, and S_{coag} are terms for dilution loss, wall loss, and coagulation loss, respectively.

Formation rates of particles of diameter 2.5 nm were reported as a 2.5 nm particle is thermodynamically stable and larger than the critical radius [23]. 2.5 nm particles are also commonly measured in ambient campaigns and thus it is valuable for comparison. The total number concentration of particles with diameters 2.5 nm and above was measured using the nCNC.

Activation diameter

During the CLOUD experiments, when there was an activation event, the particle size bins just above the activation diameter tended to have low concentrations, due to fast growth after activation (faster than the time resolution of the instrument). The activation diameter was therefore determined by identifying the first time step where a bimodal distribution occurred, and the largest size bin of the smaller mode, where the concentration dropped, was identified as the activation diameter. For further information on this technique see the supporting information of Wang *et al*. (2020)[24].

Modelling ammonium nitrate

The flux of ammonia and nitric acid to a certain size particle is calculated using the following equation.

$$\phi_{i,p} = N_p^s \pi d_p^2 \underbrace{\left(\frac{E_{i,p}^{\mu} \varepsilon_{i,p} e_{i,p} \alpha_{i,p} \bar{s}_i B_{i,p}}{4}\right)}_{\text{Collision speed: } s_{I,p}^{\perp}} \underbrace{\left[c_i^v - a_{i,p}^s K_{i,p} c_i^o\right]}_{\text{Driving force: } F_{i,p}^{v,s}} \quad \text{(S.3)}$$

Area: A_p^s

Flux per unit surface area: $\varphi_{i,p}^{v,s}$

$$\bar{s}_i = \sqrt{\frac{8 k_b T}{\pi m_i}} \quad \text{(S.4)}$$

The subscript *i* denotes the gas species, i.e. NH_3 or HNO_3 (depending on which is limiting), and the subscript *p* refers to the particle size. Where N_p^s is the particle number and d_p is the diameter. The collision speed is derived from the average molecular speed (Equation (S.4)), and includes terms reflecting Van der Waals interactions between the vapour and particle (charge - dipole, dipole -

induced dipole, and induced dipole - induced dipole), $E_{i,p}^{\mu} = E^{\mu}(H_{i,p})$ where $H_{i,p}$ is the Hamaker constant in Joules; the non-zero size of the vapour, $\varepsilon_{i,p} = \left(d_i^2 + d_p^2\right)/d_p^2$; and the non-infinite mass of small clusters, $e_{i,p} = \sqrt{(m_i + m_p)/m_p}$. A term for gas-phase diffusion limitations is $B_{i,p} \simeq 1$ for large Knudsen numbers. The mass accommodation coefficient, $\alpha_{i,p}$, can also be included, this was assumed to be 1 for these calculations. The driving force depends on vapour concentration, c_i^v, and saturation concentration, c_i^o, as well as the activity in the solid phase and the kelvin term. Since the Hamaker constant for ammonia is 0, the enhancement from Van der Waals interaction is only relevant in acid-limiting conditions, and has the greatest effect at lower sized particles. This enhancement was not included in the thermodynamic model for this paper, but it may explain some of the difficulty in duplicating the experiment in Figure 2 Run 2, since the enhancement of growth at small sizes would have the small particles grow faster than the large particles in the CS.

We simplify the flux per unit surface area calculation to

$$\varphi_{i,p}^{v,s} = s_{i,p}^{\perp}\, c_i^v\, \gamma_{i,p} \tag{S.5}$$

$$\gamma_{i,p} = \left[1 - \frac{a_{i,p}^s}{a_i^v} K_{i,p}\right] \tag{S.6}$$

where $\gamma_{i,p}$ is defined as the uptake coefficient and can be defined in terms of the saturation ratio of the gas, where the saturation ratio is equal to the activity in the vapour phase divided by the activity in the solid phase times the kelvin term to account for the curvature of the surface of a particle.

$$\gamma_{i,p} = \left(1 - \frac{1}{S_{i,p}}\right) = \frac{S_{i,p} - 1}{S_{i,p}} = \frac{S_{i,p}^{XS}}{S_{i,p}} \tag{S.7}$$

$$S_{i,p} = \frac{a_i^v}{a_{i,p}^s K_{i,p}} \tag{S.8}$$

We can consider the flux as equal due to the 1:1 stoichiometry of condensation of ammonium nitrate, and thus we define a collision ratio, r^v_{AB}, which is the concentration ratio scaled by the collision speed of each molecule. The subscripts A and B are now used for acid and base.

$$\varphi_{A,p}^{v,s} = \varphi_{B,p}^{v,s} \tag{S.9}$$

$$s_{A,p}^{\perp}\, c_A^v\, \gamma_{A,p} = s_{B,p}^{\perp}\, c_B^v\, \gamma_{B,p} \tag{S.10}$$

$$\gamma_{B,p} = \frac{s_{A,p}^{\perp}\, c_A^v}{s_{B,p}^{\perp}\, c_B^v} \gamma_{A,p} \tag{S.11}$$

$$\gamma_{B,p} = r_{AB}^{v}\, \gamma_{A,p} \tag{S.12}$$

$$r_{AB}^{v} = \frac{s_{A,p}^{\perp}\, c_A^v}{s_{B,p}^{\perp}\, c_B^v} \tag{S.13}$$

In the case of base limiting experiments, $S_{B,p}$ is then found iteratively using the following equation, solved by combining Equations (S.7), (S.9) and (S.10). If the experiment is acid limiting, the difference in solving for $S_{A,p}$ is to replace r^v_{AB} with $1/r^v_{AB}$.

$$S_{B,p} = \frac{S_{AB,p}}{2}\left[\left(\frac{r^v_{AB}-1}{r^v_{AB}}\right) + \sqrt{\left(\frac{r^v_{AB}-1}{r^v_{AB}}\right)\frac{4}{r^v_{AB}S_{AB,p}}}\right] \quad \text{(S.14)}$$

Where $S_{AB,p}$ is the saturation of ammonium nitrate

$$S_{AB,p} = \frac{a^v_A a^v_B K^{eq}_{AB}}{K_{AB,p}} = \frac{x^v_A x^v_B}{K_{AB,p}K_p} \quad \text{(S.15)}$$

$$K_p = \frac{p^o_B p^o_A}{K^{eq}_{AB}} \quad \text{(S.16)}$$

Where x^v_A and x^v_B are the mixing ratios of nitric acid and ammonia respectively, K^{eq}_{AB} is the equilibrium constant for $NH_3(s) + HNO_3(s) \rightleftharpoons NH_4{\cdot}NO_3(s)$, K_p is an overall dissociation constant for ammonium nitrate condensation, i.e. $NH_3(v) + HNO_3(v) \rightleftharpoons NH_4{\cdot}NO_3(s)$, [25], and $K_{AB,p}$ is the Kelvin term for ammonium nitrate, correcting for the curvature effect of different sized particles.

$$K_{AB,p} = 10^{\left(d_{K10}/d_p\right)} \quad \text{(S.17)}$$

The Kelvin diameter for ammonium nitrate at 5 °C was calculated by fitting the data from CLOUD experiments (Figure S2) according to the relationship shown in Equation (S.18).

$$S_{AB,p} = 10^{\left(d_{K10}/d_{act}\right)} \quad \text{(S.18)}$$

Modelling nitric acid

In the two CLOUD experiments with high condensation sink (Figure 2), there were no accurate measurements of HNO_3 due to depleted reagent ions, and therefore the time-series presented are modelled concentrations. A box model was set up where HNO_3 was solved for based on sums of production and losses at each time step.

$$\frac{\partial HNO_3}{\partial t} = source_{injection} + source_{NO_2 + \cdot OH} - loss_{wall\,+\,dilution} - loss_{condensation\ sink} \quad \text{(S.19)}$$

This model was tested on other CLOUD experiments and agreed with the measurements from the Br^- CI-API-TOF-MS within a factor of two.

OH was modelled in a similar way using the AtChem online solver where the chemical mechanistic information was taken from the Master Chemical Mechanism, MCM v3.3.1 [26,27]. Inputs were measured time series of various trace gases, photolysis rates of ozone and HONO, and chamber wall and dilution losses specific to CLOUD.

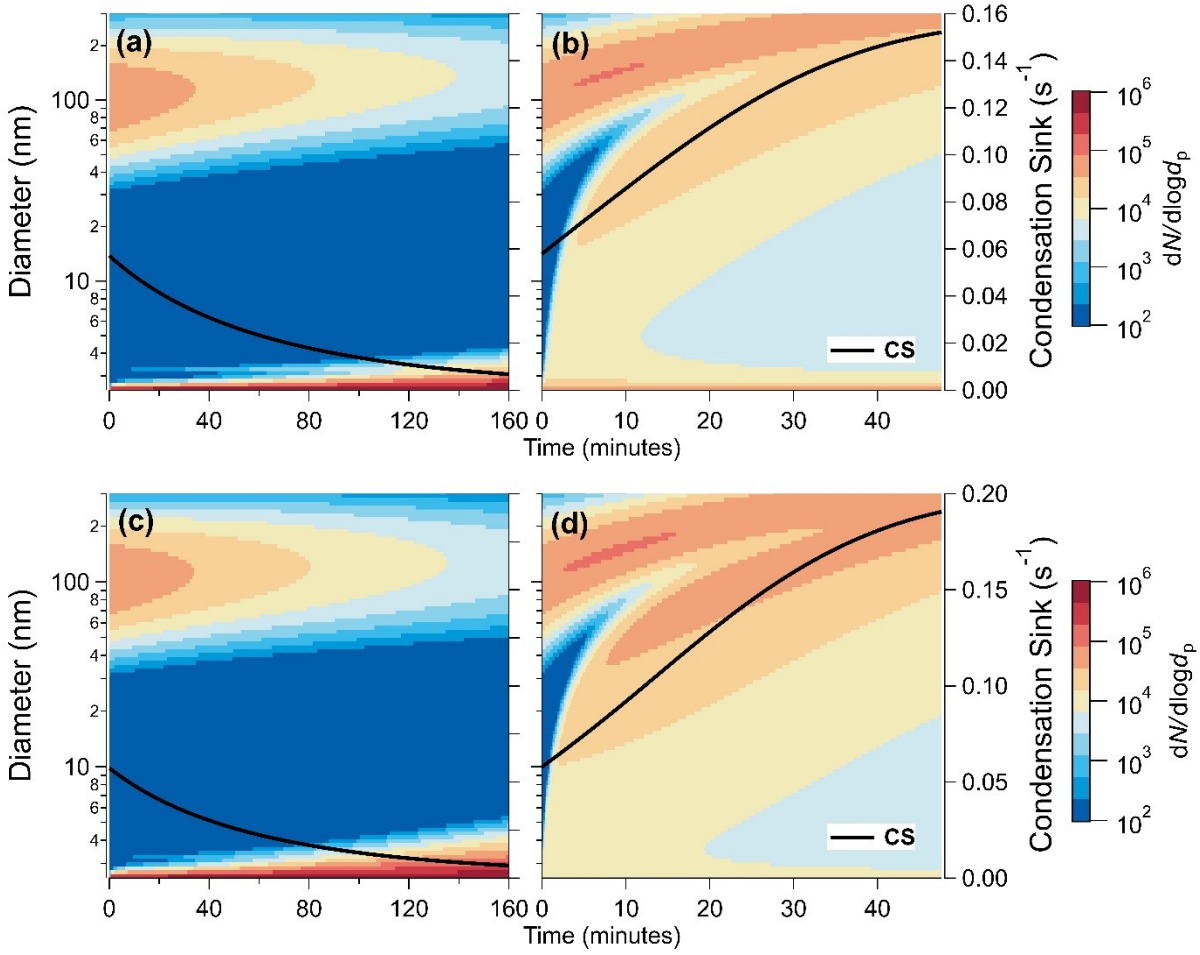

***Figure S1: Sensitivity tests on gas phase concentrations and formation rates on modelled results of Figure 2**: This figure is a repeat model of the runs in Figure 2 d and i of the main text but with **a-b)** $J_{2.5}$ constrained to 10 cm^3s^{-1}, and **c-d)** $J_{2.5}$ constrained to 10 cm^3s^{-1} as well as H_2SO_4 and NH_3 concentrations switched between the two experiments. All other experimental conditions are the same. The model results are similar to those in Figure 2 panels d and i, with little to no growth in the low HNO_3 case (a,c), and the "smear" of particles of all sizes in the high HNO_3 case (b, d).*

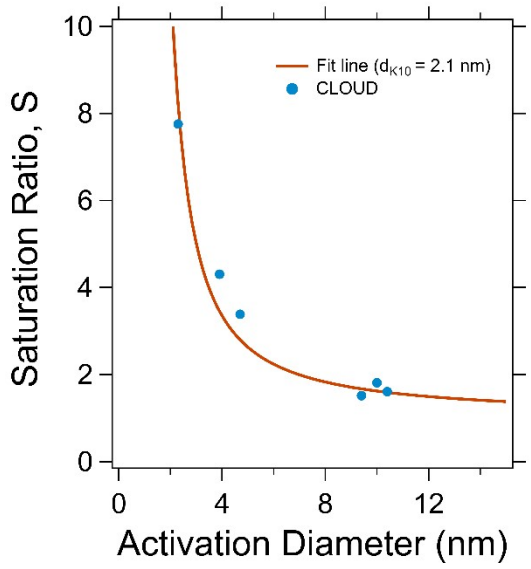

235

236 ***Figure S2: Saturation ratio vs activation diameter:*** *Blue markers represent measured activation diameters from CLOUD*
237 *experiments and saturation ratios calculated from measured HNO_3 and NH_3 gas phase concentrations. The red fit line is fit to*
238 *this data and then used to calculate the Kelvin diameter for use in the model.*

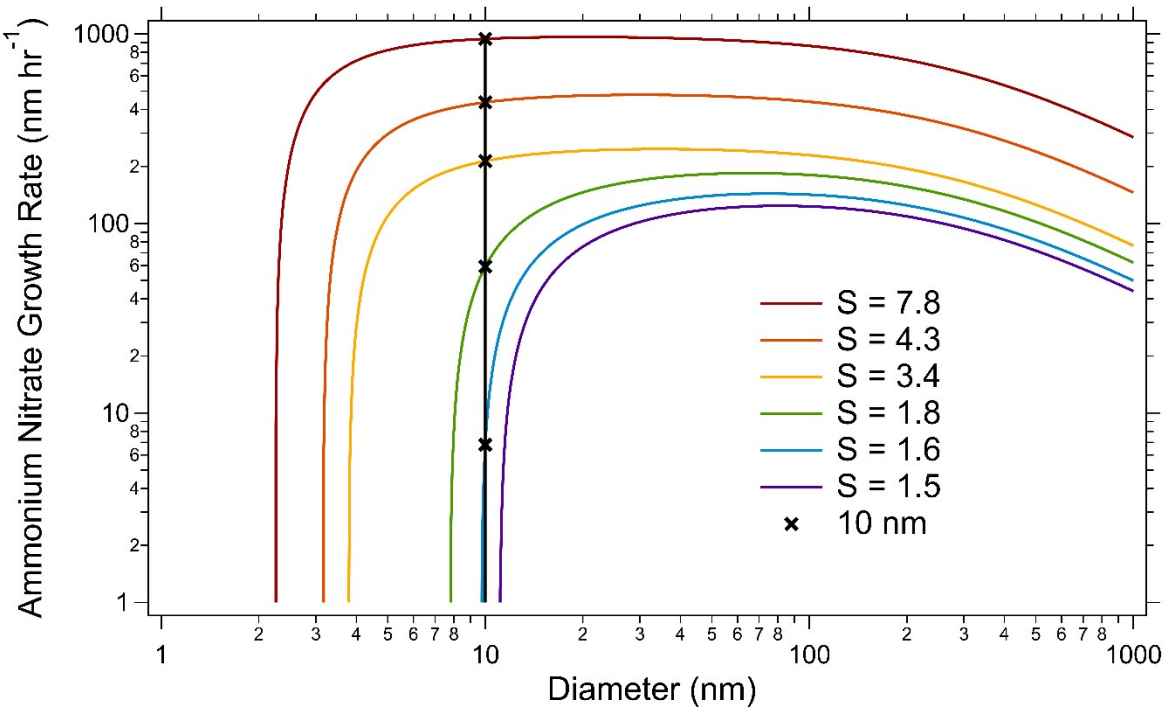

239

240 ***Figure S3: Diameter vs calculated growth rates from flux equations –*** *The curves are calculated using the equations in the*
241 *section "Modelling ammonium nitrate". The six S curves plotted are using S calculated from the HNO_3 and NH_3 gas*
242 *concentrations from the six CLOUD experiments shown in Figure 1. It is apparent that at low diameters the growth varies*
243 *dramatically, around the activation diameter for each S value.*

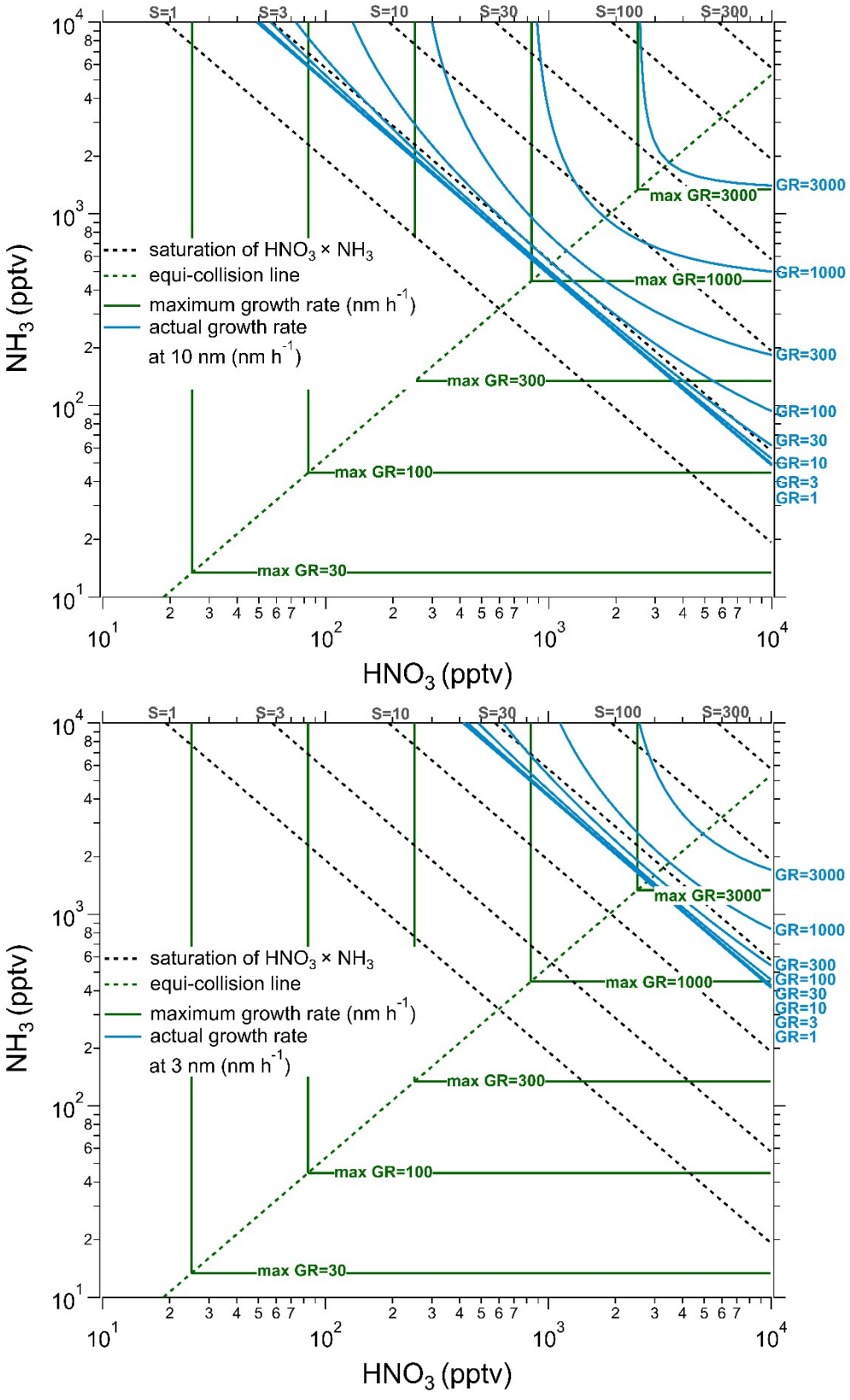

Figure S4: Calculated growth rates of condensation of ammonium nitrate: *The phase space shown is between 1 pptv and 10,000 pptv (10 ppbv) at 5 °C. The top panel shows growth rates for a particle of 10 nm and the bottom panel shows growth rates for a particle of 3 nm (the same size used for calculating growth rates in Figure 2) The calculations for growth rate include the Kelvin effect using the Kelvin diameter calculated (see modelling ammonium nitrate).*

References

1. Kirkby, J. *et al.* Role of sulphuric acid, ammonia and galactic cosmic rays in atmospheric aerosol nucleation. *Nature* **476**, 429–433 (2011).
2. Duplissy, J. *et al.* Effect of ions on sulfuric acid-water binary particle formation: 2. Experimental data and comparison with QC-normalized classical nucleation theory: BINARY PARTICLE FORMATION EXPERIMENTS. *J. Geophys. Res. Atmos.* **121**, 1752–1775 (2016).
3. Voigtländer, J., Duplissy, J., Rondo, L., Kürten, A. & Stratmann, F. Numerical simulations of mixing conditions and aerosol dynamics in the CERN CLOUD chamber. *Atmos. Chem. Phys.* **12**, 2205–2214 (2012).
4. Stolzenburg, D. *et al.* Enhanced growth rate of atmospheric particles from sulfuric acid. *Atmos. Chem. Phys.* **20**, 7359–7372 (2020).
5. Kürten, A., Rondo, L., Ehrhart, S. & Curtius, J. Performance of a corona ion source for measurement of sulfuric acid by chemical ionization mass spectrometry. *Atmos. Meas. Tech.* **4**, 437–443 (2011).
6. Tröstl, J. *et al.* The role of low-volatility organic compounds in initial particle growth in the atmosphere. *Nature* **533**, 527–531 (2016).
7. Kirkby, J. *et al.* Ion-induced nucleation of pure biogenic particles. *Nature* **533**, 521–526 (2016).
8. Canaval, E. *et al.* Rapid conversion of isoprene photooxidation products in terrestrial plants. *Commun Earth Environ* **1**, 44 (2020).
9. Breitenlechner, M. *et al.* PTR3: An Instrument for Studying the Lifecycle of Reactive Organic Carbon in the Atmosphere. *Anal. Chem.* **89**, 5824–5831 (2017).
10. Pfeifer, J. *et al.* Measurement of ammonia, amines and iodine species using protonated water cluster chemical ionization mass spectrometry. *Atmospheric Measurement Techniques Discussions* 1–36 (2019) doi:10.5194/amt-2019-215.
11. Vanhanen, J. *et al.* Particle Size Magnifier for Nano-CN Detection. *Aerosol Science and Technology* **45**, 533–542 (2011).

12. Stolzenburg, D., Steiner, G. & Winkler, P. M. A DMA-Train for precision measurement of sub-10nm aerosol dynamics. *Atmospheric Measurement Techniques* **10**, 1639–1651 (2017).
13. Kong, W. *et al.* The nano-scanning electrical mobility spectrometer (nSEMS) and its application to size distribution measurements of 1 . 5-25 nm particles. 1–26 (2021).
14. Cai, R. *et al.* Data inversion methods to determine sub-3 nm aerosol size distributions using the particle size magnifier. *Atmos. Meas. Tech.* **11**, 4477–4491 (2018).
15. Lehtipalo, K. *et al.* Methods for determining particle size distribution and growth rates between 1 and 3 nm using the Particle Size Magnifier. **19**, 22.
16. Tröstl, J. *et al.* Fast and precise measurement in the sub-20nm size range using a Scanning Mobility Particle Sizer. *Journal of Aerosol Science* **87**, 75–87 (2015).
17. Jurányi, Z. *et al.* A 17 month climatology of the cloud condensation nuclei number concentration at the high alpine site Jungfraujoch. *J. Geophys. Res.* **116**, D10204 (2011).
18. Wiedensohler, A. *et al.* Mobility particle size spectrometers: harmonization of technical standards and data structure to facilitate high quality long-term observations of atmospheric particle number size distributions. *Atmos. Meas. Tech.* **5**, 657–685 (2012).
19. Stolzenburg, D. *et al.* Rapid growth of organic aerosol nanoparticles over a wide tropospheric temperature range. *Proc Natl Acad Sci USA* **115**, 9122–9127 (2018).
20. Pichelstorfer, L. *et al.* Resolving nanoparticle growth mechanisms from size- and time-dependent growth rate analysis. *Atmos. Chem. Phys.* **18**, 1307–1323 (2018).
21. Ozon, M., Stolzenburg, D., Dada, L., Seppänen, A. & Lehtinen, K. E. J. Aerosol formation and growth rates from chamber experiments using Kalman smoothing. *Atmos. Chem. Phys.* **21**, 12595–12611 (2021).
22. Dada, L. *et al.* Formation and growth of sub-3-nm aerosol particles in experimental chambers. *Nat Protoc* **15**, 1013–1040 (2020).
23. Seinfeld, J., H. & Pandis, S., N. *Atmospheric Chemistry and Physics*. vol. 2nd edn (John Wiley & Sons, 2006).

24. Wang, M. *et al.* Rapid growth of new atmospheric particles by nitric acid and ammonia condensation. *Nature* **581**, 184–189 (2020).
25. Mozurkewich, M. The dissociation constant of ammonium nitrate and its dependence on temperature, relative humidity and particle size. *Atmospheric Environment. Part A. General Topics* **27**, 261–270 (1993).
26. Bloss, C. *et al.* Development of a detailed chemical mechanism (MCMv3.1) for the atmospheric oxidation of aromatic hydrocarbons. *Atmos. Chem. Phys.* 24 (2005).
27. Jenkin, M. E., Saunders, S. M., Wagner, V. & Pilling, M. J. Protocol for the development of the Master Chemical Mechanism, MCM v3 (Part B): tropospheric degradation of aromatic volatile organic compounds. *Part B* 13 (2003).

Paper 4: Measurement of the rate coefficients between atmospheric ions and multiply charged aerosol particles in the CERN CLOUD chamber

Measurement of the rate coefficients between atmospheric ions and multiply charged aerosol particles in the CERN CLOUD chamber

Joschka Pfeifer[1,7], Naser G. A. Mahfouz[2,3,4], Benjamin C. Schulze[5], Serge Mathot[1], Dominik Stolzenburg[6], Rima Baalbaki[6], Zoé Brasseur[6], Lucia Caudillo[7], Lubna Dada[8], Manuel Granzin[7], Xu-Cheng He[6,9], Houssni Lamkaddam[8], Brandon Lopez[3], Vladimir Makhmutov[10,11], Ruby Marten[8], Bernhard Mentler[12], Tatjana Müller[7], Antti Onnela[1], Maxim Philippov[10], Ana A. Piedehierro[9], Birte Rörup[6], Meredith Schervish[2,13], Ping Tian[14], Nsikanabasi S. Umo[15], Dongyu S. Wang[8], Mingyi Wang[5], Stefan K. Weber[1,7], André Welti[9], Yusheng Wu[6], Marcel Zauner-Wieczorek[7], Antonio Amorim[16], Imad El Haddad[8], Markku Kulmala[6], Katrianne Lehtipalo[6,9], Tuukka Petäjä[6], António Tomé[17], Sander Mirme[18,19], Hanna E. Manninen[1], Neil M. Donahue[2,3], Richard C. Flagan[5], Andreas Kürten[7], Joachim Curtius[7], Jasper Kirkby[1,7]

[1]CERN, 1211 Geneva, Switzerland
[2]Center for Atmospheric Particle Studies, Carnegie Mellon University, Pittsburgh, PA 15213, USA
[3]Department of Chemical Engineering, Carnegie Mellon University, Pittsburgh, PA 15213, USA
[4]Program in Atmospheric and Oceanic Sciences, Princeton University, Princeton, NJ 08544, USA
[5]Department of Environmental Science and Engineering, California Institute of Technology, Pasadena, CA 91125, USA
[6]Institute for Atmospheric and Earth System Research (INAR)/ Physics, Faculty of Science, University of Helsinki, Helsinki, FI-00560, Finland
[7]Institute for Atmospheric and Environmental Sciences, Goethe University Frankfurt, 60438 Frankfurt am Main, Germany
[8]Laboratory of Atmospheric Chemistry, Paul Scherrer Institute (PSI), 5232 Villigen-PSI, Switzerland
[9]Finnish Meteorological Institute, 00560 Helsinki, Finland
[10]P.N. Lebedev Physical Institute of the Russian Academy of Sciences, 119991 Moscow, Russian Federation
[11]Moscow Institute of Physics and Technology (National Research University), 117303 Moscow, Russian Federation
[12]Institute for Ion and Applied Physics, University of Innsbruck, 6020 Innsbruck, Austria
[13]Department of Chemistry, University of California, Irvine, CA 92697, USA
[14]Beijing weather modification center, Beijing, 100089, China
[15]Institute of Meteorology and Climate Research (IMK-AAF), Karlsruhe Institute of Technology (KIT), 76344 Eggenstein-Leopoldshafen, Germany
[16]CENTRA and FCUL, University of Lisbon, 1749-016 Lisbon, Portugal
[17]IDL-Universidade da Beira Interior, Rua Marquês D"Ávila e Bolama, 6201-001 Covilhã, Portugal
[18]Institute of Physics, Unversity of Tartu, Estonia
[19]Airel Ltd., 50411, Tartu, Estonia

Correspondence to: Joschka Pfeifer (joschka.pfeifer@cern.ch)

Abstract. Aerosol particles have an important role in Earth's radiation balance and climate, both directly and indirectly through aerosol–cloud interactions. Most aerosol particles in the atmosphere are weakly charged, affecting both their collision rates with ions and neutral molecules, as well as the rates by which they are scavenged by other aerosol particles and cloud droplets. The rate coefficients between ions and aerosol particles are important since they determine the growth rates and lifetimes of ions and charged aerosol particles, and so may influence cloud dynamics and aerosol processing. However, despite their importance, very few experimental measurements exist of charged aerosol collision rates under atmospheric conditions, where galactic cosmic rays in the lower troposphere give rise to ion pair concentrations of around 1000 cm^{-3}. Here we present measurements in the CERN CLOUD chamber of the rate coefficients between ions and small (<10 nm) aerosol particles

containing up to 9 elementary charges, *e*. We find the rate coefficient of a singly charged ion with an oppositely charged particle increases from 2.0 (0.4-4.4) × 10^{-6} cm^3 s^{-1} to 30.6 (24.9-45.1) × 10^{-6} cm^3 s^{-1} for particles with charges of 1 *e* to 9 *e*, respectively, where the parentheses indicate the ±1σ uncertainty interval. Our measurements are compatible with theoretical predictions and show excellent agreement with the model of Gatti and Kortshagen (2008).

1 Introduction

Atmospheric aerosols play an important, yet uncertain, role in Earth's radiative balance. The largest source of uncertainty in current climate projections is due to aerosols and their interactions with clouds (Intergovernmental Panel on Climate Change, 2014a). For new atmospheric particles to be climatically relevant, they must grow to sizes above approximately 50 nm where they can constitute cloud condensation cloud nuclei, CCN (Intergovernmental Panel on Climate Change, 2014b). During this growth — and especially in the size range below 10 nm where they are highly mobile — new particles are highly susceptible to loss from scavenging by pre-existing larger particles. Consequently, the balance between loss rates to pre-existing particles and growth rates (due to collisions with condensable vapours) plays a central role in determining the fraction of new particles that reach CCN sizes and influence climate (Marten et al., 2022; Mahfouz and Donahue, 2021a; Kulmala et al., 2017).

Electric charge plays an important role in new particle formation by stabilising the embryonic molecular clusters against evaporation (Kirkby et al., 2016, 2011; Turco et al., 1998). The presence of charges also enhances the growth rate of molecular clusters (He et al., 2021) and newly formed particles (Stolzenburg et al., 2020). However, charge can also enhance particle losses to pre-existing particles of opposite polarity (Mahfouz and Donahue, 2021a, b), or even neutral particles via Van der Waals enhancement. To understand the role of charge in the formation of CCN requires a quantitative understanding of the charge state of the atmospheric aerosol. This, in turn, requires knowledge of particle–particle and ion–particle rate coefficients under atmospheric conditions. Previous studies have for the most part considered collisions between particles or molecules where only one is charged (e.g., Dépée et al., 2021; He et al., 2021). Yet, particles with larger numbers of charges are found in the atmosphere (e.g., Tinsley et al., 2000), and in many laboratory experiments, especially in generation of calibration aerosols.

In the atmosphere, high charges exist on aerosol particles and hydro-meteors in thunderclouds, but also on aerosol particles during fair weather resulting from the evaporation of charged cloud droplets (Tinsley et al., 2000). The excess charge on aerosol particles in cloud systems is expected to enhance "electro-scavenging" whereby charged particles are lost to bigger droplets of opposite sign (Tinsley et al., 2000; Guo and Xue, 2021). Simulations by Guo and Xue (2021) show that multiply charged particles can have a significant influence on cloud lifetime. Charge is transferred from smaller particles to larger droplets when they collide, which increases the growth rate of multiply charged CCN compared with their neutral counterparts (Guo and Xue, 2021). Moreover, there exists a charge gradient on droplets in a cloud, where droplets have positive charges atop of the cloud and negative charges at the bottom of it (Zhou and Tinsley, 2007). Quantifying the rate coefficients between available atmospheric ions and charged particles can thus inform models and understanding of cloud systems.

In this study, we report measurements of the rate coefficients between ions and charged small (<10 nm) aerosol particles containing up to 9 elementary charges, *e*, of opposite charge. Such highly overcharged particles below 10 nm are extremely rare in the atmosphere, but they provide an important and sensitive constraint for theory. Knowledge of ion–aerosol rate coefficients is important to infer the particle steady-state charge distribution and to model the dynamics of aerosol populations. In particular, the particle steady-state charge distribution is essential for mobility-based size distribution measurements, for example when using differential mobility analysers (Kangasluoma and Kontkanen, 2017; Zeleny, 1900; Winklmayr et al., 1991; Flagan, 1998). To estimate the rate coefficients under atmospheric conditions, theoretical models based on first principles are often used. Chief amongst the current paradigms to estimate the charge-enhanced collisions are models based on the limiting-sphere model as detailed (and extended) by López-Yglesias and Flagan (2013) and references therein (e.g., Fuchs, 1963; Hoppel and Frick, 1986). In the limiting-sphere model, the motion between particles that are far from each is described by continuum mechanics, but within a limiting-sphere radius, their motion is described by free molecular mechanics; at the limiting-sphere radius, both motion fluxes are set to be equal.

An alternative approach to limiting-sphere models are calculations based on mean first-time passage and dimensional analysis as discussed by Gopalakrishnan and Hogan (2012) and subsequent studies (e.g., Ouyang et al., 2012; Gopalakrishnan et al., 2013; Chahl and Gopalakrishnan, 2019; Suresh et al., 2021). Gopalakrishnan and Hogan (2012) question the validity of limiting-sphere models in the presence of potential interactions and argue their long-standing success is due to the fact that it "can be fit" to experimental data, but not necessarily "agree" with said data (Gopalakrishnan and Hogan, 2012). In their recent studies, Tamadate et al. (2020a, b) show that a hybrid modelling approach connecting the continuum regime (outside the limiting sphere) with molecular dynamics (MD; inside the limiting sphere) simulations can achieve good agreement with some laboratory experiments. Compared with limiting sphere simulations, continuum–MD simulations contain more detailed processes; chemical structures of the colliding entities are considered, as well as changes in translational, rotational and vibrational degrees of freedom (Tamadate et al., 2020a, b).

Gatti and Kortshagen (2008) propose a linear combination of three regimes (continuum, molecular, and transition) to construct a simple analytical model of rate coefficients. By conducting MD simulations between particles of diameters 10–1000 nm and gas pressures 10^{-5}–10^{5} Pa, Gatti and Kortshagen (2008) show that in the low- and high-pressure limits, results converge onto the limiting-sphere model and hydrodynamic (molecular) limit, respectively. In the transition regime, they find the limit-sphere model underpredicts the collision rates by up to 500 %. As such, the authors propose a weighted linear combination of the three regimes, accounting for three-body trapping in the transition regime. When using the proposed analytical model by Gatti and Kortshagen (2008), as reformulated by Gopalakrishnan and Hogan (2012), we find that it shows the best agreement with our experimental results presented in this study.

We measure the rate coefficients of singly charged ions with multiply charged aerosol particles under atmospheric conditions in the CERN CLOUD chamber. We use an electrospray aerosol generator to generate multiply charged particles of around 10 nm diameter carrying positive charges. The particles are exposed with an X-ray source for control experiments with singly charged and neutral particles. The evolution of most relevant properties of the particles are monitored with a

comprehensive suite of instruments that continuously sample air from the CLOUD chamber. The positive charge on the particles gradually decays due to collisions with negative ions produced by galactic cosmic rays traversing the chamber. From our measurements, we derive the ion–aerosol rate coefficients for particles carrying up to nine positive charges.

Previously, experimentally determined ion–aerosol rate coefficients for multiply charged particles have been reported only for aerosol particles larger than 100 nm (e.g., Dépée et al., 2021). For particles smaller than 10 nm, only singly charged ion–ion recombination coefficients have been experimentally reported (Franchin et al., 2015). The collision rate of uncharged monomers with singly charged aerosol particles below 2 nm size has been measured by He et al. (2021). Owing to the dearth of experimental measurements for multiply charged particles, Tamadate et al. (2020b) compared their modelled coefficients with measured multiply charged PEG particles from an electrospray. To our knowledge, our study represents the first experimental measurement of ion–aerosol rate coefficients for multiply-charged, small (<10 nm) aerosol particles under atmospheric conditions. We compare our results to several theoretical predictions and find they are generally compatible, while identifying some models that show excellent agreement.

120 **Table 1. Parameter list**

Parameter	Description	Units
$\boldsymbol{I}_{\mathrm{calc}}$	Calculated current in NAIS	A
$\mathbf{H}$	Instrument apparatus matrix of NAIS	A cm^3
$\boldsymbol{\phi} = (\phi_1, \phi_2, \ldots \phi_{25})$	Lognormal distribution coefficients	cm^{-3}
$\widehat{\Omega}$	Lognormal probability density function	
$\Omega_{\pm}$	Calculated singly charged (positive/negative) number distribution	cm^{-3}
Ω_0	Calculated neutral number distribution	cm^{-3}
$\boldsymbol{I}_{\mathrm{meas}}$	Measured current in NAIS (vector representing 25 channels)	A
t	Time in seconds; t_{end} is the time at the end of the decay stage	s
j	Number of charges (i.e., charging state)	
$\widehat{\omega_j}$	Assumed probability density function for charging state j	
γ_j	The total number concentration of particles in a given charging state j	cm^{-3}
ω_j	Calculated number distribution at charging state j	cm^{-3}
Z_p	Electric mobility	cm^2 V^{-1} s^{-1}
q	Elementary charge constant	C
C_{c}	Cunningham's slip correction factor	
d_{p}	Particle diameter	nm
η	Particle viscosity	Pa s
k	Loss rate constant	s^{-1}
k_{wall}	Wall loss rate coefficient	s^{-1}
C_{wall}	Wall loss rate proportionality factor	cm^{-1} s$^{-1/2}$
k_{dil}	Dilution loss rate coefficient	s^{-1}
D_{p}	Particle diffusion coefficient	cm^2 s^{-1}
β_j	Rate coefficient between an ion and a particle with charging state j	cm^3 s^{-1}
K	Coagulation coefficient between neutral particles	cm^3 s^{-1}
CS	Coagulation sink to neutral particles	cm^{-3} s^{-1}
L_j	Total loss rate (wall loss, dilution loss, and coagulation sink to neutral particles)	cm^{-3} s^{-1}
$\breve{\sigma}_j$	Modified Coulombic enhancement between an ion and a particle with charging state j	
σ_j	Normalized $\breve{\sigma}_j$	
$\omega_{j,0}$	Number distribution at charging state j at start of decay stage	cm^{-3}
$\omega_{j,\infty}$	Instrument background number distribution at charging state j	cm^{-3}

2 Methods

The overall goal of the experiments herein is to infer the rate coefficients between negative atmospheric ions and positively overcharged small atmospheric aerosols. To achieve this, particles were produced using the CHARGE instrument (Sect. 2.1.2) and injected into the CERN CLOUD chamber (Sect 2.1.1). A comprehensive suite of instruments (Sect. 2.1.4) is used to monitor particles and charge states through the experiment to constrain and infer (Sect. 2.2) the ion–aerosol rate coefficients.

2.1 Experimental approach

2.1.1 CLOUD chamber

The Cosmic Leaving Outdoor Droplets (CLOUD) chamber at CERN is a 26.1 m^3 stainless steel container that enables aerosol experiments to be performed under atmospheric conditions with very low contaminant levels (Kirkby et al., 2011; Pfeifer et al., 2020). The chamber uses synthetic air from cryogenic nitrogen and oxygen. All parameters of the air in the chamber — such as temperature, relative humidity, UV light intensities and trace vapours — can be controlled with high precision (Dias et al., 2017; Kupc et al., 2011). For experiments under neutral (uncharged) conditions, an electric field of around 20 kV/m can be established with two electrodes, which sweeps charged small ions from the chamber in under 1 s. All experiments described here were carried out in dark conditions, that is, no UV lamps were switched on. The relative humidity was maintained at 80 %, and ozone at 40 ppbv. The electrospray generator used a dilute sulphuric acid solution in water. No other trace gases were added during the experiments.

2.1.2 CHARGE instrument

We developed the CHarged AeRosol GEnerator (CHARGE) electrospray instrument to study multiply charged particles under atmospheric conditions. Electrospray is used in various research fields to enable the generation of singly and multiply charged particles (Sterling et al., 2011; Hogan and de la Mora, 2011; Marginean et al., 2008). By applying a strong voltage gradient at the tip of a capillary, a liquid solution emerging from the capillary is drawn into a so-called Taylor cone. Highly charged droplets stream from the tip of the Taylor cone. Once exposed to sub-saturated air, the charged droplets evaporate and shrink until the repulsive electrostatic force causes them to break up into several multiply charged smaller droplets (Rayleigh, 1882; Smith et al., 2002). Following López-Herrera et al. (2004), we used electrospray solutions consisting of sulfuric acid (0.02 wt. %) and purified water (0.98 wt. %) to generate positively charged particles using a positive voltage of 5200 V (Myhre et al., 1998; Kebarle and Verkerk, 2009). CHARGE incorporated an X-ray ion generator along the path of the charged particles. When switched on, this generated a highly concentrated bipolar ion distribution, thereby forcing the particles to their particle charge steady state. This way, multiply charged particles in one experiment could be directly compared to an otherwise identical experiment performed with a particle distribution in charge steady state, presumably containing neutral and singly charged particles.

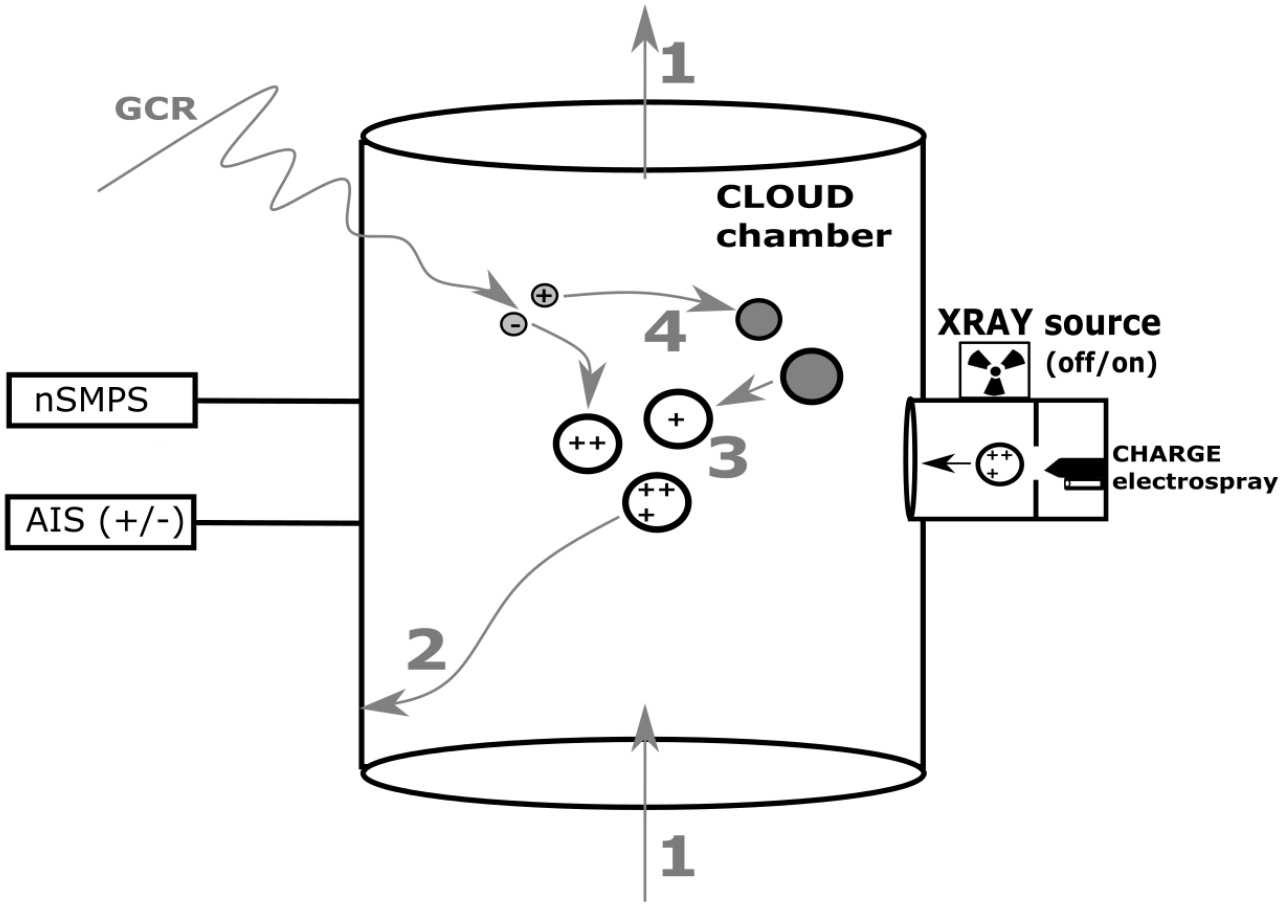

Figure 1: Schematic representation of the experimental measurements. Charged particles are produced by the CHARGE electrospray instrument (right). With the X-ray source switched off, charged particles enter the CLOUD chamber. With the X-ray source switched on, the particles are neutralised, i.e. have a steady-state charge distribution, before entering the CLOUD chamber. After an injection period of around 30 min, particle injection from CHARGE is switched off and the evolution of the particle charges during the "decay stage" is monitored by sampling instruments such as the nSMPS and AIS (left). The evolution of particle and ion charges in the chamber is analysed as a function of the production and loss terms: (1) dilution loss, (2) wall loss, (3) aerosol–aerosol collisions, (4) collisions of aerosols with ions produced by galactic cosmic rays.

2.1.3 Experimental overview

Figure 1 shows a schematic representation of the experiments reported in this study. We performed two distinct experiments: with and without X-ray. All experiments started with the injection of particles to the chamber from CHARGE; the number of particles and their charge then decayed inside the chamber. During injection, we injected particles through a large-diameter tube (100 mm in diameter) at a high carrier flow rate of approximately 200 l min^{-1}. During the decay stage, we turned off all voltages and flows in CHARGE and observed the decay of the particle and ion distributions in the chamber. Since no more particles were added during this stage, the decay could be described by the production and loss terms shown in Figure 1 and

described in Sect. 2.2.3. Between experiments, we removed particles and ions by increasing the flow rate of the chamber and the fan speed as well as turning on the high-voltage electrode grids to remove any remaining charged particles and ions.

2.1.4 Instrumentation and measurements

Relative humidity was measured with a Tunable Diode Laser system, TDL (Skrotzki, 2012). In addition, a chilled dew point mirror (Edgetech Instruments) was used to derive the relative humidity utilizing water vapor pressure calculations (Murphy and Koop, 2005). An ozone monitor (Thermo Electron Corporation Model 49C) was used to measure the ozone concentrations. Sulfuric acid and gaseous compounds were measured with a Nitrate CI-APi-TOF (Kürten et al., 2014). The instrument was operated and calibrated following Kürten et al. (2012).

The total particle concentration was measured with a NanoScan Mobility Particle Sizer, nSMPS, TSI, Model 3936 (Lehtipalo et al., 2014; Tritscher et al., 2013; Wiedensohler et al., 2012). The concentrations were compared to the Scanning Mobility Particle Sizer (SMPS) results (Birmili et al., 1997; Wiedensohler, 1988). Total particle concentrations for diameters larger than 2.5 nm were obtained with a Particle Size Magnifier, PSM, and a Condensation Particle Counter, CPC (Vanhanen et al., 2011; Liu et al., 2006).

Ion concentrations and the concentrations of charged particles with both polarities were measured with a Neutral cluster and Air Ion Spectrometer (NAIS). To increase time resolution during the experiments, the NAIS was only used to measure ions, that is, in "Ion Mode" (Manninen et al., 2009, 2016; Mirme and Mirme, 2013); as such, we refer to it as AIS (Air Ion Spectrometer) for the rest of this study. Measurements from AIS were also compared with measurements from a nano-radial DMA (Amanatidis et al., 2021).

To analyse the experiments, we primarily use data from the AIS (charged distribution) and from the nSMPS (total distribution). All data have been converted from the measured mobility diameter to mass diameter (Ku and de la Mora, 2009; Larriba et al., 2011). A comparable setup for chamber measurements of particle and ion distributions is described in more detail by Dada et al. (2020).

2.2 Data analysis

2.2.1 AIS inversion

The AIS instrument is based on the design of electrical aerosol spectrometers (e.g., Flagan, 1998; Mirme et al., 2007). The mobility analyser consists of multiple electrode rings to measure a differential ion distribution. Two analysers are arranged in parallel with different polarities, where the sample flow (54 l min^{-1}) is split. This allows measuring particle distributions of positive and negative polarity in parallel. While the instrument can also measure neutral particles by first filtering natural ions (using an electric field) and afterwards charging the remaining neutral particles (with a corona needle), only charged particles were measured in our experiments; as such, the ion filter and the corona needle were switched off. The AIS version used in

our experiments has 25 electrode channels. It is capable of measuring charged particles, cluster ions, and small ions in the mobility range from 3.2 to 0.0013 $cm^2 V^{-1} s^{-1}$ (Mirme and Mirme, 2013; Manninen et al., 2016).

We follow the inversion function presented by Mirme and Mirme (2013) in analysing the AIS measurements However, we find that we need to adjust the approach in the case of multiply charged particles. First, we observed that the established (Mirme and Mirme, 2013) AIS inversion jumps suddenly during our experiments. However, we did not see this jump in the measured current of the differential AIS channels. Furthermore, as shown in the next paragraphs, we want to describe the AIS measurement as a linear combination of several lognormal distributions with charge number j. The original inversion function used squares of cosine functions as basis functions to obtain a mobility distribution from the measured current. Accordingly, the measured current of the AIS channels would ultimately be described by several squares of cosine distributions, which afterwards would be fitted using several lognormal distributions. It thus seems more natural for our measurements to use lognormal distributions to describe transfer functions instead; and it seems to be a more natural choice for lognormally distributed aerosol distributions. We additionally skip the Tikhonov regularization previously employed (Tikhonov, 1963; Mirme and Mirme, 2013) as our updated inversion seems not to benefit from it.

The calculated current, $\boldsymbol{I}_{\mathrm{calc}}$, can be expressed as a product of the instrument apparatus matrix $\mathbf{H}$ and the lognormal distribution coefficients vector $\boldsymbol{\phi}$ as $\boldsymbol{I}_{\mathrm{calc}} = \mathbf{H}\boldsymbol{\phi}$ (Mirme and Mirme, 2013; Manninen et al., 2016). The matrix $\mathbf{H}$ is determined through instrument calibration (Mirme and Mirme, 2013). In our case, $\boldsymbol{\phi}$ is a vector of the coefficients of 25 individual lognormal distributions, that is, it is a vector of the total number concentrations of each one of them. These 25 distributions correspond to 25 AIS channels; the mean and standard deviation of each of the 25 distributions are calculated by fitting the matrix $\mathbf{H}$ to lognormal distributions, but not supplanting it.

If we let the lognormal probability distribution function be $\widehat{\Omega}_i$, then the full calculated distribution is $\Omega = \sum_{i=1}^{25} \phi_i \widehat{\Omega}_i$, where ϕ_i are the elements of $\boldsymbol{\phi}$; and Ω is the calculated total charged (negative or positive, $\Omega_{\pm}$) distribution. We minimize the residuals between the calculated current ($\boldsymbol{I}_{\mathrm{calc}}$) and the measured current ($\boldsymbol{I}_{\mathrm{meas}}$) from AIS using nonlinear least squares, with 25 concentration coefficients as free parameters. We solve the nonlinear least squares computationally and we do not supplement it with any regularization technique. The procedure is repeated for each polarity separately, hence the resulting distributions are $\Omega_{\pm}$. (More details are provided in Sect. 4 by Mirme and Mirme (2013) on the theoretical basis for $\mathbf{H}$.)

A known limitation of the AIS is its inability to detect ions whose mobility diameter is lower than 0.82 nm (Manninen et al., 2016). To this end, we extrapolate the missing measurements by assuming the ion distribution follows a lognormal distribution even below 0.82 nm. This extension allows us to account for a wider distribution of available ions, especially where the expected value of collisions is higher (smaller ions collide at a higher rate with the same reference oppositely charged particle).

While we find our approach to be more useful with multiply charged particles than the standard procedure, it does not deviate significantly from the standard procedure by Mirme and Mirme (2013) under normal operating conditions. Compared to five randomly selected nucleation experiments conducted throughout the same CLOUD campaign, where no

significant multiply charged particles are expected, we find a median of about 12 % deviation (over all mobilities) between our modified method and the original method.

2.2.2 Multi-charge inference

When operated in "Ion Mode" like in our case, the typical AIS inversion provides information directly only about singly charged particles (Manninen et al., 2016). However, we are interested in multiply charged particles which are briefly present away from steady state. To deduce information about multiply charged particles present in our experiments from the total charged distributions from Sect 2.2.1 ($\Omega_{\pm}$), we identify a time when the steady-state assumptions are expected to hold: We postulate this happens at the end of the decay stage when the ratio of the positive and negative concentrations tends to be unity. Once in steady state after interacting with ions produced from GCR, it is reasonable to assume that all multiply charged particles have been neutralized due to collisions with ions of opposite polarity.

At the end of the decay stage, $t = t_{\mathrm{end}}$, we set the concentration of singly charged positive particles to be the same as the inferred concentration from the AIS in Sect. 2.2.1; that is, as $\Omega_{+}\left(d_{\mathrm{p}};\ t = t_{\mathrm{end}}\right) = \Omega_{-}\left(d_{\mathrm{p}};\ t = t_{\mathrm{end}}\right)$, we assume all of particles in $\Omega_{+}\left(d_{\mathrm{p}};\ t = t_{\mathrm{end}}\right)$ are singly (positively) charged. Our goal is to then estimate $\Omega_{+}\left(d_{\mathrm{p}};\ t < t_{end}\right)$ as a combination of multiply charged distributions as in Eq. (1), where γ_j are free parameters that determine the total number of particles of a given charge state j and $\widehat{\omega}$ is the density function for each charging state. We further assume the dynamic evolution of $\Omega_{+}\left(d_{\mathrm{p}};\ t\right)$ can be described as a first-order loss process (to walls and dilution) as the charges themselves are simply redistributed among charging states. For ease of presentation, we set $\omega_j = \gamma_j\ \widehat{\omega}_j$ after this section.

$$\Omega_{+}(t) = \sum_{j=1}^{11} \gamma_j\ \widehat{\omega}_j = \sum_{j=1}^{11} \omega_j \tag{1}$$

We assume the probability density function $\widehat{\omega}_1$ has the same shape as $\Omega_{+}\left(d_{\mathrm{p}};\ t = t_{\mathrm{end}}\right)$ as in Eq. (2) after accounting for wall, dilution, and coagulation losses. While coagulation can play a role in the shape of the distribution $\widehat{\omega}_1$, wall loss and dilution loss are clearly dominant in our experiments (see Figure 2).

$$\widehat{\omega}_1 = \frac{\Omega_{+}\left(d_{\mathrm{p}};\ t_{\mathrm{end}}\right)}{\int_0^{\infty} \Omega_{+}\left(d_{\mathrm{p}};\ t_{\mathrm{end}}\right)\,\mathrm{d}\ln d_{\mathrm{p}}} \tag{2}$$

At the end of the decay stage, $\gamma_1 = \int_0^{\infty} \Omega_{+}\left(d_{\mathrm{p}};\ t_{\mathrm{end}}\right)\,\mathrm{d}\ln d_{\mathrm{p}}$ and $\gamma_{j\neq 1} = 0$ by definition. Since $\widehat{\omega}_1$ is now known, we can estimate $\widehat{\omega}_j$ using the Millikan equation relating electric mobility, charge number, and particle diameter (Lehtinen and Kulmala, 2003; Mirme and Mirme, 2013; Manninen et al., 2016). For the same electric mobility Z_p, different pairs of charge number j and particle diameter d_{p} are linked through Eq. (3) assuming constant viscosity η and elementary charge constant q (C_{c} is the Cunningham's slip correction factor which depends on size). We use Eq. (3) to estimate $\widehat{\omega}_j$ by shifting $\widehat{\omega}_1$ in diameter, holding everything else constant.

$$Z_{\mathrm{p}} = \frac{j\, q\, C_{\mathrm{c}}(d_{\mathrm{p}})}{3\,\pi\,\eta\,d_{\mathrm{p}}} \quad (3)$$

We finally add one correction to ω_j. As the AIS uses the electric mobility diameter, multiply charged particles will be detected at higher mobilities than their singly charged counterparts. And since they carry more charges, the measured current will be higher. Thus, we divide each ω_j by its charge state j and we use the mobility diameter throughout our calculations as retrieved by Eq. (3). All in all, ω_j can be expressed as in Eq. (4) as a size- and time-dependent function of γ_j, the positive charge concentration Ω_+, and a loss constant k_{loss} related to particle losses wall, dilution, and coagulation).

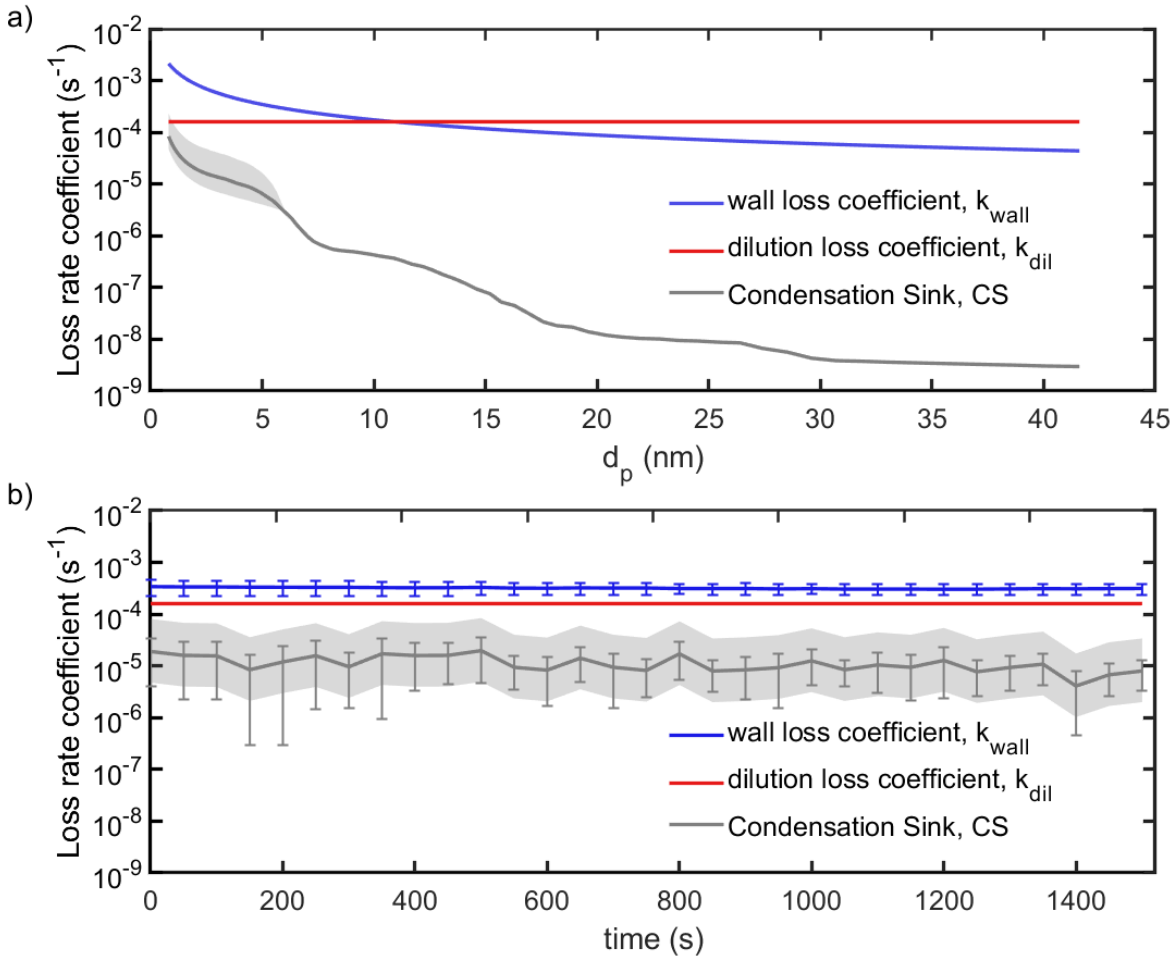

Figure 2: Summary of the particle loss rates during the decay stage. a) Size dependency of the loss rates for a distribution (ω_j) during a decay stage (averaged over an entire decay period). b) The loss rates due to different processes for a given distribution ω_j as a function of time during a decay stage. The grey bands indicate uncertainty ranges resulting from errors on measurements of the total particle number concentrations below 6 nm. We assume generous (± 400 %) errors since instruments can vary widely at small particle sizes (Kangasluoma et al., 2020).

$$\omega_j(t) = \frac{\gamma_j}{\sum_{j=1}^{11} \gamma_j}\, \Omega_+\left(d_\mathrm{p};\, t\right) e^{-k_\mathrm{loss} t} \quad \textbf{(4)}$$

We note that in estimating ω_j in Eq. (4), we assume measurements below 2 nm electric mobility diameter are singly charged or neutral as most entities present below 2 nm can be safely considered ions whose concentration is accounted for in $\Omega_\pm$ from, Sect 2.2.1. Moreover, we simplify our calculation by assuming all measurements above 10 nm electric mobility diameter to be at most singly charged as well. We are able to make these two assumptions because the CHARGE instrument produces particles of sizes around 6 nm electric mobility diameter. Consequently, the total number concentration decreases significantly above 10 nm and below 2 nm, and so does the ratio of multiply charged particles in it as well, and the timescale of neutralization (i.e., timescale to reach reaching particle charge steady state) for particles bigger than 10 nm is significantly faster than for smaller ones. While the limits of this interval are arbitrary, their values are allowed to vary within a range of ± 50 % in the error estimation calculation as discussed in the Supplementary Information.

2.2.3 Population balance

We derive the ion–aerosol rate coefficients from data collected during the decay stage. Since the CHARGE instrument produces and injects particles at high flow rate (200 l min^{-1}), the flow rates in the CLOUD chamber are not balanced immediately after an injection stage. Thus, the decay stage starts as soon as the flow inside the chamber is in steady state, which can be estimated from the flow rates exiting the chamber and from the overpressure inside the CLOUD chamber. We account for the production and loss terms of all the particles and ions inside the chamber as a function of time. After injection, particles and ions in the chamber dynamically evolve in time due to several processes, related to chamber dilution, wall processes, aerosol–aerosol collisions, and ion–aerosol collisions. The individual loss rates and their time dependence during our experiments are summarized in Figure 2.

In the CLOUD chamber during these experiments, the dilution rate coefficient, k_dil, was constant at 1.60 × 10^{-4} s^{-1}, which is the result from dividing the volume flow rate (250 l min^{-1}) by the total volume (26.1 m^3) (e.g., Simon et al., 2016; Pfeifer et al., 2020). The chamber wall loss rate coefficient is calculated using $k_\mathrm{wall} = C_\mathrm{wall}\sqrt{D_\mathrm{p}}$, where D_p is the particle diffusion coefficient and C_wall is a proportionality constant whose value has been measured as 7.70 × 10^{-3} cm^{-1} s$^{-1/2}$ based on wall loss of sulfuric acid vapour (Metzger et al., 2010; Ehrhart et al., 2016; Stolzenburg et al., 2020; He et al., 2021). For the collisions involving at least one neutral aerosol particle, we follow Seinfeld and Pandis (2016) to estimate the coagulation rate coefficient, K, between neutral particles and thus the coagulation sink, CS. We account for the effects of charges on coagulation in the calculation of β in the following paragraphs.

The main goal of our experiment is to quantify the ion–aerosol rate coefficients, which play a role in the dynamic evolution of the particle size distribution and particle charge distribution. More precisely, we estimate the rate coefficients, $\beta_j = \beta_{-,j}$, between the negative ion distribution (< 2 nm) and the particle distribution (2–10 nm) with j positive charges. By setting up the balance equations, we track the number and charge evolution over time and thus constrain $\beta_j(d_\mathrm{p})$.

Beyond these terms, we assume sources and sinks related to evaporation, condensation, and nucleation are negligible in our experiments. At 80 % relative humidity and 278 K, the evaporation of sulfuric acid is negligible (Stolzenburg et al., 2020). We assume the growth rates of particles in our experiment are on the order of 1.8 nm hour^{-1} as those reported for sulfuric acid–water systems (Nieminen et al., 2010). These growth rates are too small to influence the dynamics herein, especially compared with the duration of the experiments (at most 1500 s). Using parameterizations for the sulfuric acid-water system from Vehkamäki et al. (2002), we calculate nucleation rates of about 2.5 × 10^{-8} cm^{-3} s^{-1} for the measured sulfuric acid concentrations (about 5 × 10^{7} cm^{-3} in the beginning of a decay and during injection), which is negligible (Vehkamäki et al., 2002; Dunne et al., 2016). We assume particles produced inside the chamber during the experiments consist of sulfuric acid and water with a uniform density of 1600 kg m^{-3} (Myhre et al., 1998). (The robustness of these assumptions is verified in the Supplementary Information, where we randomly vary all parameters. For example, the density is varied between that of pure water (997 kg/m3) and that of pure sulfuric acid (1830 kg/m3), finding negligible sensitivity of the assumption herein.)

From Sect 2.2.2, using AIS measurements, we obtain $\Omega_{\pm}$ as a distribution over sizes 0.2–40 nm of diameters and ω_j as a distribution over sizes 2–40 nm of diameters. We also infer Ω_0, which is the distribution of neutral entities over sizes 2–40 nm of diameters by combining AIS and nSMPS measurements. We can thus write the balance equations for the positively charged particles compactly in Eq. (6), which is valid for $1 < j < 11$. However, because of the size dependence of Ω and ω, we introduce a coefficient σ to account for the size dependency normalized by its value at the lowest size (ion size). That is, σ is unity at the ion size (1 nm diameter) and it is less than unity for bigger sizes. This formulation yields β for the ion–aerosol coefficients while still accounting for events including charged particles and ions in the rest of distribution that are ignored earlier in using K. We use the Coulombic enhancement coefficient to calculate σ following Seinfeld and Pandis (2016; p. 564, Eq. 13A.16), with d_{p1} and d_{p2} referring to the sizes of coagulating particles in nm in Eq. (5).

$$\breve{\sigma}_j\left(d_{\mathrm{p1}}, d_{\mathrm{p2}}\right) = -\frac{j}{d_{\mathrm{p1}} + d_{\mathrm{p2}}} \frac{1}{\exp\left(-\frac{j}{d_{p1} + d_{p2}}\right) - 1}; \quad \sigma_j = \frac{\breve{\sigma}_j\left(d_{\mathrm{p1}}, d_{\mathrm{p2}}\right)}{\breve{\sigma}_j\left(d_{\mathrm{p1}} = 1\ \mathrm{nm}, d_{\mathrm{p2}}\right)} \tag{5}$$

$$\frac{\mathrm{d}\omega_j}{\mathrm{d}t} = \sigma_{j+1}\,\beta_{j+1}\,\Omega_-\,\omega_{j+1} - \sigma_j\,\beta_j\,\Omega_-\,\omega_j - L_j \tag{6}$$

In Eq. (6), the positively charged size distribution ω at each charge state j evolves in time due to production and loss. On the right-hand side, the first term denotes the gain of a particle of charge j as a result of a coagulation event between a particle of charge $j + 1$ of concentration ω_{j+1} and a negative ion of concentration Ω_-. The second term denotes the loss of a particle of charge j and of concentration ω_j as it collides with a negative ion of concentration Ω_-. The third term lumps all other losses, which are to the wall, dilution, and coagulation sink (CS; including in-distribution losses, that is, coagulation within the distribution of particles of diameters 2–10 nm) as shown in Eq. (7).

$$L_j = \omega_j(k_{\mathrm{wall}} + k_{\mathrm{dil}} + \mathrm{CS}) = \omega_j(k_{\mathrm{wall}} + k_{\mathrm{dil}}) + \omega_j \sum_l K_l\,\omega_l \tag{7}$$

To complete the description in Eq. (6), we use Eq. (8) and Eq. (9) for the cases $j = 1$ and $j = 11$, respectively. In Eq. (8), we use β_0 to denote collision coefficient between positive small ions Ω_+ (d_p < 2nm) and neutral particles Ω_0 inferred from the NAIS and nSMPS measurements. As such, β_0 is calculated in the same way K_l in Eq. (7) is calculated, following Seinfeld and Pandis (2016).

$$j = 1; \qquad \frac{d\omega_j}{dt} = \beta_0\,\Omega_+\,\Omega_0 + \sigma_{j+1}\beta_{j+1}\,\Omega_-\,\omega_{j+1} - \sigma_j\beta_j\,\Omega_-\,\omega_j - L_j \\ = K\,\Omega_+\,\Omega_0 + \sigma_{j+1}\beta_{j+1}\,\Omega_-\,\omega_{j+1} - \sigma_j\beta_j\,\Omega_-\,\omega_j - L_j \tag{8}$$

$$j = 11; \qquad \frac{d\omega_j}{dt} = -\beta_j\Omega_-\omega_j - L_j \tag{9}$$

The system of equations (Eq. 6, 7, and 8) is solved numerically for each time step during the decay stage. One time step corresponds to the duty cycle of the AIS (50 s) and the nSMPS measurement is synchronized to this time step using linear interpolation. Accordingly, for each charge number j, there exists one solution for each cycle of 50 s, where the calculation is only solved within the respective lifetime of each ω_i. The lifetime is determined using an exponential fit through the time evolution of each ω_i. For example, $j = 9$ with an estimated lifetime of 200 s yields four measurements (one each 50 s) and thus four coefficients are calculated for this charge number in this specific experiment. For smaller j, the lifetime increases and thus, more coefficients are calculated per experiment.

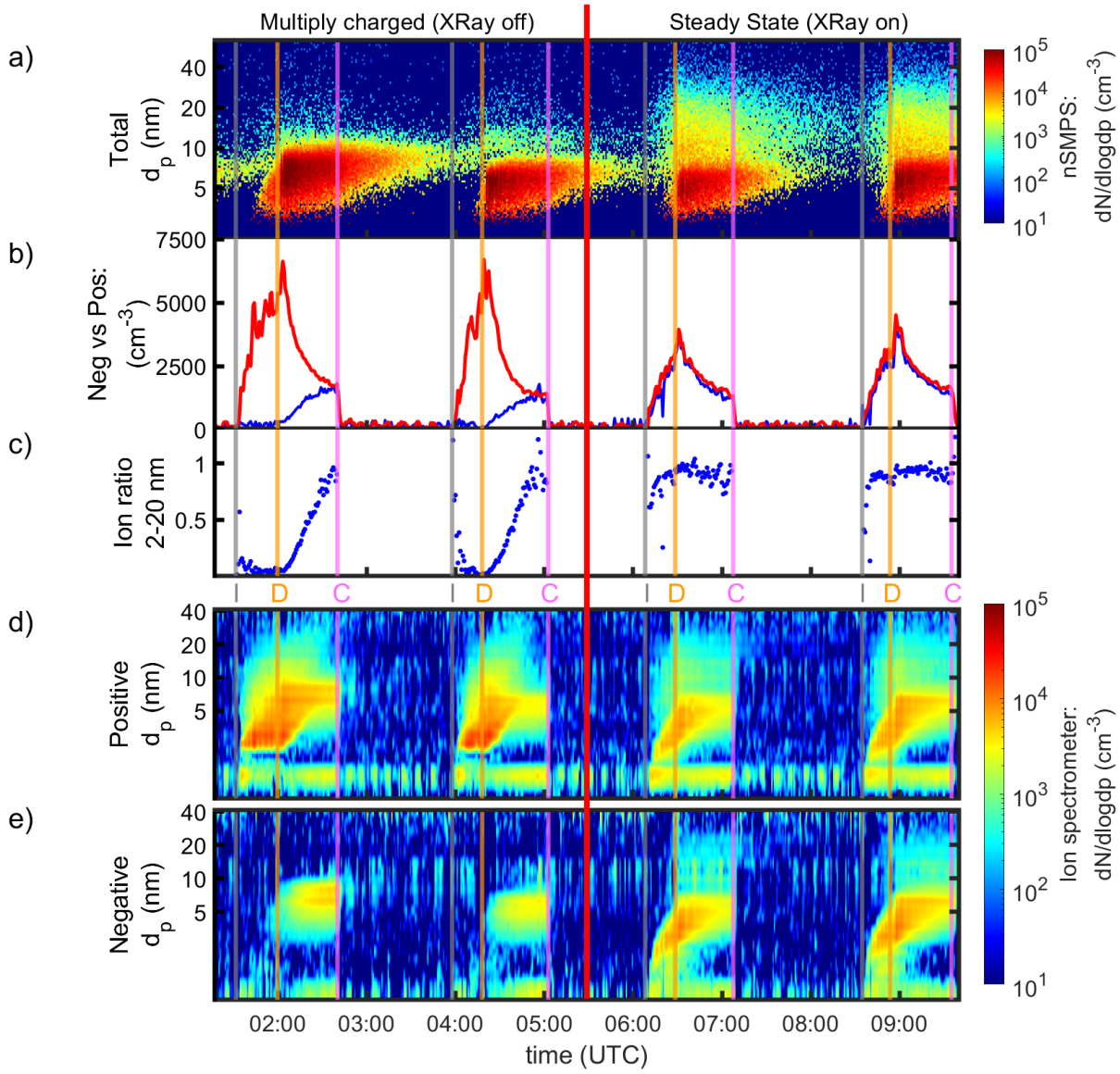

Figure 3: Example experiments performed without and with charge neutralisation by X-rays. Time series showing two experiments with X-ray off followed by two experiments with X-ray on (separated by the red vertical line). The grey vertical line marks the beginning of an injection stage (I), the orange line a decay stage (D) and the pink line a cleaning stage (C). The panels show the time series of a) particle size distributions measured with a nSMPS, b) number concentrations of positive (red) and negative (blue) charged particles, c) negative:positive charged particle ratio, and d) positive and e) negative charged particle apparent size distributions measured with an AIS. Here the apparent size incorrectly assumes singly charged particles.

3. Results

In Figure 3, we show a time series of two experiments with X-ray off and two with X-ray on. A total of four experiments without X-ray and two with X-ray were conducted to ensure reproducible results. As detailed in Sect. 2.1, particle

measurements were carried out with an NAIS (Manninen et al., 2016, 2009) and an SMPS (Tritscher et al., 2013) for the total particle concentration. Gas phase concentrations were measured using several mass spectrometers (Kürten et al., 2011, 2012; Breitenlechner et al., 2017; Wang et al., 2021). We calculate the ion–aerosol rate coefficients during the decay stage starting as soon as the chamber flow is in steady state after injection.

With the X-ray off, we observe almost no negative ions during injection. Negative ions are entirely consumed by ion–ion recombination and ion–aerosol attachment as there is a significant amount of positive charge available during injection via the positively charged particles formed. However, we observe an increase in the number of negative ions during the decay stage, which can only come from ion–aerosol attachment of (singly charged) negative ions with (neutral) particles.

With the X-ray on, we observe that the ratio between positively to negatively charged particles is almost unity. This indicates that the X-ray source effectively pushes a large fraction of particles to its steady state particle charge distribution. Thus, it seems natural that we can assume that all particles carry at most $j = 1$ charges during experiments with the X-ray on. However, when assuming charge steady state with maximum $j = 1$ charge, our calculations result in systematically smaller coefficients during the experiments with the X-ray on compared to the experiments with the X-ray off. This implies that there is an additional source term in the case of experiments with the X-ray on. Since the particles from the CHARGE Electrospray Generator pass the X-ray source at a flow rate of 200 lpm, it is plausible to assume that a few particles are still doubly charged in the beginning of the decay stages. For these experiments, we therefore calculate rate coefficients twice: once assuming charge steady state (maximum $j = 1$ charges) and once including a small fraction of doubly charged particles (assuming singly:doubly charged ratio of 5:1 at the beginning of the decay stage).

The total distribution is similar in both experiments in Figure 3 and observed deviations in the size distributions between NAIS and nSMPS are within the expected range from other measurements (Kangasluoma et al., 2020). During both experiments, as expected, a significant fraction of the particle distribution is neutral (approximately 98 %). SMPS measurements are subject to measurement errors especially below 6 nm (Kangasluoma et al., 2020); however, during our experiments, the influence of the measured total particle concentration on the calculation of the rate coefficients is relatively small, since wall loss and dilution loss dominate (see Figure 2). Further, the influence of varying the concentrations measured by the SMPS within the estimated error range is also discussed in the Supplementary Information and shown in Figure S3.

Figure 4 summarizes the calculated rate coefficients from our experiments. The error bars indicate the one-sigma confidence interval of numerical solutions from all experiments (for all time steps) for the respective charge number j. The calculations are carried out for maximum $j = 11$ charges, with the assumptions summarized in Sect. 2. To calculate the "best fit" values from all our data, we use an exponential fit through the respective experiments, which is solved using nonlinear least squares. It is based on the same production and loss rates as in case of the numerical solution in Sect. 2.2.3. In contrast to the numerical solution, steady state conditions are assumed in the case of this fit, except for ion–aerosol collisions. As such, we take time-averaged values for various coefficients in Eq. (10). As an example, for $j = 1$ charge, the approximation by the fit is described following Eq. (8) by Eq. (10) below.

$$\omega_j(t) = \omega_{j,t=0} \exp\left(-(\overline{k_{wall} + k_{dil} + CS} - \frac{\overline{\beta_0\,\Omega_+\,\Omega_0}}{\overline{\Omega_+}} + \beta_j\sigma_i\Omega_- - \frac{\beta_{j+1}\sigma_{j+1}\Omega_-\,\omega_{j+1}}{\omega_j}\right) + \omega_{j,\infty} \quad \textbf{(10)}$$

In Eq. (10), $\omega_{j,\infty}$ denotes instrumental background at the end of the decay stage and $\omega_{j,t=0}$ is the concentration at the beginning of the decay stage. The best fit of the numerical solution and the one-sigma confidence interval are summarized in Table 1. In Figure 4, we compare our measurements with leading representative models and with the MD simulations from Tamadate et al. (2020b). Our results confirm the robustness of the selected models calculating the ion–aerosol rate coefficient (López-Yglesias and Flagan, 2013; Gopalakrishnan and Hogan, 2012; Gatti and Kortshagen, 2008; D'yachkov et al., 2007), which we calculate using the particula software package, version 0.0.10 (Mahfouz et al., 2022). In particular, we find the results by Gatti and Kortshagen (2008) and López-Yglesias and Flagan (2013) to be most compatible with our experimental estimation.

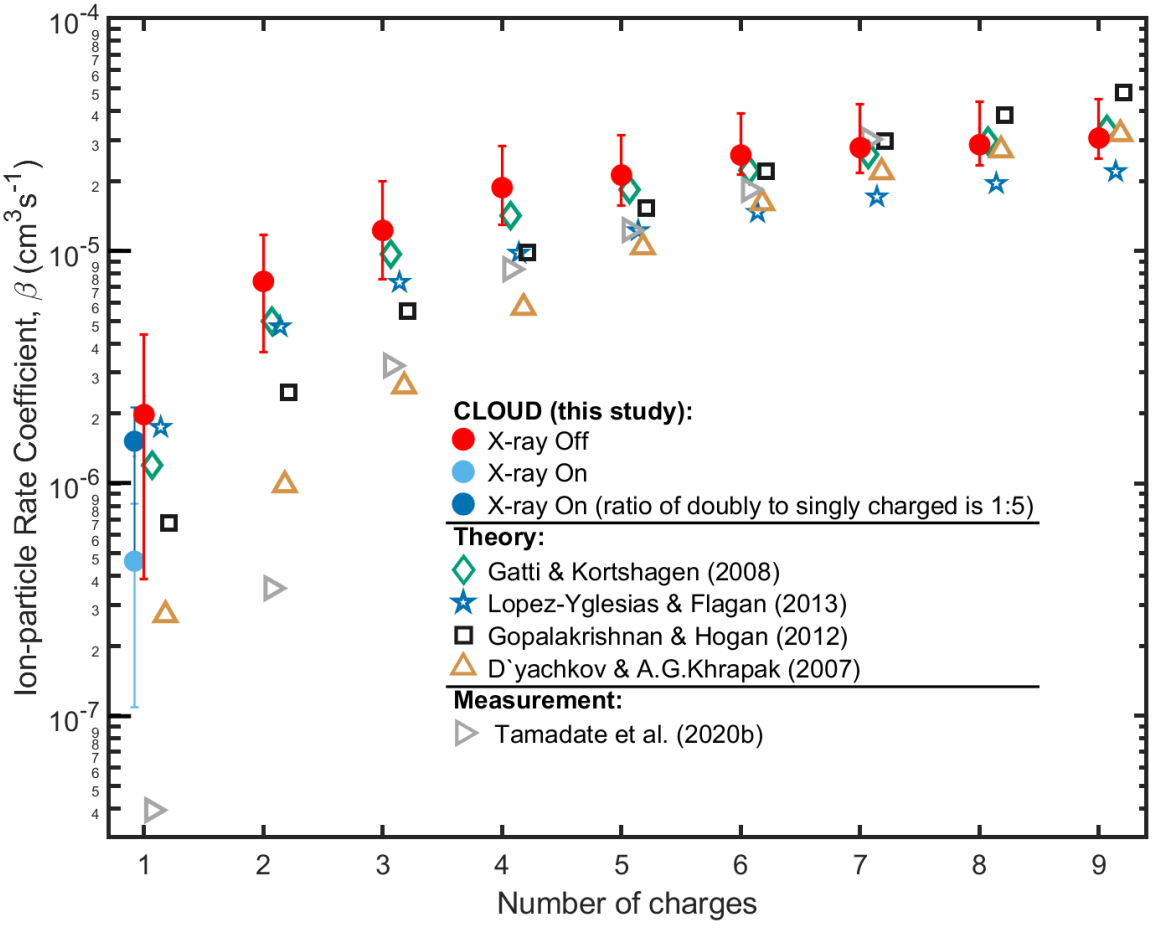

Figure 4: Ion–particle rate coefficients versus number of charges on the particle. The CLOUD measurements are indicated by filled circles that are coloured red for X-ray off experiments, blue for X-ray on experiments assuming full steady state ion distributions, and cyan for X-ray on and assuming incomplete steady state ion distributions. Theoretical predictions based on the limiting-sphere paradigm and Langevin dynamics are shown in open symbols for 1 nm negative ions colliding with positively charged particles of 6 nm diameter. Recent

results for multiply charged PEG_{4600} particles with ions are shown in grey triangles (Tamadate et al., 2020b). The symbols are offset from integer charges to improve their visibility.

Table 2. Experimentally inferred ion–aerosol rate coefficients.

Number of charges j	Best fit β_j ($cm^3 s^{-1}$) $\times 10^{-6}$	One-sigma confidence interval $\times 10^{-6}$
1	2.0	[0.4, 4.4]
(1) (X-ray on)	1.5	[0.1, 2.1]
2	7.4	[3.7, 11.7]
3	12.2	[7.5, 19.9]
4	18.7	[13.0, 28.2]
5	21.2	[15.6, 31.5]
6	25.8	[21.2, 39.0]
7	27.8	[21.7, 42.8]
8	28.6	[23.4, 44.0]
9	30.6	[24.9, 45.1]

4. Discussion

In general, we find the limiting-sphere model by López-Yglesias and Flagan (2013) and linear combination of models by Gatti and Kortshagen (2008) to best represent our experimentally determined rate coefficients. It is imperative to note that while the approach based on the limiting-sphere is fine-tuned to atmospheric applications (meaning parameterized for atmospheric ions and conditions), the approaches based on mean first-time passage and dimensional analysis (e.g., ones by Gopalakrishnan and Hogan (2012) and others following it) are more general. This could explain the discrepancy — in other words, adjusting the input parameters of the latter approach could lead to a better fit with our data. Notwithstanding this discrepancy, the results from all theoretical models point to similar trajectory. Remarkably, our results most resemble the analytical model by Gatti and Kortshagen (2008) as reformulated by Gopalakrishnan and Hogan (2012). In their model, a linear combination of continuum, free molecular, and transition regimes is used to describe collisions of nanoparticles in plasmas.

We compare our results to recent results based on continuum–MD simulations (Tamadate et al., 2020b), which are for multiply charged PEG_{4600} particles with ions. While our results align well with previous models (López-Yglesias and Flagan, 2013; Gopalakrishnan and Hogan, 2012; Gatti and Kortshagen, 2008; D'yachkov et al., 2007), we find our results deviate from those by Tamadate et al. (2020b) especially for a low number of charges (<5). This could be explained by the

geometry (and thus size) of the simulated PEG_{4600} particles. We note that our results align with all models, including the one by Tamadate et al. (2020b), for >5 charges where the effect of charge likely outweigh the effects of geometry. Moreover, the flexible nature of the ions and particles in their study likely plays a central role and cannot be compared directly to our results herein.

The primary implication of our results here is providing an experimental basis for model calculations of the ion–aerosol rate coefficient. In so doing, this enables researchers to implement and tune model calculations more readily like those based on the limiting-sphere or Langevin dynamics approaches cited earlier. This eventually provides further evidence in constraining the cosmic galactic rays' role in climate change. While availability of ions generated by cosmic rays can influence new-particle formation and growth to an extent, their influence is dampened by the fact that charged particles are more readily scavenged by existing bigger particles (Mahfouz and Donahue, 2021a). In the limit, this scavenging rate is doubled, and the probability of survival is thus squared (Mahfouz and Donahue, 2021a, b). However, questions remain open regarding ion–aerosol interactions in scenarios close to aerosol–cloud interactions and the subsequent interactions between ions and climate variability (e.g., Guo and Xue, 2021; Tinsley, 2022). This experimental procedure will enable further exploration and experimental evidence in resolving these questions, e.g., in designing and building experiments in cloud chambers.

With this first set of novel experiments, we have successfully constrained the coagulation rate coefficients between negative atmospheric ions and positively charged particle distributions in the size range 2–10 nm for up to nine charges. Using the same experimental framework, we additionally can study interactions between atmospheric ions and neutral particles, where induced charges can potentially impact the rate coefficient and thus alter the ensuing particle dynamics. Together, these efforts will not only illuminate any effect of galactic cosmic rays on climate change, but also the effect of extreme conditions — where excess of charges and ions are readily available — on particle formation and growth, subsequent aerosol dynamics, and eventually weather and climate phenomena.

5. Summary

In this study, we present novel experiments to calculate ion–aerosol rate coefficients under atmospherically relevant conditions in the CERN CLOUD chamber. After assessing the robustness of our calculations, we test our experimentally inferred results against those predicted by leading models. We find overall agreement with the selected models, but especially with one employing a linear combination of limiting behaviours across regimes (Gatti and Kortshagen, 2008). This study, and follow-up experiments, will help constrain charge-related dynamics affecting atmospheric particles, which can play an important role in the formation and growth of particles as well as the subsequent dynamics in thunderstorm and non-thunderstorm clouds.

Data availability. All data used in this study, including the codes, are available at DOI: 10.5281/zenodo.7335017. The **H** matrix used in this study is provided with permission (Mirme and Mirme, 2013) as part of the data linked.

Author contributions. JP, SM, HEM and JK developed the CHARGE electrospray generator. JP, NGAM, BS, SM, RB, ZB, LC, LD, MG, XH, BL, VM, RM, BM, AO, MP, AAP, BR, MS, PT, NSU, DSW, MW, SKW, AW, MZW, WY, IEH, KL, MK, TP, AT, SM, HEM, and JK prepared the CLOUD facility and measurement instruments. JP, NGAM, BS, LC, LD, MG, XH, HL, RM, BM, TM, AAP, BR, DSW, SKW, AW, MZW, AA, AT, SM, HEM, AK, and JK collected the data. JP, NGAM, BS and DS analysed the data. JP, NGAM, BS, SM, DS, LD, XH, SKW, AW, IEH, NMD, RCF, AK, JC and JK contributed to the scientific discussion. JP, NGAM, DS, NMD, RCF, AK and JK contributed to writing the manuscript.

Competing interests. The authors declare no competing interest.

Acknowledgements. We thank CERN for supporting CLOUD with technical and financial resources. We thank Louis-Philippe De Menezes, Ilia Krasin, Xavier Pons, and Robert Kristic for their contributions to the experiment. This research was performed before the invasion of Ukraine by Russia on 24 February 2022.

Financial support. This research has been supported by Innovative Training Networks – ITN 400 (CLOUD-Motion H2020-MSCA-ITN-2017 no. 764991), the German Ministry of Science and Education (CLOUD-16, 01LK1601A), the European Union's Horizon 2020 research and innovation programme under the Marie Sklodowska-Curie grant agreement no. 764991 ("CLOUD-MOTION H2020-MSCA-ITN2017"), the Swiss National Science Foundation (grant numbers 200021_169090, 200020_172602 and 20FI20_172622), European Union's Horizon 2020 research and innovation programme under the Marie Sklodowska-Curie grant agreement no. 895875 ("NPF-PANDA"), ACCC Flagship funded by the Academy of Finland grant number 337549, Academy professorship funded by the Academy of Finland (grant no. 302958), Academy of Finland projects no. 325656, 316114, 314798, 325647, 341349 and 349659. "Quantifying carbon sink, CarbonSink+ and their interaction with air quality" INAR project funded by Jane and Aatos Erkko Foundation, Jenny and Antti Wihuri Foundation project "Air pollution cocktail in Gigacity", European Research Council (ERC) project ATM-GTP Contract No. 742206, and the Arena for the gap analysis of the existing Arctic Science Co-Operations (AASCO) funded by Prince Albert Foundation Contract No 2859, FCT-Portuguese national funding agency for science, research and technology, project CERN/FIS-COM/0028/2019.

Review statement.

References

Amanatidis, S., Huang, Y., Pushpawela, B., Schulze, B. C., Kenseth, C. M., Ward, R. X., Seinfeld, J. H., Hering, S. V., and Flagan, R. C.: Efficacy of a portable, moderate-resolution, fast-scanning differential mobility analyzer for ambient aerosol size distribution measurements, Atmos. Meas. Tech., 14, 4507–4516, https://doi.org/10.5194/amt-14-4507-2021, 2021.

Birmili, W., Stratmann, F., Wiedensohler, A., Covert, D., Russell, L. M., and Berg, O.: Determination of Differential Mobility Analyzer Transfer Functions Using Identical Instruments in Series, Aerosol Science and Technology, 27, 215–223, https://doi.org/10.1080/02786829708965468, 1997.

Breitenlechner, M., Fischer, L., Hainer, M., Heinritzi, M., Curtius, J., and Hansel, A.: PTR3: An Instrument for Studying the Lifecycle of Reactive Organic Carbon in the Atmosphere, Anal. Chem., 89, 5824–5831, https://doi.org/10.1021/acs.analchem.6b05110, 2017.

Chahl, H. S. and Gopalakrishnan, R.: High potential, near free molecular regime Coulombic collisions in aerosols and dusty plasmas, Aerosol Science and Technology, 53, 933–957, https://doi.org/10.1080/02786826.2019.1614522, 2019.

Dada, L., Lehtipalo, K., Kontkanen, J., Nieminen, T., Baalbaki, R., Ahonen, L., Duplissy, J., Yan, C., Chu, B., Petäjä, T., Lehtinen, K., Kerminen, V.-M., Kulmala, M., and Kangasluoma, J.: Formation and growth of sub-3-nm aerosol particles in experimental chambers, Nat Protoc, 15, 1013–1040, https://doi.org/10.1038/s41596-019-0274-z, 2020.

Dépée, A., Lemaitre, P., Gelain, T., Monier, M., and Flossmann, A.: Laboratory study of the collection efficiency of submicron aerosol particles by cloud droplets – Part II: Influence of electric charges, Atmos. Chem. Phys., 21, 6963–6984, https://doi.org/10.5194/acp-21-6963-2021, 2021.

Dias, A., Ehrhart, S., Vogel, A., Williamson, C., Almeida, J., Kirkby, J., Mathot, S., Mumford, S., and Onnela, A.: Temperature uniformity in the CERN CLOUD chamber, Atmos. Meas. Tech., 10, 5075–5088, https://doi.org/10.5194/amt-10-5075-2017, 2017.

Dunne, E. M., Gordon, H., Kürten, A., Almeida, J., Duplissy, J., Williamson, C., Ortega, I. K., Pringle, K. J., Adamov, A., Baltensperger, U., Barmet, P., Benduhn, F., Bianchi, F., Breitenlechner, M., Clarke, A., Curtius, J., Dommen, J., Donahue, N. M., Ehrhart, S., Flagan, R. C., Franchin, A., Guida, R., Hakala, J., Hansel, A., Heinritzi, M., Jokinen, T., Kangasluoma, J., Kirkby, J., Kulmala, M., Kupc, A., Lawler, M. J., Lehtipalo, K., Makhmutov, V., Mann, G., Mathot, S., Merikanto, J., Miettinen, P., Nenes, A., Onnela, A., Rap, A., Reddington, C. L. S., Riccobono, F., Richards, N. A. D., Rissanen, M. P., Rondo, L., Sarnela, N., Schobesberger, S., Sengupta, K., Simon, M., Sipilä, M., Smith, J. N., Stozkhov, Y., Tomé, A., Tröstl, J., Wagner, P. E., Wimmer, D., Winkler, P. M., Worsnop, D. R., and Carslaw, K. S.: Global atmospheric particle formation from CERN CLOUD measurements, Science, 354, 1119–1124, https://doi.org/10.1126/science.aaf2649, 2016.

D'yachkov, L. G., Khrapak, A. G., Khrapak, S. A., and Morfill, G. E.: Model of grain charging in collisional plasmas accounting for collisionless layer, Physics of Plasmas, 14, 042102, https://doi.org/10.1063/1.2713719, 2007.

Ehrhart, S., Ickes, L., Almeida, J., Amorim, A., Barmet, P., Bianchi, F., Dommen, J., Dunne, E. M., Duplissy, J., Franchin, A., Kangasluoma, J., Kirkby, J., Kürten, A., Kupc, A., Lehtipalo, K., Nieminen, T., Riccobono, F., Rondo, L., Schobesberger, S., Steiner, G., Tomé, A., Wimmer, D., Baltensperger, U., Wagner, P. E., and Curtius, J.: Comparison of the SAWNUC model with CLOUD measurements of sulphuric acid-water nucleation, J. Geophys. Res. Atmos., 121, 401-412, https://doi.org/10.1002/2015JD023723, 2016.

Flagan, R. C.: History of Electrical Aerosol Measurements, Aerosol Science and Technology, 28, 301–380, https://doi.org/10.1080/02786829808965530, 1998.

Franchin, A., Ehrhart, S., Leppä, J., Nieminen, T., Gagné, S., Schobesberger, S., Wimmer, D., Duplissy, J., Riccobono, F., Dunne, E. M., Rondo, L., Downard, A., Bianchi, F., Kupc, A., Tsagkogeorgas, G., Lehtipalo, K., Manninen, H. E., Almeida, J., Amorim, A., Wagner, P. E., Hansel, A., Kirkby, J., Kürten, A., Donahue, N. M., Makhmutov, V., Mathot, S., Metzger, A., Petäjä, T., Schnitzhofer, R., Sipilä, M., Stozhkov, Y., Tomé, A., Kerminen, V.-M., Carslaw, K., Curtius, J., Baltensperger, U., and Kulmala, M.: Experimental investigation of ion–ion recombination under atmospheric conditions, Atmos. Chem. Phys., 15, 7203–7216, https://doi.org/10.5194/acp-15-7203-2015, 2015.

Fuchs, N. A.: On the stationary charge distribution on aerosol particles in a bipolar ionic atmosphere, Geofisica Pura e Applicata, 56, 185–193, https://doi.org/10.1007/BF01993343, 1963.

Gatti, M. and Kortshagen, U.: Analytical model of particle charging in plasmas over a wide range of collisionality, Phys. Rev. E, 78, 046402, https://doi.org/10.1103/PhysRevE.78.046402, 2008.

Gopalakrishnan, R. and Hogan, C. J.: Coulomb-influenced collisions in aerosols and dusty plasmas, Phys. Rev. E, 85, 026410, https://doi.org/10.1103/PhysRevE.85.026410, 2012.

Gopalakrishnan, R., Meredith, M. J., Larriba-Andaluz, C., and Hogan, C. J.: Brownian dynamics determination of the bipolar steady state charge distribution on spheres and non-spheres in the transition regime, Journal of Aerosol Science, 63, 126–145, https://doi.org/10.1016/j.jaerosci.2013.04.007, 2013.

Guo, S. and Xue, H.: The enhancement of droplet collision by electric charges and atmospheric electric fields, Atmos. Chem. Phys., 21, 69–85, https://doi.org/10.5194/acp-21-69-2021, 2021.

He, X.-C., Iyer, S., Sipilä, M., Ylisirniö, A., Peltola, M., Kontkanen, J., Baalbaki, R., Simon, M., Kürten, A., Tham, Y. J., Pesonen, J., Ahonen, L. R., Amanatidis, S., Amorim, A., Baccarini, A., Beck, L., Bianchi, F., Brilke, S., Chen, D., Chiu, R., Curtius, J., Dada, L., Dias, A., Dommen, J., Donahue, N. M., Duplissy, J., El Haddad, I., Finkenzeller, H., Fischer, L., Heinritzi, M., Hofbauer, V., Kangasluoma, J., Kim, C., Koenig, T. K., Kubečka, J., Kvashnin, A., Lamkaddam, H., Lee, C. P., Leiminger, M., Li, Z., Makhmutov, V., Xiao, M., Marten, R., Nie, W., Onnela, A., Partoll, E., Petäjä, T., Salo, V.-T., Schuchmann, S., Steiner, G., Stolzenburg, D., Stozhkov, Y., Tauber, C., Tomé, A., Väisänen, O., Vazquez-Pufleau, M., Volkamer, R., Wagner, A. C., Wang, M., Wang, Y., Wimmer, D., Winkler, P. M., Worsnop, D. R., Wu, Y., Yan, C., Ye, Q., Lehtinen, K., Nieminen, T., Manninen, H. E., Rissanen, M., Schobesberger, S., Lehtipalo, K., Baltensperger, U., Hansel, A., Kerminen, V.-M., Flagan, R. C., Kirkby, J., Kurtén, T., and Kulmala, M.: Determination of the collision rate coefficient between charged iodic acid clusters and iodic acid using the appearance time method, Aerosol Science and Technology, 55, 231–242, https://doi.org/10.1080/02786826.2020.1839013, 2021.

Hogan, C. J. and de la Mora, J. F.: Ion Mobility Measurements of Nondenatured 12–150 kDa Proteins and Protein Multimers by Tandem Differential Mobility Analysis–Mass Spectrometry (DMA-MS), J. Am. Soc. Mass Spectrom., 22, 158–172, https://doi.org/10.1007/s13361-010-0014-7, 2011.

Hoppel, W. A. and Frick, G. M.: Ion—Aerosol Attachment Coefficients and the Steady-State Charge Distribution on Aerosols in a Bipolar Ion Environment, Aerosol Science and Technology, 5, 1–21, https://doi.org/10.1080/02786828608959073, 1986.

Intergovernmental Panel on Climate Change (Ed.): Climate Change 2013 - The Physical Science Basis: Working Group I Contribution to the Fifth Assessment Report of the Intergovernmental Panel on Climate Change, Cambridge University Press, Cambridge, https://doi.org/10.1017/CBO9781107415324, 2014a.

Intergovernmental Panel on Climate Change (Ed.): Clouds and Aerosols, in: Climate Change 2013 - The Physical Science Basis, Cambridge University Press, Cambridge, 571–658, https://doi.org/10.1017/CBO9781107415324.016, 2014b.

Kangasluoma, J. and Kontkanen, J.: On the sources of uncertainty in the sub-3 nm particle concentration measurement, Journal of Aerosol Science, 112, 34–51, https://doi.org/10.1016/j.jaerosci.2017.07.002, 2017.

Kangasluoma, J., Cai, R., Jiang, J., Deng, C., Stolzenburg, D., Ahonen, L. R., Chan, T., Fu, Y., Kim, C., Laurila, T. M., Zhou, Y., Dada, L., Sulo, J., Flagan, R. C., Kulmala, M., Petäjä, T., and Lehtipalo, K.: Overview of measurements and current instrumentation for 1–10 nm aerosol particle number size distributions, Journal of Aerosol Science, 148, 105584, https://doi.org/10.1016/j.jaerosci.2020.105584, 2020.

Kebarle, P. and Verkerk, U. H.: Electrospray: From ions in solution to ions in the gas phase, what we know now, Mass Spectrom. Rev., 28, 898–917, https://doi.org/10.1002/mas.20247, 2009.

Kirkby, J., Curtius, J., Almeida, J., Dunne, E., Duplissy, J., Ehrhart, S., Franchin, A., Gagné, S., Ickes, L., Kürten, A., Kupc, A., Metzger, A., Riccobono, F., Rondo, L., Schobesberger, S., Tsagkogeorgas, G., Wimmer, D., Amorim, A., Bianchi, F., Breitenlechner, M., David, A., Dommen, J., Downard, A., Ehn, M., Flagan, R. C., Haider, S., Hansel, A., Hauser, D., Jud, W., Junninen, H., Kreissl, F., Kvashin, A., Laaksonen, A., Lehtipalo, K., Lima, J., Lovejoy, E. R., Makhmutov, V., Mathot, S., Mikkilä, J., Minginette, P., Mogo, S., Nieminen, T., Onnela, A., Pereira, P., Petäjä, T., Schnitzhofer, R., Seinfeld, J. H., Sipilä, M., Stozhkov, Y., Stratmann, F., Tomé, A., Vanhanen, J., Viisanen, Y., Vrtala, A., Wagner, P. E., Walther, H., Weingartner,

E., Wex, H., Winkler, P. M., Carslaw, K. S., Worsnop, D. R., Baltensperger, U., and Kulmala, M.: Role of sulphuric acid, ammonia and galactic cosmic rays in atmospheric aerosol nucleation, Nature, 476, 429–433, https://doi.org/10.1038/nature10343, 2011.

Kirkby, J., Duplissy, J., Sengupta, K., Frege, C., Gordon, H., Williamson, C., Heinritzi, M., Simon, M., Yan, C., Almeida, J., Tröstl, J., Nieminen, T., Ortega, I. K., Wagner, R., Adamov, A., Amorim, A., Bernhammer, A.-K., Bianchi, F., Breitenlechner, M., Brilke, S., Chen, X., Craven, J., Dias, A., Ehrhart, S., Flagan, R. C., Franchin, A., Fuchs, C., Guida, R., Hakala, J., Hoyle, C. R., Jokinen, T., Junninen, H., Kangasluoma, J., Kim, J., Krapf, M., Kürten, A., Laaksonen, A., Lehtipalo, K., Makhmutov, V., Mathot, S., Molteni, U., Onnela, A., Peräkylä, O., Piel, F., Petäjä, T., Praplan, A. P., Pringle, K., Rap, A., Richards, N. A. D., Riipinen, I., Rissanen, M. P., Rondo, L., Sarnela, N., Schobesberger, S., Scott, C. E., Seinfeld, J. H., Sipilä, M., Steiner, G., Stozhkov, Y., Stratmann, F., Tomé, A., Virtanen, A., Vogel, A. L., Wagner, A. C., Wagner, P. E., Weingartner, E., Wimmer, D., Winkler, P. M., Ye, P., Zhang, X., Hansel, A., Dommen, J., Donahue, N. M., Worsnop, D. R., Baltensperger, U., Kulmala, M., Carslaw, K. S., and Curtius, J.: Ion-induced nucleation of pure biogenic particles, Nature, 533, 521–526, https://doi.org/10.1038/nature17953, 2016.

Ku, B. K. and de la Mora, J. F.: Relation between Electrical Mobility, Mass, and Size for Nanodrops 1–6.5 nm in Diameter in Air, Aerosol Science and Technology, 43, 241–249, https://doi.org/10.1080/02786820802590510, 2009.

Kulmala, M., Kerminen, V.-M., Petäjä, T., Ding, A. J., and Wang, L.: Atmospheric gas-to-particle conversion: why NPF events are observed in megacities?, Faraday Discuss., 200, 271–288, https://doi.org/10.1039/C6FD00257A, 2017.

Kupc, A., Amorim, A., Curtius, J., Danielczok, A., Duplissy, J., Ehrhart, S., Walther, H., Ickes, L., Kirkby, J., Kürten, A., Lima, J. M., Mathot, S., Minginette, P., Onnela, A., Rondo, L., and Wagner, P. E.: A fibre-optic UV system for H2SO4 production in aerosol chambers causing minimal thermal effects, Journal of Aerosol Science, 42, 532–543, https://doi.org/10.1016/j.jaerosci.2011.05.001, 2011.

Kürten, A., Rondo, L., Ehrhart, S., and Curtius, J.: Performance of a corona ion source for measurement of sulfuric acid by chemical ionization mass spectrometry, Atmos. Meas. Tech., 4, 437–443, https://doi.org/10.5194/amt-4-437-2011, 2011.

Kürten, A., Rondo, L., Ehrhart, S., and Curtius, J.: Calibration of a Chemical Ionization Mass Spectrometer for the Measurement of Gaseous Sulfuric Acid, J. Phys. Chem. A, 116, 6375–6386, https://doi.org/10.1021/jp212123n, 2012.

Kürten, A., Jokinen, T., Simon, M., Sipilä, M., Sarnela, N., Junninen, H., Adamov, A., Almeida, J., Amorim, A., Bianchi, F., Breitenlechner, M., Dommen, J., Donahue, N. M., Duplissy, J., Ehrhart, S., Flagan, R. C., Franchin, A., Hakala, J., Hansel, A., Heinritzi, M., Hutterli, M., Kangasluoma, J., Kirkby, J., Laaksonen, A., Lehtipalo, K., Leiminger, M., Makhmutov, V., Mathot, S., Onnela, A., Petäjä, T., Praplan, A. P., Riccobono, F., Rissanen, M. P., Rondo, L., Schobesberger, S., Seinfeld, J. H., Steiner, G., Tomé, A., Tröstl, J., Winkler, P. M., Williamson, C., Wimmer, D., Ye, P., Baltensperger, U., Carslaw, K. S., Kulmala, M., Worsnop, D. R., and Curtius, J.: Neutral molecular cluster formation of sulfuric acid–dimethylamine observed in real time under atmospheric conditions, Proc. Natl. Acad. Sci. U.S.A., 111, 15019–15024, https://doi.org/10.1073/pnas.1404853111, 2014.

Larriba, C., Hogan, C. J., Attoui, M., Borrajo, R., Garcia, J. F., and de la Mora, J. F.: The Mobility–Volume Relationship below 3.0 nm Examined by Tandem Mobility–Mass Measurement, Aerosol Science and Technology, 45, 453–467, https://doi.org/10.1080/02786826.2010.546820, 2011.

Lehtinen, K. E. J. and Kulmala, M.: A model for particle formation and growth in the atmosphere with molecular resolution in size, Atmos. Chem. Phys., 3, 251–257, https://doi.org/10.5194/acp-3-251-2003, 2003.

Lehtipalo, K., Leppä, Johannes, Kontkanen, J., Kangasluoma, J., Franchin, A., Wimmer, D., Schobesberger, S., Junninen, H., Petäjä, T., Sipilä, M., Mikkilä, J., Vanhanen, J., Worsnop, D. R., and Kulmala, M.: Methods for determining particle size

distribution and growth rates between 1 and 3 nm using the Particle Size Magnifier, Boreal Environment Research, 19, 215–236, 2014.

Liu, W., Kaufman, S. L., Osmondson, B. L., Sem, G. J., Quant, F. R., and Oberreit, D. R.: Water-Based Condensation Particle Counters for Environmental Monitoring of Ultrafine Particles, Journal of the Air & Waste Management Association, 56, 444–455, https://doi.org/10.1080/10473289.2006.10464520, 2006.

López-Herrera, J. M., Barrero, A., Boucard, A., Loscertales, I. G., and Márquez, M.: An experimental study of the electrospraying of water in air at atmospheric pressure, J. Am. Soc. Mass Spectrom., 15, 253–259, https://doi.org/10.1016/j.jasms.2003.10.018, 2004.

López-Yglesias, X. and Flagan, R. C.: Ion–Aerosol Flux Coefficients and the Steady-State Charge Distribution of Aerosols in a Bipolar Ion Environment, Aerosol Science and Technology, 47, 688–704, https://doi.org/10.1080/02786826.2013.783684, 2013.

Mahfouz, N. G. A. and Donahue, N. M.: Atmospheric Nanoparticle Survivability Reduction Due to Charge-Induced Coagulation Scavenging Enhancement, Geophys Res Lett, 48, https://doi.org/10.1029/2021GL092758, 2021a.

Mahfouz, N. G. A. and Donahue, N. M.: Technical note: The enhancement limit of coagulation scavenging of small charged particles, Atmos. Chem. Phys., 21, 3827–3832, https://doi.org/10.5194/acp-21-3827-2021, 2021b.

Mahfouz, N. G. A., Gorkowski, K. J., Chuang, W. K., and Kumar, A.: particula: v0.0.7, , https://doi.org/10.5281/ZENODO.6634653, 2022.

Manninen, H. E., Petäjä, T., Asmi, E., Riipinen, I., Nieminen, T., Mikkilä, J., Hörrak, U., Mirme, A., Mirme, S., Laakso, L., Kerminen, V.-M., and Kulmala, M.: Long-term field measurements of charged and neutral clusters using Neutral cluster and Air Ion Spectrometer (NAIS), Boreal Environment Research, 14, 591–605, 2009.

Manninen, H. E., Mirme, S., Mirme, A., Petäjä, T., and Kulmala, M.: How to reliably detect molecular clusters and nucleation mode particles with Neutral cluster and Air Ion Spectrometer (NAIS), Atmos. Meas. Tech., 9, 3577–3605, https://doi.org/10.5194/amt-9-3577-2016, 2016.

Marginean, I., Kelly, R. T., Prior, D. C., LaMarche, B. L., Tang, K., and Smith, R. D.: Analytical Characterization of the Electrospray Ion Source in the Nanoflow Regime, Anal. Chem., 80, 6573–6579, https://doi.org/10.1021/ac800683s, 2008.

Marten, R., Xiao, M., Rörup, B., Wang, M., Kong, W., He, X.-C., Stolzenburg, D., Pfeifer, J., Marie, G., Wang, D. S., Scholz, W., Baccarini, A., Lee, C. P., Amorim, A., Baalbaki, R., Bell, D. M., Bertozzi, B., Caudillo, L., Chu, B., Dada, L., Duplissy, J., Finkenzeller, H., Carracedo, L. G., Granzin, M., Hansel, A., Heinritzi, M., Hofbauer, V., Kemppainen, D., Kürten, A., Lampimäki, M., Lehtipalo, K., Makhmutov, V., Manninen, H. E., Mentler, B., Petäjä, T., Philippov, M., Shen, J., Simon, M., Stozhkov, Y., Tomé, A., Wagner, A. C., Wang, Y., Weber, S. K., Wu, Y., Zauner-Wieczorek, M., Curtius, J., Kulmala, M., Möhler, O., Volkamer, R., Winkler, P. M., Worsnop, D. R., Dommen, J., Flagan, R. C., Kirkby, J., Donahue, N. M., Lamkaddam, H., Baltensperger, U., and El Haddad, I.: Survival of newly formed particles in haze conditions, Environmental Science: Atmospheres, 2, 491–499, https://doi.org/10.5445/IR/1000146549, 2022.

Metzger, A., Verheggen, B., Dommen, J., Duplissy, J., Prevot, A. S. H., Weingartner, E., Riipinen, I., Kulmala, M., Spracklen, D. V., Carslaw, K. S., and Baltensperger, U.: Evidence for the role of organics in aerosol particle formation under atmospheric conditions, Proceedings of the National Academy of Sciences, 107, 6646–6651, https://doi.org/10.1073/pnas.0911330107, 2010.

Mirme, A., Tamm, E., Mordas, G., Vana, M., Uin, J., Mirme, S., Bernotas, T., Laakso, L., Hirsikko, A., and Kulmala, M.: A wide-range multi-channel Air Ion Spectrometer, Boreal Environment Research, 12, 247–264, 2007.

Mirme, S. and Mirme, A.: The mathematical principles and design of the NAIS – a spectrometer for the measurement of cluster ion and nanometer aerosol size distributions, Atmos. Meas. Tech., 6, 1061–1071, https://doi.org/10.5194/amt-6-1061-2013, 2013.

Murphy, D. M. and Koop, T.: Review of the vapour pressures of ice and supercooled water for atmospheric applications, Q. J. R. Meteorol. Soc., 131, 1539–1565, https://doi.org/10.1256/qj.04.94, 2005.

Myhre, C. E. L., Nielsen, C. J., and Saastad, O. W.: Density and Surface Tension of Aqueous H_2SO_4 at Low Temperature, J. Chem. Eng. Data, 43, 617–622, https://doi.org/10.1021/je980013g, 1998.

Nieminen, T., Lehtinen, K. E. J., and Kulmala, M.: Sub-10 nm particle growth by vapor condensation – effects of vapor molecule size and particle thermal speed, Atmos. Chem. Phys., 10, 9773–9779, https://doi.org/10.5194/acp-10-9773-2010, 2010.

Ouyang, H., Gopalakrishnan, R., and Hogan, C. J.: Nanoparticle collisions in the gas phase in the presence of singular contact potentials, The Journal of Chemical Physics, 137, 064316, https://doi.org/10.1063/1.4742064, 2012.

Pfeifer, J., Simon, M., Heinritzi, M., Piel, F., Weitz, L., Wang, D., Granzin, M., Müller, T., Bräkling, S., Kirkby, J., Curtius, J., and Kürten, A.: Measurement of ammonia, amines and iodine compounds using protonated water cluster chemical ionization mass spectrometry, Atmos. Meas. Tech., 13, 2501–2522, https://doi.org/10.5194/amt-13-2501-2020, 2020.

Rayleigh, Lord: XX. *On the equilibrium of liquid conducting masses charged with electricity*, The London, Edinburgh, and Dublin Philosophical Magazine and Journal of Science, 14, 184–186, https://doi.org/10.1080/14786448208628425, 1882.

Seinfeld, J. H. and Pandis, S. N.: Atmospheric chemistry and physics: from air pollution to climate change, Third edition., John Wiley & Sons, Hoboken, New Jersey, 1120 pp., 2016.

Simon, M., Heinritzi, M., Herzog, S., Leiminger, M., Bianchi, F., Praplan, A., Dommen, J., Curtius, J., and Kürten, A.: Detection of dimethylamine in the low pptv range using nitrate chemical ionization atmospheric pressure interface time-of-flight (CI-APi-TOF) mass spectrometry, Atmos. Meas. Tech., 9, 2135–2145, https://doi.org/10.5194/amt-9-2135-2016, 2016.

Skrotzki, J.: High-accuracy multiphase humidity measurements using TDLAS: application to the investigation of ice growth in simulated cirrus clouds, https://doi.org/10.11588/HEIDOK.00013141, 2012.

Smith, J. N., Flagan, R. C., and Beauchamp, J. L.: Droplet Evaporation and Discharge Dynamics in Electrospray Ionization, J. Phys. Chem. A, 106, 9957–9967, https://doi.org/10.1021/jp025723e, 2002.

Sterling, H. J., Cassou, C. A., Trnka, M. J., Burlingame, A. L., Krantz, B. A., and Williams, E. R.: The role of conformational flexibility on protein supercharging in native electrospray ionization, Phys. Chem. Chem. Phys., 13, 18288, https://doi.org/10.1039/c1cp20277d, 2011.

Stolzenburg, D., Simon, M., Ranjithkumar, A., Kürten, A., Lehtipalo, K., Gordon, H., Ehrhart, S., Finkenzeller, H., Pichelstorfer, L., Nieminen, T., He, X.-C., Brilke, S., Xiao, M., Amorim, A., Baalbaki, R., Baccarini, A., Beck, L., Bräkling, S., Caudillo Murillo, L., Chen, D., Chu, B., Dada, L., Dias, A., Dommen, J., Duplissy, J., El Haddad, I., Fischer, L., Gonzalez Carracedo, L., Heinritzi, M., Kim, C., Koenig, T. K., Kong, W., Lamkaddam, H., Lee, C. P., Leiminger, M., Li, Z., Makhmutov, V., Manninen, H. E., Marie, G., Marten, R., Müller, T., Nie, W., Partoll, E., Petäjä, T., Pfeifer, J., Philippov, M., Rissanen, M. P., Rörup, B., Schobesberger, S., Schuchmann, S., Shen, J., Sipilä, M., Steiner, G., Stozhkov, Y., Tauber, C.,

Tham, Y. J., Tomé, A., Vazquez-Pufleau, M., Wagner, A. C., Wang, M., Wang, Y., Weber, S. K., Wimmer, D., Wlasits, P. J., Wu, Y., Ye, Q., Zauner-Wieczorek, M., Baltensperger, U., Carslaw, K. S., Curtius, J., Donahue, N. M., Flagan, R. C., Hansel, A., Kulmala, M., Lelieveld, J., Volkamer, R., Kirkby, J., and Winkler, P. M.: Enhanced growth rate of atmospheric particles from sulfuric acid, Atmos. Chem. Phys., 20, 7359–7372, https://doi.org/10.5194/acp-20-7359-2020, 2020.

Suresh, V., Li, L., Redmond Go Felipe, J., and Gopalakrishnan, R.: Modeling nanoparticle charge distribution in the afterglow of non-thermal plasmas and comparison with measurements, J. Phys. D: Appl. Phys., 54, 275205, https://doi.org/10.1088/1361-6463/abf70c, 2021.

Tamadate, T., Higashi, H., Seto, T., and Hogan, C. J.: Calculation of the ion–ion recombination rate coefficient via a hybrid continuum-molecular dynamics approach, J. Chem. Phys., 152, 094306, https://doi.org/10.1063/1.5144772, 2020a.

Tamadate, T., Higashi, H., Hogan, C. J., and Seto, T.: The charge reduction rate for multiply charged polymer ions *via* ion–ion recombination at atmospheric pressure, Phys. Chem. Chem. Phys., 22, 25215–25226, https://doi.org/10.1039/D0CP03989F, 2020b.

Tikhonov, A. N.: Solution of incorrectly formulated problem and the regularization method, Soviet Math. Dokl, 4, 1035–1038, 1963.

Tinsley, B. A.: Uncertainties in Evaluating Global Electric Circuit Interactions With Atmospheric Clouds and Aerosols, and Consequences for Radiation and Dynamics, JGR Atmospheres, 127, e2021JD035954, https://doi.org/10.1029/2021JD035954, 2022.

Tinsley, B. A., Rohrbaugh, R. P., Hei, M., and Beard, K. V.: Effects of Image Charges on the Scavenging of Aerosol Particles by Cloud Droplets and on Droplet Charging and Possible Ice Nucleation Processes, J. Atmos. Sci., 57, 2118–2134, https://doi.org/10.1175/1520-0469(2000)057<2118:EOICOT>2.0.CO;2, 2000.

Tritscher, T., Beeston, M., Zerrath, A. F., Elzey, S., Krinke, T. J., Filimundi, E., and Bischof, O. F.: NanoScan SMPS – A Novel, Portable Nanoparticle Sizing and Counting Instrument, J. Phys.: Conf. Ser., 429, 012061, https://doi.org/10.1088/1742-6596/429/1/012061, 2013.

Turco, R. P., Zhao, J.-X., and Yu, F.: A new source of tropospheric aerosols: Ion-ion recombination, Geophys. Res. Lett., 25, 635–638, https://doi.org/10.1029/98GL00253, 1998.

Vanhanen, J., Mikkilä, J., Lehtipalo, K., Sipilä, M., Manninen, H. E., Siivola, E., Petäjä, T., and Kulmala, M.: Particle Size Magnifier for Nano-CN Detection, Aerosol Science and Technology, 45, 533–542, https://doi.org/10.1080/02786826.2010.547889, 2011.

Vehkamäki, H., Kulmala., M., Napari, I., Lehtinen, K. E. J., Timmreck, M., Noppel, M., and Laaksonen, A.: An improved parameterization for sulfuric acid–water nucleation rates for tropospheric and stratospheric conditions, J. Geophys. Res., 107, AAC 3-1-AAC 3-10, https://doi.org/10.1029/2002JD002184, 2002.

Wang, M., He, X.-C., Finkenzeller, H., Iyer, S., Chen, D., Shen, J., Simon, M., Hofbauer, V., Kirkby, J., Curtius, J., Maier, N., Kurtén, T., Worsnop, D. R., Kulmala, M., Rissanen, M., Volkamer, R., Tham, Y. J., Donahue, N. M., and Sipilä, M.: Measurement of iodine species and sulfuric acid using bromide chemical ionization mass spectrometers, Atmos. Meas. Tech., 14, 4187–4202, https://doi.org/10.5194/amt-14-4187-2021, 2021.

Wiedensohler, A.: An approximation of the bipolar charge distribution for particles in the submicron size range, Journal of Aerosol Science, 19, 387–389, https://doi.org/10.1016/0021-8502(88)90278-9, 1988.

Wiedensohler, A., Birmili, W., Nowak, A., Sonntag, A., Weinhold, K., Merkel, M., Wehner, B., Tuch, T., Pfeifer, S., Fiebig, M., Fjäraa, A. M., Asmi, E., Sellegri, K., Depuy, R., Venzac, H., Villani, P., Laj, P., Aalto, P., Ogren, J. A., Swietlicki, E., Williams, P., Roldin, P., Quincey, P., Hüglin, C., Fierz-Schmidhauser, R., Gysel, M., Weingartner, E., Riccobono, F., Santos, S., Grüning, C., Faloon, K., Beddows, D., Harrison, R., Monahan, C., Jennings, S. G., O'Dowd, C. D., Marinoni, A., Horn, H.-G., Keck, L., Jiang, J., Scheckman, J., McMurry, P. H., Deng, Z., Zhao, C. S., Moerman, M., Henzing, B., de Leeuw, G., Löschau, G., and Bastian, S.: Mobility particle size spectrometers: harmonization of technical standards and data structure to facilitate high quality long-term observations of atmospheric particle number size distributions, Atmos. Meas. Tech., 5, 657–685, https://doi.org/10.5194/amt-5-657-2012, 2012.

Winklmayr, W., Reischl, G. P., Lindner, A. O., and Berner, A.: A new electromobility spectrometer for the measurement of aerosol size distributions in the size range from 1 to 1000 nm, Journal of Aerosol Science, 22, 289–296, https://doi.org/10.1016/S0021-8502(05)80007-2, 1991.

Zeleny, J.: The velocity of the ions produced in gases by Röntgen rays, Proc. R. Soc. Lond., 66, 238–241, https://doi.org/10.1098/rspl.1899.0095, 1900.

Zhou, L. and Tinsley, B. A.: Production of space charge at the boundaries of layer clouds, J. Geophys. Res., 112, D11203, https://doi.org/10.1029/2006JD007998, 2007.

Supplementary Information for:

Measurement of the rate coefficients between atmospheric ions and multiply charged aerosol particles in the CERN CLOUD chamber

Joschka Pfeifer[1,7], Naser G. A. Mahfouz[2,3,4], Benjamin C. Schulze[5], Serge Mathot[1], Dominik Stolzenburg[6], Rima Baalbaki[6], Zoé Brasseur[6], Lucia Caudillo[7], Lubna Dada[8], Manuel Granzin[7], Xu-Cheng He[6,9], Houssni Lamkaddam[8], Brandon Lopez[3], Vladimir Makhmutov[10,11], Ruby Marten[8], Bernhard Mentler[12], Tatjana Müller[7], Antti Onnela[1], Maxim Philippov[10], Ana A. Piedehierro[9], Birte Rörup[6], Meredith Schervish[2,13], Ping Tian[14], Nsikanabasi S. Umo[15], Dongyu S. Wang[8], Mingyi Wang[5], Stefan K. Weber[1,7], André Welti[9], Yusheng Wu[6], Marcel Zauner-Wieczorek[7], Antonio Amorim[16], Imad El Haddad[8], Markku Kulmala[6], Katrianne Lehtipalo[6,9], Tuukka Petäjä[6], António Tomé[17], Sander Mirme[18,19], Hanna E. Manninen[1], Neil M. Donahue[2,3], Richard C. Flagan[5], Andreas Kürten[7], Joachim Curtius[7], Jasper Kirkby[1,7]

[1]CERN, 1211 Geneva, Switzerland
[2]Center for Atmospheric Particle Studies, Carnegie Mellon University, Pittsburgh, PA 15213, USA
[3]Department of Chemical Engineering, Carnegie Mellon University, Pittsburgh, PA 15213, USA
[4]Program in Atmospheric and Oceanic Sciences, Princeton University, Princeton, NJ 08544, USA
[5]Department of Environmental Science and Engineering, California Institute of Technology, Pasadena, CA 91125, USA
[6]Institute for Atmospheric and Earth System Research (INAR)/ Physics, Faculty of Science, University of Helsinki, Helsinki, FI-00560, Finland
[7]Institute for Atmospheric and Environmental Sciences, Goethe University Frankfurt, 60438 Frankfurt am Main, Germany
[8]Laboratory of Atmospheric Chemistry, Paul Scherrer Institute (PSI), 5232 Villigen-PSI, Switzerland
[9]Finnish Meteorological Institute, 00560 Helsinki, Finland
[10]P.N. Lebedev Physical Institute of the Russian Academy of Sciences, 119991 Moscow, Russian Federation
[11]Moscow Institute of Physics and Technology (National Research University), 117303 Moscow, Russian Federation
[12]Institute for Ion and Applied Physics, University of Innsbruck, 6020 Innsbruck, Austria
[13]Department of Chemistry, University of California, Irvine, CA 92697, USA
[14]Beijing weather modification center, Beijing, 100089, China
[15]Institute of Meteorology and Climate Research (IMK-AAF), Karlsruhe Institute of Technology (KIT), 76344 Eggenstein-Leopoldshafen, Germany
[16]CENTRA and FCUL, University of Lisbon, 1749-016 Lisbon, Portugal
[17]IDL-Universidade da Beira Interior, Rua Marquês D"Ávila e Bolama, 6201-001 Covilhã, Portugal
[18]Institute of Physics, Unversity of Tartu, Estonia
[19]Airel Ltd., 50411, Tartu, Estonia

Correspondence to: Joschka Pfeifer (joschka.pfeifer@cern.ch)

S1 Sulfuric acid measurements

Figure S1 shows the sulfuric acid concentration measured during the experiments. The gas phase concentration was measured using a Nitrate CI-APi-TOF (Kürten et al., 2011). Our rate coefficients in the main text were obtained during decay stages. In Figure S1, we that under the experimental conditions (278 K at 80 % relative humidity), nucleation, and vapor condensation

can be neglected during these stages (Vehkamäki et al., 2002; Nieminen et al., 2010; Dunne et al., 2016). As an example, for sulfuric acid concentrations of 5×10^7 cm^{-3}, condensation growth rates are below 2 nm hour^{-1} and the nucleation rate is below 1×10^{-2} cm^{-3} s^{-1} (Dunne et al., 2016). Moreover, while these values are already small compared to the observed time scale of the rate coefficients of multiply charged particles, sulfuric acid concentrations of ~5×10^7 cm^{-3} are only measured at the beginning of a decay stage and quickly drop well below 1×10^7 cm^{-3}. Figure S1 also shows that gas phase sulfuric acid concentration is comparable during both multiply charged experiments (LHS) and Steady State experiments (RHS).

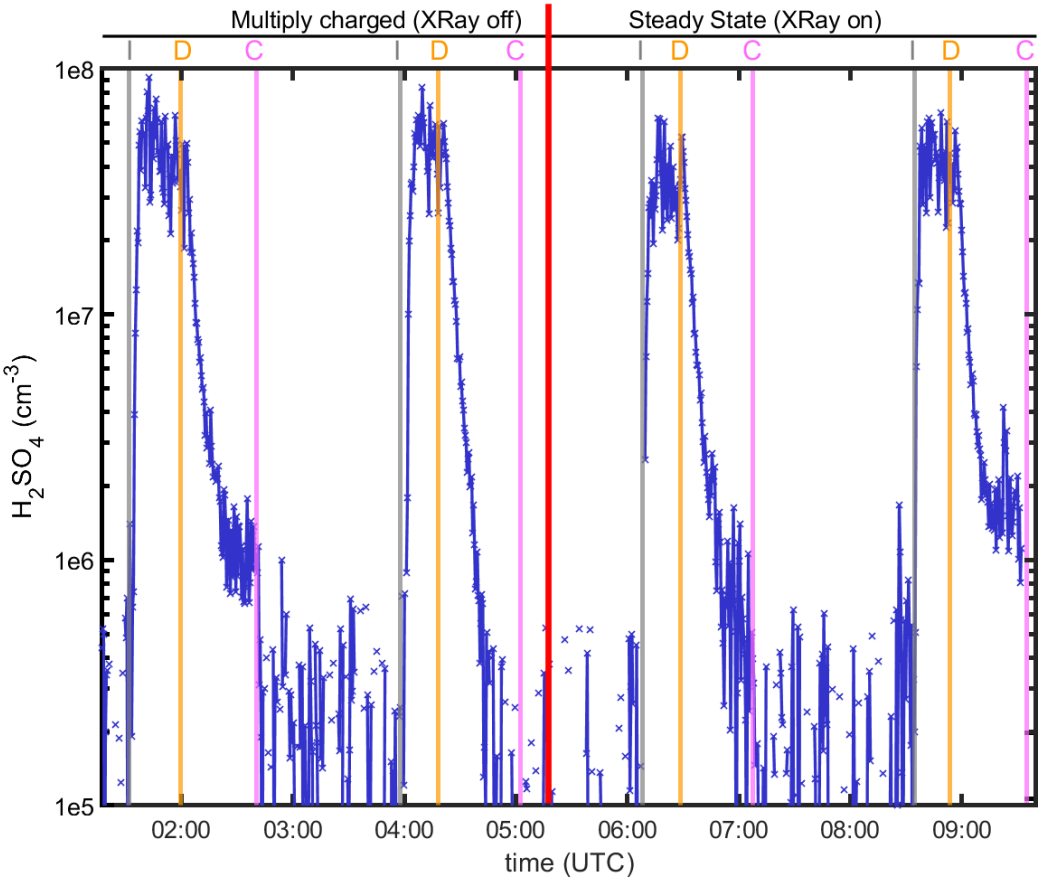

Figure S1: Measured Sulfuric Acid concentration during the experiments. The letters I, D and C show the transition from "Injection" (I) to "Decay" (D) to "Cleaning" (C) stage.

S2 Validation of inferred rate coefficients

The resultant error in calculating the ion–aerosol rate coefficients consists of statistical and systematic errors. We verify the robustness of our calculations by varying parameters and constants within ranges of uncertainty (Figure S2). We repeat our

numerical calculations (Eq. 5–9) for each experiment 1000 times by varying all parameters that contribute to systematic errors in our inference. During these calculations, the parameters are drawn from a normal distribution around the used values.

In Eq. (4) (main text), the inferred multiply charged distribution ω_j depends on assumed maximum number of charges j, the loss timescale coefficient k_{loss}, and the baseline distribution $\Omega_+(t=0)$. In our uncertainty estimate, we allow the maximum j to vary between 6 and 15 charges. The loss timescale $k(d_\mathrm{p}, t)$ is allowed to vary by ± 500% to account for neglected loss rates and for possible errors in the particle measurements. Additionally, we allow variation of ± 50 % of the baseline distribution atop of its value and ±10 % below. We set the statistical error on the measured NAIS current to be in the range of ± 0.2 fA (which is an uncertainty obtained from chamber background measurements). This value is randomly varied prior to inversion.

The systematic error of the nSMPS instrument (coupled with a condensation particle counter 2.5 nm, CPC 2.5) is large for the size range of our experiments (about 70 %) (Kangasluoma et al., 2020). We see this uncertainty confirmed for our experiments in comparison with another Condensation Particle Counter (CPC 2.5), which is why we treat the SMPS instrument with a 400 % uncertainty. This rather large uncertainty does not affect the conclusion from our calculations because wall and dilution losses clearly dominate loss rates of the affected particles (Figure 2, main text). During these calculations, we also allow the particle density to vary between pure water (998 kg m^{-3}) and pure sulfuric acid (1830 kg m^{-3}). An example of the procedure for the allowed number of charged and for particle density is shown in Figure S2. The figure also shows the weighting scheme applied to the calculated coefficients.

In Table S1, we summarize the allowed uncertainty for all parameters during the procedure shown in Figure S2. Figure S3 shows the ± 1 standard deviation range of these calculations and compares it with the coefficients shown in Figure 4 (main text). The variations confirm the robustness of our calculated rate coefficients and even a drastic variation of the initial assumptions and an allowance for large instrumental errors confirms our results.

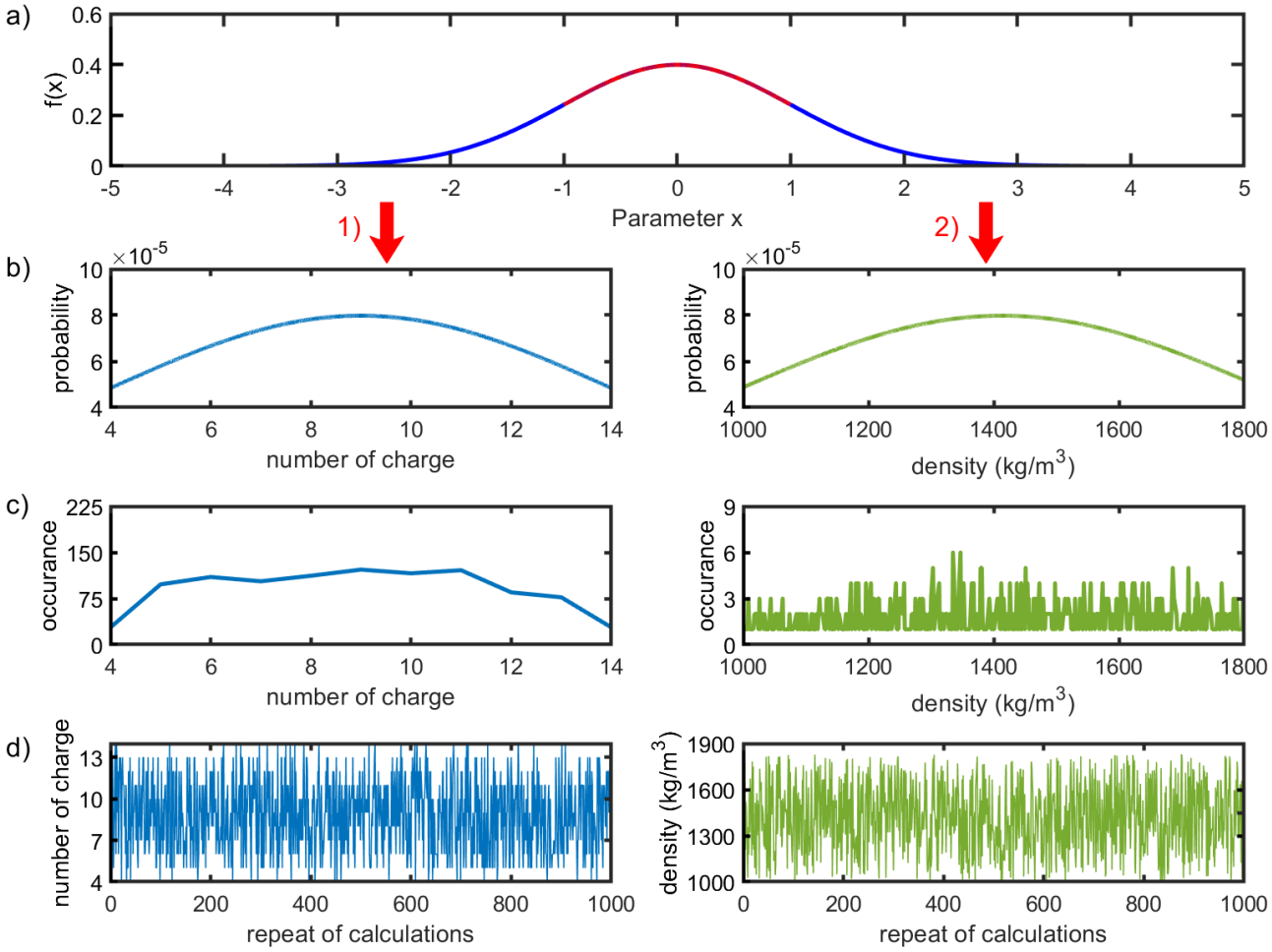

Figure S2: Validating the robustness of rate coefficients calculation. Example for procedure to randomly vary input parameters (here for number of charges and particle density). Panel a) shows the weighting scheme applied to all parameters. The calculations shown in equations (1) to (9) in the main paper are then repeated 1000 times for all experiments (Panel d). During this, all parameters that could introduce statistical and systematic errors are randomly varied. A weighting scheme towards the central value of the variations is applied according to a normal distribution (Panel b and c). The derived probability distribution is applied over a specific range that is also summarized in Table S1 (Panel 2). The resulting values for number of charges and particle density and their occurrence throughout the 1000 repeats are shown in the panels c) and d).

Table S1: Variation of different parameters that contribute to the total error of the calculated coefficients. We show the central value, as well as the variation. The parameters are weighted according to a Gaussian distribution, as shown in Figure S2.

Parameter	Unit (Parameter)	Central value	Variation
Smallest diameter	nm	2	± 10 %
Largest diameter	nm	10	± 50 %
$k_{\mathrm{loss}}(\mathrm{d_p}, \mathrm{t})$	$\mathrm{s^{-1}}$	± 500 %	± 500 %
Number of charge (j)	-	9	± 5
Particle density (ρ)	$\mathrm{kg\ m^{-3}}$	1413	416
AIS: $\Omega_{\pm}, \omega_{\mathrm{j}}$	fA	Measured Value	± 0.2
nSMPS: Ω_0	$\mathrm{cm^{-3}}$	Measured Value	± 400 %

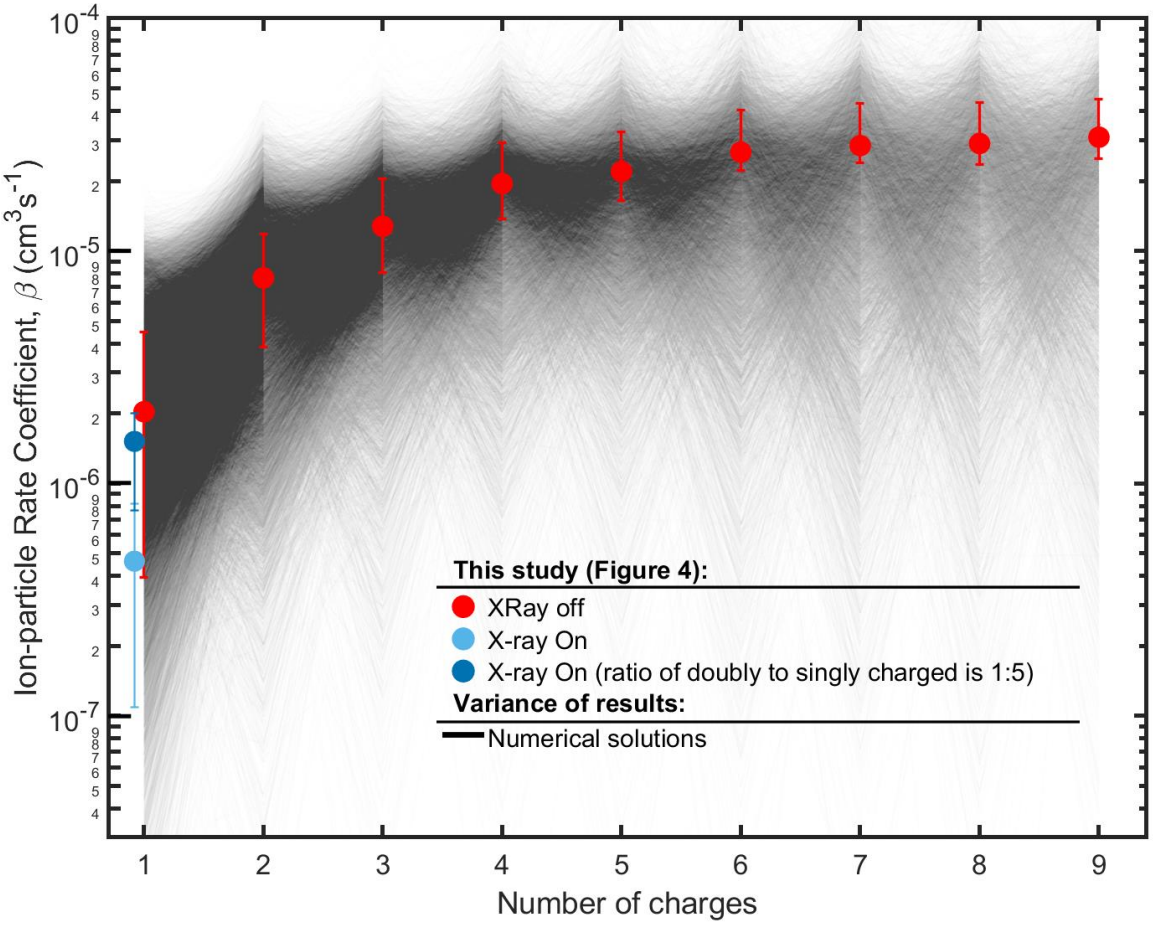

Figure S3: **Uncertainty estimate of our calculated rate coefficients overlayed with our results from Figure 4. Black lines show all numerical solutions (from all repeated calculations), with the validation scheme from Figure S2 applied.**

References

Dunne, E. M., Gordon, H., Kürten, A., Almeida, J., Duplissy, J., Williamson, C., Ortega, I. K., Pringle, K. J., Adamov, A., Baltensperger, U., Barmet, P., Benduhn, F., Bianchi, F., Breitenlechner, M., Clarke, A., Curtius, J., Dommen, J., Donahue, N. M., Ehrhart, S., Flagan, R. C., Franchin, A., Guida, R., Hakala, J., Hansel, A., Heinritzi, M., Jokinen, T., Kangasluoma, J., Kirkby, J., Kulmala, M., Kupc, A., Lawler, M. J., Lehtipalo, K., Makhmutov, V., Mann, G., Mathot, S., Merikanto, J., Miettinen, P., Nenes, A., Onnela, A., Rap, A., Reddington, C. L. S., Riccobono, F., Richards, N. A. D., Rissanen, M. P., Rondo, L., Sarnela, N., Schobesberger, S., Sengupta, K., Simon, M., Sipilä, M., Smith, J. N., Stozkhov, Y., Tomé, A., Tröstl, J., Wagner, P. E., Wimmer, D., Winkler, P. M., Worsnop, D. R., and Carslaw, K. S.: Global atmospheric particle formation from CERN CLOUD measurements, Science, 354, 1119–1124, https://doi.org/10.1126/science.aaf2649, 2016.

Kangasluoma, J., Cai, R., Jiang, J., Deng, C., Stolzenburg, D., Ahonen, L. R., Chan, T., Fu, Y., Kim, C., Laurila, T. M., Zhou, Y., Dada, L., Sulo, J., Flagan, R. C., Kulmala, M., Petäjä, T., and Lehtipalo, K.: Overview of measurements and current instrumentation for 1–10 nm aerosol particle number size distributions, Journal of Aerosol Science, 148, 105584, https://doi.org/10.1016/j.jaerosci.2020.105584, 2020.

Kürten, A., Rondo, L., Ehrhart, S., and Curtius, J.: Performance of a corona ion source for measurement of sulfuric acid by chemical ionization mass spectrometry, Atmos. Meas. Tech., 4, 437–443, https://doi.org/10.5194/amt-4-437-2011, 2011.

Nieminen, T., Lehtinen, K. E. J., and Kulmala, M.: Sub-10 nm particle growth by vapor condensation – effects of vapor molecule size and particle thermal speed, Atmos. Chem. Phys., 10, 9773–9779, https://doi.org/10.5194/acp-10-9773-2010, 2010.

Vehkamäki, H., Kulmala., M., Napari, I., Lehtinen, K. E. J., Timmreck, M., Noppel, M., and Laaksonen, A.: An improved parameterization for sulfuric acid–water nucleation rates for tropospheric and stratospheric conditions, J. Geophys. Res., 107, AAC 3-1-AAC 3-10, https://doi.org/10.1029/2002JD002184, 2002.

3- Conclusion

This work focuses on two new atmospheric measurement methods, both developed and quantified at the CLOUD chamber at CERN. In the first part of the work, a new measurement technique for measuring ammonia, amines and iodine compounds was presented (the Water Cluster CI-APi TOF). The instrument was characterized and ammonia detection limits of 0.5 parts per trillions were reported at 278 Kelvin and 80% relative humidity. The instrument combines a particularly short response time with minimized instrumental background, due to minimized surface areas. Using the Water Cluster CI-API TOF, the condensation of ammonia and nitric acid on newly formed particles was quantitatively demonstrated during experiments conducted at CLOUD. It has been shown that once newly formed particles reach a critical diameter (about 4-5nm), particles grow promptly in the presence of ammonia and nitric acid. The short response time and the low instrumental background of the Water Cluster CI-APi TOF allowed to show that ammonia condenses on the particles and thus is removed from the gas phase. This process can explain new particle formation and growth events under haze conditions, for example in polluted megacities.

Future field studies will have to classify to what extent the rapid particle growth through ammonia and nitric acid condensation really occurs in megacities. The survival probability of newly formed particles could also be explained differently in these regions, for example if not every collision with larger particles leads to capture of the smaller particle (as is often assumed) (Kulmala et al., 2017). For this purpose, field measurements are required, which can be carried out, among other things, with the Water Cluster CI-APi-TOF shown in this work. First field measurements, using satellite data, indicate that ammonia also occurs in the upper troposphere (Höpfner et al., 2016, 2019). Recent laboratory experiments indicate that ammonia and nitric acid also contribute to new particle formation in this area, despite the low concentrations expected there (Wang et al., 2022). Field measurements with high time resolution in this area could shed light on the involvement of ammonia and nitric acid in these areas and will be part of future studies.

In the second part of this work, an instrument to produce multiply charged particles under atmospherically relevant conditions was developed (the CHARGE). The instrument was first optimized based on electrostatic simulations and on laboratory experiments. Afterwards, it was used at the CLOUD chamber. The particles generated by CHARGE were either fed directly to the CLOUD chamber or neutralized using an XRay source. Measurements with Electric Aerosol Analyzers show that CHARGE successfully generates multiply charged particles in sufficient quantities. The instrument allows to conduct quantitative experiments on the effects of multiply charged particles in the atmosphere. Several new experiments to determine charge effects in the atmosphere have been developed and will be refined in the future. The experiments are described in the introductory part of this work. A new method was developed to numerically calculate ion-aerosol attachment coefficients as a function of the number of charges. The results were compared with current theories for calculating these coefficients.

Since there are very few previous measurements in this area (especially as a function of number of charge), the ion-aerosol attachment coefficients shown in this work will be helpful in the

future, for example when new models for predicting collision rates between ions with aerosols in the atmosphere are developed. They can also be helpful in classifying the results of MD simulations and serve as a basis for comparison (Tamadate et al., 2020a, b). In the future, CHARGE can be used to evaluate the numerous simulations and theories suggesting numerous charge effects in clouds, such as “electro-scavenging” or charge-induced precipitation under the influence of earth’s electric field (Tinsley et al., 2000; Guo and Xue, 2021). Simulations, as shown in Guo and Xue (2021), can be tested and charge transfer of particles during collision can be evaluated quantitatively. Expansion studies under the influence of different electric fields (using CHARGE) can be conducted to evaluate the simulations from Guo and Xue (2021) and to compare charge effects with aerosol effects.

4- Schlussfolgerung (Deutsch)

Diese Arbeit konzentriert sich auf zwei atmosphärische Messmethoden, die beide in der CLOUD-Kammer am CERN neu entwickelt und quantifiziert wurden. Im ersten Teil der Arbeit wurde eine neue Messtechnik zur Messung von Ammoniak, Aminen und Jodverbindungen vorgestellt (das „Water Cluster CI-APi TOF“). Bei der folgenden Charakterisierung des Instruments wurden Ammoniak-Nachweisgrenzen von 0.5pptv (Moleküle pro 10^{12} in der Luft vorhandener Moleküle) bei 278 Kelvin und 80 % relativer Feuchtigkeit festgestellt. Das Instrument kombiniert eine besonders kurze Reaktionszeit mit minimiertem instrumentellem Hintergrund aufgrund minimierter Oberflächen im instrumentellen Aufbau. Mit dem Wassercluster CI-API TOF wurde die Kondensation von Ammoniak und Salpetersäure auf neu gebildeten Partikeln quantitativ bei CLOUD nachgewiesen. Es zeigte sich dabei, dass sobald neu gebildete Partikel einen kritischen Durchmesser (von etwa 4–5 nm) erreichen, Partikel in Gegenwart von Ammoniak und Salpetersäure rapide wachsen können. Die kurze Ansprechzeit und der geringe instrumentelle Hintergrund des Water Cluster CI-API TOF erlaubten es, zu zeigen, dass Ammoniak aus der Gasphase entfernt wird und somit auf den Partikeln kondensiert. Dieser Prozess kann die Bildung neuer Partikel- und ihr anschließendes Wachstum in Großstädten mit hoher Umweltverschmutzung erklären.

In der Realität ist die Wahrscheinlichkeit, dass Partikel bei einer hohen Kondensationssenke dennoch anwachsen bevor sie durch größere Partikel entfernt werden höher, als in der Theorie vorhergesagt. Zukünftige Studien müssen einordnen, inwieweit das beobachtete schnelle Partikelwachstum durch Ammoniak- und Salpetersäure-Kondensation in Großstädten wirklich stattfindet. Die höhere Überlebenswahrscheinlichkeit neu gebildeter Partikel könnte in diesen Regionen auch anders erklärt werden, beispielsweise wenn nicht jede Kollision mit größeren Partikeln zur Entfernung des kleineren Partikels führt (wie oft angenommen wird) (Kulmala et al., 2017). Dazu sind jedoch Feldmessungen erforderlich, die unter anderem mit dem in dieser Arbeit gezeigten Water Cluster CI-API-TOF durchgeführt werden können. Erste Feldmessungen anhand von Satellitendaten weisen darauf hin, dass Ammoniak auch in der oberen Troposphäre vorkommt (Höpfner et al., 2016, 2019). Neuere Laborexperimente zeigen zudem, dass Ammoniak und Salpetersäure trotz der dort zu erwartenden geringen Konzentrationen zur Partikelneubildung in diesem Bereich beitragen könnten (Wang et al., 2022). Feldmessungen mit hoher Zeitauflösung in diesem Bereich könnten Aufschluss über die Beteiligung von Ammoniak und Salpetersäure geben und werden Teil zukünftiger Studien sein.

Im zweiten Teil dieser Arbeit wurde ein Instrument zur Erzeugung mehrfach geladener Teilchen unter atmosphärisch relevanten Bedingungen entwickelt (der „CHARGE“). Das Instrument wurde zunächst basierend auf elektrostatischen Simulationen und Laborexperimenten optimiert. Danach wurde es in der CLOUD-Kammer verwendet. Die von CHARGE erzeugten Partikel wurden entweder direkt der CLOUD-Kammer zugeführt oder mit einer XRay Quelle neutralisiert. Messungen mit Elektroaerosolanalysatoren zeigen, dass CHARGE erfolgreich mehrfach geladene Teilchen in ausreichender Menge erzeugt. Das Instrument ermöglicht die Durchführung quantitativer Experimente zur Evaluation der Effekte mehrfach geladener Teilchen in der Atmosphäre. Mehrere neue Experimente zur Bestimmung

dieser Effekte wurden entwickelt, mit speziellem Fokus auf atmosphärische Relevanz. Die Experimente sind im einleitenden Teil dieser Arbeit beschrieben. Es wurde eine neue Methode entwickelt, um Kollisionsratenkoeffizienten zwischen Ionen und Aerosolen als Funktion der Anzahl der Ladungen (am Aerosol) numerisch zu berechnen. Die Ergebnisse wurden mit aktuellen Theorien zur Berechnung dieser Koeffizienten verglichen.

Da es in diesem Bereich nur sehr wenige oder keine Messungen gibt (insbesondere in Abhängigkeit von der Anzahl der Ladungen), werden die in dieser Arbeit gezeigten Kollisionsratenkoeffizienten in Zukunft hilfreich sein, beispielsweise wenn neue Modelle zur Vorhersage von Kollisionsraten zwischen Ionen mit Aerosolen in der Atmosphäre evaluiert werden sollen. Sie können auch bei der Einordnung der Ergebnisse von mittlerweile häufig verwendeten sogenannten Molekular Dynamik-Simulationen hilfreich sein und als Vergleichsgrundlage dienen (Tamadate et al., 2020a, b). In Zukunft kann CHARGE verwendet werden, um Simulationen und Theorien zu bewerten, die Ladungseffekte in Wolken nahelegen. Beispielsweise kann evaluiert werden, wie schwer der Effekt von ladungsinduziertem Niederschlag unter dem Einfluss des elektrischen Felds der Erde im Vergleich zu anderen atmosphärischen Prozessen (wie etwa dem Aerosoleffekt) wiegt (Tinsley et al., 2000; Guo and Xue, 2021). Simulationen, wie in Guo und Xue (2021) gezeigt, können getestet und der Ladungstransfer von Partikeln während der Kollision quantitativ bewertet werden. Expansionsstudien unter dem Einfluss verschiedener elektrischer Felder (unter Verwendung von CHARGE) können durchgeführt werden, um die Simulationen von Guo und Xue (2021) zu bewerten.